

Life Cycle Performance Evaluation of an Air-Based Solar Thermal System

By

Joshua Reed Plaisted

A thesis submitted in partial fulfillment of the
requirements for the degree of

Master of Science
(Mechanical Engineering)

at the
University of Wisconsin – Madison
2000

Copyright 2000 Joshua Reed Plaisted

Approved by

Professor William A. Beckman

May 30, 2000

Abstract

Performance at the McKay center after 22 years of operation was characterized through experimental measurements of component parameters. Effects of the component parameters on systems level performance was evaluated using numerical simulation tools (TRNSYS) calibrated against actual operation of the building. Calibration of the collector arrays indicated degradations of 16 percent in $F_r(\tau\alpha)$ and 19 percent in F_rU_L on average for the two arrays installed at the site. Thermal losses from the pebble beds were characterized by conductances of 7.5 and 3.0 W/m²-C for the two beds, which far exceed the design conductance of 0.65 W/m²-C. Flow distributions within the beds were highly non-uniform with an average 3:1 flow ratio across the pebble beds.

Effects of component degradations did not directly translate into similar systems level degradations. Annual simulations performed under typical meteorological year (TMY2) conditions indicated that the high bed losses and non-uniform flow have resulted in a 1 percentage point decrease in the solar fraction. Degradations in the collector array had a more significant effect on system performance, lowering the solar fraction by 12 percentage points. Together, physical deteriorations of the solar components have lowered the solar fraction from an optimum of 45 percent to 32 percent.

The single largest effect on system performance was not attributable to a physical component, but to the control logic that governs system operation. Faulty operation of an air damper within the system and improper location of a control sensor were responsible for the low solar fraction of 15 percent representative of how the system was found at the inception of this study.

In-situ testing methods and novel calibration techniques are described that result in minimal cost and interference of system operation. Systems level calibrations employing daily integrated energy comparisons are also discussed along with the sensitivity of the model to load dynamics. Possible methods of fault detection for solar thermals systems and a minimal instrumentation package are presented that may prevent similar faults from compromising the performance of present and future solar installations.

Acknowledgements

No work stands on its own, but is instead the culmination of ideas, thoughts, and insights of others. Without the guidance of professors Bill Beckman and John Mitchell, very few of the ideas contained in this text would be culminated, they would simply remain half scattered thoughts. Thank you both for keeping me on track over the years, which for those who know me is no easy feat. My gratitude is extended to the Heckrodt foundation for providing the funding for this study, and to the staff of the UW physical plant and the McKay center for their help in carrying out the experimental investigations.

A special thanks is also extended to professor Sandy Klein, who humbles his students in intermediate thermodynamics, but later inspires them with his uncanny knowledge of how to approach unsolvable problems. Thank you Sandy for teaching me to apply the laws of thermodynamics and system boundaries in clever ways, even though I never seemed able to use them during those fifty-minute exams.

Without the humor and good spirit that exists in the solar lab, my time here would have felt much longer. Thanks to little Egypt and Germany for the company.

For providing balance in my studies, I'd like to thank everyone involved in the Institute for Environmental Studies. Without you I'd still believe that gasoline was cheaper than soda-pop, and that reed canary grass was a houseplant. Thank you for giving me a reason to study solar energy and the knowledge to back it up.

For my original child-like curiosities, my drive to understand everything, and the will to try, I thank my family. To my mother for teaching me that there are no stupid questions, just those afraid of asking them, and to my father who has always believed in me regardless of all the seemingly stupid questions I've pursued.

Well Michelle it's your turn now ... while I can thank everyone else for their insights and support in this work, I credit you with the inspiration behind it all.

*Somebody has to go polish the stars,
They're looking a little bit dull.
Somebody has to go polish the stars,
For the eagles and starlings and gulls
Have all been complaining they're tarnished and worn,
They say they want new ones we cannot afford.
So please get your rags
And your polishing jars,
Somebody has to go polish the stars.*

Shel Silverstein – A Light in the Attic

Author's Note

“So Josh, you drove here from Chicago right? Did you stop to get any gas?”

“Yup”

“How much did that gas cost? “

“Dollar-eight a gallon”

“Did you get anything to drink”

“Yeah, a Coke”

“And how much did that cost?”

“Seventy cents”

“What is that ... something like seven-fifty a gallon?”

Those words were the beginning of my introduction into energy as posed by professor Sandy Klein more than two years ago. His point was that to get a gallon of gasoline you had to pump it from a mile under ground, ship it by supertanker half-way around the world, refine it at the coast, pump it 1,500 miles to the mid-west, and then truck it to the gas station before it could be sold for a dollar-eight a gallon. By contrast, the soda started its life as tap water no more than a few hundred miles away. After being carbonated, sweetened, and colorized, the soda was canned and hauled a days drive to sell for seven-fifty a gallon. The final question Sandy asked was this: do you think you can compete with a source of energy that is 85% cheaper than soda-pop? That was the ante for renewable energy, beat soda-pop by 85% or fold your hand.

The trick in beating the “soda-pop” challenge is to think like an economist and not an engineer. The way the question was phrased assumed that the price of gasoline at the pump was identical to the cost of gasoline to society. Equating the values of price and cost is a dangerous assumption that is almost never valid in the world today. To explain how this so we must continue the “soda-pop” debate from the viewpoint of an environmental economist.

“When you filled up the car with gas, what happened to the old gas?”

“What do you mean?”

“Where did the gas that was put into the car last week go, did you drain it out?”

“No, it was burned in the engine.”

“So, the gas was vaporized, combusted, and then exhausted from the tailpipe?”

“Exactly”

“What was contained in this ‘exhaust’?”

“Well, a combination of things like nitrogen-oxides and unburned fuel vapors.”

“You mean the chemical precursors to ground level ozone?”

“Chemical huh to ground level what?”

“Those nitrogen-oxides and fuel vapors chemically react in the atmosphere to produce the smog and haze that hangs over most major U.S. cities.”

The environmental economist would proceed to tell you that smog and haze are strongly linked to asthma attacks (JAMA 1997), and that there are approximately 5 million children in this country affected by asthma¹. They will tell you that 50 million Americans (1 in every 5) live in areas where medical science has determined the air to be polluted to the point where it adversely affects human health². The final knot in their argument will be to tell you that 80% of all air pollution is caused by the combustion of fossil fuels for energy production. Their final question to you will be this: “Do you really think that the exposure of one-fifth of the population to elevated health risks is in any way comparable to the price of soda-pop?”

The true price of energy, as expressed through externalized health and environmental costs remains an area of much debate. Simply attempting to calculate the cost of pollution is an enormous endeavor³, and attempting to collect on those costs is even more difficult. What we must remember from this narrative is that a price does not always reflect the true cost, and that as a society we always pay the true cost, whether it is extracted from our health, our environment, or our personal finances. Wealth is not the amount of money in your pocket, it is the quality of your life.

Some in the policy arena have attempted to bring the cost and price of energy into equilibrium through the use of pollution permits (SO₂ cap and trade for acid rain), regulations (the Clean Air Act, and Montreal and Kyoto protocols), and even lawsuits (New York’s recent lawsuit against mid-western utilities for NO_x emissions). Applying any of these methods requires a

¹ The total number of people affected in the U.S. is more than 14 million (JAMA 2000).

² These pollution levels are defined by National Ambient Air Quality Standards (NAAQS) set by the Clean Air Act (CAA). Actual annual data on compliance with NAAQS is available from the USEPA.

³ If interested, the reader should review a health cost study recently performed by the Harvard School of Public Health (Levy et. al 2000), which estimates the health impact from 2 utility coal plants in Massachusetts as exceeding \$1,000,000,000 annually.

complex and costly series of actions on state, federal, and sometimes international levels. Such actions might not always be economically efficient, socially equitable, or legally sufficient to protect basic human rights.

The optimal balance between economic prosperity and environmental quality that energy policy initiatives hope to achieve may not be possible. The economy and the environment are not competing interests to be weighed against one another, they are the same thing. The economy is in fact a wholly owned subsidiary of the natural ecosystem (Daly 1996). Everything you have at one time came from the environment and will at some time return to it, our planet is a closed system. From this vantage, the use of the earth's atmosphere as a combustion chamber for fossil fueled energy is not only ill-advised from an environmental perspective, it is economically inefficient.

There is a source of energy that can power the human economy without degrading the environmental economy. This source of energy has no known detrimental effects, it has existed without interruption for several billion years, and more of it falls on this planet every day than our current population of 6 billion people would consume in the next 27 years (NREL 2000). When you wake up tomorrow morning, look up and look out. Thermonuclear fusion energy is not science fiction, it's a scientific fact that is hanging in the sky. You can call me a fusion scientist, but I prefer the more practical title of solar engineer.

What follows is a story about sunshine. It's about an old system that provides some of the heating needs for a nature center here on campus. It's a story of what was done right, and well ... what we wished we'd done right in retrospect. Perhaps more importantly, it contains some hints and methods of how to diagnose solar heating systems, how to decide what's important within them, and how to design better ones for the future. In essence, the next few hundred pages are simply a polishing rag.

To an inspiration of so many children and adults alike ... sorry it took so long getting this one out Shel, I simply forgot that some stars are not all that far away.

Josh Plaisted
Madison, WI 2000

Table of Contents

1	Introduction.....	1
1.1	Methodology.....	1
1.2	History of the McKay Center.....	3
2	Physical Layout of the McKay Center.....	7
2.1	Building Orientation.....	7
2.2	HVAC System Layout.....	7
2.3	Arrangement of Collector Array.....	8
2.4	Construction of Pebble Bed Storage.....	9
2.5	Auxiliary Equipment.....	11
3	Empirical Measurements.....	13
3.1	Thermal Energy in Duct Airflows.....	13
3.2	Temperature Measurements within Air Ducts.....	13
3.3	Ambient Temperature Measurements.....	15
3.4	Velocity Measurements Within Air Ducts.....	17
3.5	Measurements of Solar Radiation.....	19
3.6	Solar Test Interval.....	20
3.7	System Calibration Interval.....	20
4	Solar Collector Array.....	21
4.1	Analytical Framework for Evaluation of Flat-plate Collectors.....	21
4.2	Absorbed Solar Radiation.....	24
4.3	Standard SRCC Ratings Procedure.....	26
4.4	Two Point Collector Characterization.....	31
4.5	Determination of the Incidence Angle Modifier.....	37
4.6	Predictions of Original Array Performance.....	38
4.6.1	Simple Method of Flow Rate Correction.....	39
4.6.2	Detailed Method of Flow Rate Corrections.....	39
4.6.3	Results of the Detailed Correction Method.....	44
4.7	Visual Inspection of Collector Arrays.....	47
4.8	Synopsis.....	48
5	Pebble Bed Storage.....	51
5.1	Schumann Analysis of Pebble Bed Storage.....	51
5.2	Variables Employed in Schumann Analysis.....	52

5.3	Numerical Solutions of the Schumann Equations	53
5.4	Results of the Simple Schumann Model.....	53
5.5	Empirical Determination of Bed Loss Coefficient	55
5.6	Non-Uniform Flow Through Pebble Bed	57
5.7	Relaxing The Uniform Flow Constraint	58
5.7.1	Ordered Profile	59
5.7.2	Cosine Flow Distribution.....	65
5.8	Visual Inspection of Bed Interior.....	71
5.9	Final Pebble Bed Model Used in TRNSYS Simulations.....	72
5.10	Flow Profiles Under Discharge Conditions	74
5.11	Inferring Mass Flows from Thermal Profiles	77
5.12	Calibration of Pebble Bed Temperature Sensors	79
5.13	Air Quality Tests.....	84
5.14	Synopsis.....	86
6	Building Loads and Auxiliary Equipment	89
6.1	Thermal Model of Building Zones	89
6.1.1	Interior Capacitance.....	90
6.1.2	Zone Air Mass	91
6.1.3	The Building Shell.....	92
6.2	Passive Solar Gains.....	95
6.3	Internal Gains.....	95
6.4	Sol-Air Temperature	97
6.5	Auxiliary Furnace Capacity	100
6.6	Synopsis.....	101
7	TRNSYS Model Development	105
7.1	Simulation Framework & Component Layout	105
7.2	Simulation Control Logic	105
7.2.1	Forced Mode Operation	106
7.2.2	Existing Control Logic.....	108
7.2.3	Optimal Storage Control Logic.....	110
7.3	Temperature Interrupts	112
7.4	Ambient Conditions.....	112
7.5	Zone Simulation Outputs.....	113

7.6	TRNSED Simulation Decks	114
7.7	Simulation Summary Interface	115
7.8	Synopsis.....	116
8	Forced Mode Calibration	117
8.1	Comparison of Energies Within Each Mode of Operation	117
8.1.1	Malfunctioning Air Dampers.....	120
8.1.2	Use of Temperature Interrupts	123
8.1.3	Results of Mode Energy Comparisons	125
8.2	Zone Energy Calibrations	129
8.3	Dynamic Mode Calibration of Pebble Bed Sensors.....	137
8.4	Synopsis.....	140
9	Free Mode Calibration	143
9.1	Defining the Proper Operation of Building Modes.....	143
9.2	Performance of Simulated Control Logic	145
9.3	Synopsis.....	149
10	Annual Simulation Results	151
10.1	Definition of Key Performance Metrics	151
10.1.1	Solar Fraction (SF).....	151
10.1.2	Cost Reduction Factor (CRF)	152
10.1.3	Emissions Reduction Factor (ERF)	153
10.1.4	Coefficient of Performance (COP)	154
10.2	Description of Simulated Configurations	154
10.3	Results of Annual Simulations	156
10.4	Synopsis.....	163
11	Sensitivity of the Simulation to Load Dynamics	165
11.1	Scheduling of Internal Gains	165
11.2	Effects of the Sol-Air Temperature.....	166
11.3	Effects of the Simulation Timestep.....	168
11.4	Synopsis.....	170
12	Discussion and Recommendations	173
12.1	Component Degradation and System Performance	173
12.2	Recommendations and Future Work	174
12.3	A Narrative on Component and System Calibrations.....	177

Bibliography	181
Appendix A History of Dairy Forage and Vet-Med Center	185
Appendix B Air Handler Flow Rates.....	189
Appendix C TRNSYS Simulation Framework.....	191
Appendix D CD-ROM Files	195

List of Figures

Figure 1.2.1 View of the McKay center from the South-West side.....	3
Figure 2.1.1 Floor plan of McKay Center.....	7
Figure 2.2.1 Layout of solar zone heating systems.....	8
Figure 2.3.1 Internal ducting of series 2000 collectors. Row labeled 2004 does not exist at the McKay Center (Solaron Corp.).....	9
Figure 2.4.1 Top view of pebble bed layout.....	10
Figure 2.4.2 Isometric view of typical pebble bed construction (Solaron Corp.).....	10
Figure 3.2.1 Calibration curve for Johnson Controls 2000 series RTD sensor. Polynomial fit used for final temperature adjustments also shown.	15
Figure 3.3.1 Ambient air temperature sensor location and housing at the McKay Center	16
Figure 3.3.2 Comparison of hourly ambient temperatures measured by NOAA weather station to those measured with portable instrumentation at the McKay Center from November 18 th to December 31 st 1999. Solid line illustrates where identical temperatures would lay.....	17
Figure 3.4.1 Hot wire anemometer calibration showing linear regression of the correction factor (0.7025) and the RMS fit.....	18
Figure 3.4.2 Velocity profile on back side of basement solar air handler.	19
Figure 4.1.1 Layout and construction schematic of Soilaron series 2000 collector.	21
Figure 4.2.1 Incidence angle modifier effects representative of single and double glazed cover systems.....	25
Figure 4.3.1 Plot of operating points for Solaron 2000 air heater based on equation 4.3.1. Collector has been characterized at two specific mass flow rates (G_o is mass flow rate per unit collector area).	27
Figure 4.3.2 SRCC plot of Solaron 2000 air heater performance. Collector flow rate is G_o and H_T corresponds to surface irradiance I (Oonk 1976).	29
Figure 4.3.3 SRCC plot for office collector array for clear sky days during the system calibration interval (February 22) and the solar test interval (May 13). b_o was assumed to be -0.45 for the cover system.	30
Figure 4.4.1 Dimensionless temperature difference vs. dimensionless capacitance rate for collectors under night-time testing. Shaded bands indicate operating ranges of both office and basement arrays over the solar test interval.	33

Figure 4.4.2 Illustration of 2 point fit for the office array. Operating points below 35 degrees are plotted and then least squares fit with a line defined by the slope of $F_r U_L$ to determine the intercept $F_r(\tau\alpha)$.	34
Figure 4.4.3 Measured (points) and predicted (solid line) office collector array outlet temperatures TS-5 over the solar test interval. Shaded bands indicate intervals used for parameter fitting.	35
Figure 4.4.4 Measured (points) and predicted (solid line) basement collector array outlet temperatures TS-5 over the solar test interval. Shaded bands indicate intervals used for parameter fitting.	36
Figure 4.4.5 Calibration plots for the collector arrays over the solar test interval.	36
Figure 4.5.1 Incident angle modifiers for standard untreated 2-cover system (solid line) and Solaron 2000 2-cover system (points).	37
Figure 4.6.1 SRCC curves of the original and measured performance for the arrays. Shaded bands indicate uncertainty in measured performance.	46
Figure 4.7.1 Closeup photographs of collectors within the arrays showing a variety of degradation mechanisms including catastrophic failure of the cover seals (a,b) and the associated moisture penetration, condensation, and deposits inside the cover system (c).	47
Figure 5.4.1 Measured (points) and predicted (solid line) basement bed outlet temperatures TS-8 for the simple Schumann model over the solar test interval.	54
Figure 5.5.1 Accumulated bed energies over the solar test interval for actual (points) and predicted (solid line) bed outlet temperatures for $U_{bed} = 0$. Dashed line illustrates the losses.	56
Figure 5.5.2 Accumulated bed energies in the basement system over the solar test interval for actual (points) and predicted (solid line) bed outlet temperatures for $U_{bed} = 3 \text{ W/m}^2\text{C}$.	57
Figure 5.7.1 Layout of 10 bed segment model used in non-uniform flow models. Location of actual inlet (TS-7) and outlet (TS-8) temperature sensors shown.	58
Figure 5.7.2 Volumetric flow distribution through pebble bed found by Persons (1978) in work on the Arlington house.	59
Figure 5.7.3 Flow distributions through bed segments according to equation 5.7.2 where $R_{bed} = 2$ (a) and $R_{bed} = 4$ (b). The sum of flow percentages for all segments will always be unity.	61

Figure 5.7.4 Contour plot of integrated error ($Error_{bed}$) for basement pebble bed subject to flow distributions of equation 5.7.2.....	62
Figure 5.7.5 Measured (points) and predicted (solid line) bed outlet temperatures (TS-8) for the ordered profile distribution of the Schuman model over the solar test interval. $R_{bed}=3.44, n=1.01, U_{bed}=3$	63
Figure 5.7.6 Calibration plot of measured vs. model predicted bed outlet temperatures of figure 5.7.5.....	64
Figure 5.7.7 Flow velocity non-uniformities found by Hollands (1984) in experimental pebble bed. Relative air velocities represent R_{bed} and are measured 1/6 th of the way down the bed height. Pressure ratios correspond to pressure drop in the plenum (P_d) over the pressure drop through the pebble mass (ΔP). Pressure ratios increase for larger diameter rocks due to lower pressure drop through pebble mass.	65
Figure 5.7.8 Top view of the bed showing the division of segment areas for the cosine flow distribution. Segments are equally spaced from center to edge.....	66
Figure 5.7.9 Distribution of air velocities and flow rates under the cosine distribution model for $R_{bed}=2$ (solid line) and $R_{bed}=4$ (dashed line) in the basement bed.	67
Figure 5.7.10 Plot of integrated error ($Error_{bed}$) for basement pebble bed subject to cosine flow distribution.	69
Figure 5.7.11 Measured (points) and predicted (solid line) bed outlet temperatures TE-8 for cosine flow distribution of the Schuman model over the solar test interval. $R_{bed}=1.94, U_{bed}=6$	70
Figure 5.7.12 Calibration plot of measured vs. model predicted bed outlet temperatures of figure 5.7.11.....	71
Figure 5.8.1 Views of plenum interiors on basement bed taken through boroscope. Vertical bar in upper plenum is a standard duct support, top of pebble mass is visible at base of photo. Bottom plenum shows bond beam blocks, lath grating and the bottom edge of the pebble mass.....	72
Figure 5.9.1 Calibration plots of measured vs. model predicted bed outlet temperatures over the solar test interval for 3 segment infinite NTU models employed in TRNSYS.....	74
Figure 5.10.1 Comparison of measured (points) to predicted (solid lines) office bed performance over second solar test interval. Model was driven with measured bed inlet temperature TS-7 to predict outlet temperature at TS-8 during mode 3	

(charging bed). During mode 2 (discharging bed), the bed was driven in reverse flow by TS-8 to predict the temperature leaving the top of the bed at TS-7.....	75
Figure 5.10.2 Junction box of TE-7 for the basement system on left with access hole to c-channel highlighted. Picture on right shows the junction box cover onto which the mastic putty sealant has melted and fallen.....	76
Figure 5.10.3 Flow distributions found by Persons (1978) during bed discharge.....	77
Figure 5.11.1 Measured bed inlet temperature TS-7 (points) and predicted bed outlet temperatures (solid lines) at 1008 and 1512 ft ³ /min over the last two days of the solar test interval. The modeled flow rates represent levels 20 percent above and below the actual flow rate of 1260 ft ³ /min for the basement bed.	78
Figure 5.11.2 Integrated bed error for various assumed flow rates in basement system. System flow rate as measured by hot wire anemometer was 1260 CFM.	79
Figure 5.12.1 Measured bed inlet temperature TS-7 (solid line) and sensor temperature TS-9 (points) over solar test interval.	80
Figure 5.12.2 Schematic of wall layout used for numerical modeling of sensor parameters.....	81
Figure 5.12.3 Measured (points) and modeled (solid line) basement bed sensor temperature (TS-9) over the solar test interval after parameter optimization.....	82
Figure 5.12.4 Measured (points) and modeled (solid line) office bed sensor temperature (TS-9) over the solar test interval after parameter optimization.....	83
Figure 5.13.1 Spectrographs of air samples taken at the McKay center (courtesy University Health Services).	85
Figure 6.1.1 Schematic of thermal zone model.	89
Figure 6.1.2 Isotherms and heat paths through soil for building foundations (ASHRAE 1997).....	94
Figure 6.1.3 Heat paths and loss coefficients for building foundations taken from Latta and Bolieau.	94
Figure 6.4.1 Representation of solar radiation components incident on building shell.....	99
Figure 7.2.1 Operating mode histogram for office system over system calibration interval. Operating instances reflects the number of times the actual system operated at the specified runtime fraction (calculated for 15 minute timesteps).	107
Figure 7.2.2 Integrated mode run times for exact measured (points) and rounded (solid lines) values for the office system over system calibration interval.....	108

Figure 7.2.3 Control Logic diagrams for the enabling of the solar arrays (on left) and HVAC system operation (on right). Differential control logic setpoints are provided in table 7.2.1.	109
Figure 7.5.1 Screen-shot of online plotter showing collector and bed outlet temperatures for the basement over the solar calibration interval (temperature interrupts are enabled).....	113
Figure 7.6.1 Screen-shot of TRNSED interface (on left) and TRNSYS input file (on right) for the basement zone.	115
Figure 7.7.1 Sample screen-shot of annual integrated building energies including total predicted gas usage (including hot water loads and furnace efficiencies).....	116
Figure 8.1.1 Measured (points) and simulated (solid lines) integrated mode energies for basement system with temperature interrupts. Energies have been parsed to account for full duration of operation at the McKay center.	119
Figure 8.1.2 Measured (points) and simulated (solid lines) integrated mode energies for office system with temperature interrupts. Energies have been parsed to account for full duration of operation at the McKay center.....	120
Figure 8.1.3 Measured (points), originally predicted (dashed line), and calibrated (solid line) bottom plenum temperatures for basement pebble bed. Shaded bands indicate times of near constant furnace firings (mode 4) when solar system was idle.....	121
Figure 8.1.4 Measured (points), originally predicted (dashed line), and calibrated (solid line) bottom plenum temperatures for basement pebble bed. Shaded bands indicate times of near constant furnace firings (mode 4) when solar system was idle.....	122
Figure 8.1.5 Measured (points) and simulated (solid lines) integrated mode energies for basement system with only TS-3 temperature interrupt enabled. Energies have been parsed to account for full duration of operation at the McKay center.	124
Figure 8.1.6 Measured (points) and simulated (solid lines) integrated mode energies for office system with only TS-3 temperature interrupt enabled. Energies have been parsed to account for full duration of operation at the McKay center.	125
Figure 8.1.7 Calibration plots of daily integrated energies for office and basement systems. Temperature interrupts limited to TS-3.....	126
Figure 8.1.8 Measured (points) and predicted (solid line) pebble bed discharge temperature (TS-7) over portion of system calibration interval.	127

Figure 8.1.9 Daily integrated energies from modes 2 and 3 of operation for the office pebble bed.....	128
Figure 8.2.1 Comparison of cumulative integrated values of $q_{required}$ (points) and q_{supply} (solid line) for the basement zone.....	130
Figure 8.2.2 Percent deviations in q_{supply} from $q_{required}$ based on daily integrated values for the basement zone.....	131
Figure 8.2.3 Zone temperatures in the basement zone resulting from energy supply and demand requirements specified in figure 8.2.1. Measured zone temperatures are indicated by points, and modeled temperature shown as solid line.....	131
Figure 8.2.4 Comparison of cumulative integrated values of $q_{required}$ (points) and q_{supply} (solid line) for the office zone.....	133
Figure 8.2.5 Percent deviations in q_{supply} from $q_{required}$ based on daily integrated values for the basement zone.....	133
Figure 8.2.6 Zone temperatures in the basement zone resulting from energy supply and demand requirements specified in figure 8.2.1. Measured zone temperatures are indicated by points, and modeled temperature is shown as solid line.....	134
Figure 8.2.7 Comparison of cumulative integrated values of $q_{required}$ (points) and q_{supply} (solid line) for the office zone with days 59, 62, and 65 removed from the records.....	135
Figure 8.2.8 Comparison of cumulative integrated values of $q_{required}$ (points) and q_{supply} (solid line) for the lecture hall.....	136
Figure 8.2.9 Percent deviations in q_{supply} from $q_{required}$ based on daily integrated values for the lecture hall.....	136
Figure 8.3.1 Measured (points) and modeled (solid line) temperatures for pebble bed sensor TS-9 in basement system. Shaded bands indicate durations where model departs from measured values.....	137
Figure 8.3.2 Measured (points) and modeled (solid line) temperatures for pebble bed sensor TS-9 in basement system. Stagnation fraction is 0.75.....	139
Figure 8.3.3 Measured (points) and modeled (solid line) temperatures for pebble bed sensor TS-9 in office system. Stagnation fraction is 0.75.....	140
Figure 9.1.1 Cumulative mode energies for basement HVAC system over system calibration interval as calculated through forced mode calibrations.....	144
Figure 9.1.2 Cumulative mode energies for office HVAC system over system calibration interval as calculated through forced mode calibrations.....	144

Figure 9.2.1 Comparison of cumulative mode energies for basement HVAC system over system calibration interval. Fixed mode quantities are indicated by points and free mode quantities are shown as solid lines.	145
Figure 9.2.2 Comparison of cumulative mode energies for office HVAC system over system calibration interval. Fixed mode quantities are indicated by points and free mode quantities are shown as solid lines. Values from days 59, 62, and 65 have been removed from the data set.	147
Figure 9.2.3 Comparison of cumulative mode energies for basement HVAC system over system calibration interval with the thermal capacitance of the wall and air mass switched. Fixed mode quantities are indicated by points and free mode quantities are shown as solid lines.	148
Figure 9.3.1 Flowchart of model calibration process.	149
Figure 10.3.1 Integrated energy quantities supplied to load for case 2.	157
Figure 10.3.2 Integrated operating costs for case 2.	157
Figure 10.3.3 Integrated CO ₂ emissions for case 2.	158
Figure 10.3.4 Annual operating histograms for collector arrays under existing controls (case 3) and optimal controls (case 4). The bins on the x-axis define the collector operating point, and the dashed line indicates the operating point for zero collector efficiency.	161
Figure 11.1.1 Comparison of annual solar operating energies for case 7 of calibrated model (points) and identical system with uniform internal gains.	166
Figure 11.2.1 Comparison of annual solar operating energies for case 7 of calibrated model (points) and identical system with uniform internal gains and omission of the sol-air temperature.	167
Figure 11.3.1 Operating energies for case 7 run with 15 minute (points), 30 minute (solid line), and 60 minute (dashed line) timesteps.	170
Figure 12.2.1 Schematic of ideal diagnostic sensor locations for air based systems.	177

List of Tables

Table 3.2.1 Resistance offsets used for calibration of air duct sensors.	14
Table 3.4.1 System loop airflows for solar and main air handlers.....	19
Table 4.4.1 Collector array parameters.....	34
Table 4.6.1 Variables used to estimate T_{pm} at test conditions.....	44
Table 4.6.2 Variables used to estimate tau-alpha of the cover absorber system.....	44
Table 4.6.3 Summary of collector array properties for isothermal boundary condition in absorber flow channel.....	46
Table 4.6.4 Summary of collector array properties for adiabatic boundary condition in absorber flow channel.....	46
Table 5.9.1 Summary of variables used for modeling pebble beds within TRNSYS	73
Table 5.13.1 Averaged fungal spore counts from various sample sites at the McKay center.....	86
Table 5.14.1 Final pebble bed parameters employed in TRNSYS simulation model.	87
Table 6.1.1 Values of interior thermal capacitance (based on floor area) used in simulation model.....	90
Table 6.1.2 Calculation of wall resistance in lecture hall. Wall U-value is 0.47 W/m ² -C.....	93
Table 6.3.1 Electric consumption for McKay Center for 1999.	96
Table 6.3.2 Air handler fan motor power consumption at steady state operation. Solar air handlers were operated in mode 3.	97
Table 6.5.1 Furnace temperature rises and capacities.....	100
Table 6.6.1 Summary of building zone parameters used in simulation model.....	103
Table 7.2.1 Differential controller inputs and deadbands.....	110
Table 10.3.1 Annual simulation results for cases under study.....	159
Table 11.1.1 Comparison of performance metrics for case 7, and case 7 with uniform gains. All energies are in therms.....	166
Table 11.2.1 Comparison of performance metrics for case 7, and case 7 with uniform gains and omission of the sol-air temperature. All energies are in therms.	168
Table 11.3.1 Comparison of performance metrics for case 7, and case 7 with uniform gains and no sol-air temperature. All energies are in therms.....	169

Nomenclature

Roman

A_{bed}	Cross sectional area of pebble bed in direction of flow (m^2)
b_o	Incidence angle modifier coefficient
Bi	Biot number
C_{air}	Specific heat of air (J/kg)
C_{rock}	Specific heat of rocks in pebble bed (J/kg)
Cst	Cost (\$USD)
D_{rock}	Diameter of rocks in pebble bed (m)
F'	Collector efficiency factor
F_R	Collector flow factor
G_o	Mass flow rate per unit area ($kg/m^2\cdot s$)
h	Convection heat transfer coefficient ($W/m^2\cdot ^\circ C$)
h_o	Combined radiation and convection heat transfer coefficient ($W/m^2\cdot ^\circ C$)
h_r	Linearized radiation heat transfer coefficient ($W/m^2\cdot ^\circ C$)
h_v	Volumetric heat transfer coefficient ($W/m^3\cdot ^\circ C$)
I	Incident solar radiation (W/m^2)
$K_{\alpha\alpha}$	Incidence angle modifier
L_{bed}	Effective length of pebble bed (m)
\dot{m}	Mass flow rate (kg/s)
n	Inflection of bed flow distribution
N_{nodes}	Number of finite element nodes for modeling of pebble bed
NTU_c	Corrected NTU for conduction within rocks
Nu	Nusselt Number
P	Power (W)
P_{bed}	Perimeter of pebble bed wall (m)
R	Thermal Resistance ($m^2\cdot ^\circ C/W$)
R_{flow}	Ratio of maximum to minimum flow within pebble bed
R_{stag}	Stagnation ratio in upper plenum of pebble bed

Ra	Rayleigh Number
Re	Reynolds Number
q''	Energy flux per unit area (W/m^2)
Q	Energy (J)
\hat{Q}	Energy delivered to load (J)
S	Absorbed solar radiation (W/m^2)
t	Time (s)
T	Temperature ($^{\circ}C$)
U_{b-e}	Back and edge loss coefficients of solar collector ($W/m^2-^{\circ}C$)
U_{bed}	Conductance of wall insulation in pebble bed ($W/m^2-^{\circ}C$)
U_L	Solar collector plate loss coefficient ($W/m^2-^{\circ}C$)
U_o	Conductance from collector fluid to environment ($W/m^2-^{\circ}C$)
\dot{V}	Volumetric flow rate (m^3/s)

Greek

α	Absorbance of surface
β	Slope
ε	NTU effectiveness, long-wave emittance
η	Thermodynamic efficiency
θ	Dimensionless capacitance rate
ρ_{air}	Density of Air (kg/m^3)
ρ_{rock}	Density of rocks in pebble bed (kg/m^3)
τ	Short wave transmittance
v	Void fraction in pebble bed

Acronyms and Abbreviations

ACH	Air Changes per Hour
AHU	Air Handling Unit
ASHRAE	American Society of Heating Refrigeration and Air-conditioning Engineers
CFM	Cubic Feet per Minute
COP	Coefficient of Performance
CRF	Cost Reduction Factor
ERF	Emission Reduction Factor
EES	Engineering Equation Solver
HVAC	Heating Ventilation and Air-conditioning
ISIS	Integrated Surface Irradiance Study
MAHU	Main Air Handling Unit
MD	Motorized Damper
NBS	National Bureau of Standards
NIST	National Institute of Standards and Technology
NOAA	National Oceanographic and Atmospheric Administration
NREL	National Renewable Energy Laboratory
PDCB	Para-Dichlorobenzene
RTD	Resistance Temperature Detector
SAHU	Solar Air Handling Unit
SF	Solar Fraction
SRCC	Solar Ratings and Certification Center
TMY	Typical Meteorological Year
TRNSYS	Transient Simulation Program
TRNSED	Transient Simulation Program Editor
TS	Temperature Sensor

1 Introduction

The central theme of this study is to determine whether solar thermal systems installed two decades ago still perform within original expectations. Moreover, if the systems have degraded what was the cause, what is the solution, and how is it best diagnosed?

Answering these questions requires a range of technologies from measurement techniques to high level simulation tools, that when combined together are able to offer broad insights into system performance. Through the use of numerical tools, datasets of over 1,000,000 measurements are reduced to a small handful of performance parameters describing each building component. These components are then combined in a simulation modeling environment to predict performance of the entire system. Once this simulated system has been trained to behave identically to the actual solar system through successive calibrations, it is used to extrapolate behavior of the system to annual operation under a range of conditions. What follows is a description of how these tools are developed, how they can be applied, and what they are able to predict, diagnose, and suggest for the solar system installed 22 years ago at the McKay center.

1.1 Methodology

Of the three solar systems installed at the University of Wisconsin in the late 70's and early 80's, only one is examined in detail in this study. The system at the Dairy Forage Center was removed in 1995 due to water damage from the solar array and a similar installation at the Veterinary Medicine Building may suffer the same fate. A discussion of the histories of both these systems can be found in appendix A. The cornerstone of this work is the system at the McKay center located in the University of Wisconsin Arboretum.

Starting from a component level, the system at the McKay center was experimentally characterized with respect to model parameters typically used in the field. These included the $F_r U_l$ and $Fr(\tau\alpha)$ of the collector array, and the effectiveness and flow distribution within the pebble bed storage. These calibrated components were then combined together with the actual building load and control logic in a computer simulation environment (TRNSYS) to predict annual building energy use. Final model validations were based on a comparison of integrated energy quantities over a month-long period in the late winter of 1999. The solar fraction of the installed system was then calculated by running the model with Typical Meteorological Year (TMY) weather data over a simulated year of operation.

Degradation of system components was assessed through a comparison of current parameters to those derived from test data of the original collectors made by the manufacturer. The effects of component degradation on total system performance were then determined by adjusting these component parameters with the model. Additionally, the effects of control strategies on system performance were calculated with reference to a theoretically optimal control strategy. Other avenues of interest were explored as the limits of certain modeling assumptions were discovered during the calibrations. Scheduling of internal gains, the sol-air temperature, and the building capacitance all had significant effects on the modeling results. Proper treatment of these effects is discussed in the relevant sections of the text.

Methods of in-situ testing for solar installations are also described. Because the McKay center is not a dedicated research installation, only non-intrusive methods were employed that minimally interfered with normal system operation. The methods should therefore find ready application in troubleshooting and performance monitoring of other real world systems. The equipment required for characterization was found to be minimal and total system calibration was possible with only three temperature sensing elements. Moreover, thermal characteristics of the pebble bed storage made it possible to infer airflow rates within the system loop from these same temperature elements thereby eliminating the need for mass flow instrumentation. With the models and methodology described in this work it would be possible to replicate these results with very low cost automated data logging equipment in a 5-day span.

1.2 History of the McKay Center



Figure 1.2.1 View of the McKay center from the South-West side

The McKay center was originally constructed in 1976 without the solar system due to budget constraints. However, the design did include a 55 degree slope on the south roof and a east-west orientation so that it could later accommodate the solar array. Listed below is a brief timeline of the history of the solar installation at McKay that will guide our discussion.

- November 1976: UW Chancellor Edwin Young authorizes the release of \$30,000 dollars in arboretum trust funds to match an equal amount provided by the state building commission for installation of the solar system.
- April 1977: Chief designers Harold Olsen and Dan Dudley draft original document that forms the basis of a request for proposals from equipment manufacturers on the solar system
- August 1977: Oregon Heating & Air Conditioning provides lowest bid of \$53,790 for installation of an air based system from the Solaron Corporation and is awarded the contract.

- March 1978: Final inspections made by Oregon Heating & Air Conditioning including measurements of flow rates, pressure drops, and fan speeds. Solar system accepted by University planning and construction subject to small corrections¹.
- February 1980: Dr. George Löff, president of the Solaron Corporation makes a visit to the McKay center at the request of Dr. Jack Duffie, director of the Solar Energy Laboratory. Several issues concerning the air handlers, damper operation and snow accumulation are the topics of discussion. These issues are apparently remedied in the following months.
- August 1987: Dan Dudley, one of the original systems designers performs a visual inspections of system operation as well as an approximate energy analysis based on degree days and gas meter usage. Results indicate that since 1983 the system has not significantly contributed to building energy requirements. Faulty damper operation and poor location of motors for the air handlers are identified as the main causes.
- May 1991: Johnson Controls receives contract to completely retrofit the HVAC systems at the McKay center with direct digital controls (DDC) for \$18,000. Over two dozen temperature sensing elements are included to monitor operation of the solar subsystem.
- September 1998: Through a grant provided by the Heckrodt foundation, this work began to calibrate and assess systems level performance at the McKay center

Many of the early issues that surfaced for Dr. Löff's visit in 1980 resulted from an inexperience of individuals in the solar field with the new technology. Accumulation of snow on the overhang just below the collector array is one of myriad examples. Following any significant snowfall, the snow layer covering the array would slide off and deposit on the overhang immediately below. After several storms, the accumulation of snow on the overhang would force the layer to build up on the array itself. To alleviate this problem, Dr. Löff suggested the addition of a black anodized sheet connecting the base of the array to the edge of the overhang on the collector sections that housed the control sensor. Snow would then slide directly off these collectors to the deck below clearing these collectors. The control sensor would then enable the

¹ Issues indicated in the March 28th correspondance from R.E. Zach relate to access locations on temperature elements, proper labeling of components and schematics, damper linkage adjustment, and balancing of airflows between the main and solar air handling units.

entire array, leading it into what could best be described as a “defrosting” mode. In a memorandum to then state senator Fred Risser, the only other alternative was mentioned in the following excerpt taken from a memorandum written by the director of the McKay Center:

“If this test fails [the anodized sheet] we shall probably have to build a catwalk on which a snowblower can be operated to remove accumulations as they start, below the panels.”

The anodized sheet was a success and it can be seen on the left side of the array in figure 1.2.1. Other issues persisted with the largest being the location of the fan motors, which went uncorrected until Dan Dudley’s investigation of 1987. By installing the fan motors inside the air handlers, Solaron had exposed them directly to collector outlet temperatures that could exceed 180 °F. Neither the motors nor the wiring were rated for these temperatures and in the winter of 1978 a similar Solaron Air Handler installed at the Solar Energy Laboratory’s Arlington house caught fire when the insulation on the factory installed wiring overheated (Wallace 1978). Failures at the McKay center were less dramatic, but just as severe requiring the frequent replacement of burned-out fan motors. Following the recommendations outlined in Dudley’s report, physical plant personnel cut slots in the cabinets of the air handlers and located the blower motors on external frames with the belts running through the cabinet walls. A drawback of this design is infiltration of air through the belt slots creating a leak in the system.

Operation of the system controls has remained an ongoing issue which resulted in the complete retrofit of 1995. Original installation plans excluded mode monitors and temperature indicators due to financial constraints. Without any diagnostic tools, troubleshooting of system operation was near impossible and in 1980 mode controllers were installed as were thermometers located at key sites in the ductwork. In the mid to late 80’s this system appeared to fail as well. Without any documentation or schematics, the physical plant decided that the best course of action was a complete retrofit to the DDC system offered by Johnson Controls. This was the last major work performed on the system before this study commenced.

2 Physical Layout of the McKay Center

2.1 Building Orientation

The center is located on the West side of the University of Wisconsin arboretum. Figure 2.1.1 shows that the center is properly oriented to accommodate a solar array. The long axis of the building is set east-west, and 1,460 square feet of roof area is oriented due south at a slope of 55 degrees. The upstairs of the building contains a reception area, offices, and lecture hall. The basement houses an additional workforce of 15 individuals as well as mechanical rooms and storage. The building footprint on each level is approximately 4,600 ft².

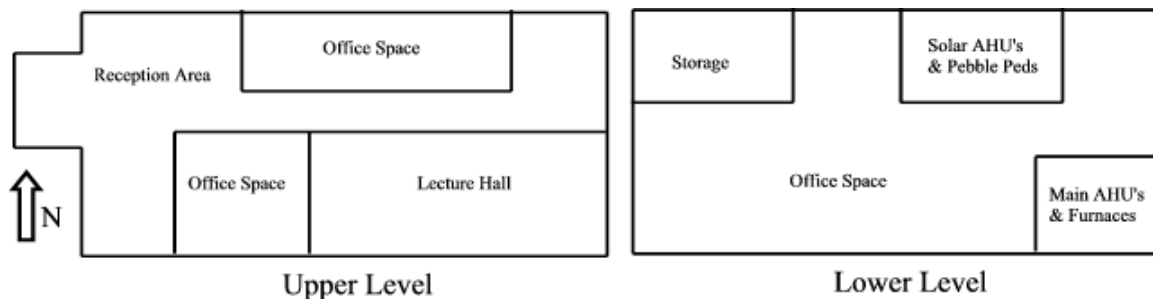


Figure 2.1.1 Floor plan of McKay Center

2.2 HVAC System Layout

Three separate air handling systems service the different zones within the building. Both the upstairs offices (including the reception area) and the basement are serviced by solar subsystems while the lecture hall relies on a traditional HVAC design with no solar component. A schematic of the HVAC system layout for the solar assisted zones (upstairs offices and basement) is shown in figure 2.2.1 and is identical for both zones. Labeling of the temperature sensors and motorized dampers is made in this figure to inform the reader of the physical location of these items when referred to in later sections. The solar enabled HVAC systems are able to operate in one of four possible modes as dictated by the control system:

Mode 1: Direct heating of building space with airflow from the solar array. Solar fan is enabled, MD-1 and MD-4 are opened, MD-2 and MD-3 are closed.

Mode 2: Heating of building space with solar energy stored in the pebble bed. Solar fan is enabled, MD-1 and MD-3 are opened, MD-2 and MD-4 are closed.

Mode 3: Charging of pebble bed with airflow from the solar array. Solar fan is enabled, MD-2 and MD-4 are opened, MD-1 and MD-3 are closed.

Mode 4: Direct heating of building space with airflow from the furnace. Solar fan is disabled, MD-2 and MD-4 are opened, MD-1 and MD-3 are closed.

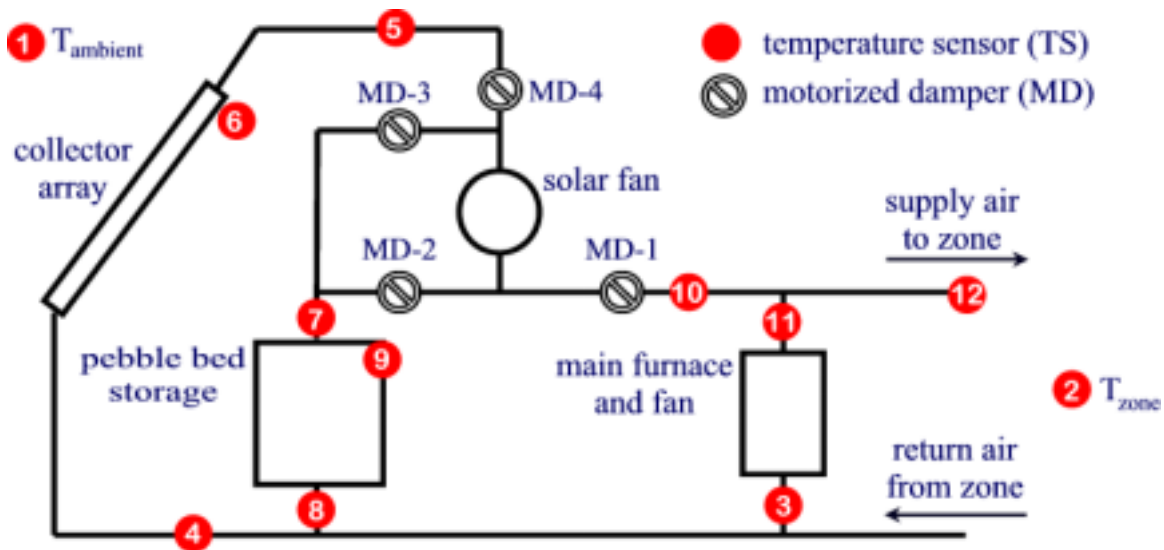


Figure 2.2.1 Layout of solar zone heating systems

Modes are enabled by energizing the appropriate motorized dampers to direct airflows and enabling the fan blower if appropriate. Mode control is dictated by temperature sensors located on the collector absorber plate (TS-6) and within the pebble beds (TS-9). The remaining temperature sensors are used solely for diagnostics and troubleshooting. A complete description of the control sequence is provided in section 7.2.2.

2.3 Arrangement of Collector Array

What appears to be a continuous bank of collectors on the south roof is actually ducted to the two separate solar air handling systems. The 30 collectors on the west side are connected to the basement zone while the remaining 40 are connected to the upstairs office zone. Figure 2.3.1

shows how the collectors are internally ducted to minimize roof penetrations². The array is oriented due south at a slope of 55 degrees.

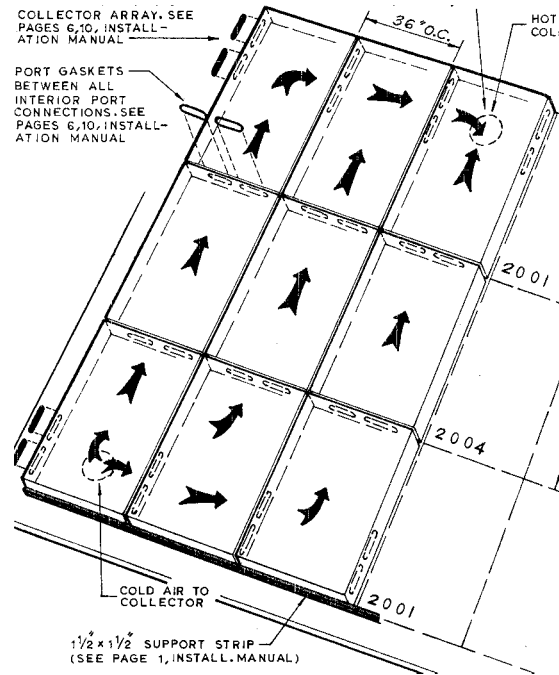


Figure 2.3.1 Internal ducting of series 2000 collectors. Row labeled 2004 does not exist at the McKay Center (Solaron Corp.)

2.4 Construction of Pebble Bed Storage

A total of 16 tons of pebble bed storage is located along the north wall of the basement in the solar mechanical room. Beds for both the office and basement systems share the same retaining walls as shown in figure 2.4.1. Two of the retaining walls constitute the high density concrete of the building foundation. The beds are separated by a 6 gauge sheet metal partition caulked at the edges. The bed interior is lined with 2" styrofoam on all four sides and the floor.

² The total number of roof penetrations for the array is 16.

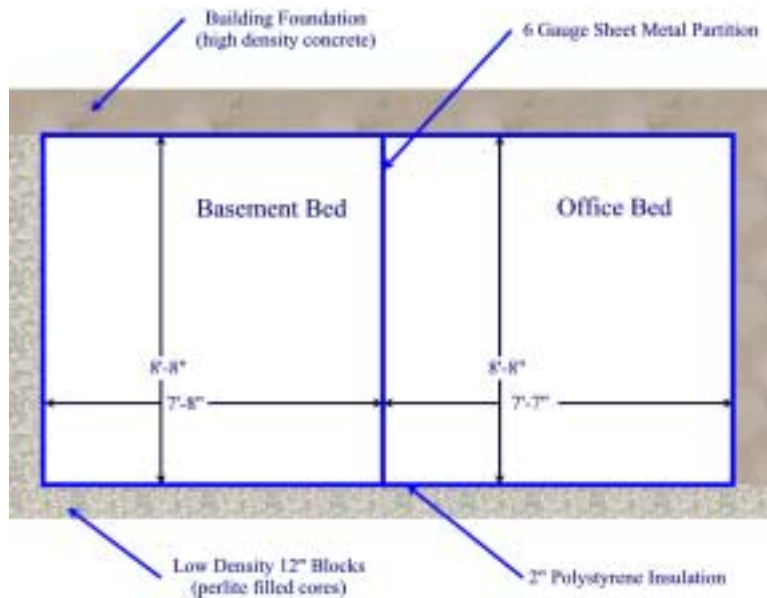


Figure 2.4.1 Top view of pebble bed layout

Figure 2.4.2 is an isometric view of this type of pebble bed showing the upper and lower plenums, the latter of which is formed by bond beam blocks and a wire mesh that support the pebble mass. The pebbles themselves are washed and screened 1.5" river gravel filled to a depth of 5'-2" in both sections. The bed cover is a sandwich of 1/2" plywood with a core of 2" polystyrene insulation anchored to the bed retaining walls with lag bolts placed every 2' along the perimeter and sealed with caulk. Supply and return air ducts are fastened and sealed to the outer retaining walls.

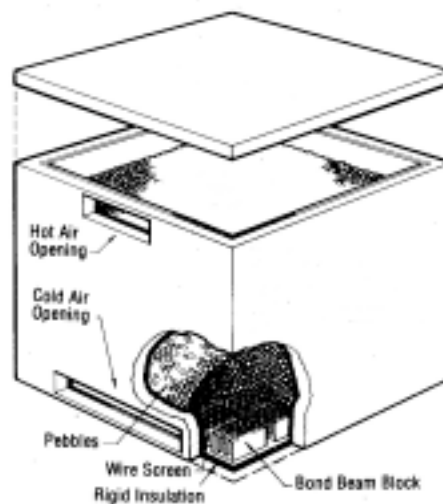


Figure 2.4.2 Isometric view of typical pebble bed construction (Solaron Corp.)

2.5 Auxiliary Equipment

To supply building heating requirements in times of low solar availability, the main air handlers are equipped with direct fired gas furnaces. Furnaces for the basement and lecture hall zones are the original equipment from 1976 while the office furnace has recently been replaced with a high efficiency condensing unit. The basement and office zones are equipped with an economizer damper that is left open at 10% to provide ventilation air requirements during the winter season. In addition to the furnaces, the only other gas load within the building is a small 20 gallon water heater used to service the hot water faucets in the restrooms.

3 Empirical Measurements

In quantifying the performance of solar heating systems, energy is the main variable of interest. Calibration of system components in this study was based on comparisons of energy inputs and outputs between the simulation model and the physical system at the McKay center. Energy is typically not measured directly, but is instead inferred from secondary measurements including temperature, mass flow, and thermal conductivity of the individual building components. Accurate energy calculations require that these secondary measurements be carried out both reliably and accurately. The manner in which these physical measurements were made and how the particular energy rates were calculated are the focus of this section.

3.1 Thermal Energy in Duct Airflows

Thermal energy entrained in duct airflows for the solar and auxiliary HVAC systems was central to this study. This energy was limited to the sensible component of the air, which can be defined as

$$q_{airflow} = \dot{V}\rho_{air} C_{air}T_f \quad [3.1.1]$$

With a constant volume output \dot{V} , the thermal energy $q_{airflow}$ is a sole function of the airstream temperature T_f and density ρ_{air} . Since fan pressures are nearly identical in the different operating modes, air density is determined solely by the temperature of the flow³. All energy analysis pertaining to HVAC duct flows in this study consider variable mass flow rates through the air handlers driven by air densities calculated from the inlet temperature to the fan units.

3.2 Temperature Measurements within Air Ducts

Temperature sensors inside the air ducts (TS 3-12) were model 6000-100 Nickel wire wound RTD's supplied by Johnson Controls during the 1995 control system retrofit. The sensor elements are supported on nylon standoffs attached to an aluminum C-channel sections protruding 6" into the ducts. Temperature sensors critical to energy balances on the collector array and pebble bed storage were calibrated in ice baths for both the office and basement

³ Static pressure across the basement solar air handler were measured as 1.05, 1.17, and 1.00 inches of water for modes 1, 2, and 3 respectively. Results were similar for the office system.

systems. Datalogger channels were independently calibrated against a 1000 ohm precision resistor. Temperatures in the final data sets were then corrected using the temperature calibration curve in figure 3.2.1 supplied by Johnson Controls (after offsets in both the sensors and datalogger channels were accounted for). The required resistive offsets for the sensors and datalogger channels are provided in table 3.2.1.

Direct calibration of the collector inlet sensor (TS-4) in the basement, and the bottom duct sensor in the office pebble bed (TS-8) were not possible due to a fault in the wiring and an inaccessible location. TS-8 of the office system was indirectly calibrated against the collector inlet sensor (TS-4) in mode 3 of operation. With no more than 10' of insulated ductwork at positive pressure separating them, the temperatures were assumed to be identical. Data from TS-4 of the basement was replaced with the bottom duct sensor of the pebble bed (TS-8) during component calibrations. Again a short run of ductwork under positive pressure ensures nearly identical temperatures in the airflow.

Table 3.2.1 Resistance offsets used for calibration of air duct sensors.

	TS-5_{basement}	TS-7_{basement}	TS-8_{basement}	TS-4_{office}	TS-5_{office}	TS-7_{office}
Sensor offset resistance at 0°C (Ω)	+0.4	+0.4	+0.4	+1.4	+2.0	-3.6
Channel offset at 1,000 ohms (Ω)	-0.5	+1.0	+0.4	-1.4	-1.1	+13.0
Combined offset (Ω)	-0.1	+1.4	+0.8	0	+0.9	+9.4

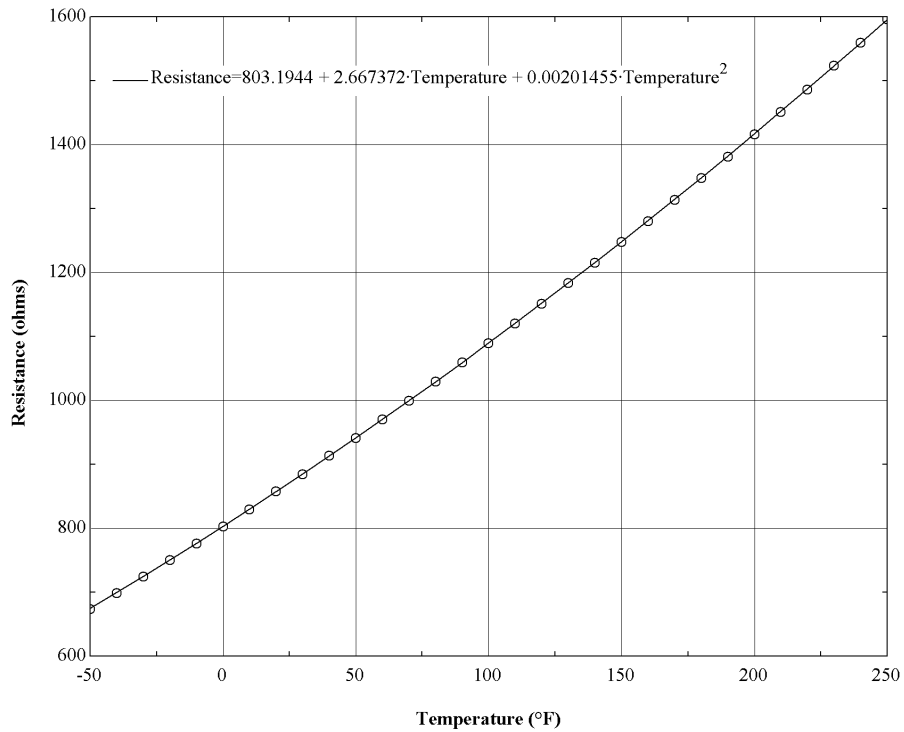


Figure 3.2.1 Calibration curve for Johnson Controls 2000 series RTD sensor. Polynomial fit used for final temperature adjustments also shown.

3.3 Ambient Temperature Measurements

A shaded ambient temperature sensor is installed on the basement foundation at the McKay center, but has been found to yield unreliable readings. Construction of the sensor housing (figure 3.3.1), thermally bridged the sensor to the uninsulated foundation through conduction in the sensor mount, which is screwed into the masonry wall.

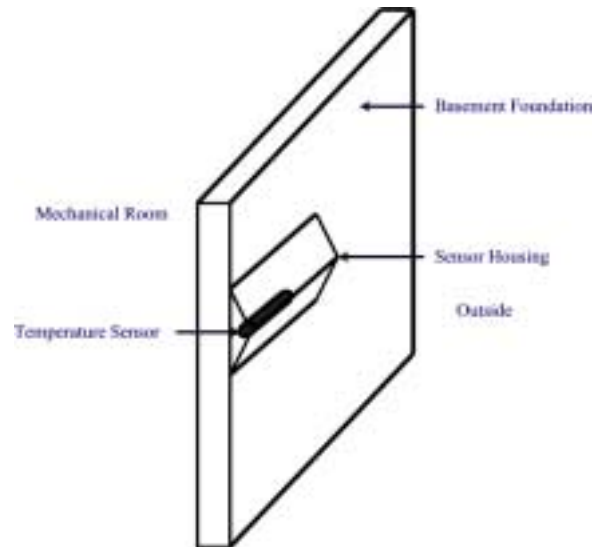


Figure 3.3.1 Ambient air temperature sensor location and housing at the McKay Center

Recent independent ambient temperature measurements were made at the McKay center from November 18th to December 31st of 1999. A comparison of these recorded temperatures to measurements made by NOAA instrumentation at the Madison airport is provided in figure 3.3.2. The higher temperatures recorded at the McKay center may be due to measurement location, which was below the south facing deck adjacent to the building foundation. While this location provided shading of the sensor, the well protected area and close proximity to both the decking and ground may have resulted in the higher temperature. Neither site should experience micro-climatic differences and their separation of only 3 miles should provide nearly identical temperatures. Without a definite knowledge of what the appropriate offset should be, temperatures recorded from the NOAA instrumentation at the airport were directly substituted for those at the McKay center. In sections of this study where the results are particularly sensitive to ambient temperatures (principally in the collector array), a sensitivity analysis will be performed to estimate the possible error in substituting the airport temperatures in place of those at the McKay center.

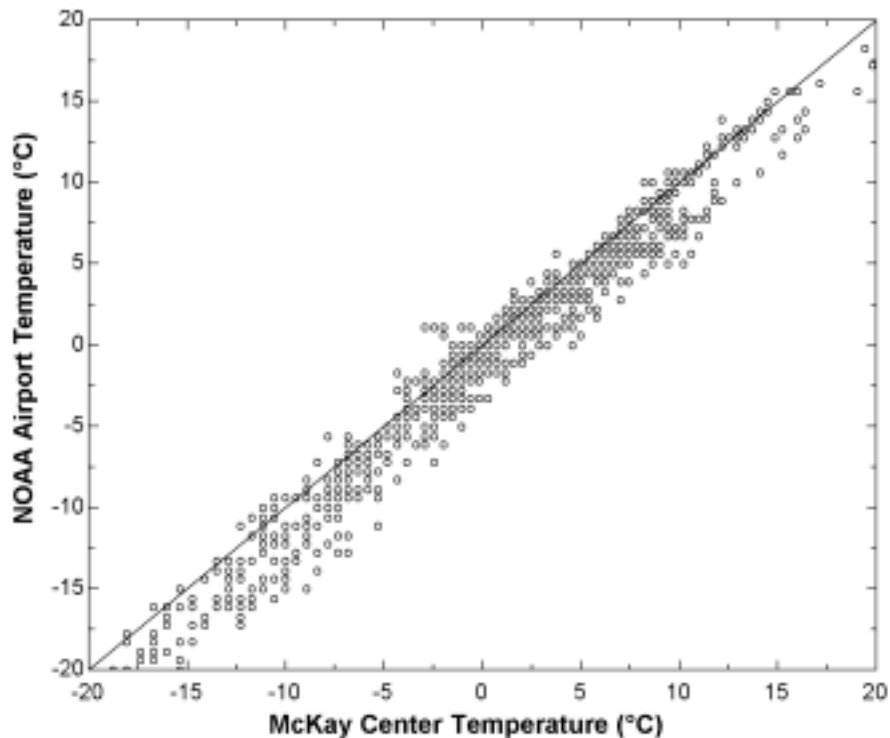


Figure 3.3.2 Comparison of hourly ambient temperatures measured by NOAA weather station to those measured with portable instrumentation at the McKay Center from November 18th to December 31st 1999. Solid line illustrates where identical temperatures would lay.

3.4 Velocity Measurements Within Air Ducts

Airflow velocities within the ducts were measured using a model 6000 hot-wire anemometer from Solmet. Calibration of the instrument was made against a fixed orifice plate with a NIST traceable differential pressure gauge. Figure 3.4.1 shows that the anemometer was poorly calibrated, reading 30 percent below the actual flow rates. All measurements and plots within this study represent corrected values using the correction factor of 0.7025 from figure 3.4.1.

Volume flow rates in the ducts were calculated using a 20 or 25 point traverse across each duct location where flow was to be determined. This method is in accordance with both ASHRAE and Industrial Ventilation Handbook standards. Figure 3.4.2 is a plot of the velocity profile taken from the backside of the office solar air handler. All velocity measurements represent one-minute averaged readings for each point along the traverse.

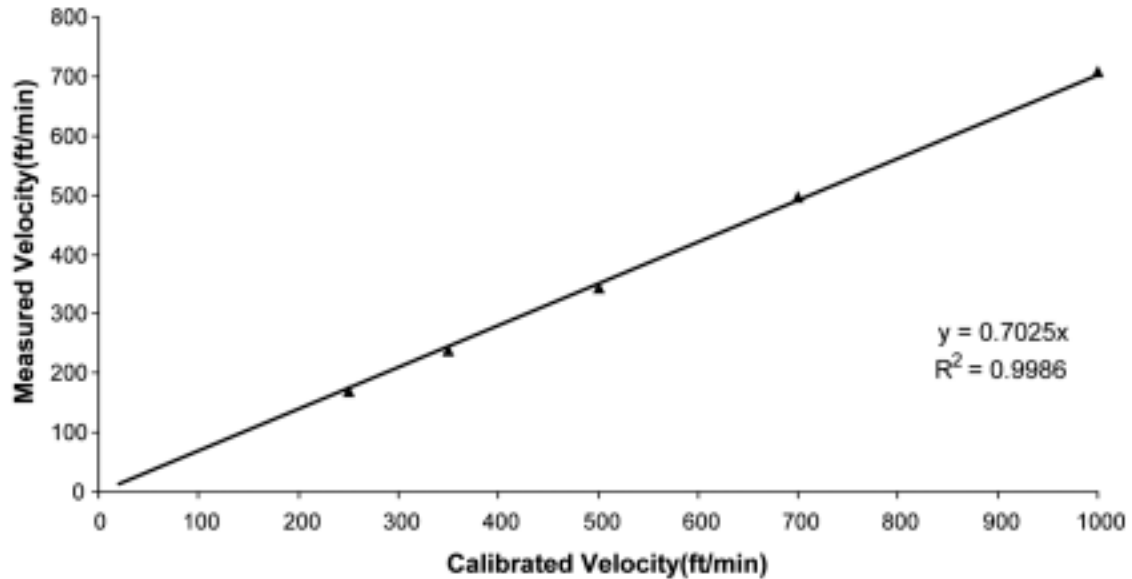


Figure 3.4.1 Hot wire anemometer calibration showing linear regression of the correction factor (0.7025) and the RMS fit.

Two traverses were made on each solar loop near the locations of TS-4 and TS-5 to measure airflow to and from the collector array while operating in mode 3. Main air handler measurements were made on the back side of the fans. Small leaks in the box cover and air handlers are responsible for the small discrepancies between measurements in the solar loop, and the average of the two is used in calibrating solar components. Because pressure drops across the air handlers handler are similar in all operating modes, the airflows of table 3.4.1 were used throughout the study. A complete listing of all velocity measurements can be found in Appendix B.

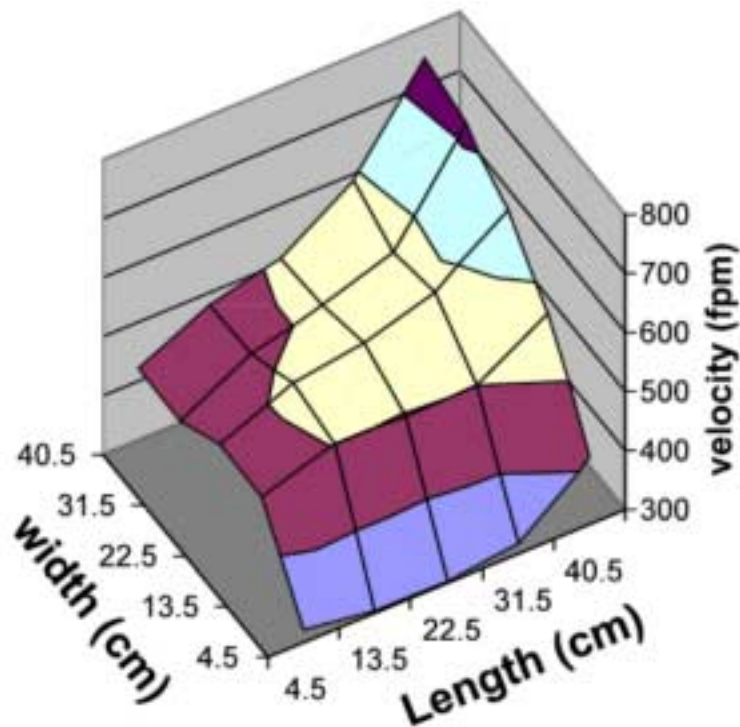


Figure 3.4.2 Velocity profile on back side of basement solar air handler.

Table 3.4.1 System loop airflows for solar and main air handlers.

	Basement solar air handler	Office solar air handler	Basement main air handler	Office main air handler	Lecture main air handler
Backside of air handler (CFM)	1,273	2,156	2,093	2,377	2,173
Supply to collector (CFM)	1,247	1,998	N/A	N/A	N/A
Average (CFM)	1,260	2,077	2,093	2,377	2,173

3.5 Measurements of Solar Radiation

Solar radiation was calculated using a pyranometer and pyroheliometer located on the roof of the Solar Energy Laboratory that measured the global horizontal and direct beam components. This instrumentation is maintained by the National Atmospheric and Oceanographic Administration (NOAA) as part of their Integrated Surface Irradiance Study (ISIS). Instrumentation is rotated through on an annual schedule with the replacements having been calibrated to NIST standards.

Radiation on the actual surface of the array, located 2 miles away was determined using the Perez (1987) model with the global and beam components measured through the ISIS instrument cluster. Ground reflectance was assumed to be 0.20 for the open field in front of the McKay center when no snow cover was present. The effect of snow on ground reflected radiation was included in the analysis based on daily snow cover readings from a NOAA automated weather station located at the Madison airport 5 miles east of the McKay center. Effects of snow cover are also included in simulations employing TMY2 weather data compiled by the National Renewable Energy Laboratory (NREL). A ground reflectance of 0.80 was used for snow covered ground at any depth.

3.6 Solar Test Interval

Calibration of the pebble beds and collector array took place during a nine day period starting May 22nd (days of year 139-148) 1999 after the heating season had ended. During this period the solar loop was forced to operate continuously in mode 3 (charging of storage from the solar array). Because the components ran in quasi steady-state operation during this solar test interval, effects of thermal capacitance on the collectors and temperature sensors could be neglected. Additionally, the number of free parameters required to characterize the pebble bed drops significantly thereby simplifying parameter optimization of this component.

3.7 System Calibration Interval

Operation of the entire building heating system was calibrated for the 27 day period from February 11th until March 28th (days 44-78 of the year) 1999. During this period the building ran in normal operation as dictated by the building control logic. This interval was chosen because it represented the longest continuous data set recorded at the center. Power spikes and failure to reset the data collection program have caused short periods (on the order of days) to go unrecorded in other data sets. Ambient temperatures during the system calibration interval ranged from 10°F to 70°F with approximately 5 days of snow cover on days 70 to 75 of the year. A broad enough range of operating conditions occurred over this period to make it representative of annual operation. Methods and results of fitting the simulation model to this calibration interval are covered in sections 8 and 9.

4 Solar Collector Array

The collector array is a principal component of any active solar installation. From a modeling standpoint, it is critical to be able to predict the useful gain of the array under a wide range of operating conditions. The analytical framework used to predict performance will be introduced in this section along with the empirical methods that are used to calibrate the model parameters. The original collector performance will be estimated using manufacturer test data corrected to the current flow rates in the collectors. Degradation of the arrays will then be quantified through a comparison of the current measured performance to the predicted original performance.

4.1 Analytical Framework for Evaluation of Flat-plate Collectors

The original analytical descriptions of flat-plate collectors were performed by Hottel and Whillier (1958) in their work on the MIT solar houses. To this day, the Hottel-Whillier model for flat plate collectors remains the standard method for assessing performance and is included in nearly all simulation tools used today. Understanding the formulation of this model provides the basic knowledge of how operating conditions and collector construction influence performance.

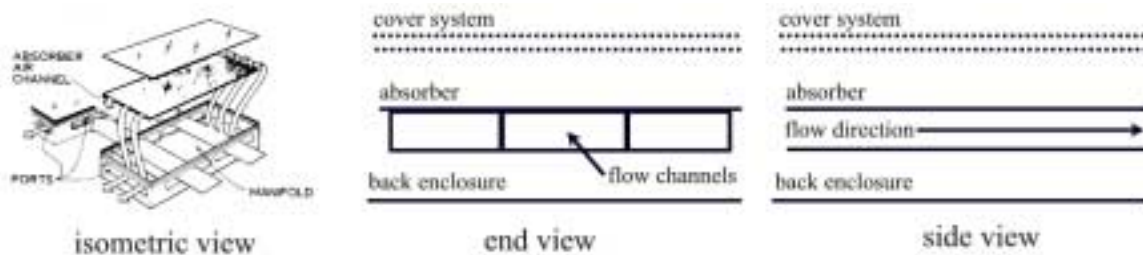


Figure 4.1.1 Layout and construction schematic of Soilaron series 2000 collector.

The starting point for the thermal analysis is an energy balance on the absorber plate of the collector shown in figure 4.1.1.

$$q''_{air} = S - U_L(T_p - T_{amb}) \quad [4.1.1]$$

Where q''_{air} is the rate of energy gain into the airstream, S is the rate of solar energy gain on the absorber, U_L is the conductance from the absorber to ambient, and T_p and T_{amb} represent the local absorber and ambient air temperatures. Elimination of the absorber temperature T_p can be accomplished by writing a second energy balance on the airstream.

$$q''_{air} = h_f(T_p - T_f) \quad [4.1.2]$$

Where h_f is the overall heat transfer coefficient between the fluid and absorber and T_f is the local fluid temperature. Equations 4.1.1 and 4.1.2 can then be combined and solved for the local plate temperature.

$$T_p = \frac{S + U_L T_{amb} + h_f T_f}{U_L + h_f} \quad [4.1.3]$$

This plate temperature is then substituted back into the energy balance on the absorber of equation 4.1.1 to solve for the useful gain in terms of the local fluid temperature. After some algebraic manipulation, the useful gain at any location within the collector can be expressed as

$$q''_{air} = F' [S - U_L (T_f - T_{amb})]$$

where [4.1.4]

$$F' = \frac{h_f}{h_f + U_L} = \frac{U_o}{U_L}$$

The term F' is often referred to as the collector efficiency factor and represents the actual collected energy to that which would be collected if the absorber plate were at the local fluid temperature (i.e. if either U_L were zero or h_f were infinity). If the fluid is entirely enclosed in the absorber channel then F' can be described as the ratio of conductance from the fluid to ambient (U_o) over the plate to ambient (U_L).

While equation 4.1.4 is valid at any location within the collector, the only location where T_f is known is at the collector inlet. Much like a conventional heat exchanger, evaluation of the useful gain at the inlet fluid temperature provides the maximum possible gain to the fluid. Actual

heat exchange between the absorber and fluid will be less than this due to increasing fluid temperatures along the length of the absorber channel. It is common to define an effectiveness ε that relates the actual gain of the fluid to the maximum theoretical gain.

$$\varepsilon = \frac{q''_{actual}}{q''_{maximum}} = \frac{\dot{m}C_{air}(T_{fi} - T_{fo})}{F'(S - U_L(T_{fi} - T_{amb}))} \quad [4.1.5]$$

Here, T_{fi} and T_{fo} are the air temperatures at the collector inlet and outlet with $\dot{m}C_{air}$ defining the capacitance rate of the airstream per unit area of the collector. Calculation of the outlet fluid temperature requires an energy balance on the fluid in the direction of flow.

$$\dot{m}C_{air} \frac{dT_f}{dx} - F'[S - U_L(T_f - T_{amb})] = 0 \quad [4.1.6]$$

If F' and U_L are assumed independent of position in the flow direction then integrating from inlet to outlet provides the following result for T_{fo}

$$\frac{T_{fo} - T_{amb} - S/U_L}{T_{fi} - T_{amb} - S/U_L} = \exp\left(-\frac{F'U_L}{\dot{m}C_{air}}\right) \quad [4.1.7]$$

Solving for T_{fo} and substituting into equation 4.1.5, the effectiveness can be expressed as

$$\varepsilon = \frac{1}{\theta} [1 - \exp(-\theta)]$$

[4.1.8]

where

$$\theta = \frac{F'U_L}{\dot{m}C_{air}}$$

The useful energy gain from the collector can now be defined in terms of the collector effectiveness and maximum theoretical gain

$$q''_{air} = \epsilon q''_{maximum} = F_R [S - U_L (T_{fi} - T_{amb})] \quad [4.1.9]$$

where

$$F_R = \epsilon F'$$

4.2 Absorbed Solar Radiation

The absorbed solar radiation S of equation 4.1.9 is not measured directly, but must be calculated from the solar radiation incident on the collector surface I and the transmission-absorption product (tau-alpha) of the cover and absorber plate system.

$$S = I(\tau\alpha) \quad [4.2.1]$$

To account for reflectance of the cover system at high incidence angles, it is common to define an incidence angle modifier $K_{\tau\alpha}$ that relates the tau-alpha product at normal incidence to that at higher angles⁴.

$$S = IK_{\tau\alpha}(\tau\alpha)_{normal} \quad [4.2.2]$$

$K_{\tau\alpha}$ is a strong function of the number of glazings in the cover system and the incidence angle. Souka and Safwat (1966) have developed a general relation for the dependence of $K_{\tau\alpha}$ with respect to incidence angle and cover construction.

$$K_{\tau\alpha} = \frac{(\tau\alpha)}{(\tau\alpha)_{normal}} = 1 + b_o \left(\frac{1}{\cos(\theta)} - 1 \right) \quad [4.2.3]$$

Typical behavior of the incidence angle modifier for one and two cover systems is illustrated in figure 4.2.1. The incident angle modifier coefficient b_o is typically measured as part

⁴ While equation 4.2.2 treats the incident radiation as a single component I , actual radiation on the collector aperture consists of both beam and diffuse components, which must be treated separately (Duffie and Beckman 1991). For the purposes of collector calibrations however, beam radiation is the dominant component and equation 4.2.1 provides an accurate correlation.

of collector characterization tests. The general relation of equation 4.2.3 is considered accurate up to angles of 60 degrees, which covers the operating range of collector operation.

By substituting the absorbed solar energy of equation 4.2.2 into equation 4.1.9, the useful gain of the collector can be expressed in terms of simple operating conditions and performance parameters. This form of the Hottel-Whillier model as presented below should be familiar to most readers as it is one of the most commonly employed equations in the solar thermal field.

$$q''_{air} = F_r [I(\tau\alpha) - U_L(T_{fi} - T_{amb})]$$

[4.2.4]

where

$$(\tau\alpha) = K_{\tau\alpha}(\tau\alpha)_{normal}$$

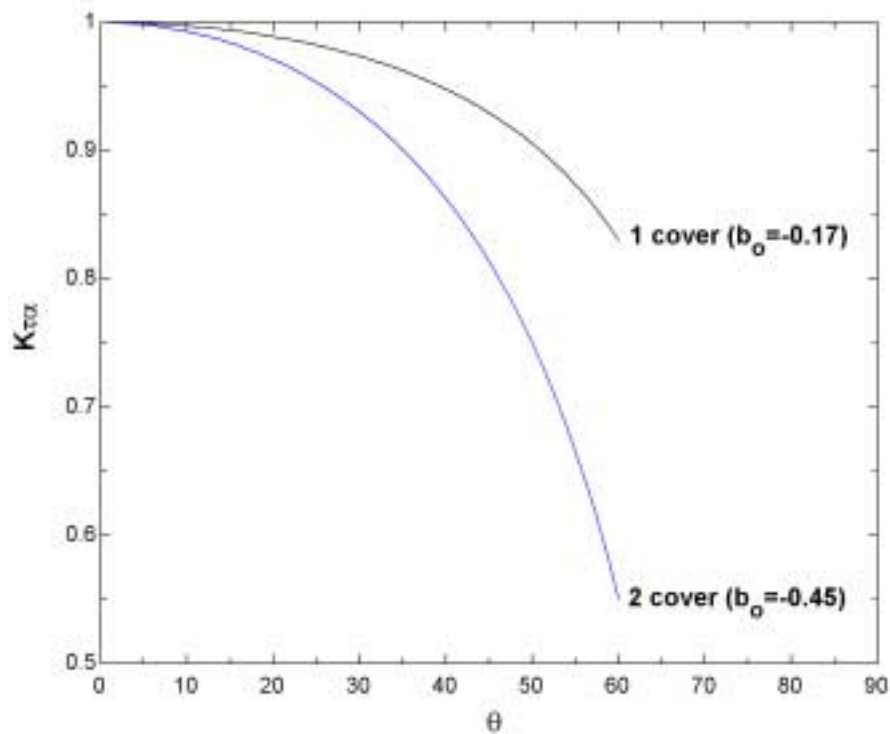


Figure 4.2.1 Incidence angle modifier effects representative of single and double glazed cover systems.

4.3 Standard SRCC Ratings Procedure

The useful collector gain of equation 4.2.4 contains two parameters, which are the products of $F_r(\tau\alpha)$ and F_rU_L . For any given design and flow rate these parameters will be constants that describe the collector over a wide range of operating conditions. Calculation of $F_r(\tau\alpha)$ and F_rU_L are typically performed by plotting the collector efficiency over a wide range of operating conditions. Collector efficiency is simply defined as the useful collector output divided by the total solar radiation incident on the collector aperture

$$\eta = \frac{q''_{air}}{I} = F_r(\tau\alpha) - F_rU_L \frac{(T_{fi} - T_{amb})}{I} \quad [4.3.1]$$

It becomes immediately apparent that collector efficiency is a linear relation of the two collector parameters $F_r(\tau\alpha)$ and F_rU_L . By measuring T_{fi} , T_{fo} , T_{amb} , I and the collector flow rate, it is possible to plot the efficiency as a function of $(T_{fi} - T_{amb})/I$ for a range of operating conditions. Figure 4.3.1 is a plot of these points for a Solaron Series 2000 collector from tests performed at the Marshall Space Flight Center Solar Simulator by Wyle Laboratories (1978). Through linear regression analysis, the parameters $F_r(\tau\alpha)$ and F_rU_L can be calculated as the y-intercept and slope of a best fit line through the data.

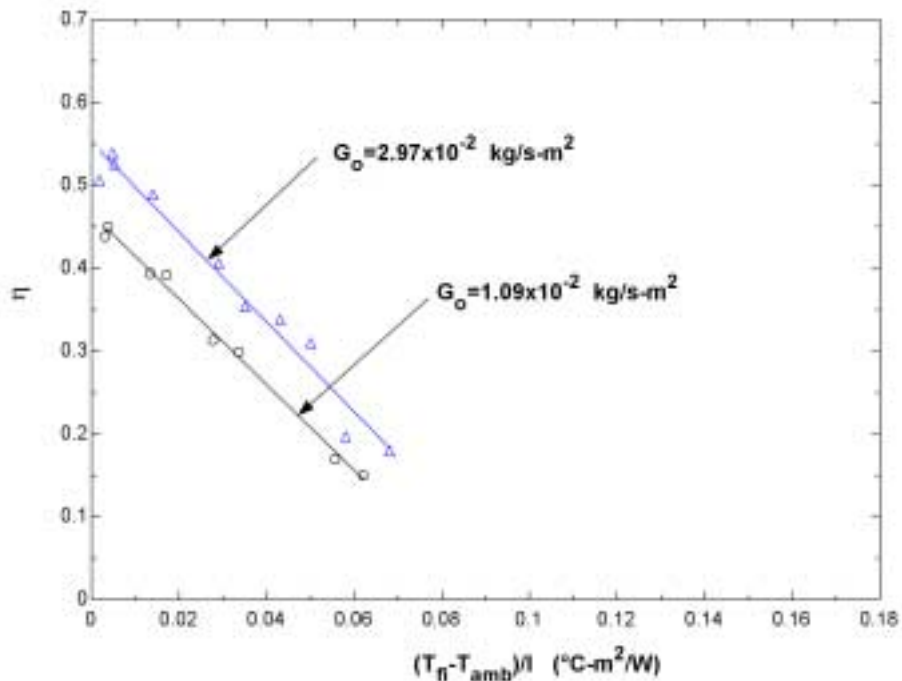


Figure 4.3.1 Plot of operating points for Solaron 2000 air heater based on equation 4.3.1. Collector has been characterized at two specific mass flow rates (G_o is mass flow rate per unit collector area).

This method of fitting the collector parameters was first outlined by Hill and Streed (1976) for collector testing at the National Bureau of Standards (NBS) and has since been incorporated in a similar form by the American Society of Heating Ventilation and Air-conditioning Engineers (ASHRAE) standard 93-77. Current testing of solar thermal systems is managed by the Solar Ratings and Certification Center (SRCC) of Galveston Florida and the formulation of the Hottel-Whillier model as depicted in equation 4.3.1 and figure 4.3.1 will be referred to as an SRCC plot or curve.

The ASHRAE 93-77 standards under which collector characterizations are performed is quite detailed with regards to the conditions under which collector characterizations may be performed and only the most applicable criteria are listed below.

- A series of 8 operating points are required for characterization with symmetrical measurements made on each side of solar noon to eliminate any possible capacitance effects.

- Suggested collector inlet temperatures are at the ambient temperature plus 10, 30, 50, and 70 percent of the difference between ambient and absorber plate stagnation temperature.
- Irradiance on the collector aperture must be no less than 630 W/m^2 during the testing interval.
- Incidence angles must be less than 30 degrees at all test conditions to eliminate any effects of the incidence angle on absorbed radiation.
- Wind speeds may not exceed 4.5 m/s during the testing interval.
- The range of ambient temperatures over the entire test interval must not exceed $30 \text{ }^\circ\text{C}$.

The effect of these restrictions is to significantly reduce confounding factors that could scatter the results and make them irreproducible between testing sites. In order to obtain data over the wide operating range, testing stations often employ pre-heaters in the air inlet stream to the collectors. In this manner, they are able to achieve the desired spread in the variable set $(T_{fi} - T_{amb})/I$ while still adhering to the narrow band of allowed ranges for T_{amb} and I . Additionally, some collector tests are run on azimuthal mounts that track the beam radiation to maintain the irradiance requirement over the course of the entire day.

Maintaining the rigid testing standards of ASHRAE 93-77 is often not possible at actual installations. There is little control over ambient conditions at the building site, and the user cannot simply rotate the building on which the collectors are mounted. Moreover, there are often limitations on what can be done to affect the inlet stream temperature as pre-heaters are not a part of the installed equipment. Figure 4.3.2 shows an SRCC plot obtained for the Solaron series 2000 air heater by Oonk (1976) at the Solaron Corporate headquarters in Commerce City Colorado.

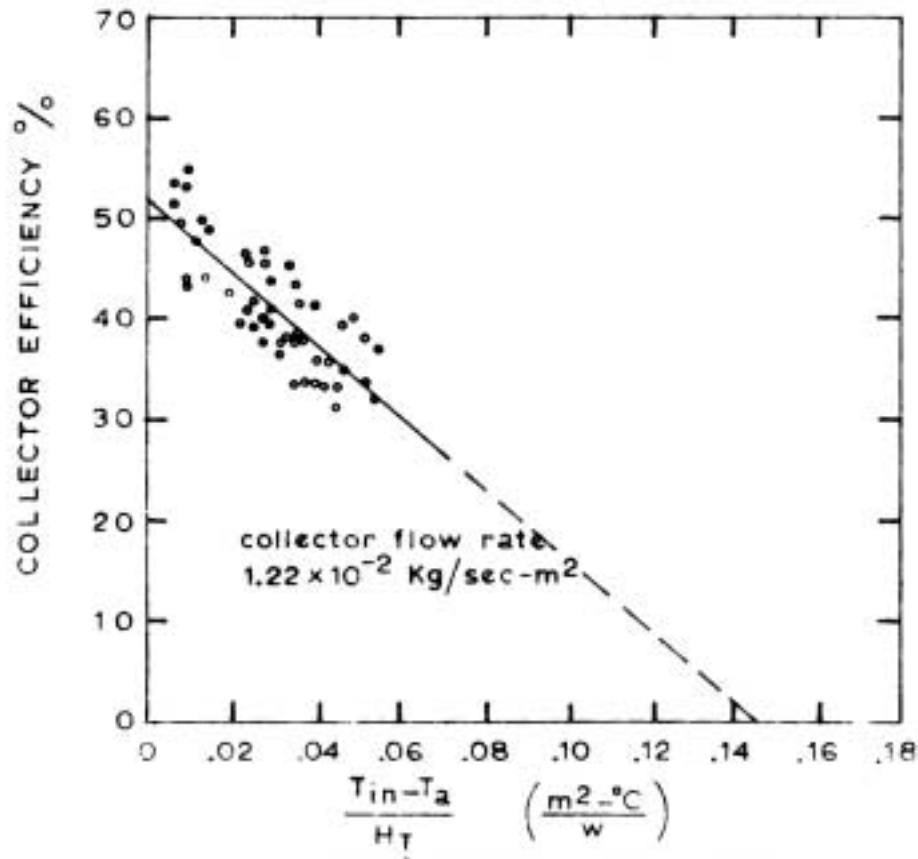


Figure 4.3.2 SRCC plot of Solaron 2000 air heater performance. Collector flow rate is G_o and H_T corresponds to surface irradiance I (Oonk 1976).

The higher degree of scatter is attributable to both the thermal capacitance of the collector and possibly looser adherence to the restrictions on ambient temperature and windspeed. The operating range of the collector was restricted by the upper limit of the water based heat exchanger used to preheat the collector inlet stream. Although a best-fit line is plotted for the data, there is arguably a large possible error in the slope due to both scatter and the limited operating range.

SRCC plots performed at the McKay center are generally even more restricted in the operating range than those of figure 4.3.2. The SRCC plot for the McKay center shown in figure 4.3.3 is for incidence angles up to 50 degrees (as compared to the 30 degree maximum allowed in ASHRAE 93-77 and employed by Solaron). The use of high incidence angles was required to provide a significant operating range for the evaluation of $F_r U_L$, which is the slope of the best fit line. Employing high incidence angles requires an assumption of $K_{\tau a}$ such that the non-linear

effects of the incidence angle can be accounted for⁵. Operation late into the day provides the high collector inlet temperature T_{fi} and low irradiance I necessary to produce a spread in the variable set $(T_{fi}-T_{amb})/I$.

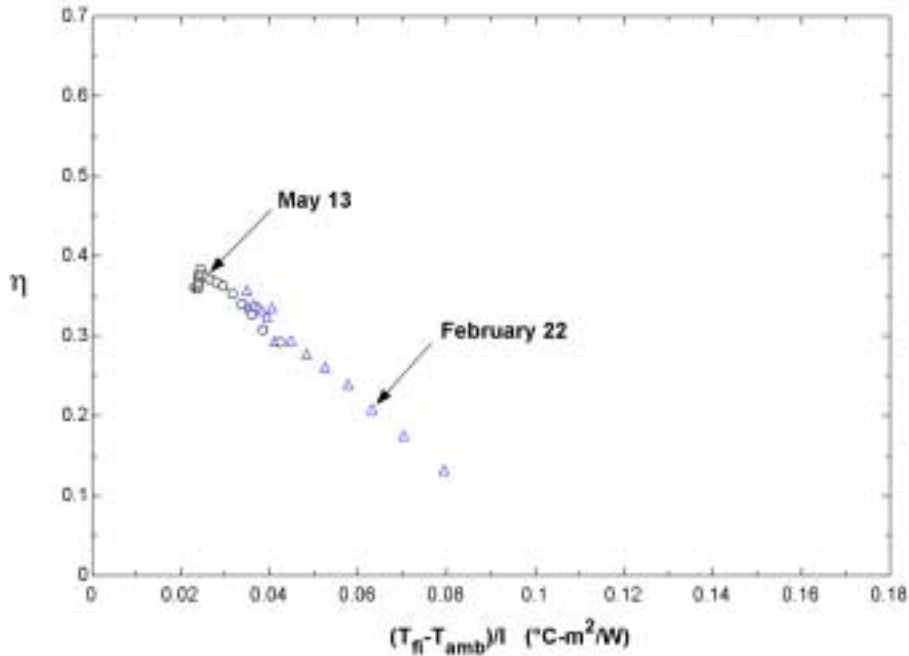


Figure 4.3.3 SRCC plot for office collector array for clear sky days during the system calibration interval (February 22) and the solar test interval (May 13). b_0 was assumed to be -0.45 for the cover system.

For February 22nd, the low ambient temperatures provided a wide range of operating conditions such that linear regression can be performed on the operating points. During the solar test interval, which contained May 13th and for the next several months, high ambient temperatures limited the operating range of the collector to a band too narrow for regression analysis. During warmer months not even the increase in range of allowed incidence angles is able to extend the operating conditions to a usable spread. Ideally, it would be desirable to find a method for determining collector coefficients that can be used during warmer months and does not contain an assumption on the incidence angle modifier $K_{\tau\alpha}$.

⁵ ASHRAE 93-77 and the previous NBS standard eliminate this assumption by testing only at low incidence angles.

4.4 Two Point Collector Characterization

The two point method of collector characterization relies on operating the collector at night to determine the loss parameter $F_r U_L$ of the array. During night-time operation, when the solar gain I on the surface is zero, the Hottel-Whillier model simplifies to

$$q''_{air} = -F_r U_L (T_{fi} - T_{amb}) \quad [4.4.1]$$

Knowing the fluid temperatures and flow rate, the parameter $F_r U_L$ can be calculated by simply dividing the loss of the airstream by the temperature difference between the inlet and ambient. This method of night-time characterization was originally proposed and performed by Whiller (1953) in his doctoral work on the MIT solar houses, but it has unfortunately received little attention since. The single largest benefit of characterizing the collector losses in this manner is that it does not require any assumptions on the incident angle modifier, and it is not restricted to narrow ranges for linear regression. To achieve accurate results of the loss product, the temperature drop across the collector must be large enough to be accurately measured by the duct sensors. This requirement entails a significant difference between the fluid inlet temperature T_{fi} and the ambient. These conditions are readily achieved during the constant charging cycle of the solar test interval. Maximum collector inlet temperatures occur near sunset when the thermal wave breaks through the pebble bed. When coupled with lower ambient temperatures at night, it is often possible to achieve a 10 °C temperature drop across the collector array.

The accuracy of the night-time characterization can be more accurately assessed by breaking down the Hottel-Whillier model to its basic components to glimpse what is actually being measured through this method. Substituting the derivations of collector efficiency factor F' , collector effectiveness ϵ , and loss of the airstream yields a more explicit form of equation 4.4.1.

$$\dot{m}_{air} C_{air} (T_{fo} - T_{fi}) = -\frac{\dot{m}_{air} C_{air}}{F' U_L} \left[1 - \exp\left(-\frac{F' U_L}{\dot{m}_{air} C_{air}}\right) \right] F' U_L (T_{fi} - T_{amb}) \quad [4.4.2]$$

By defining F' as U_o/U_L and rearranging the terms of equation 4.4.2, it is possible to express the dimensionless capacitance rate of the collector θ , in terms of a dimensionless temperature differences across the collector

$$\theta = \frac{F'U_L}{\dot{m}C_{air}} = \frac{U_o}{\dot{m}C_{air}} = -\ln\left(\frac{T_{fo} - T_{amb}}{T_{fi} - T_{amb}}\right) \quad [4.4.3]$$

What is being measured during night-time testing is simply the dimensionless capacitance rate of the collector θ , from which U_o can be calculated. A plot of the dimensionless capacitance rate vs. the dimensionless temperature difference is shown in figure 4.4.1. Due to the nature of the function, it is necessary to operate the collector at high inlet temperatures for an accurate determination of θ , and therefore U_o . At lower temperatures, any uncertainty in the measurements can result in high errors for U_o .

The operating range over which both collector arrays were characterized in this study is shown by the vertical shaded bands, which represent a duration from one hour after sunset until one hour before sunrise. For estimated uncertainties of 0.1 °C in the duct sensors and 5 °C in the ambient temperature, the RMS error for the dimensionless capacitance rate θ averages 7 percent for both systems evaluated at the mean of each operating range. When combined with a 5 percent error in flow rates through the ducts, the RMS error in the collector loss parameter $F_r U_L$ of the arrays will be 19 percent.

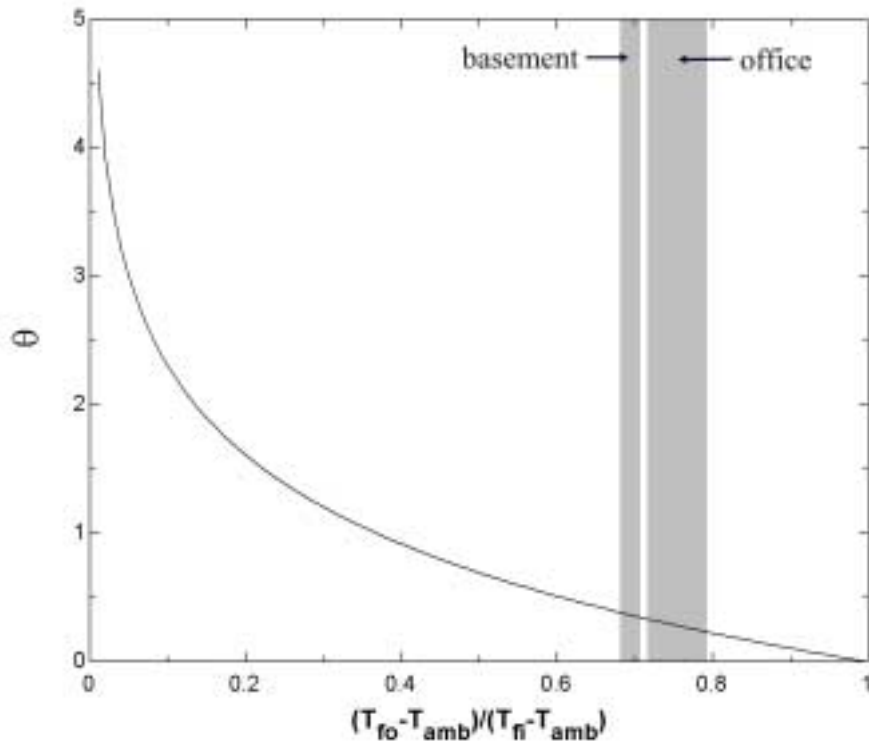


Figure 4.4.1 Dimensionless temperature difference vs. dimensionless capacitance rate for collectors under night-time testing. Shaded bands indicate operating ranges of both office and basement arrays over the solar test interval.

Determining $F_r(\tau\alpha)$ is a simple matter of fitting the slope of the SRCC performance curve, as defined by $F_r U_L$ during night-time testing, through a limited set of operating points centered around solar noon. The operating points are limited to incidence angles less than 35 degrees such that they do not contain incidence angle effects. An illustration of this concept is shown below in figure 4.4.2. Accounting for uncertainties in the duct and ambient temperatures together with a 5 percent uncertainty in the incident radiation for these clear sky days translates into a 8 percent RMS error for the $F_r(\tau\alpha)$ of the arrays evaluated at the mean of the operating range. The temperature sensors used to measure collector inlet and outlet temperatures are TS-4 and TS-5, which are both located in the solar equipment room. Collector parameters therefore reflect any duct losses or infiltration between the physical collector outlet and the point of measurement. These discrepancies are believed to be minimal however as both the supply and return ductwork are sealed with silicon sealant and wrapped in 2" foil faced insulation.

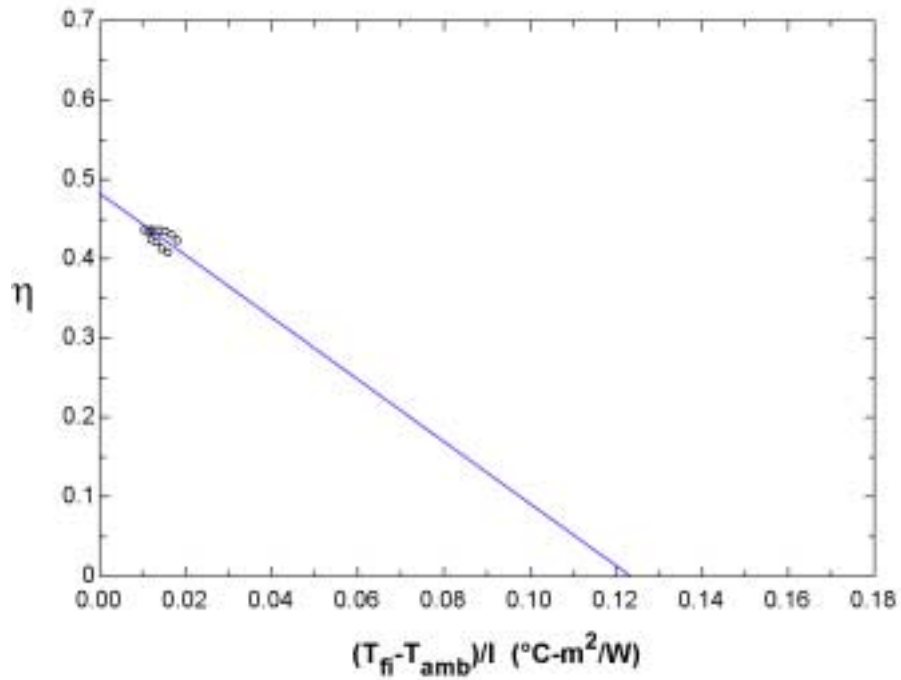


Figure 4.4.2 Illustration of 2 point fit for the office array. Operating points below 35 degrees are plotted and then least squares fit with a line defined by the slope of $F_r U_L$ to determine the intercept $F_r(\tau\alpha)$.

Final results for both the office and basement collector arrays are summarized in table 4.4.1 together with the calculated uncertainties. A large fraction of these uncertainties stem from the possible error in ambient temperature readings, which are discussed in section 3.3. Unfortunately, collector characterizations could not be compared after the ambient sensor was replaced in November 1999. Replacement of the fan motor bearings in the solar air-handler units near this time increased flow rates through the collectors, causing a significant impact on the fluid heat transfer coefficient h_f and therefore collector parameters. The best that could be done within this work was to recognize the uncertainty in the ambient temperature and propagate the error through to the final results.

Table 4.4.1 Collector array parameters

	θ	ε	U_o (W/m ² -C)	$F_r(\tau\alpha)$	$F_r U_L$ (W/m ² -C)
Basement	0.357±0.063	0.841±0.025	4.77±0.85	0.479±0.039	4.01±0.72
Office	0.273±0.052	0.875±0.022	4.47±0.86	0.485±0.041	3.91±0.76

A comparison of the measured and predicted outlet temperatures for both the office and basement arrays over the solar test interval are shown in figures 4.4.3 and 4.4.4 respectively. The shaded bands in each figure indicate the noon and night-time fitting intervals that were used in the two point characterization. The collectors were characterized only during these last two days of the solar test interval. Using the fitted parameters of $F_r(\tau\alpha)$ and F_rU_L , the array outlet temperature T_{fo} was then predicted over the entire interval. Agreement with measured data is quite good over the entire operating range and is even able to follow the actual collector through rapidly changing levels of irradiance as can be seen on day 140. Calibration plots for both arrays over the solar test interval are provided in figure 4.4.5

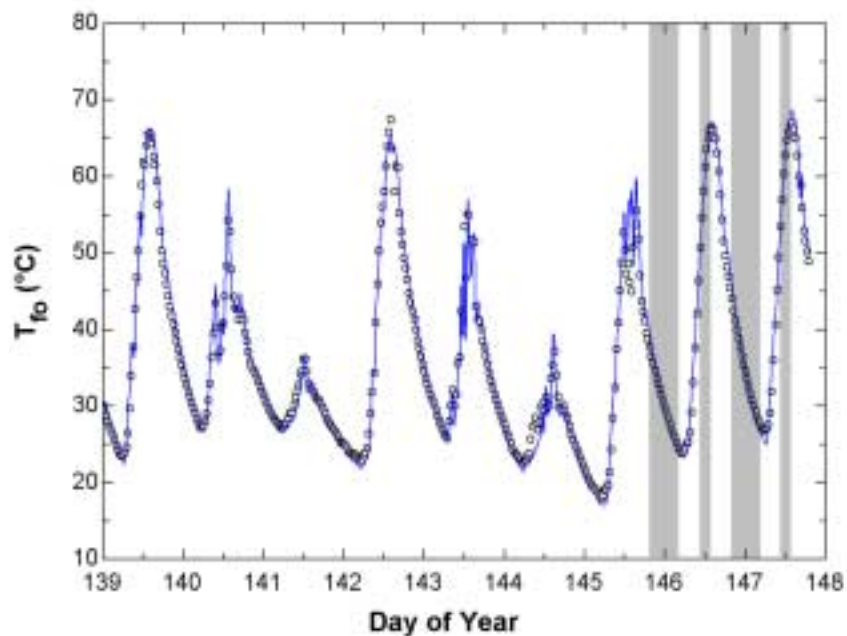


Figure 4.4.3 Measured (points) and predicted (solid line) office collector array outlet temperatures TS-5 over the solar test interval. Shaded bands indicate intervals used for parameter fitting.

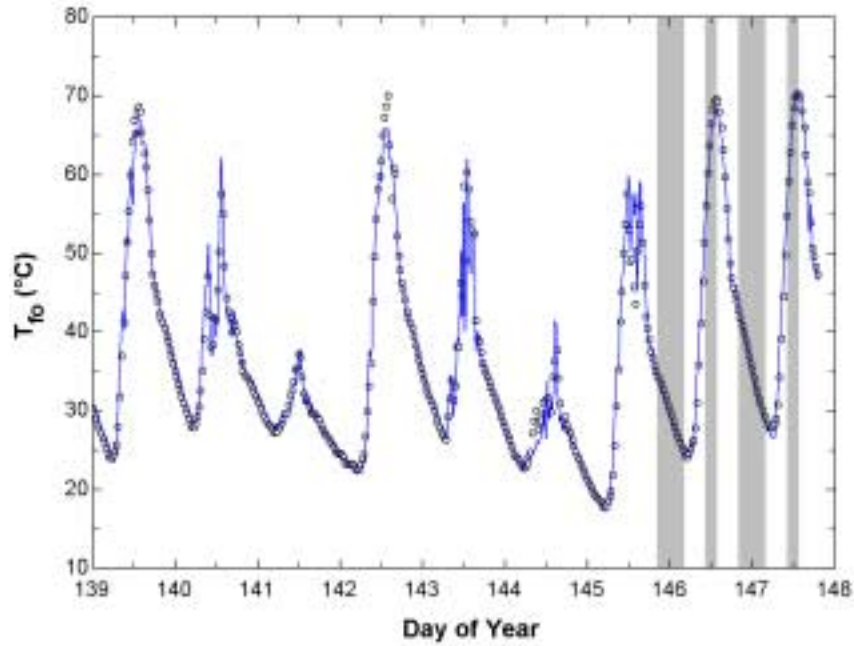


Figure 4.4.4 Measured (points) and predicted (solid line) basement collector array outlet temperatures TS-5 over the solar test interval. Shaded bands indicate intervals used for parameter fitting.

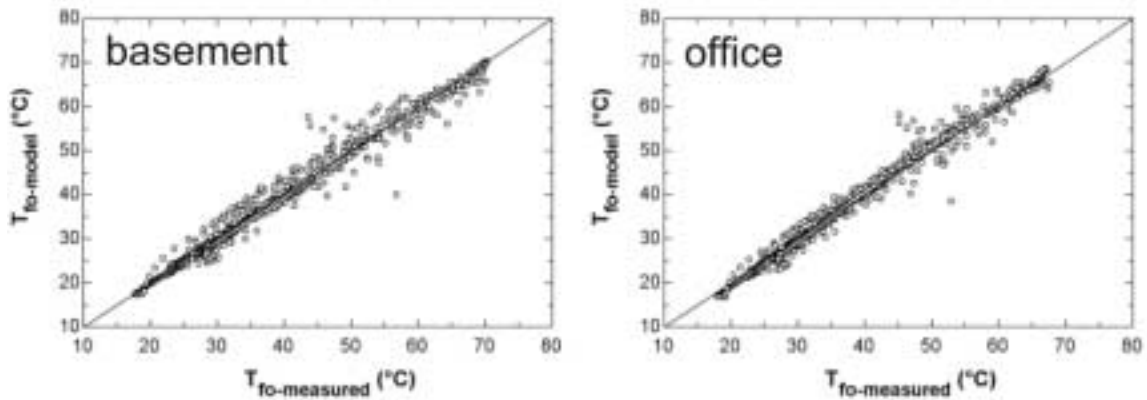


Figure 4.4.5 Calibration plots for the collector arrays over the solar test interval

4.5 Determination of the Incidence Angle Modifier

While it is theoretically possible to solve for the incidence angle modifier $K_{\tau\alpha}$ using the data and fitted parameters from the McKay center⁶, scatter and uncertainty in the data set limit the accuracy of such a method. Better measurements were available from the tests run at the Marshall space flight test center. Figure 4.5.1 is a plot of the incidence angle modifier as tested for the Solaron 2000 series collector and that predicted for a standard low-iron 2-cover system using the general relation of equation 4.2.3.

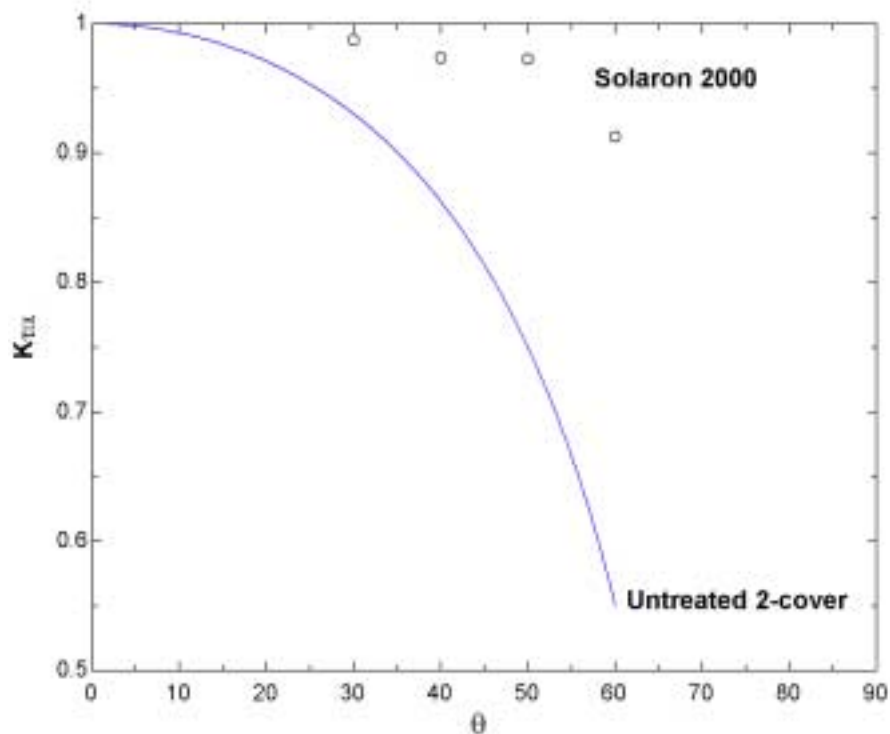


Figure 4.5.1 Incident angle modifiers for standard untreated 2-cover system (solid line) and Solaron 2000 2-cover system (points).

The negligible decrease in $K_{\tau\alpha}$ for the tested Solaron 2000 unit is likely attributable to an anti-reflective coating on the glass. The purpose of this coating is readily apparent from figure 4.5.1 in that it increases the transmitted solar radiation by up to 35 percent at high incidence

⁶ This can be done by predicting the incident radiation I from equation 6.3.1 using the calibrated collector parameters $F_r(\tau\alpha)$ and $F_r U_L$ together with temperatures and the flow rate. This predicted value of I is then divided by the measured value on the collector aperture. The ratio of these two values is defined as $K_{\tau\alpha}$.

angles. Over the traditional 0-60 degree operating range of the collector, $K_{\tau\alpha}$ is near unity for the Solaron unit, and therefore no incidence angle effects were included in the model.

The effect of incidence angle modifiers on predicting the slope of the performance curve as discussed in section 4.3 can be significant. This occurs because the operating points for high incidence angles will be incorrect. If the absorbed solar radiation were based on the $K_{\tau\alpha}$ of the standard 2-cover system, then the value of I in equation 4.3.1 would be under-predicted, and the operating points would be shifted both up and to the right from their proper locations. For low incident angles there is little error introduced to the operating points because $K_{\tau\alpha}$ is near unity for both treated and untreated surfaces. When a line is now fitted to these operating points the slope $F_r U_L$ will be offset due to the mislocation of the operating points at high incidence angles. The intercept $F_r(\tau\alpha)$ will also be affected, but to a lesser degree. In order to perform collector characterizations at high incidence angles as is often required when the SRCC method is applied to actual installations, the incidence angle modifier $K_{\tau\alpha}$ must be known with confidence such that the proper value of incident radiation I can be used in equation 4.3.1.

4.6 Predictions of Original Array Performance

To quantify the amount of degradation in the collector array, the current performance must be compared to how the array operated originally. With no data available for the array as installed in 1978, the performance was estimated using the manufacturer's parameters of $F_r(\tau\alpha)$ and $F_r U_L$ corrected for flow rates and the series connection employed at the McKay center. When evaluated in this manner, the original performance characteristics reflect a system that was properly installed and without any leaks.

A series of detailed corrections must be made to the original collector test parameters for them to reflect the conditions that would have been present at the McKay center. The most critical of these corrections is that the flow rate through the arrays at the McKay center are 82 CFM per collector for the basement system and 90 CFM for the office system, which are more than double the 38 CFM per collector at which the performance characteristics were determined by the manufacturer. This increase of flow rates is required to maintain collector performance when they are run in series. The effects of increased flow rate are to increase the heat transfer coefficient h_f between the plate and the airstream, as well as to decrease the mean plate temperature at which the collector operates. The change in these variables can have a significant effect on the both F' and U_L within the collector and must be accounted for.

4.6.1 Simple Method of Flow Rate Correction

The most commonly noted impact for a shift in flow rate is to change the dimensionless capacitance rate and therefore the effectiveness of the collector. If heat transfer coefficients are assumed constant, then the capacitance rate scales linearly with the change in flow rate according to equation 4.4.3. The resultant change in collector parameters is then simply the ratio of collector effectiveness at the new flow rate compared to that at the tested flow rate.

$$r = \frac{\varepsilon_{new}}{\varepsilon_{tested}} = \frac{\dot{m}_{new} C_{air}}{\dot{m}_{tested} C_{air}} \cdot \frac{\left[1 - \exp\left(\frac{U_o}{\dot{m}_{new} C_{air}}\right) \right]}{\left[1 - \exp\left(\frac{U_o}{\dot{m}_{tested} C_{air}}\right) \right]} \quad [4.6.1]$$

where

$$U_o = \dot{m}_{tested} C_{air} \ln\left(1 - \frac{(F_r U_L)_{tested}}{\dot{m}_{tested} C_{air}}\right)$$

The benefit of this correction method is that it can be performed using only the original test parameters and flow rate. Because of its simplicity, corrections in the form of equation 4.6.1 are often employed in simulation tools such as TRNSYS. A significant assumption in this method is that F' remain identical between test and use conditions. For this to be true, the heat transfer coefficient between the fluid and absorber h_f would have to remain constant. For either large changes in flow rates, or where the heat transfer coefficient is particularly sensitive to flow rate (such as in air collectors), these assumptions are not valid and F' must be determined at the new conditions.

4.6.2 Detailed Method of Flow Rate Corrections

The most sensitive variable for any change in collector flow rate is h_f , which drives the heat transfer from the absorber. Changes in this heat transfer coefficient affect the mean plate temperature, which in turn can influence U_L through the convection coefficients within the collector and cover system. More importantly, changes in h_f ripple through all the terms of the Hottel-Whillier model including the effectiveness ε and F' , both of which have profound effects on the performance parameters $F_r(\tau\alpha)$ and $F_r U_L$. The goal of the detailed correction method is to

determine h_f at test conditions by analytically deconstructing the collector within the framework of Hottel-Whillier. The value of h_f at use conditions can then be scaled through known heat transfer relations and the collector can be analytically reconstructed to yield $F_r(\tau\alpha)$ and $F_r U_L$ at the use conditions without the assumptions of a constant value for F' .

As a starting point in the analysis, the parameters $F_r(\tau\alpha)$ and $F_r U_L$ are available along with the flow rate at which they were obtained. This set of two equations and three unknowns (F_r , $\tau\alpha$ and U_L) can be solved if one of the variables is specified. Out of the possibilities, the tau-alpha product of the cover absorber system is typically the best known and easiest to estimate for any collector configuration. Once this variable is specified, both F_r and U_L can be determined. From here it is possible to define F_r as the product of the effectiveness and efficiency factor, which can be expressed as

$$F_r = F' \varepsilon = \frac{\dot{m} C_{air}}{U_L} \left[1 - \exp\left(\frac{U_o}{\dot{m} C_{air}} \right) \right] \quad [4.6.2]$$

With all the other variables known, the conductance from fluid to the ambient as defined by U_o can now be solved for. Depending on the boundary conditions inside the absorber channel, this conductance may take one of two forms. The form of equation 4.6.3 is for an isothermal boundary condition on the flow channel. A slightly more complicated form assumes an adiabatic boundary condition on the back-side of the channel with radiation exchange across the channel. This form of U_o is given by equation 4.6.4, where the linearized heat transfer coefficient h_r is based on the mean plate temperature T_{pm} and absorptance of the channel interior, which is assumed to be equal to the top absorber coating.

$$U_{o(isothermal)} = \frac{1}{\frac{1}{U_L} + \frac{1}{h_f}} \quad [4.6.3]$$

$$U_{o(adiabatic)} = \frac{1}{\frac{1}{U_L} + \frac{1}{0.5h_f + \frac{1}{\frac{1}{0.5h_f} + \frac{1}{h_r}}}}$$

[4.6.4]

where

$$h_r = \frac{4\sigma T_{pm}^3}{\frac{2}{\alpha_{plate}} - 1}$$

Using either the isothermal or adiabatic boundary condition, the heat transfer coefficient h_f at test conditions can be determined. If flow in the channel is assumed turbulent⁷, then the heat transfer coefficient can be scaled to the new flow rate using the Nusselt number. The correlations used in this work were those proposed by Hollands (1981)

$$h = Nu \frac{k}{d}$$

where

$$Nu = 0.03 Re^{0.74}$$

[4.6.5]

Because the flow channel geometries are identical at both flow rates, the change in heat transfer coefficients is a simple function of the ratio of flow velocities raised to a power.

$$\frac{h_{test}}{h_{use}} = \left(\frac{\dot{V}_{test}}{\dot{V}_{use}} \right)^{0.74}$$

[4.6.6]

With the new heat transfer coefficient, the array can be analytically rebuilt through the equation set to determine the collector parameters $F_r(\tau\alpha)$ and $F_r U_L$ at use conditions. If the parameters are to represent two collectors in series as at the McKay center, then the fluid

⁷ Although the exact geometry of the flow channel is not known, a rough estimate of the Reynolds number from the isometric sketch of figure 6.6.1 is approximately 2600. Also, it would be assumed that Solaron would have designed the channel for turbulence to avoid the large performance penalties that would be associated with laminar or transition flow.

capacitance rate must be halved during the analytical reconstruction to account for the doubling in collector area.

If the isothermal boundary condition on the flow channel of equation 4.6.3 were assumed and the effects of mean plate temperature on convection coefficients were neglected then the flow rate corrections would be complete at this point. If either of these items cannot be assumed then the mean plate temperature must be calculated and the effects on either heat transfer coefficient (U_L or h_r) assessed. If U_L is defined for the mean plate temperature such that

$$q''_{air} = S - U_L (T_{pm} - T_{amb}) \quad [4.6.7]$$

Substituting the airstream gain q''_{air} into equation 4.1.9 and solving for the mean plate temperature results in the form

$$T_{pm} = T_{fi} + \frac{F_r S - F_r U_L (T_{fi} - T_{amb})}{F_r U_L} (1 - F_r) \quad [4.6.8]$$

From this mean plate temperature, both h_r and U_L can be calculated for the use and test conditions. The loss coefficient U_L consists of two parts constituting the back and edge losses defined by U_{b-e} and the top losses through the cover system defined by U_t . While U_{b-e} stays constant with plate temperature, U_t is affected by the changes in the natural convection coefficients caused by temperature gradients within the system.

Calculation of the convection coefficient between the absorber plate and the glazings within the cover system was based on the correlation of Hollands (1976), which provides the Nusselt number as a function of the Rayleigh number and collector slope β .

$$Nu = 1 + 1.44 \left[1 - \frac{1708(\sin(1.8\beta))^2}{Ra \cos(\beta)} \right] \left[1 - \frac{1708}{Ra \cos(\beta)} \right]^+ + \left[\left(\frac{Ra \cos(\beta)}{5830} \right)^{1/3} - 1 \right]^+ \quad [4.6.9]$$

Where the + exponent on the bracketed terms signifies that only positive values of these terms are to be considered (i.e. negative values are replaced with zero).

The final convection coefficient to be considered is that from the top cover to ambient. Because the collectors are assumed to be free-standing during the performance tests, the correlation of Sparrow (1979), which was experimentally determined in wind tunnel tests on flat plates is employed

$$Nu = 0.86 Re^{0.5} Pr^{0.33} \quad [4.6.10]$$

The characteristic length of the collector for this relation is four times the area divided by the perimeter. Knowing the Nusselt numbers for both situations, the convective heat transfer coefficients can be evaluated as

$$Nu = \frac{hL}{k} \quad [4.6.11]$$

In addition to these convective coefficients, radiative losses also need to be considered. Due to the plate spacings in the absorber and cover system, the view factors can be considered near unity and the radiative heat transfer evaluated as

$$q''_{radiation} = \frac{\sigma(T_1^4 - T_2^4)}{\frac{1}{\varepsilon_1} + \frac{1}{\varepsilon_2} - 1} \quad [4.6.12]$$

Where the subscripts on the surface temperatures T and emittance ε refer to the two surfaces participating in heat exchange. Energy balances including the radiation and convection terms can be written for the absorber plate and each of the glass covers to define the heat loss from the absorber through the cover system. This loss term can then be divided by the temperature difference between the absorber and ambient to provide an effective top loss coefficient.

$$U_t = \frac{q''_{absorber-ambient}}{(T_{pm} - T_{amb})} \quad [4.6.13]$$

Because the heat transfer coefficients are dependent on the plate and cover temperatures, the entire collector equation set must be solved simultaneously to yield the final parameters of F' and U_L , which can then be used to calculate $F_r(\tau\alpha)$ and $F_r U_L$ of the array at use conditions.

4.6.3 Results of the Detailed Correction Method

To solve the equation set outlined in section 4.6.2, several operating parameters that dictate the mean plate temperature must be specified. Fortunately, many of these operating conditions are specified by ASHRAE 93-77 under which the tests were performed. Reviewing these specification as stated in section 4.3, we see items specifying the irradiance levels, inlet temperature test levels, wind speed and ambient temperature range. Combining these restrictions together with some educated guesses it is possible to specify the required parameters as listed in table 4.6.1. The values used to predict h_f in the numerical analysis are based on these figures along with their range of uncertainty. The final collector parameters adjusted for the series connection and flow rate will have an RMS uncertainty determined by these uncertainties propagated through the equation set. Cover and absorber properties used to predict the tau-alpha product are quite standard for the low-iron glass and painted absorbers used in the Solaron 2000 collector and are listed in table 4.6.2.

Table 4.6.1 Variables used to estimate T_{pm} at test conditions.

	Estimated Value	Uncertainty	Reason
I (W/m^2)	850	± 100	ASHRAE 93-77
V_{wind} (mph)	7.5	± 2.5	ASHRAE 93-77
β (degrees)	45	± 15	ASHRAE 93-77 & Practical considerations
T_{fi} ($^{\circ}C$)	30	± 15	ASHRAE 93-77 & Practical considerations
T_{amb} ($^{\circ}C$)	20	± 10	ASHRAE 93-77 & Practical considerations
U_{b-e} ($W/m^2 \text{ } ^{\circ}C$)	1	$\pm 20\%$	Practical considerations

Table 4.6.2 Variables used to estimate tau-alpha of the cover absorber system.

Property	Value
τ_{glass} (solar spectrum)	0.90
α_{glass} (thermal spectrum)	0.88
Glass extinction coefficient	0.014
Glass refractive index	1.526
$\alpha_{absorber}$	0.935
$\epsilon_{absorber}$	0.935

The calculated tau-alpha product of the cover absorber system defined by the properties in table 4.6.2 is 0.762. when Solaron's catalog test values of 0.49 for $F_r(\tau\alpha)$ and 2.89 for F_rU_L are used (Solaron 1977), all the collector variables can be determined⁸. The resultant collector parameters at test conditions are summarized in the first rows of tables 4.6.3 and 4.6.4 for the isothermal and adiabatic boundary conditions. A simple check on the value of U_L as predicted by the equation set to that which results directly from the collector parameters agrees within 1 percent, assuring that the estimates of tables 4.6.1 and 4.6.2 are accurate and self consistent. The next two rows of the tables show the results for the basement and office arrays after the heat transfer coefficient has been scaled to the new flow rates. These values of $F_r(\tau\alpha)$ and F_rU_L represent how the collector arrays should have performed in their as-installed condition.

The only significant difference between the isothermal and adiabatic cases is a small drop in the fluid heat transfer coefficient in the latter due to the thermal resistance of the radiative exchange. This causes only a 1 to 2 percent drop in F' , $F_r(\tau\alpha)$, and F_rU_L relative to the isothermal case. Additionally, the effect of flow rates on the collector loss coefficient U_L is negligible because while the flow rates have increased through the collector, the series connection halves the fluid capacitance rate per unit area, thus bringing it back to near the original value. The result is that the mean plate temperature is kept nearly constant, and therefore the loss coefficient remains static. In any instance where the fluid capacitance rate is kept constant between configurations, the effects of plate temperature on U_L will likely be minimal and can be ignored. This simplification eliminates the need to specify the conditions under which the collector was tested as outlined in table 4.6.1 and only the material properties of the cover absorber system need to be provided.

Figure 4.6.1 shows SRCC plots of the collector parameters as currently measured in their degraded state and as they should have theoretically performed at the current flow rates. Although there is a large uncertainty in the current values, a level of degradation is readily apparent in both systems with a drop of approximately 16 percent in $F_r(\tau\alpha)$ and a 23 percent increase in F_rU_L from the mean values for both arrays as listed in table 4.4.1. These degradations are beyond what can be explained by the uncertainty in either the measured values of current performance or the calculated values of the original predicted performance.

⁸ There exists some confusion as to what the original tested collector parameters are. The results of Solaron (1977) and Sadler (1988) are comparable with those of Oonk (1976). Results from Wyle (1978) and Cole-Appel (1978) however, show loss coefficients F_rU_L that are twice as high as those of Solaron, Sadler, and Oonk for what should be an identical collector. This study assumes the lower loss coefficient as defined by Solaron (1977) and verified by Sadler (1988) for an installation similar to that on the McKay center.

Table 4.6.3 Summary of collector array properties for isothermal boundary condition in absorber flow channel.

	V_{flow} (CFM/ft ²)	θ	ε	h_f (W/m ² -°C)	U_o (W/m ² -°C)	U_L (W/m ² -°C)	F'	T_{pm} (°C)	$F_r\tau\alpha$	F_rU_L (W/m ² C)
SRCC ¹	2.0	0.32±0.02	0.86±0.007	14±0.5	3.4±0.03	4.5	0.76±0.006	96±12	0.50	2.90
Basement	4.3	0.31±0.02	0.86±0.007	27±0.9	3.7±0.04	4.3±0.03	0.86±0.003	88±12	0.57±0.002	3.21±0.01
Office	5.2	0.30±0.02	0.87±0.007	28±0.9	3.7±0.04	4.3±0.04	0.87±0.003	87±12	0.58±0.002	3.24±0.02

Table 4.6.4 Summary of collector array properties for adiabatic boundary condition in absorber flow channel.

	V_{flow} (CFM/ft ²)	θ	ε	h_f (W/m ² -°C)	U_o (W/m ² -°C)	U_L (W/m ² -°C)	F'	T_{pm} (°C)	$F_r\tau\alpha$	F_rU_L (W/m ² C)
SRCC	2.0	0.32±0.02	0.86±0.007	14±0.5	3.4±0.03	4.5	0.76±0.006	96±12	0.50	2.90
Basement	4.3	0.31±0.02	0.86±0.007	24±0.8	3.7±0.04	4.4±0.03	0.85±0.004	89±12	0.56±0.002	3.17±0.01
Office	5.2	0.29±0.02	0.87±0.007	25±0.9	3.7±0.04	4.3±0.03	0.85±0.004	88±12	0.57±0.002	3.20±0.02

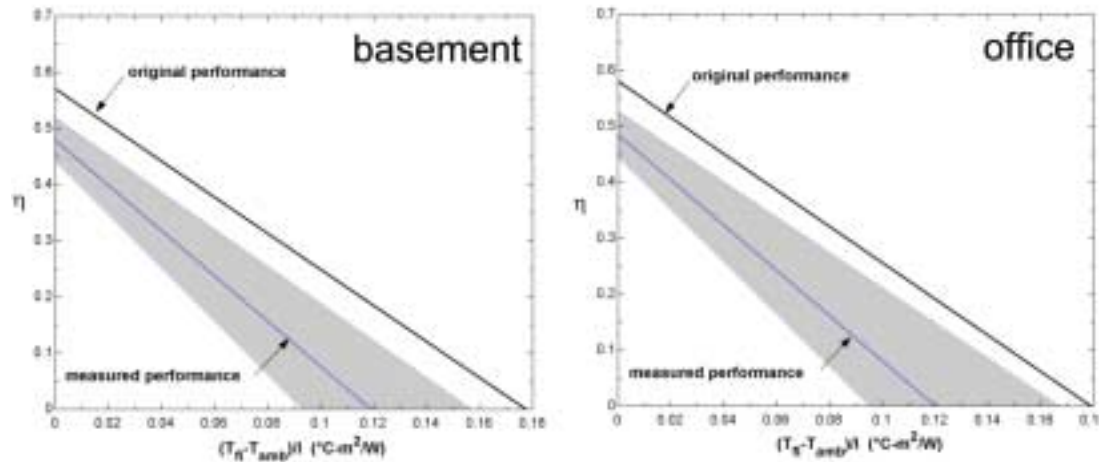


Figure 4.6.1 SRCC curves of original and measured performance for the arrays. Shaded bands indicate uncertainty in measured performance.

¹ SRCC refers to the original tested flow rates and conditions for the collectors during characterization by Solaron (1977).

4.7 Visual Inspection of Collector Arrays

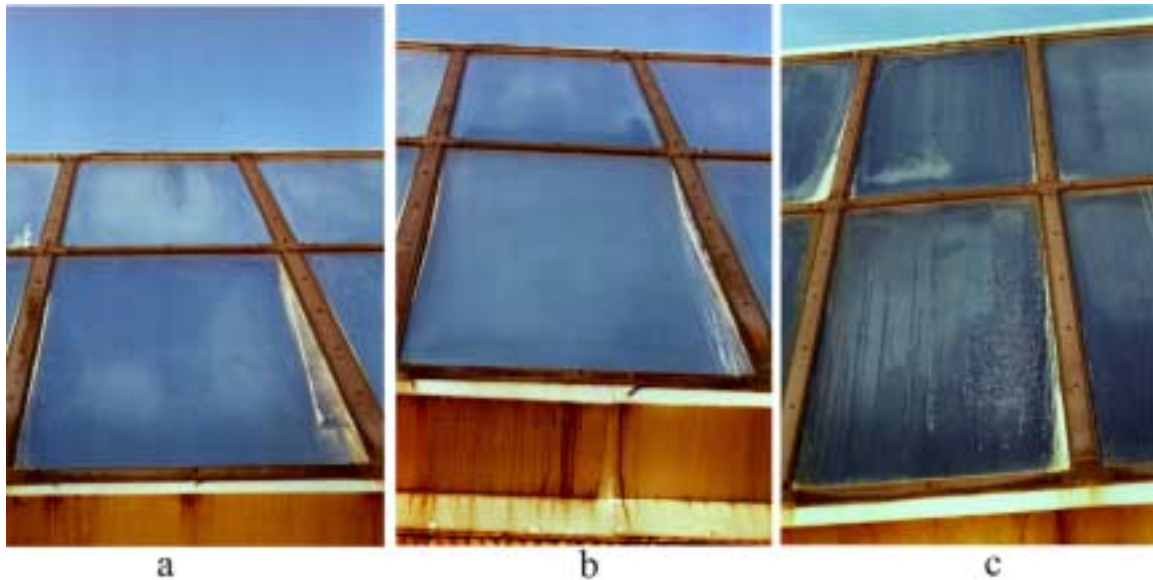


Figure 4.7.1 Closeup photographs of collectors within the arrays showing a variety of degradation mechanisms including catastrophic failure of the cover seals (a,b) and the associated moisture penetration, condensation, and deposits inside the cover system (c).

From a cursory look at figure 4.7.1, the previous quantitative analysis of collector degradation may appear as an attempt to master the obvious. Nearly all of the 70 collector cover systems have lost the integrity of their seals allowing moisture to penetrate and condense inside the covers as seen in figure 4.7.1c. Many covers displayed severe mechanical damage to the spacer between the glazings with the spacer often bowed inwards towards the center of the collector along the long axis as seen in figure 4.7.1b (the spacer appears as a chalky white strip). The complete separation of the spacer as seen on the right side of figure 4.7.1a may be due to cold working of the aluminum strip from continual bowing and relaxation.

Failure of the cover seals is believed to have been caused by excessive pressure variations in the air gap between the covers. The double cover systems appeared to be of a typical commercial construction built on a 12 mm aluminum spacer with butyl rubber sealant forming the airspace. Maximum stagnation temperatures within this airspace have been calculated at 150 °C for the summer months using the detailed collector model of section 4.6. If the airspace was created with room temperature air at 23 °C, then the resultant pressure variation inside the covers could exceed 25 kPa over this temperature range. This represents a tensile force of nearly 10,000 lbs on the collector seals. Alternately, the covers would have to separate by 3 mm, or the spacer

would have to bow to maintain atmospheric pressure in the airspace. The equilibrium between these two extremes would be dictated by the elasticity of the butyl sealant and the lateral displacement (i.e. bowing) of the aluminum spacer to accommodate the pressure fluctuations. At some point it is likely that the integrity of the seal was breached due to either detachment of the seal under tensile strain or lateral displacement of the spacer. At this point the pressure in the airspace would come into equilibrium with atmospheric conditions.

The large number of spacers bowed towards the center of the collectors may be due to a re-equalization of pressures at low temperature operation. When the seals were broken at high temperature operation, the mass content of air at the new equilibrium stagnation conditions would be much less than when the airspace was originally sealed at 23 °C. As the collector cooled down at night, the gage pressures in the airspace would begin to turn negative, creating a compressive force on the butyl seal that could then seal the leak. Constrained by the rigid aluminum spacer, the only displacement that could accommodate the pressure variation would be a lateral bowing of the spacer. Although these speculations cannot be verified, they are a plausible explanation of the current status of the covers.

Although the covers were not removed for a direct inspection of the absorber plate there were several collectors where condensation and deposits were light enough to appraise the absorber appearance through the covers. On all of the collectors that could be inspected in this manner, the absorbers appeared fully intact and without any sign of deterioration. No flaking or delamination of the painted absorber coating was apparent in any of the inspected collectors. Although the cover systems had experienced catastrophic failure, damage appeared restricted to the interior airspace of the covers with no water damage, accumulated deposits, or delamination of the absorber coating visible.

4.8 Synopsis

The collector arrays were experimentally characterized using the Hottel-Whillier framework to determine the performance parameters $F_r(\tau\alpha)$ and F_rU_L . These parameters were fitted using a combination of night-time and solar noon data to avoid the reliance on incident angle modifiers in determining the variation in the tau-alpha product. High uncertainties of 5 °C in the ambient temperatures prevented an exact characterization of the performance parameters, but the estimated performance parameters show degradations of 16 percent in $F_r(\tau\alpha)$ and 22 percent F_rU_L on average for the two arrays when compared to theoretical performance at identical flow rates.

Visual inspections of the collectors showed severe moisture penetration of the cover system, which would lower the transmittance. The higher loss coefficients in both arrays are likely due to air infiltration in either the ductwork or the internal manifolds within the array.

5 Pebble Bed Storage

The 9 tons of river gravel in each of the pebble beds serves a critical role in the performance of the solar system. During high irradiance days the instantaneous output from the collector array at 62 kW can greatly exceed the heating demands of the building. The pebble beds offer a useful store for this excess energy so that it can later be retrieved to service the building load during times of low solar irradiance (i.e. early morning, night, and cloudy days).

Accurate modeling of the pebble beds is required to determine the storage rate, capacity, and availability of energy stored in the beds. Through a proper model framework and empirical calibration, these parameters can be accurately determined and the dynamic performance of the bed predicted under the wide range of conditions encountered in solar thermal systems. This section discusses the analytical model employed in the simulation and the various methods used to empirically fit bed parameters such as the flow distributions, loss coefficient, and sensor placement.

5.1 Schumann Analysis of Pebble Bed Storage

Although detailed models have been developed for the modeling of pebble bed storage by Riaz (1977) and summarized by Adebisi and Chenevert (1996), the Schumann (1921) model remains the simplest and is well suited to conditions encountered in solar thermal storage. In essence, the pebble bed in the Schumann model is viewed as a combined heat exchanger and storage device. Breaking the bed into lengthwise nodes, the heat transfer between the airflow and pebbles within each node can be described by

$$\frac{\rho_{rock} C_{rock} (1 - v_{bed}) L_{bed} A_{bed}}{N_{nodes}} \frac{dT_{rock}}{dt} = \dot{V}_{air} \rho_{air} C_{air} \epsilon (T_{air} - T_{rock}) \quad [5.1.1]$$

Where the bed effectiveness ϵ represents the ratio of actual to theoretical maximum heat transfer as defined by the NTU method of equation 5.1.2. Here, a small correction has been made to the standard NTU of the pebble bed to correct for conduction within the pebbles themselves. The corrected value NTU_c as defined in equation 5.1.3 was originally proposed by Jeffreson (1972).

$$\varepsilon = 1 - e^{\frac{-NTU_c}{N_{nodes}}} \quad [5.1.2]$$

$$NTU_c = \frac{NTU}{1 + \frac{Bi}{5}} \quad [5.1.3]$$

where

$$NTU = \frac{h_v L_{bed} A_{bed}}{\dot{V}_{air} \rho_{air} C_{air}}$$

The volumetric heat transfer coefficient h_v was determined using the empirical relations of Lof and Hawley (1948) as stated in equation 5.1.4 where all variables must be provided in standard SI units and the value of h_v is yielded in $W/m^3 \cdot C$.

$$h_v = 650 \left(\frac{\dot{V} \rho_{air}}{A_{bed} D_{rock}} \right)^{0.7} \quad [5.1.4]$$

An energy balance on each node, including losses to the ambient, is described by equation 5.1.5 to complete the equation set. A more rigorous treatment of the analysis for pebble bed storage is presented in Duffie and Beckman (1992).

$$\frac{\rho_{rock} C_{rock} (1 - v_{bed}) L_{bed}}{N_{nodes}} \frac{dT_{rock}}{dt} + \frac{U_{wall} P_{bed} L_{bed}}{N_{nodes}} (T_{air} - T_{amb}) = \varepsilon \frac{\dot{V}_{air} \rho_{air} C_{air}}{A_{bed}} \frac{dT_{air}}{dL_{bed}} \quad [5.1.5]$$

where

$$dL_{bed} = \frac{L_{bed}}{N_{nodes}}$$

5.2 Variables Employed in Schumann Analysis

The pebble beds at the McKay center are filled with washed and screened 1.5" diameter river gravel. An aggregate heat capacity (C_{rock}) of 840 J/Kg was used for the pebbles with a density (ρ_{rock}) of 3720 kg/m³. The void fraction v within the bed was estimated at 43 percent yielding an effective bed density of 1600 kg/m³. These values have been found to be

representative of pebble bed storage systems of this type by Hughes (1975) and Persons (1978) in their work at the Arlington House. The bed loss coefficient U_{bed} was calculated at $0.65 \text{ W/m}^2\text{C}$ for the 2" of polystyrene insulation around the box perimeter. The effective bed length L_{bed} differs from the actual depth of the pebble mass due to the capacitance of the bond beam blocks forming the lower plenum in figure 2.4.2. Equating the thermal mass of the blocks to an effective length of the pebbles adds 5" to the actual bed length bringing L_{bed} to 5'7". Air temperature within the room containing the solar equipment was set to 30°C , eight degrees higher than the room setpoints. The higher temperature is due to heat gains from not only the ductwork but the boxes themselves that raise the solar room temperature to approximately this level.

5.3 Numerical Solutions of the Schumann Equations

While some analytical solutions to the Schumann equations can be found for step responses in inlet temperatures, any practical application to solar thermal processes requires finite difference methods. Equations 5.1.1 and 5.1.5 represent differential equations across time and length respectively. Solution of the equation set requires finite difference methods, and time intervals of 15 minutes were used as this is the same period in which duct temperatures were recorded. The pebble bed was divided into 25 discrete vertical segments resulting in a node length nearly equal to the pebble diameter. The equation set was then solved implicitly using a Crank-Nicolson approach with the average rock temperature over each timestep used to estimate T_{rock} in equation 5.1.1. The numerical engine then employs a marching step strategy to propagate the thermal wave through the bed with respect to both depth and time. Although all node temperatures for both the fluid and pebbles are calculated at each timestep, only the exiting air temperature was used for model calibration of the bed. Predicted bed exit temperatures were compared with measured values over the solar test interval to determine model accuracy and alternately for use in parameter fitting.

5.4 Results of the Simple Schumann Model

The bed exit temperatures shown in figure 5.4.1 are the result of solving the Schumann model over the solar test interval subject to the parameters specified in section 5.2. The model was driven by the actual bed inlet temperatures as recorded by TS-7 in 15 minute intervals.

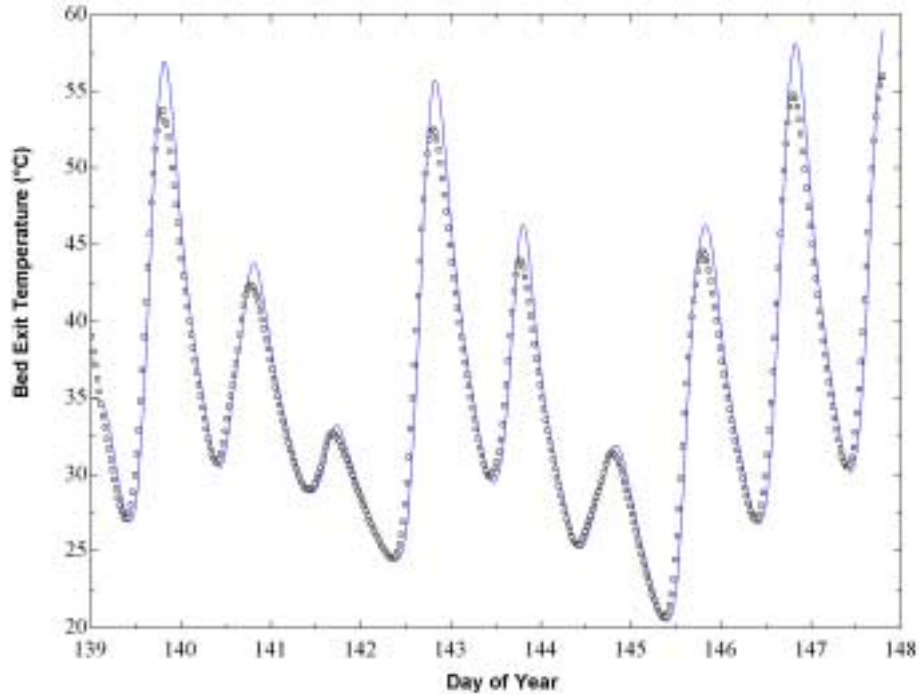


Figure 5.4.1 Measured (points) and predicted (solid line) basement bed outlet temperatures TS-8 for the simple Schumann model over the solar test interval.

Two discrepancies are apparent between the model and measured data. The most obvious is that the model consistently over-predicts the peak exit temperature of the bed by a significant margin. The second difference is the small shift in the times of minimum and maximum exit temperatures from what was actually measured. This shift in peaks is accompanied by an apparently sharper and delayed profile of the modeled exit temperature. These discrepancies are attributable to two inaccurate assumptions in the model. The first is the estimation of the bed loss coefficient U_{bed} derived from construction drawings. It is possible to empirically determine this parameter from an overall energy balance on the bed, and this analysis is pursued in the section 5.5. The second issue is an inherent assumption of uniform flow through the bed that is built into the Schumann model. Section 5.6 describes how this assumption can be relaxed by modeling the bed as separate segments operating at different flow rates. These two modifications to the simple Schumann model will be shown to provide a near perfect fit to the measured data.

5.5 Empirical Determination of Bed Loss Coefficient

While figure 5.4.1 alludes to an improper bed loss coefficient, it is hard to estimate what the proper value should be from a simple plot of exit temperatures. A better representation of energy lost through the bed walls can be produced by calculating it through an integrated energy balance. If the entire bed can be taken as the system then the accumulated energy in it can be defined by equation 5.5.1 if losses are neglected.

$$Q_{accumulated} = \int \dot{V}_{air} \rho_{air} C_{air} (T_{in} - T_{out}) \quad [5.5.1]$$

Where T_{in} is the temperature recorded from TS-7 and T_{out} is either the temperature recorded from TS-8 or the predicted outlet temperature of the Schumann model. Figure 5.5.1 is a plot of the accumulated energy as calculated from both the measured and predicted outlet temperatures without losses. The periodic cycle in accumulated energy represents the daily storage and release of energy within the bed as the thermal wave passes through. When the bed has no thermal losses, the amount of energy flowing into the bed exactly equals the amount released over the course of a day and the curve cycles around zero with a half-period roughly equal to the traversal time of the thermal wave. The steady upward rise in the actual bed profile of figure 5.5.1 represents energy that went into the bed and never came out through the ductwork. This energy cannot be accumulated in the bed over the solar test interval, but instead represents the missing term in the energy balance. This term is the energy lost through the walls of the pebble bed and can be calculated from figure 5.5.1 by taking the difference between the measured profile and the ideal profile as predicted without losses. This difference in accumulated energy is redefined as the bed loss and is depicted as the dashed line of figure 5.5.1.

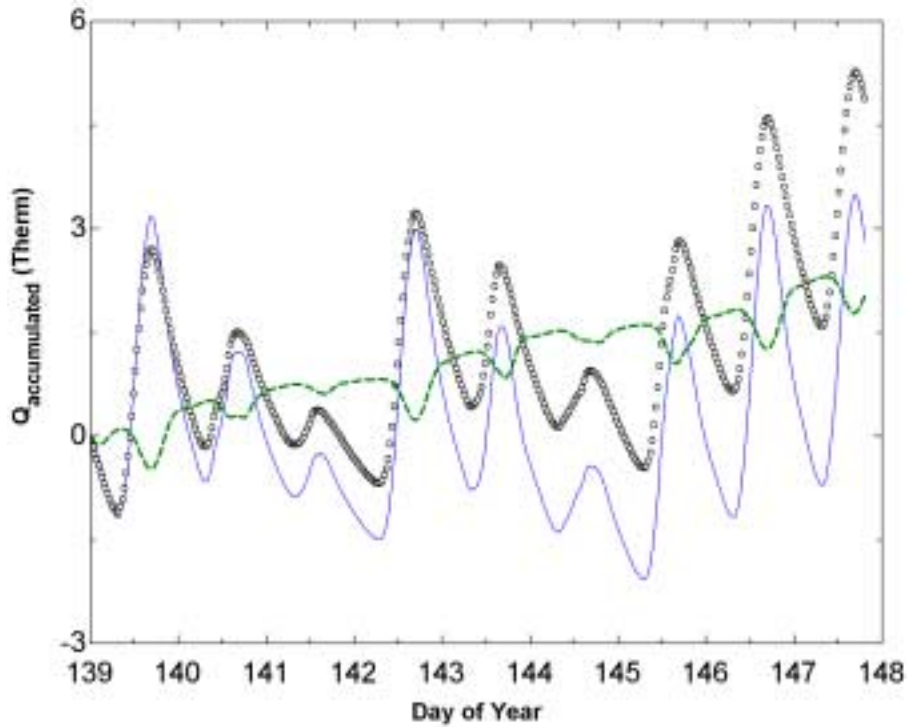


Figure 5.5.1 Accumulated bed energies over the solar test interval for actual (points) and predicted (solid line) bed outlet temperatures for $U_{bed} = 0$. Dashed line illustrates the losses.

Bed losses can be quantified by varying the parameter U_{bed} of equation 5.1.5 until the accumulated energies of both the model and actual bed match over the solar test interval. When this occurs, the energy balance of the model will close and the U_{bed} will represent the actual loss coefficient that satisfies the thermodynamic constraints on the system (as defined when no energy is accumulated in the bed over the solar test interval). Figure 5.5.2 shows the result of such a comparison where U_{bed} is set to $3 \text{ W/m}^2\text{C}$ in the model. There is still a slight variation in the accumulated energies of the model and true system that oscillates about zero. This variation is due to non uniform flow within the bed and will be addressed in the following section.

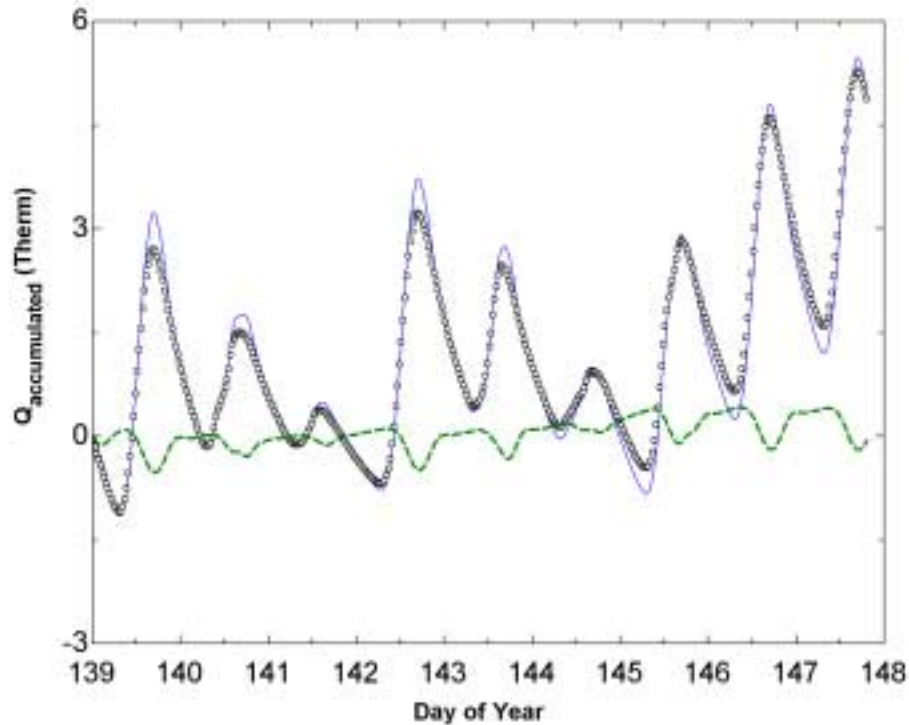


Figure 5.5.2 Accumulated bed energies in the basement system over the solar test interval for actual (points) and predicted (solid line) bed outlet temperatures for $U_{bed}=3 \text{ W/m}^2\cdot\text{C}$.

5.6 Non-Uniform Flow Through Pebble Bed

One of the largest constraints on the Schumann model for predicting actual bed performance is that it assumes uniform plug flow through the pebble bed. Pressure variations in the upper and lower plenums can often create situations where this assumption is not valid. Both Persons (1978) and Hollands (1984) have experimentally determined flow uniformity through pebble beds. In the work of Hollands, flow rates through the bed were well correlated to the expected pressure distributions in the plenums with the highest flow velocities occurring near the walls. The work of Persons displayed a more random distribution, which may be due in part to ductwork that was located in the upper plenum. Both studies were able to measure the speed of the thermal wave in each bed section by relying on networks of over 90 temperature sensing elements dispersed through the beds. From the traversal speed of the thermal waves, they were able to interpret flow rates based on the Schumann equations.

At the McKay center there are no temperature elements within the beds to determine the distribution of flows, and the flows must be determined solely from the two temperature sensors located at the inlet (TS-7) and outlet (TS-8) of the bed. The following sections describe how numerical optimization methods developed around the findings of Persons and Hollands can be applied to solve for the flow distributions even with limited data sets.

5.7 Relaxing The Uniform Flow Constraint

The assumption of uniform flow in the Schumann model was relaxed by employing several separate and simultaneous bed models coupled at the inlet and outlet. The non uniform bed was split into several separate beds, each having a uniform flow rate that was allowed to differ from neighboring bed segments. This idea is shown schematically in figure 5.7.1 where the beds are driven by the same supply temperature (TS-7), but may have varying speeds of the thermal waves within. Outlet flows from the segments are then recombined to produce an aggregate bed exit temperature that correlates to the duct temperature measured by TS-8. For computational purposes, the maximum number of bed segments modeled in this work was 10. Although this method still assumes that flows within the individual segments do not mix, it is a significant relaxation of the uniform flow constraint.

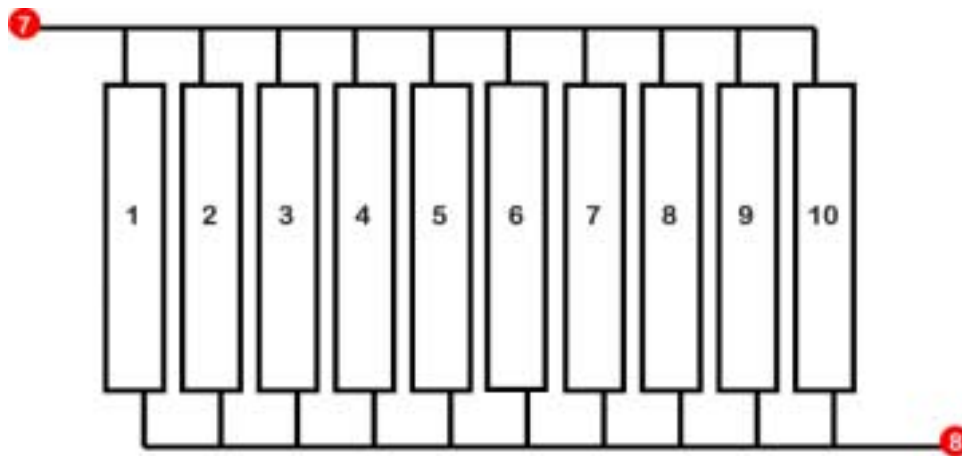


Figure 5.7.1 Layout of 10 bed segment model used in non-uniform flow models. Location of actual inlet (TS-7) and outlet (TS-8) temperature sensors shown.

Proper flow distributions within the bed were determined through an optimization of flow profiles through the bed segments such that the aggregate bed exit temperature produced a best fit

to the measured exit temperature as recorded by TS-8 over the solar test interval. The objective function was therefore a minimization of the integrated temperature error as defined by equation 5.7.1 in units of degree hours ($^{\circ}\text{C}\cdot\text{hr}$). The integrated error was measured from 48 hours after the start of the solar test interval until the end to allow for initial conditions within the bed to fade.

$$Error_{bed} = \int |TS8_{modeled} - TS8_{measured}| dt \quad [5.7.1]$$

With ten bed segments, the number of free parameters for minimization of the integrated error would be nine¹. Numerical optimization with this many free parameter is undesirable from both a computational efficiency as well as an accuracy standpoint. Finding a minimum may take several hours of computation and even then, the routine may find a local and not a global minimum.

By formulating flow distributions around the finding of Persons (1978) or alternately those of Hollands (1984), the number of free parameters can be limited to one or two for which optimization routines are readily capable of obtaining solutions.

5.7.1 Ordered Profile

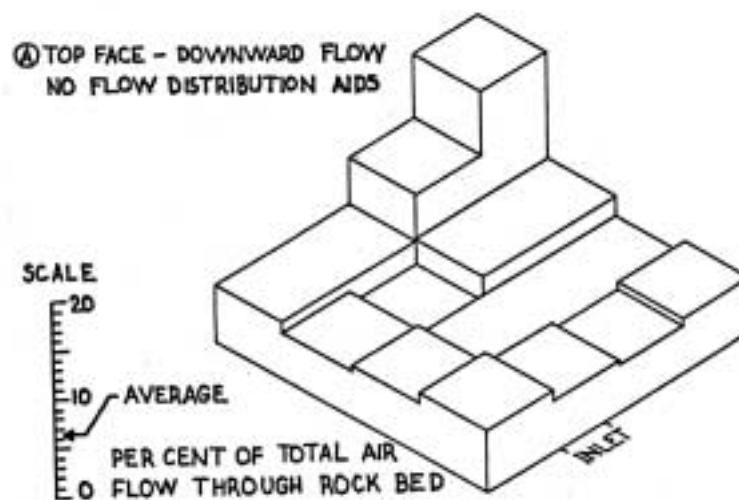


Figure 5.7.2 Volumetric flow distribution through pebble bed found by Persons (1978) in work on the Arlington house.

¹ The last parameter is dictated by the flow rate that brings the total of the segments to the total bed flow.

The flow distribution of figure 5.7.2 found by Persons does not appear to be ordered in any manner. However, if the individual bed segments are numbered in order of ascending flow rate then a specific pattern develops. When numbered in such a manner, the flow distribution can be described by a function that increases with bed number. Such a function may be as simple as a line defined by $y=a \cdot x$, but to allow for some non-linear distribution in the flow ranking, an exponential function in the form of equation 5.7.2 was used in this study.

$$y = R_{bed} x^n \quad [5.7.2]$$

Bed segment numbers are defined as x with the flow percentage within the node defined by y . R_{flow} characterizes the ratio of maximum to minimum flow percentages found in all segments and n determines the inflection of the curve, being concave for values less than unity and convex for larger values. At a value of one for n , the equation simplifies to a linear increase in flow rates across the segments. A better illustration of the behavior of this function is presented in figure 5.7.3 where the resulting flow distributions are shown for a variety of conditions.

By ranking the bed segments in ascending order and defining the distribution through equation 5.7.2 it is possible to limit the degrees of freedom from nine to two as defined by the variables R_{flow} and n . This simplification of flow distributions is made possible by the fact that the outlet temperature profile of the bed (the final objective of the analysis) is independent of how the segments are arranged. The flow distributions could be rotated 180°, or even arbitrarily swapped and still yield the same thermal profile for the bed.

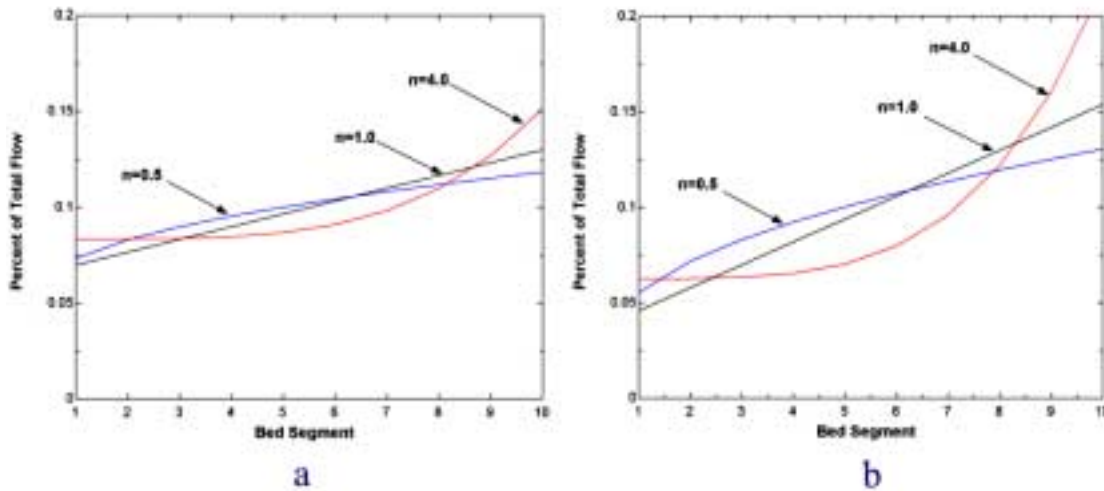


Figure 5.7.3 Flow distributions through bed segments according to equation 5.7.2 where $R_{bed} = 2$ (a) and $R_{bed} = 4$ (b). The sum of flow percentages for all segments will always be unity.

Bed losses were assigned equally to all segments in the model. Although higher losses should be assigned to segments on the perimeter, and even higher to those located in corners, we have no insight as to where the bed segments are located in the theoretical model. The highest flow rate may occur in a corner as found by Persons, or it may be located in the center. Without an array of sensors in the bed itself, the link between segment location and flow rate is not known and the best approximation is to equally distribute the losses.

Simulations were run over a range of R_{flow} from 1 (uniform flow) to 4 with values of n ranging from highly concave at a value of 4.0 to highly convex at 0.2. Solution contours for the integrated error defined by equation 5.7.1 over this range are shown in figure 5.7.4.

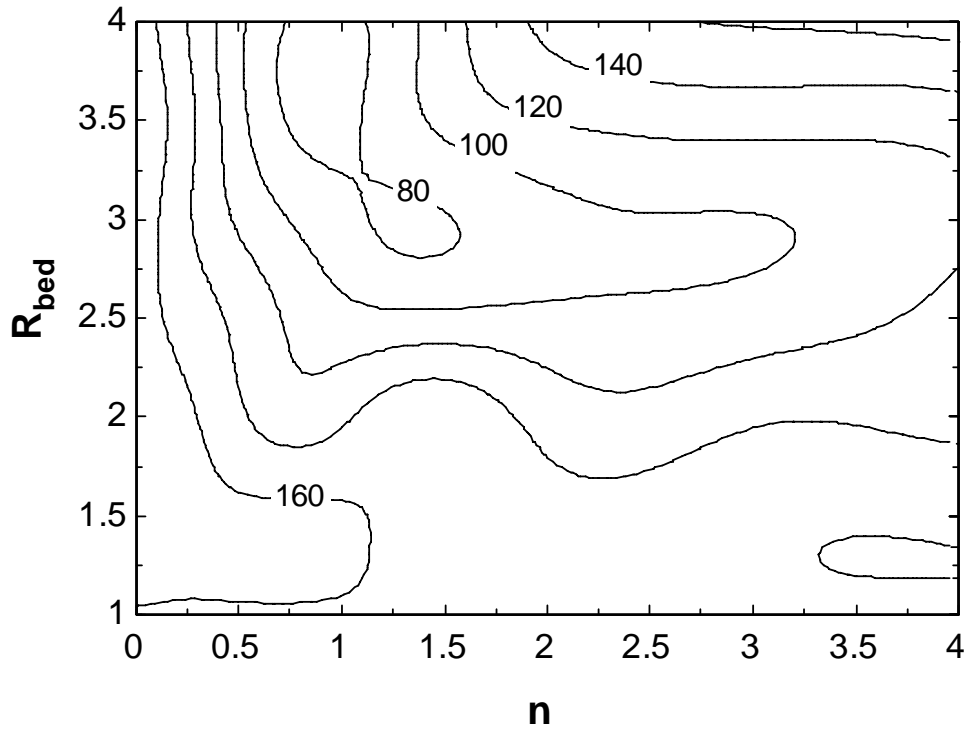


Figure 5.7.4 Contour plot of integrated error ($Error_{bed}$) for basement pebble bed subject to flow distributions of equation 5.7.2.

The best fit to the measured data was produced with an R_{flow} of 3.44 and n equal to 1.01. The integrated error was 63.9 degree-hours² under these criteria yielding the predicted outlet temperature profile shown in figure 5.7.5. A corresponding calibration plot of the measured vs. modeled bed outlet temperatures (TS-8) is provided in figure 5.7.6 and illustrates that the model fits the data well over the entire range.

² When averaged over the 9 days over the solar test interval, this integrated error results in an average deviation of 0.3 °C.

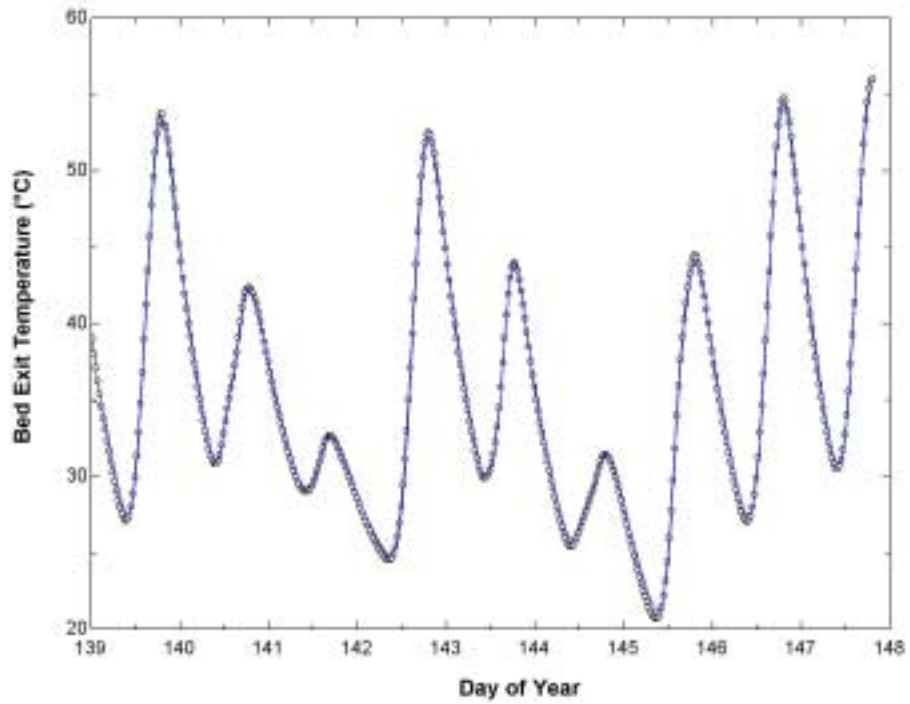


Figure 5.7.5 Measured (points) and predicted (solid line) bed outlet temperatures (TS-8) for the ordered profile distribution of the Schuman model over the solar test interval. $R_{bed}=3.44$, $n=1.01$, $U_{bed}=3$.

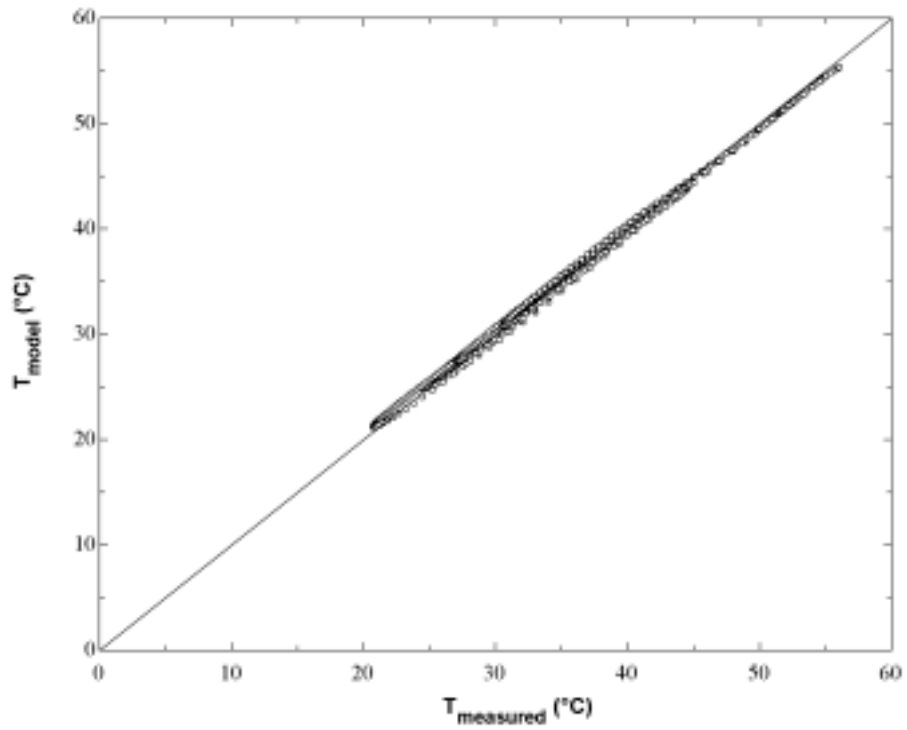


Figure 5.7.6 Calibration plot of measured vs. model predicted bed outlet temperatures of figure 5.7.5.

5.7.2 Cosine Flow Distribution

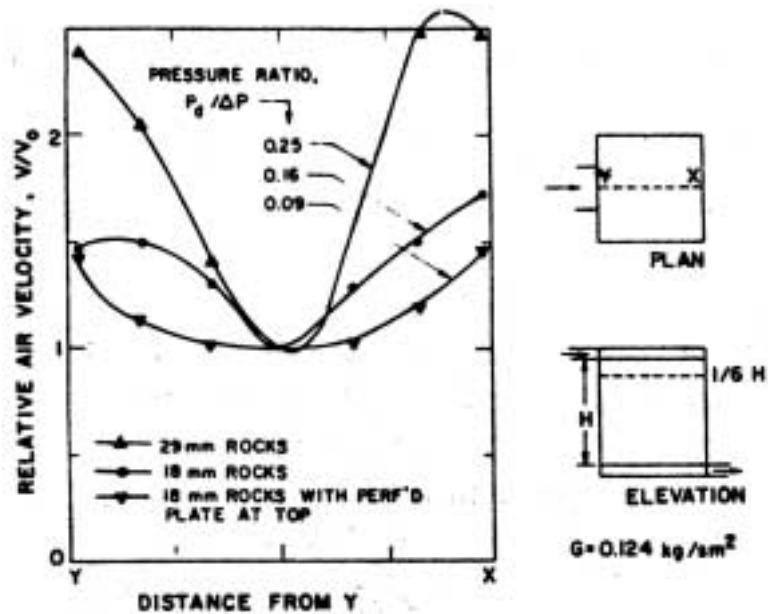


Figure 5.7.7 Flow velocity non-uniformities found by Hollands (1984) in experimental pebble bed. Relative air velocities represent R_{bed} and are measured $1/6^{\text{th}}$ of the way down the bed height. Pressure ratios correspond to pressure drop in the plenum (P_0) over the pressure drop through the pebble mass (ΔP). Pressure ratios increase for larger diameter rocks due to lower pressure drop through pebble mass.

A separate attempt at assigning flow distributions through the bed was based on the trends observed by Hollands (1984) in his extensive studies on pebble bed storage. For all rock sizes and flow rates, a near cosine distribution was observed with the minimum flow occurring near the center of the bed as shown in figure 5.7.7. Modeling the bed non-uniformity in this manner actually preceded the analysis of the ordered flow profile presented in section 5.6.1. The results of this early analysis on the cosine flow distribution showed only a negligible effect of R_{bed} on the thermal profile, and the work on the cosine distribution was dropped in favor of the ordered profile distribution, which provided a better fit to the measured data. Recent work on the cosine distribution model has showed that an early assumption on the bed loss coefficient was responsible for the poor results and that a good fit to the measured data is possible using the cosine flow distribution. Although the final simulation model is based on the ordered profile, an explanation of how the cosine flow distribution can be used to fit the measured results is presented here for the interested reader.

The initial results showing only a minimal influence of R_{bed} on the thermal profile occurred because of the correlation between area assignments of the segments and the

corresponding flow rates dictated by the cosine flow distribution. Unlike the arbitrary assignment of bed sections in the ordered profile analysis, those of the cosine profile have a fixed order in the concentric rings of figure 5.7.8 with the area of the segments growing linearly from 1 percent of the total at the center up to 19 percent for the outermost segment. The cosine velocity profiles of figure 5.7.7 are then mapped onto these concentric segments providing the flow distributions pictured in figure 5.7.9. It becomes apparent from this figure that the overwhelming majority of the flow is concentrated at periphery with 57 percent of the flow in the outer 3 segments and less than 6 percent in the innermost 3.

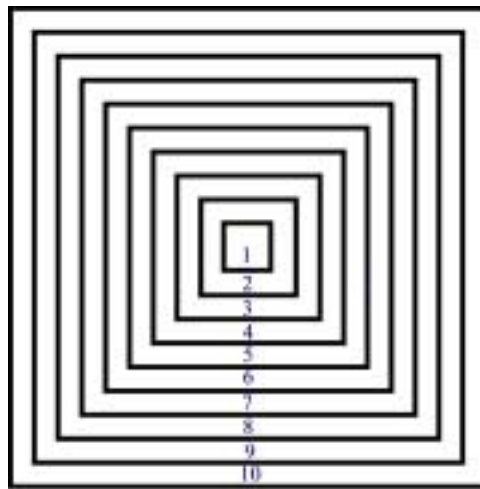


Figure 5.7.8 Top view of the bed showing the division of segment areas for the cosine flow distribution. Segments are equally spaced from center to edge.

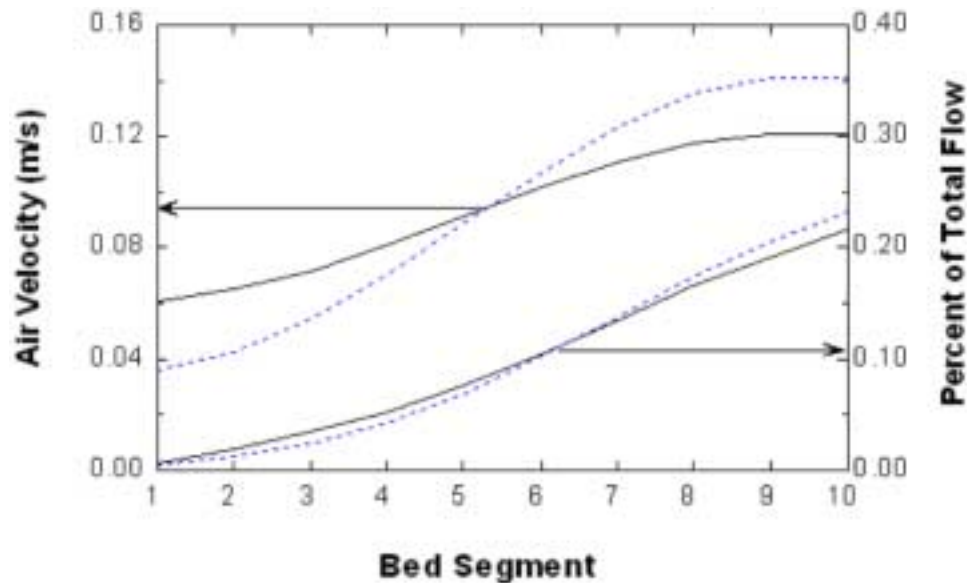


Figure 5.7.9 Distribution of air velocities and flow rates under the cosine distribution model for $R_{bed}=2$ (solid line) and $R_{bed}=4$ (dashed line) in the basement bed.

To significantly shift the exiting temperature profile of the box requires that thermal waves carrying large portions of the box flow break through at separate times. However, with such a concentration of flow on the periphery, the slower thermal waves at the center were unable to influence the temperature profile, even under a velocity ratio of 4:1 over the bed. To significantly alter the profile, a slower thermal wave would have to pass through a large bed area such that it carried a significant percentage of flow. This would entail a low flow velocity at the bed periphery, which would undermine the basic findings of Hollands as presented in figure 5.7.7. It was this paradox that initially caused the cosine flow distribution to be dropped in favor of the ordered profile.

The critical oversight of the early analysis that produced poor agreement with the data was that the bed loss coefficient was set at the theoretical value of $0.87 \text{ W/m}^2\text{C}$, which will not close the overall energy balance. When all the bed losses are attached to the bed segment on the periphery, a loss coefficient of $6 \text{ W/m}^2\text{C}$ is required to satisfy the overall energy balance. This value is twice the empirically calculated value of $3 \text{ W/m}^2\text{C}$ from section 5.4. The increase in the loss coefficient is attributable to the amount of flow from which the losses are taken in each analysis. In section 5.4 and the ordered flow analysis of section 5.6.1, the losses were removed equally from the entire mass flow rate of the bed. In the cosine flow distribution, the losses are extracted only from the outer segment, which carries only 20 percent of the bed flow in most

cases. Due to the lower flow rate, the heat loss from this segment drastically reduces the temperature of the flow as it traverses the length of the bed. As the temperature is lowered, the heat loss is also reduced for a fixed loss coefficient (U_{bed}). The result is that a much higher loss coefficient is required to create the bed losses necessary to close the energy balance.

This high periphery loss coefficient provides a low temperature thermal wave carrying approximately 20 percent of the bed flow. It is this lower temperature thermal wave at the perimeter that can combine with the other waves traveling through the bed to shift the overall thermal profile. With this condition, the flow profiles specified by Hollands can be maintained and still produce good agreement with the measured data.

In modeling the cosine flow distributions, the only free parameter is the relative air velocity ratio defined by R_{bed} . Figure 5.7.10 shows the integrated bed error ($Error_{bed}$) of equation 5.7.1 resulting from simulations with R_{bed} ranging from 1 to 4. The best fit occurred at a value of 1.94 for R_{bed} with an integrated error of 63.0 °C-hours. Temperature and calibration plots at this value are presented in figures 5.7.11 and 5.7.12 showing a good agreement with the measured data.

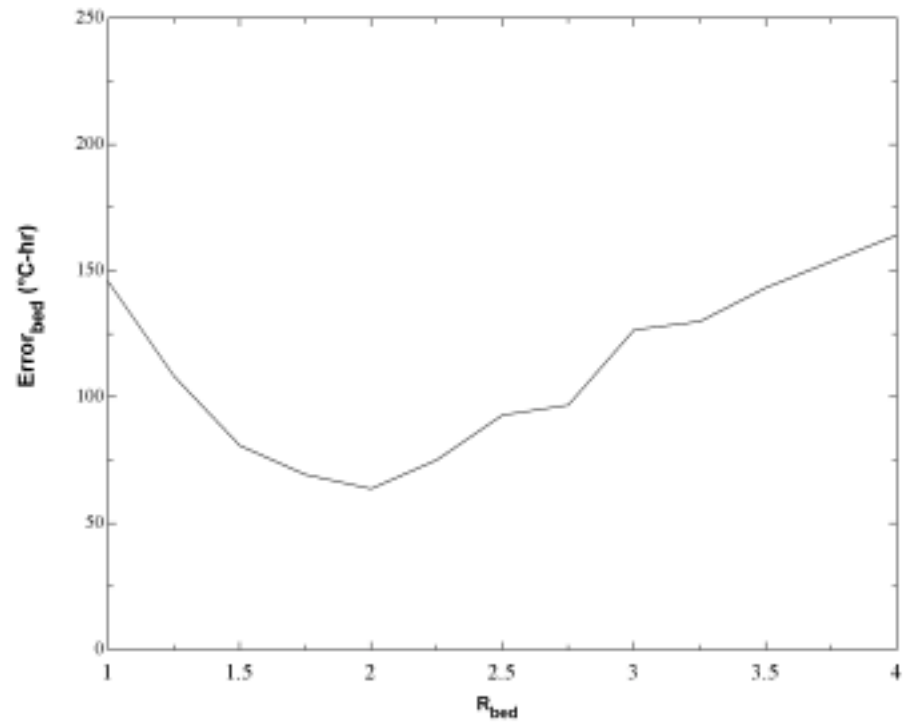


Figure 5.7.10 Plot of integrated error ($Error_{bed}$) for basement pebble bed subject to cosine flow distribution.

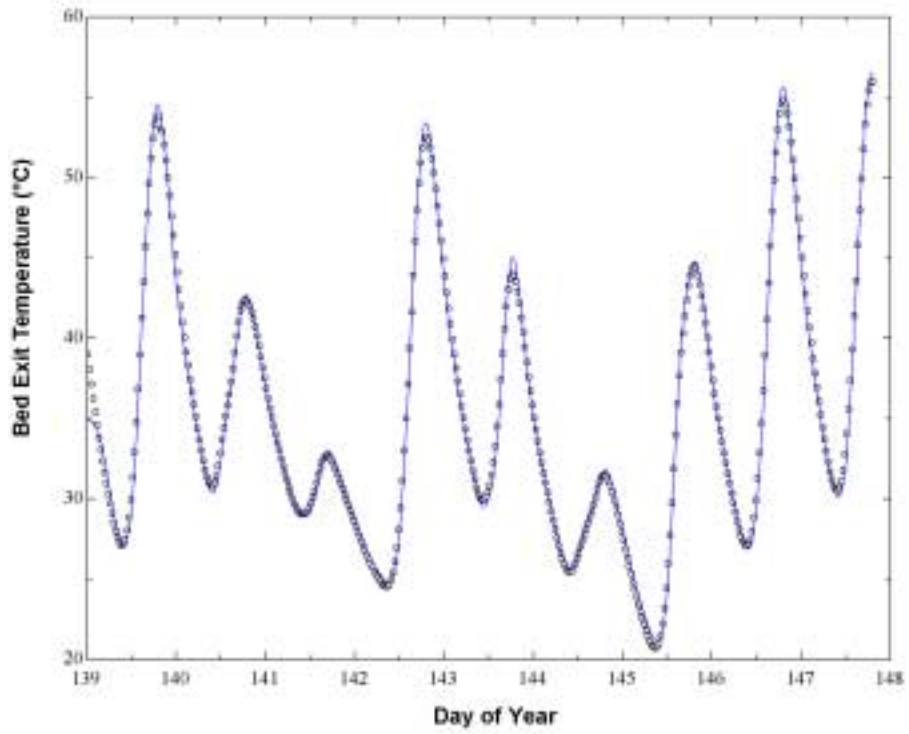


Figure 5.7.11 Measured (points) and predicted (solid line) bed outlet temperatures TE-8 for cosine flow distribution of the Schuman model over the solar test interval. $R_{bed}=1.94$, $U_{bed}=6$.

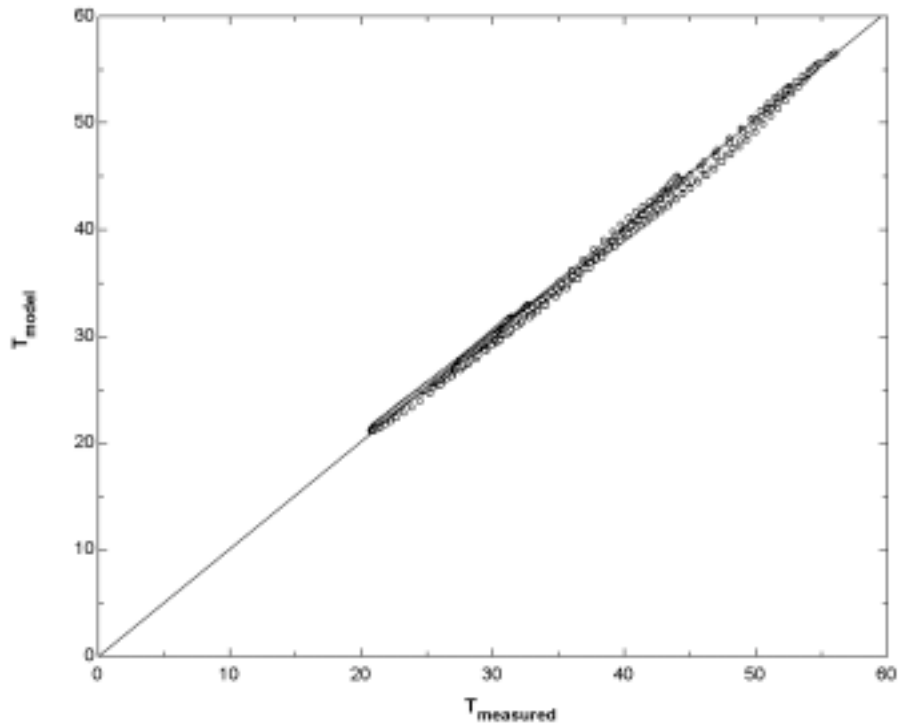


Figure 5.7.12 Calibration plot of measured vs. model predicted bed outlet temperatures of figure 5.7.11.

5.8 Visual Inspection of Bed Interior

Visual inspections of the upper and lower plenums of the basement pebble bed were made following the numerical analysis to determine the physical causes of the high heat loss and flow non-uniformity. Inspection on both the upper and lower plenum were performed with a boroscope inserted through holes drilled in the ductwork attached to the bed. Figure 5.8.1 is a photograph taken of the inside of both plenums. The thin sheet lying across the upper plenum is the bottom lamination of the box cover. Temperature and humidity cycling are believed to have caused successive expansion and contraction of the cover causing the bottom layer to delaminate. Separation of the delaminated layer was likely caused by abrasion against the edge of the concrete walls where it was bolted under compression.



Figure 5.8.1 Views of plenum interiors on basement bed taken through boroscope. Vertical bar in upper plenum is a standard duct support, top of pebble mass is visible at base of photo. Bottom plenum shows bond beam blocks, lath grating and the bottom edge of the pebble mass.

Visual inspections were unable to identify whether the perimeter insulation was still intact. Accumulation of dust and low light levels made it impossible to distinguish between a concrete block wall and what would be the surface of the polystyrene sheet on the far bed wall. Additionally, perimeter insulation may have been started below the upper level of the pebbles to allow for insertion of the ductwork during construction. The bond beam blocks and wire grating that create the lower plenum appear in good order with no obstructions present and the arrangement of blocks still in their original layout.

Physical layout of the beds made access to the office section extremely difficult and no visual inspections were made. Since both beds have identical constructions and similar operating conditions, it is quite feasible that the bed cover in the office section has also delaminated causing the flow non-uniformities there as well.

5.9 Final Pebble Bed Model Used in TRNSYS Simulations

Although both the cosine flow and ordered profile distributions were able to accurately predict bed performance, visual inspections support the physical interpretation of the 3.44:1 flow ratio found in the ordered profile. This profile is easily explained by the delaminated cover section that forces a near linear increase in bed flow from the left to right in figure 5.8.1.

For several reasons, the ordered profile analysis presented in section 5.6.1 could not be directly implemented in TRNSYS. Of primary concern was the computational time that would be required for an annual analysis with 10 bed segments. While the seven day simulations over the

solar test interval can be performed in reasonable timeframes, expanding the simulations out to an entire year brings severe penalties to the solution times. The second area for concern is that the numerical analysis of pebble beds in TRNSYS is slightly different from that presented in this work. TRNSYS simplifies the analysis by assuming the pebble bed to have an infinite NTU making the fluid and rock temperatures identical within each node. This simplification reduces the combined set of equations 5.1.1 and 5.1.5 to a single equation describing heat transfer within the bed. An analysis of the accuracy of this assumption and its effects on bed performance was performed by Hughes (1978).

The final description of the pebble bed component within TRNSYS was an equivalent infinite NTU model employing three bed segments. The numerical model used in sections 5.6.1 and 5.6.2 was cut down to three bed segments and the bed effectiveness was forced to unity. Assignment of flows within the three segments was not restricted by equation 5.7.2, and the flow rates were instead allowed to vary at random. Flow percentages through two bed segments³ were then used as variables in an optimization to minimize the integrated error of the bed as defined by equation 5.7.1. While such a model loses the physical significance of previous analyses, it provides an equivalent prediction of bed exit temperatures with significantly reduced computation time.

Figure 5.9.1 and table 5.9.1 show the final results of the three segment random distribution that is used directly in TRNSYS. Integrated errors of 77.5 and 47.6 degree hours were found for the basement and office beds respectively. The calibration plots show good fits over the temperature range for both beds giving further confidence that these equivalent models are sufficiently accurate for systems level simulations.

Table 5.9.1 Summary of variables used for modeling pebble beds within TRNSYS .

	Segment 1 flow (%)	Segment 2 flow (%)	Segment 3 flow (%)	U_{bed} (W/m ² °C)	Error _{bed} (°C-hr)
Basement	19.3	31.6	49.1	3.0	77.5
Office	23.9	28.2	47.9	7.5	47.6

³ The flow percentage through the third segment is fixed by the requirement that all flow percentages add to unity.

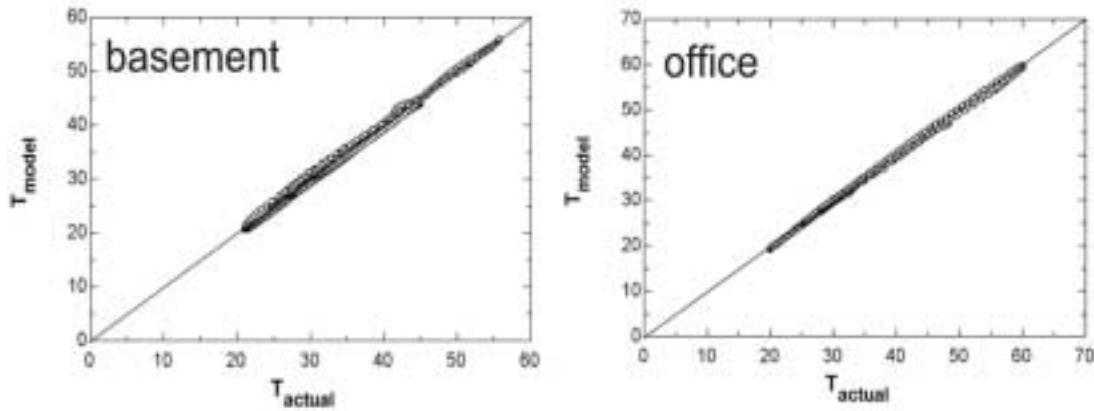


Figure 5.9.1 Calibration plots of measured vs. model predicted bed outlet temperatures over the solar test interval for 3 segment infinite NTU models employed in TRNSYS.

5.10 Flow Profiles Under Discharge Conditions

An attempt to characterize the flow distributions under the reverse flow conditions was made during a separate week-long solar test interval in early November 1999. Again, the system was forced into mode 3 of operation (charging storage) for a one week period. At 4:00 PM on the last day, the system was forced into mode 2 of operation (discharging storage) until 6:00 AM of the following morning. By running the bed in quasi steady state for a one week period, the simulation model was able to accurately infer all node temperatures within each bed segment. These segments were then immediately discharged following the end of the charging cycle such that all node temperatures were known at the beginning of the discharge cycle. Discharge temperatures from the model were then compared with those measured at TS-7 (top of pebble bed). Two free parameters defining the flow distribution through the bed under reverse conditions were used for fitting the discharge profiles.

A TRNSYS simulation deck was used with the bed parameters of table 5.9.1 to predict the office bed behavior during both the charge and discharge intervals. Figure 5.10.1 shows the results for the last 4 days of this second solar test interval. For the charging cycle (mode 3) the model accurately predicts the bed behavior as expected, but it is unable to predict the discharge temperature in mode 2 under any possible distribution of flows. This disagreement with the model produced some confusion as a large degree of confidence had been established in the ability of the model to accurately predict performance under charging conditions.

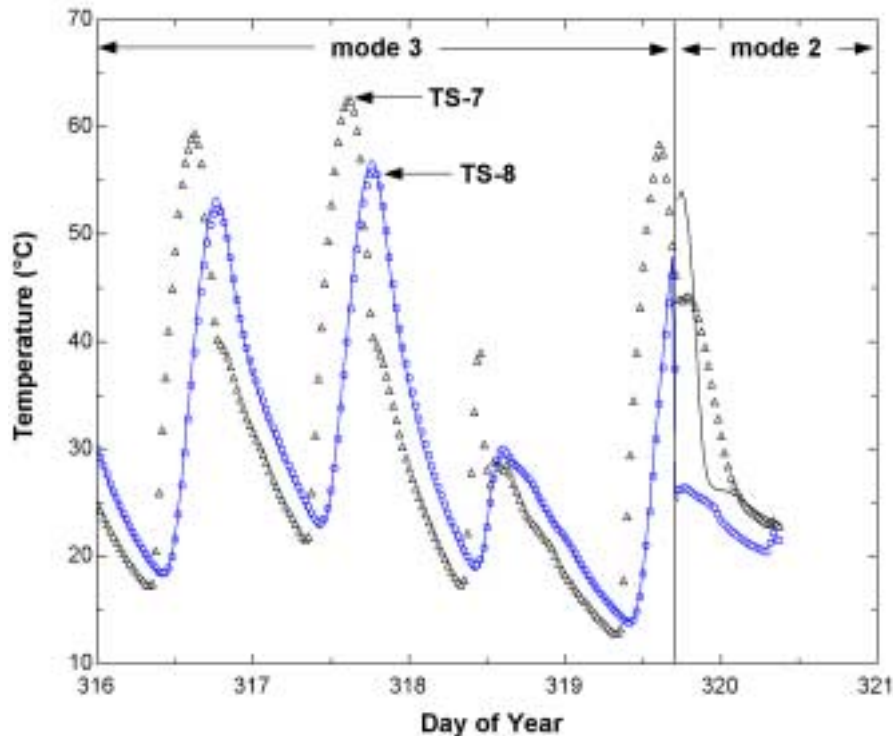


Figure 5.10.1 Comparison of measured (points) to predicted (solid lines) office bed performance over second solar test interval. Model was driven with measured bed inlet temperature TS-7 to predict outlet temperature at TS-8 during mode 3 (charging bed). During mode 2 (discharging bed), the bed was driven in reverse flow by TS-8 to predict the temperature leaving the top of the bed at TS-7.

Closer inspection of the bed behavior at the very start of the discharge interval reveals that the bed began discharging at a temperature several degrees below what had last entered during the charging cycle minutes before. Such behavior should not be physically possible as the top few feet of the bed would all have temperatures above this due to the high temperature charging cycle over the previous several hours. The only possible explanation for the discrete jump in the discharge temperature measured by TS-7 would be an air leak onto the sensor from the solar room when the duct pressure went from positive to negative during the mode changes. This hypothesis was validated after an inspection of the junction boxes for TS-7 on both systems showed that the mastic putty seals on both junction boxes had melted. The resulting opening shown in figure 5.10.2 allowed an airstream to directly enter the c-channel sensor mount during the negative duct pressures of the discharge cycle. The temperature sensor then read a blended temperature somewhere between that of the duct and infiltrating air stream. It was this blended

temperature that appears as TS-7 during the discharge cycle in figure 5.10.1 and for which the model was not be able to predict.



Figure 5.10.2 Junction box of TE-7 for the basement system on left with access hole to c-channel highlighted. Picture on right shows the junction box cover onto which the mastic putty sealant has melted and fallen.

Removal of the temperature sensors for ice bath calibrations during the summer of 1999 revealed that all the mastic seals were intact at that time and that earlier temperature readings over the system calibration interval and the initial solar test interval were therefore not subject to any infiltration of airflows. The mastic seals are believed to have failed during the continuous high temperature charging cycle of the November 1999 run. Temperature sensor access holes have since been properly sealed with rubber plugs to prevent infiltration flows at these locations.

Because discharge characterization requires several days of a testing cycle, for which normal building operation is interrupted, a follow-up test was not run. Flow distributions under discharge conditions were assumed to be uniform through the bed, which is in accordance with the findings of Persons (1978) as depicted in figure 5.10.3. The more uniform flow that results under discharge conditions may be the result of better flow dispersion in the lower plenum caused by the presence of the bond beam blocks.

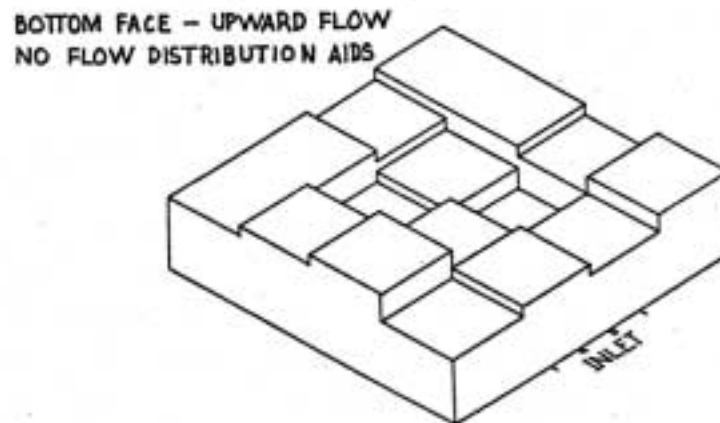


Figure 5.10.3 Flow distributions found by Persons (1978) during bed discharge.

5.11 Inferring Mass Flows from Thermal Profiles

An interesting result of an analysis on pebble bed storage is the ability of the rock mass to serve as a flow meter. The thermal capacitance of the pebble mass has the effect of delaying the temperature wave passing through the bed. The traversal time of the thermal wave for a step response under infinite NTU conditions can be described by

$$\tau = \frac{\rho_{rock}(1 - v)C_{rock}L_{bed}}{\dot{V}_{air}\rho_{air}C_{air}} \quad [5.11.1]$$

Although this equation is only valid for a step response, it provides a form of the solution and the relevant variables. Traversal time is inversely proportional to the air flow for a given thermal mass of the bed. By knowing the geometry of the bed, the void fraction, and pebble characteristics, it is possible to determine the flow rate using the traversal time τ . This traversal time can be recorded through temperature sensors located at the bed inlet and outlet.

In solar applications, step responses never occur and both flow non-uniformities and finite NTU's act to blend the outlet profile. Traversal times can still be calculated, but they must be evaluated numerically. Even under non-uniform flow distributions, there will be a single aggregate flow rate \dot{V}_{air} through the bed that is able to provide the measured exit temperature profile. Figure 5.11.1 shows the predicted outlet temperature under uniform flow rates 20 percent above and below the actual flow rate in the bed. The change in the traversal time τ is readily

apparent, and the proper flow rate can be determined by matching the modeled traversal time to that measured at the bed outlet through a minimization of the integrated bed error (equation 5.7.1).

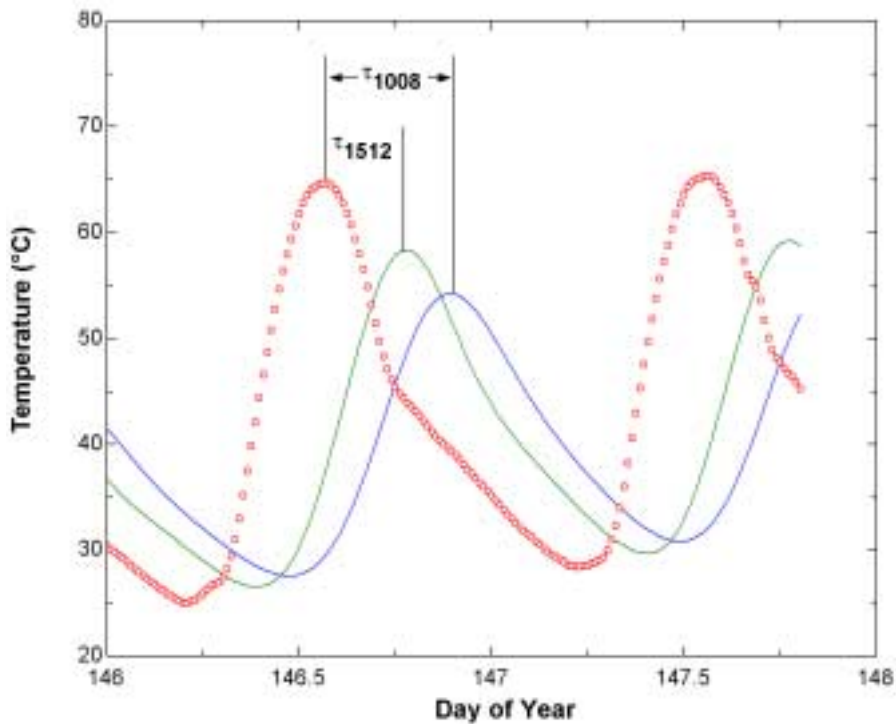


Figure 5.11.1 Measured bed inlet temperature TS-7 (points) and predicted bed outlet temperatures (solid lines) at 1008 and 1512 ft³/min over the last two days of the solar test interval. The modeled flow rates represent levels 20 percent above and below the actual flow rate of 1260 ft³/min for the basement bed.

Figure 5.11.2 shows the results of a minimization of the integrated bed error for non-uniform flow distributions dictated by the ordered profile over a wide range of flow rates. The minimal error occurs at a flow rate of 1320 CFM, 50 CFM above the measured value of 1270. This small inconsistency is likely due to overestimates of thermal mass of the bed as defined in the numerator of equation 5.11.1. Of particular interest is the result that the integrated error is quite sensitive to flow rate through the bed with a 100 percent change in the integrated error for a relatively small 20 percent change in flow rates. If the thermal mass of the bed can be predicted with good accuracy, as is often possible, then numerical tools can be used to predict the flow rate. Moreover, if the thermal mass of the bed is calibrated to a measured flow rate, then any change in

flow rate over the life of the system can be accurately inferred through simple temperature measurements.

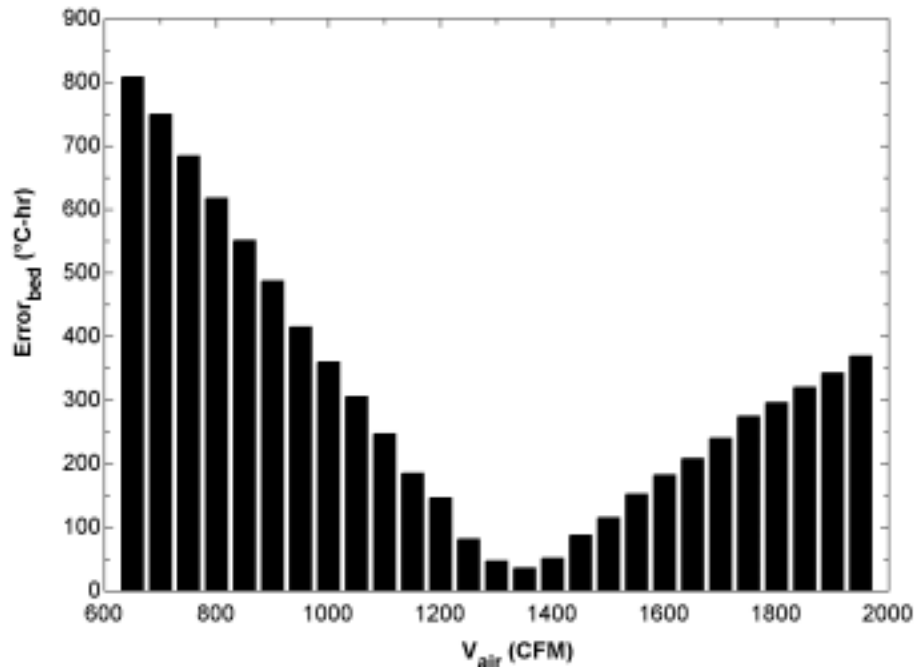


Figure 5.11.2 Integrated bed error for various assumed flow rates in basement system. System flow rate as measured by hot wire anemometer was 1260 CFM.

The ability to infer mass flow rates from thermal profiles is of particular interest in the performance monitoring of thermal systems as only one spot measurement of flows at installation of the system needs to be made to calibrate the bed mass. For any future flow measurements, the bed mass can act as a secondary standard to calculate system flows. By using the bed as a flow meter, expensive flow metering equipment can be removed altogether, thus lowering the cost and increasing the reliability of such measurements. The same two temperature sensors that measure the bed traversal time (TS-7 and TS-8) can also be used to calibrate the collector array as well.

5.12 Calibration of Pebble Bed Temperature Sensors

What should have been a straight-forward calibration ended up requiring a detailed analysis and significant modeling effort. The pebble bed sensors (TS-9), which measure the temperature of the thermal storage, should ideally be located within the top few centimeters of the

pebble mass. This reading of the upper bed temperature (TS-9) supplies the controller with information as to whether there is enough energy within the bed to enable mode 2 of operation. Figure 5.12.1 shows the bed inlet temperature (TS-7) and pebble bed sensor temperatures over the solar test interval. If correctly located, the sensor temperature should be nearly identical to the bed inlet temperature with only a small offset resulting from the capacitance of the 1 or 2" of pebbles lying over the sensor. The significant disagreement between the modeled and recorded temperatures indicate improper model assumptions and the need to adjust or calibrate the sensor location and environment. Proper sensor calibration is critical to performance of the entire system as it is the temperature of this single sensor (TS-9) that dictates the control logic of modes 2 and 3. Regardless of the physical performance of the rock mass itself, the controls strategy determines how the bed is operated, and therefore the sensor must be properly modeled in order to reflect the true dynamics of the pebble beds.

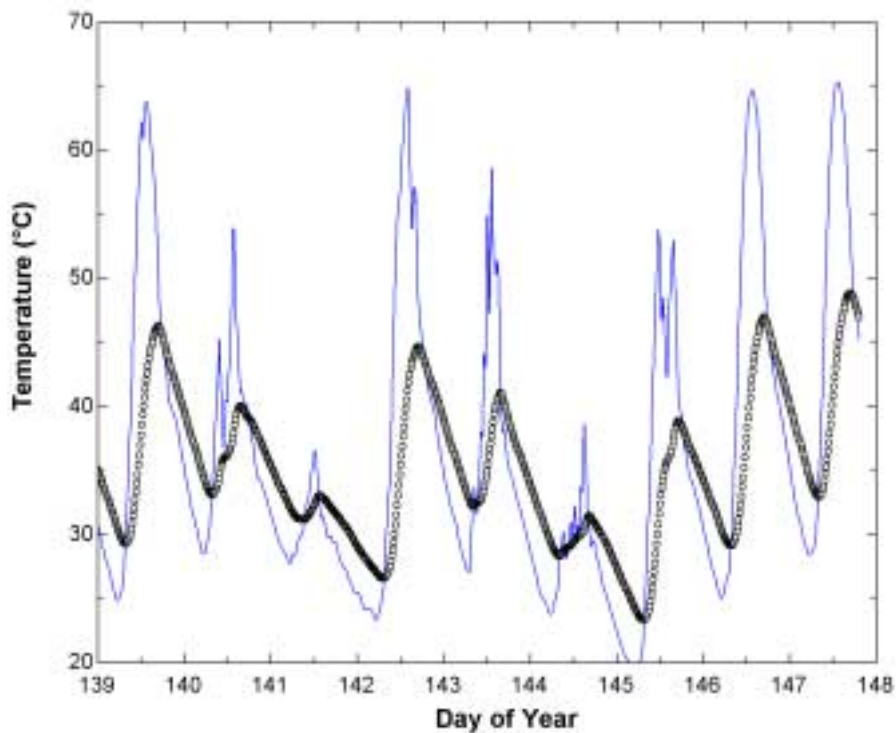


Figure 5.12.1 Measured bed inlet temperature TS-7 (solid line) and sensor temperature TS-9 (points) over solar test interval.

It was initially believed that the smoothed and shifted temperature profile of the sensor was caused by the sensor being located further down in the bed mass. However, measurements of the

pilot hole in which the sensor was inserted fixed the vertical location exactly at the top of the pebble mass. Because the sensors were installed in 1995, after the bed was assembled and filled, it would be impossible for the contractor to install the sensor in the pebble mass itself. The best that could have been done would leave the tip of the sensor in contact with the edge of the pebble mass as depicted in figure 5.12.2. More likely, the sensor was thermally bridged at some depth further back into the wall. Based on this hypothetical location, a numerical model was constructed assuming a sensor location inside the bed retaining wall.

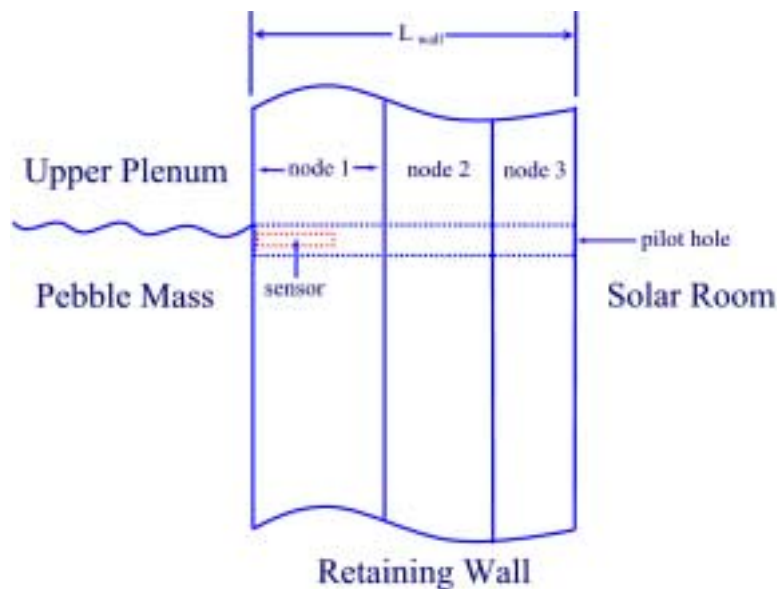


Figure 5.12.2 Schematic of wall layout used for numerical modeling of sensor parameters.

The numerical model used to calibrate the sensor parameters consisted of a three node disturbed capacitance retaining wall. The width of the first node wall was allowed to vary between 1 and 10 cm with the remainder of the wall thickness distributed equally between the remaining 2 nodes. Sensor temperature was modeled at the center of the first node. Boundary conditions on the outer surface of the wall consisted of free convection ($3 \text{ W/m}^2\text{C}$) to the solar room temperature of 30°C . Heat transfer coefficients on an area basis for the inside surface of the bed were calculated using the relation of Lof and Hawley (1948).

$$h = \frac{Dh_v}{6\alpha(1 - v)} \quad [5.12.1]$$

The surface shape factor α was assumed to be 1.5, which is typical for smooth river gravel. The volumetric heat transfer coefficient of equation 5.1.4 was used with the remaining variables as defined in section 5.11.1 to solve for the heat transfer coefficient. Interior wall temperatures were fixed at the bed inlet temperatures shown in figure 5.12.1. The 2 remaining variables of the resistance of the perimeter insulation and the distance of the sensor from the bed interior were used as optimization parameters. The objective of the optimization was to produce a best fit to the measured sensor profile over the solar test interval⁴.

Results of the optimization routine for the basement sensor are shown in figure 5.12.3 for a polystyrene resistance of $0.14 \text{ m}^2\text{C/W}$ and a sensor depth 5 cm from the interior of the bed wall. The extremely low value of the insulation resistance is in accord with the high U_{bed} values found in section 5.4. This indicates that the perimeter insulation is either not present or begins at a depth below the sensor location, which is level with the top of the pebble mass.

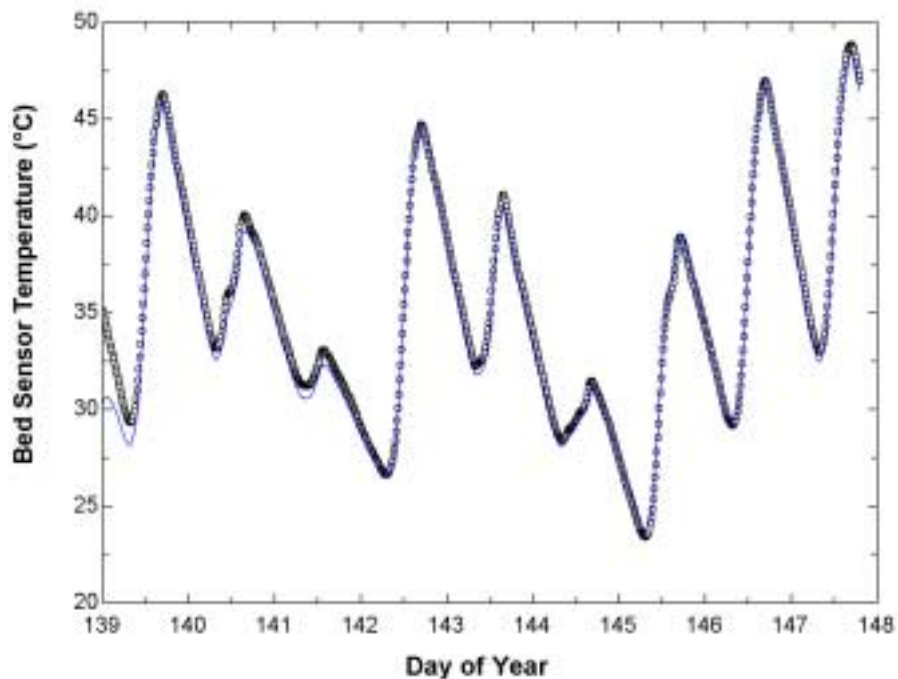


Figure 5.12.3 Measured (points) and modeled (solid line) basement bed sensor temperature (TS-9) over the solar test interval after parameter optimization.

⁴ The metric used to quantify the fit was an integrated error similar to equation 5.7.1, but taking the temperature difference between the model and TS-9 for the integrand.

Optimization of the office bed sensor proved more difficult requiring that the free convection coefficient on the exterior of the wall be reduced to $0.34 \text{ W/m}^2\text{C}$. This value represents an effective conductance from the outer wall node to the room. Therefore the low conductance indicates some form of thermal break between the final wall node and ambient. The thermal resistance of this break would have to be $2.61 \text{ m}^2\text{C/W}$ to produce the low conductance. Such a thermal break may occur if the block cores were not completely filled in the upper wall section where this sensor was located.

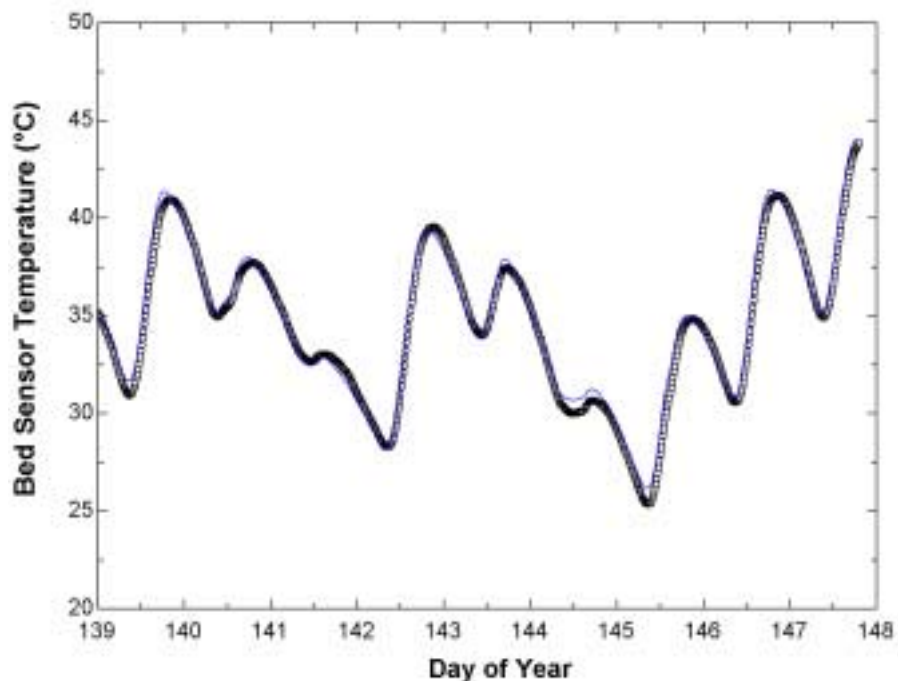


Figure 5.12.4 Measured (points) and modeled (solid line) office bed sensor temperature (TS-9) over the solar test interval after parameter optimization.

In addition to the thermal break, the office bed sensor appeared to be located further back in the wall at a distance of 14 cm from the interior, placing it in the second node of the model instead of the first.

Perhaps the most surprising finding of this calibration is that the office bed sensor is not even located in the office section of the bed retaining wall, but is instead located 60 cm from the separating partition placing it distinctly within the basement section. This inadvertent location was the closest the installer could have placed the sensor as the supply and return plenums from the office bed completely blocked access to the proper location. Calibrations of the office bed

sensor shown in figure 5.12.4 accounts for this improper location by modeling the office sensor in the basement bed.

The best possible explanation for the shallow insertion depths of both sensors is based on commercial availability of masonry drill bits. Most masonry drills come in 12” lengths with 1-1.5” that will be inserted into the drill chuck. If the installer had a typical masonry drill bit then the closest the sensor would be is 1.5” from the bed interior. The further setback of the office sensor may be the result of drilling on a diagonal to locate the sensor closer to the office bed. To verify either pilot hole depth would require drilling out the sensors, which would interrupt system operation and destroy the RTD’s.

5.13 Air Quality Tests

In 1988 the occupants of the McKay center complained of odors within the office zone of the building and suspected the solar system as the source. On November 23rd 1988 and again in July of 1989 infrared spectral analysis of the air at the center was performed. Air samples were analyzed over a band from 2 to 14 μm with a Miran 1A spectrophotometer in an effort to detect the signatures of any known chemicals that may be present. Air samples were compared from the following locations:

- Fresh outdoor air at the southern exposure.
- Air within the ductwork located at TS-7 (top of pebble bed) in the office system.
- Air within the ductwork located at TS-8 (bottom of pebble bed) in the office system.
- Air within the ductwork located at TS-4 (supply to collectors) in the office system.

A comparison between the outdoor sample and the sample taken at TS-7 is provided in figure 5.13.1 and shows no significant difference in the spectra. Moreover, no discernable difference was observed in the spectra of any of the ductwork samples within the solar subsystem.

University health service technicians eliminated the solar system as a possible source and began a comprehensive search of the building and grounds. An offending odor was recognized outside the mens room and identified through spectral analysis as being that of para-dichlorobenzenene⁵ (PDCB) used in the urinal cakes. Exhaust fans in the restroom are only activated when it is

⁵ para-dichlorobenzene (PDCB) is better known by it’s commercial name: mothballs.

occupied leading to increased levels of PDCB. A return air grill located directly opposite of the restroom could thereby entrain the odor in the recirculated airstream. Recommendations by the university health service technicians entailed the removal of the urinal cakes and installation of a heat recovery ventilator to supply ventilation air to the building.

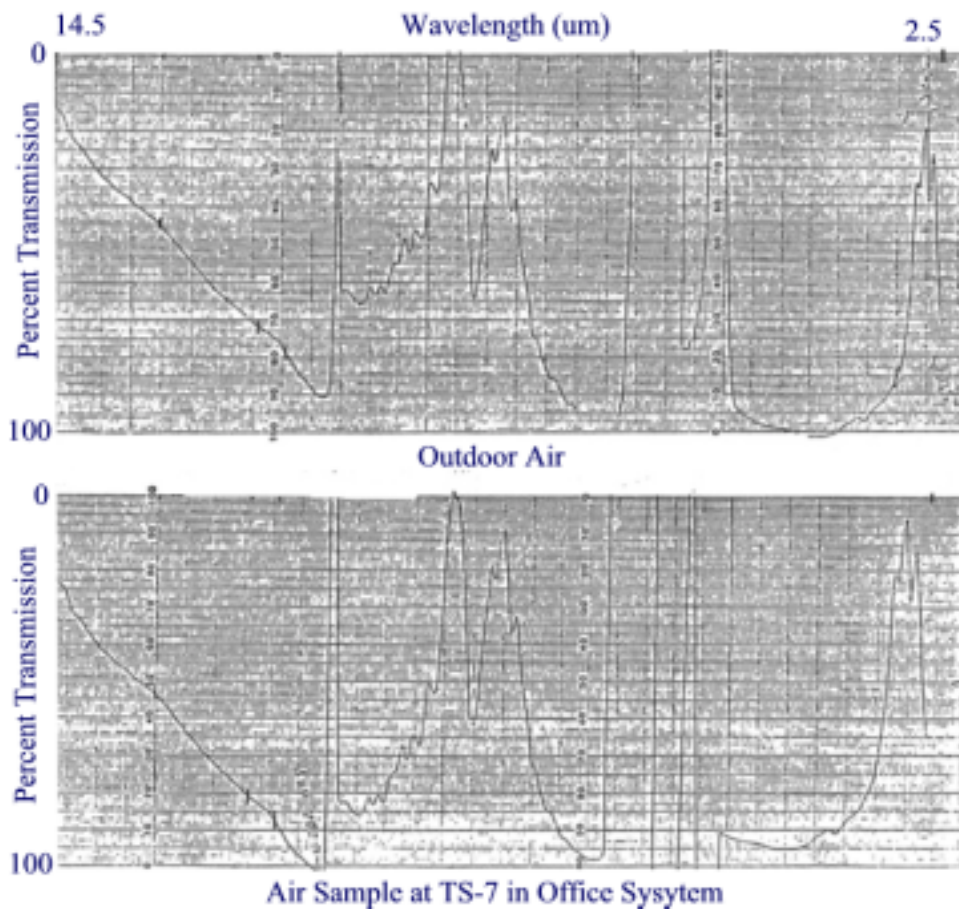


Figure 5.13.1 Spectrographs of air samples taken at the McKay center (courtesy University Health Services).

On November 10th 1999, University health services ran mold sample tests within the solar ductwork at the request of the author. This testing was not to remedy a suspected problem, but simply to determine whether any mold growth had occurred in the pebble bed storage systems⁶. Air samples were taken at the following sites with a single stage Anderson sampler using malt extract agar as the growth medium:

⁶ Because of the stagnant air conditions over the summertime, some individuals have suspected that pebble beds are able to serve as favorable growth sites for mold colonies.

- Air within the ductwork located at TS-8 (bottom of rock box) in the basement system.
- Air within the ductwork located at TS-8 (bottom of rock box) in the office system.
- Open air within the basement zone
- Fresh outdoor air

After four days of incubation at room temperature the number of colony forming fungal spore units were counted. The counts listed in table 5.13.1 are the average of the two samples taken at each location. Normal indoor fungal spore counts should be no more than 1/3rd the outdoor counts. Spore counts within the solar subsystem ductwork were well below this ratio as was the open basement zone air. Additionally, the types and predominance of outdoor spore samples matches those found indoors, indicating that no amplification or preferential growth is occurring within the pebble beds or building space.

Table 5.13.1 Averaged fungal spore counts from various sample sites at the McKay center.

	TS-8 (Basement)	TS-8 (Office)	Basement Zone	Outdoor Air
Spore Count	88	122	70	1802

5.14 Synopsis

Pebble bed models were developed based on the Schumann equations. Loss coefficients were empirically determined to be several times greater than dictated by construction drawings. This was attributable to losses through the building foundation, which forms two sides of the bed retaining wall and are thermally coupled to the soil. Also, calibration of bed sensors indicate a lack of interior perimeter insulation, at least in the upper plenums. The sensors themselves were improperly located in the bed retaining walls and not in the pebble mass itself. Moreover, the office bed sensor was located in the retaining wall of the basement bed.

High flow non-uniformities were discovered in the basement bed and we accounted for by modeling the bed according to the ordered flow profile found by Persons (1978) or the cosine flow distribution of Hollands (1984). When both the losses and flow distributions are accounted for, good fits to the measured data are possible as shown in figure 5.9.1. Final model parameters used in the TRNSYS simulations are provided in table 5.14.1. An attempt to calibrate flow

distributions under discharging of the pebble bed was inconclusive due to air infiltration over the temperature sensors TS-7 in both the office and basement systems. Uniform airflow was assumed in the discharging condition based on the findings of Persons (1978).

Air quality tests run on the solar loops showed no presence of chemical outgassing from system components and no mold growth. As a separate item, the possibility of using the thermal capacitance of the beds as a mass flow meter was explored and found to be a good indicator as long as bed properties are known with reasonable accuracy.

Table 5.14.1 Final pebble bed parameters employed in TRNSYS simulation model.

	Segment 1 flow (%)	Segment 2 flow (%)	Segment 3 flow (%)	U_{bed} (W/m ² -C)	Sensor Depth (cm)
Basement	19.3	31.6	49.1	3.0	5.0
Office	23.9	28.2	47.9	7.5	14.0

6 Building Loads and Auxiliary Equipment

The final component of the simulation model is the building itself. Far from being a static sink for energy requirements, the internal and passive solar gains combined with the capacitance of the building defines a dynamic load that the HVAC system must meet. Modeling techniques based on a simple representation are incapable of capturing the true building behavior, and a detailed model that includes the effects of a distributed capacitance is required. The framework of such a model is presented in this section together with the parameters defining the loss and gain coefficients of the building space. Final values of all building parameter used in the simulation are presented in table 6.6.1.

6.1 Thermal Model of Building Zones

The physical layout of the McKay center provides a clear separation of the building zones. The basement is isolated from the upstairs by a stairwell and doorway, and closed doors separate the lecture hall from the surrounding office space. The physical separation of the air masses allows them to be modeled independently with no thermal interactions. This simplification greatly reduces the complexity of the final model and simulation code.

Each of the three zones (basement, office, and lecture hall) is modeled in an identical manner. This model is loosely based on the framework of Borrenson (1981), in which the zone consists of three separate capacitances representing the building shell, interior capacitance and air mass depicted in figure 6.1.1.

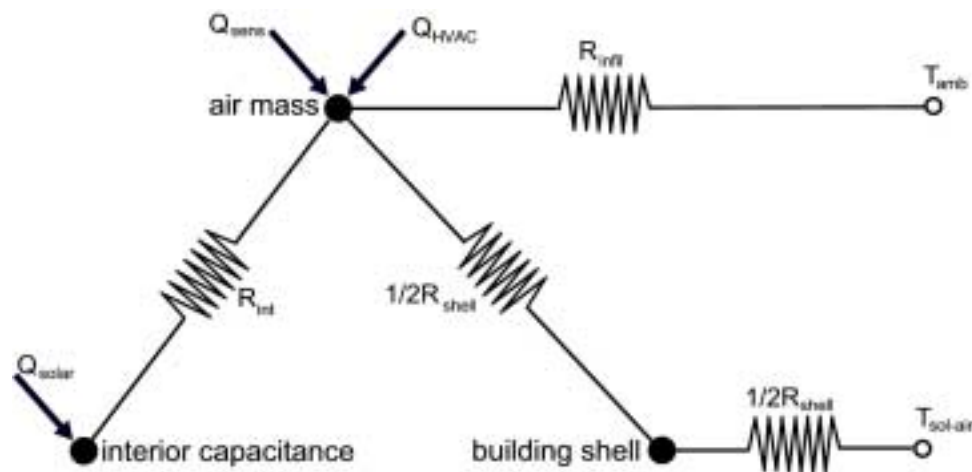


Figure 6.1.1 Schematic of thermal zone model.

Each capacitance within the zone model is thermally connected to one or more of the others, thereby creating the dynamic response of the air mass temperature. Descriptions of each capacitance and the heat transfer coefficients through which it is thermally coupled are discussed below.

6.1.1 Interior Capacitance

The interior capacitance represents furniture, partitions, and any other thermal mass within the zone that is in communication only with the zone air. The heat transfer coefficient between the interior thermal mass and the zone air is simply the product of free convection and the exposed surface area. A heat transfer coefficient of $8 \text{ W/m}^2\text{-}^\circ\text{C}$ was used based on the recommendations of ASHRAE (1997) together with an estimated surface area 4 times that of the floor space. This surface area is equivalent to that of the walls and ceiling of a typical zone, which is used as an approximation for the exposed area of the furniture and partitions.

Thermal masses were approximated for each zone based the content (i.e. bookshelves, filing cabinets, and desks) calculated per unit floor area. A literature review was performed in an attempt to locate typical values of interior capacitance for different types of content or occupancy. Unfortunately, no typical values could be located and those listed in table 6.1.1 are values based on estimates of the content in each zone. The high value used for the basement reflects the high thermal masses of the several bookcases in the libraries and the concrete blocks forming the partitions of the storage and mechanical rooms. The thermal capacitance of both the office and lecture hall would be much less than the listed value if the concrete floor did not exist. The 8" hollow block concrete floor that separates the basement from the second story was included in the capacitance of the office and lecture hall because the thermal resistance of the false ceiling and airspace in the basement isolate it from the air mass of the basement zone.

Table 6.1.1 Values of interior thermal capacitance (based on floor area) used in simulation model.

	Basement	Lecture Hall	Office
Interior Capacitance ($\text{kJ/m}^2\text{-}^\circ\text{C}$)	300	150	150

All solar gains in the building were directly coupled to the interior capacitance. Nearly all of the solar radiation passing through the windows in the office and lecture hall (the basement has no significant solar gain) falls either on the hollow block concrete floor, interior furnishing, or

partitions on the wall opposite the windows. These solar gains are ultimately released to the zone air mass as dictated by the capacitance and heat transfer coefficient of the internal mass. A detailed discussion on the values of the solar gains follows in section 6.5.

6.1.2 Zone Air Mass

The zone air mass is the central component of the building model as it is the temperature of this component that is used by the simulation model to drive the control strategies. Both the energy entrained in supply airstream of the HVAC system (Q_{HVAC}) and the sensible heat gains from the building occupants and equipment (Q_{sens}) are coupled to the zone air mass. The thermal capacitance used to represent the air in the simulation model is several times the actual value, which is necessary to stabilize the numerical model for the solution timestep. A combination of negligible capacitance and large energy inputs from the HVAC systems can produce temperature oscillations on the order of tens of degrees in the air mass during iterations of the solution. While the equilibrium temperature for the air is much less after large fractions of the energy have been conducted into the walls and interior mass, the initial solution instability created by the temperature swings creates problems for the discrete control logic. One possible solution is to shorten the simulation timesteps to damp out these temperature oscillations, but the penalty in solution times would be dramatic. Alternately, the capacitance of the air mass can be artificially inflated to damp the effects of the energy inputs. By choosing a maximum desired temperature rise over the simulation timestep, a minimal air capacitance can be defined as

$$mC_{air} = \frac{Q_{HVAC} \Delta t_{simulation}}{\Delta T_{air}} \quad [6.1.1]$$

Where Q_{HVAC} is the auxiliary furnace capacity, $\Delta t_{simulation}$ is the timestep, and ΔT_{air} is typically chosen as being on the order of twice the heating dead-band range to stabilize the control logic within the simulation. When defined in this manner, the air capacitance will decrease as the solution timestep decreases to maintain the maximum desired temperature swing ΔT_{air} . The use of such a inflated capacitance allows for convergence in perhaps a dozen iterations as opposed to what can be over a hundred iterations in the case of a true air capacitance.

Direct heat exchange between the air mass and the environment due to infiltration and ventilation was represented by an equivalent conductance based on the air exchange rate \dot{V}_{infil}

$$UA_{infil} = \frac{1}{R_{infil}} = \dot{V}_{infil} \rho_{air} C_{air} \quad [6.1.2]$$

Air exchange due to ventilation was assumed to be 10 percent of the main air handler flows based on positions of the economizer dampers located on the back side of the main air handling units. These dampers remain partially open during the winter months to provide ventilation air requirements. When constructed in 1977, the McKay center employed energy efficient building practices such as double door atriums, weather stripping on all operable openings, and storm windows to reduce infiltration. Because of the tight construction, minimal openings, and lack of commonly used entryways, infiltration in both the basement and lecture hall was limited to 0.1 air changes per hour (ACH). An infiltration rate of 0.5 ACH was assumed for the office space, which contains both of the most commonly used entryways and has more exposed wall and window area.

6.1.3 The Building Shell

The building shell is modeled as a lumped capacitance located at the center of the wall. Thermal resistances to the zone air mass and ambient are identical at half the aggregate R-value of the wall. This aggregate R-value reflects the resistance to energy conducted through the windows, walls, and roof averaged over each zone. For the upstairs office zone and lecture hall, the conductance calculations are relatively straight-forward based on wall cross sections from the original construction drawings and thermal properties that can be found in such references as ASHRAE (1997). The conductance of each building shell component (i.e. wall, window, roof, and floor) is multiplied by the exposed area and then summed for all the components to yield the total conductance and therefore resistance R_{shell} . An example of a shell resistance calculation performed on the wall of the lecture hall zone is shown in table 6.1.2 with a complete listing of the aggregate R-values for all shell components provided in table 6.6.1. The thermal resistance of the zone shell can then be used to predict the losses by

$$q''_{shell} = \frac{1}{R_{shell}} (T_{zone} - T_{sol-air}) \quad [6.1.3]$$

Where $T_{sol-air}$ is the effective ambient temperature in the presence of solar gains and will be covered in section 6.4.

Table 6.1.2 Calculation of wall resistance in lecture hall. Wall U-value is 0.47 W/m²-C.

Layer	Resistance (m ² -C/W)
Inside surface resistance	0.121
½" Vinyl covered sheet rock	0.052
Vapor barrier liner	0.0
3" Fiberglass insulation	1.176
¾" Insulating sheathing	0.20
¾" Red cedar siding	0.524
Outside air resistance	0.059
Total wall resistance	2.132

Calculating the conductance of the basement shell (i.e. the building foundation) is complicated by the thermal resistance of the soil. Heat flow paths through the soil are governed by the radial isotherms shown in figure 6.1.2. Latta and Boileau (1969) have calculated the conductance through soil accounting for the heat paths at various depths for both insulated and un-insulated foundations, which are provided in figure 6.1.3. Total conductance of the building foundation is calculated by summing the conductance area product at each depth using the tabulated values presented in figure 6.1.3. Calculations performed for the McKay center account for the perimeter insulation ($R=0.73 \text{ m}^2\text{C/W}$) to a depth of 2' and the partially exposed south face. The North, East, and West foundation walls are all fully earth bermed while the South wall has 4' of exposed high density concrete above grade. Below grade losses for the South face were calculated in the same method as the bermed sections while the above grade section was treated in the same manner as the exposed shells of the office and lecture zones.

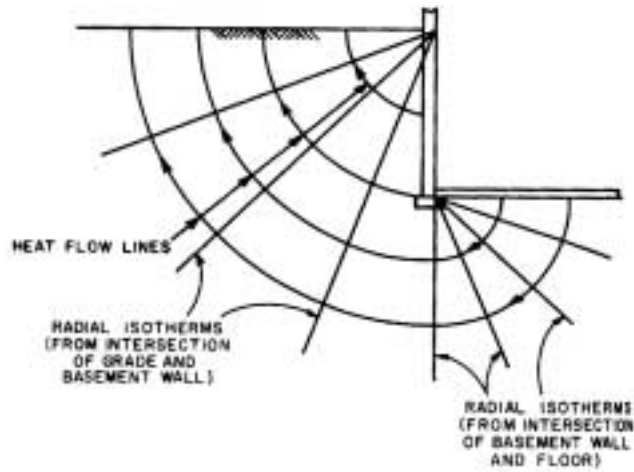


Figure 6.1.2 Isotherms and heat paths through soil for building foundations (ASHRAE 1997).

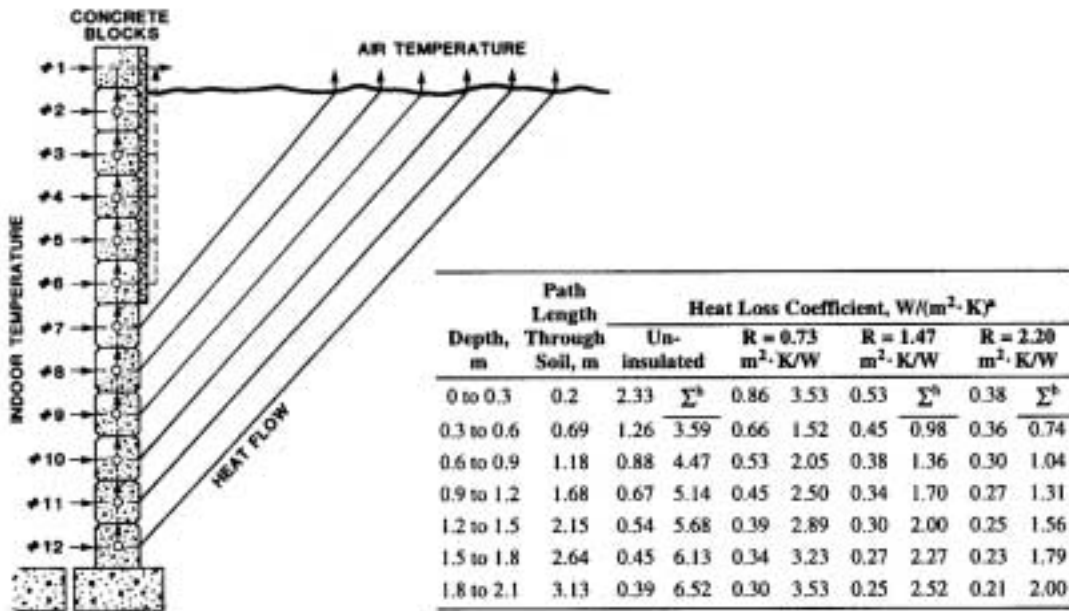


Figure 6.1.3 Heat paths and loss coefficients for building foundations taken from Latta and Boileau.

A further complication of the below grade basement foundation is the effective thermal capacitance of the soil. The foundation conductance calculated through Latta and Boileau is traditionally used for maximum design conditions and not for transient heat flow as it assumes the soil to be without capacitance. Simulating the combined effects of soil conductance and capacitance requires either finite differencing methods or an extensive analytical treatment as has

been recently performed by Karaki (1996) for steady periodic conditions. Even these exact methods can be complicated by the effects of vertical and lateral heat conduction through the foundation⁷, which makes the foundation more responsive to the ambient rather than deep soil temperatures. Effects of soil capacitance in this study were accounted for by modeling the building foundation as a thermally massive structure with a capacitance of 800 kJ/m²-C on a floor area basis. While this is not an exact model of the physical system, it captures the damping behavior of the soil on ambient temperatures. Thermal capacitance of the wood framed shell structure in the lecture and office zones were much less at 100 kJ/m²-C as proposed by Borrenson (1981) for the type of construction present at the McKay center.

6.2 Passive Solar Gains

Passive solar gains were computed within the simulation model using separate radiation processors for each window orientation (North, South, East, and West). Incident radiation on the window aperture included the shading effects of overhangs where they existed. Transmitted radiation was then calculated based on the physical properties of the double glazed units, radiation incident on the aperture, and incidence angle. Window areas and overhang geometries were measured for each zone. All transmitted solar energy was assumed to be completely absorbed by the interior capacitance of the zone.

6.3 Internal Gains

Internal gains in the zones consisted of the sensible heat output of the occupants and any energy dissipated by equipment such as computers, printers, and photocopiers within the zones. While building occupancy does vary at the center depending on the scheduling of events, an average value of 30 people was used. A sensible output of 90 Watts per individual, which is indicative of typical office level activities (ASHRAE 98) was assumed for a period of 8 hours each day. Heat gains from individuals contributes only a small fraction of the total load however, with the majority resulting from the operation of office equipment.

Calculation of internal gains from office equipment was based on monthly electric utility meter readings. Because all of the electricity will eventually be dissipated as heat within the

⁷ Thermal conductivity in the high density foundation is nearly 10 times that of the soil.

building zones, electricity consumption is an excellent measure of heat generation from equipment. The 1999 monthly meter readings on which the equipment loads were based are listed in table 6.3.1.

Table 6.3.1 Electric consumption for McKay Center for 1999.

Meter Read Date	Electric Consumption (kWh)	Avg. Daily Consumption (kWh)
01-21-00	3,507	119
12-21-99	4,605	140
11-19-99	5,924	204
04-21-99	4,700	162
03-23-99	4,275	147
02-22-99	3,142	101

The meter data has been parsed to only include winter months that have little or no cooling degree days in order to eliminate the large energy consumption of the air conditioning compressors on the office and lecture hall air handlers. A final correction considers that a significant fraction of the electricity consumption at the McKay center goes into the fan motors on both the main air handlers, which run continuously from 6:00 AM until 10:00 PM and, the solar air handlers, which run intermittently. Energy consumed by these fan motors is released to unconditioned spaces and was assumed not to contribute to the internal gains of the building zones. Average daily energy consumption for these motors was based on the product of the power consumption and daily run times. Fan power consumption was measured using a combination of a digital multi-meter and clamp on current probe to measure operating voltage and currents. The results of fan power measurements during steady state operation are listed in table 6.3.2.

Table 6.3.2 Air handler fan motor power consumption at steady state operation. Solar air handlers were operated in mode 3.

	RMS Voltage (V)	RMS Current (A)	Power (W)
Basement main AHU	120	9.8	1,176
Office main AHU	120	12.2	1,464
Lecture hall main AHU	120	9.8	1,176
Basement solar AHU	120	5.9	708
Office solar AHU	120	7.4	888

Operating times for the main air handlers are constant at 16 hours per day as programmed into the building controller while operation of the solar air handlers are intermittent and depend on the heating calls, solar availability, and system control logic. It was assumed that the operation of the solar fans recorded over the 27 day system calibration interval was typical of winter operation and the average run times of each solar air handler over this interval were used in calculating daily energy consumption of the solar units. Average daily energy consumption was 42.3 kWh for the main air handlers and 10.5 kWh for the solar air handlers. Subtracting this total of 52.8 kWh from the average of the daily consumption values in table 6.3.1 results in 336,000 kJ/day for internal gains from equipment within the building. When the sensible gains from the occupants are added, the internal gains sum to 413,800 kJ/day.

6.4 Sol-Air Temperature

In addition to the passive gains through the windows, the building shell itself behaves as a solar collector. By absorbing the solar radiation, the building siding is raised to a temperature significantly above the ambient air. This elevated siding temperature reduces the thermal losses from the building shell and thereby reduces building energy demands on sunny days.

It is helpful to specify a quantity labeled the sol-air temperature, which is the effective ambient air temperature that would produce the same heat flow through the wall as if there were no radiation exchange between the wall and surroundings. It is this sol-air temperature that replaces what would typically be the ambient temperature in the building shell losses of equation 6.1.3. The sol-air temperature can be evaluated by writing an energy balance on the exterior of the wall

$$q''_{wall} = h_o(T_{wall} - T_{amb}) - \alpha I + \varepsilon \Delta Q_{rad} \quad [6.4.1]$$

Where h_o represents the overall heat transfer from the wall surface to ambient, α and ε are the solar absorbance and long-wave emittance of the wall respectively, I is the incident solar radiation, and ΔQ_{rad} is the net difference in long-wave radiation exchange between the ambient air and surroundings. For vertical walls and the high roof slopes such as found at the McKay center, ΔQ_{rad} is usually taken to be zero. This occurs because the sky temperatures are typically lower than the ambient air, and the ground temperatures are often above the ambient. Since vertical and highly sloped surfaces have nearly equal view factors between the ground and sky, the net difference in radiation relative to the ambient air as defined by ΔQ_{rad} is small and can be neglected.

The wall heat loss can be defined in terms of the sol-air temperature by

$$q''_{wall} = h_o(T_{wall} - T_{sol-air}) \quad [6.4.2]$$

Equations 6.4.1 and 6.4.2 can be combined to yield the sol-air temperature

$$T_{sol-air} = T_{amb} + \frac{\alpha I}{h_o} \quad [6.4.3]$$

Calculation of the sol-air temperature requires that the solar absorbance α , surface irradiance I and heat transfer coefficient h_o be determined for the building shell. For most buildings, the absorbance of the painted siding is generally 0.9, which is assumed to hold for the dark stained cedar at the McKay center. It is possible to estimate the heat transfer coefficients at the site using correlations proposed by Mitchell (1976) for convection and by linearizing the radiation term. However, a survey of convection relations performed by Duffie and Beckman (1992) shows that there is a wide range of results depending on the correlation used. To simplify the analysis, a combined heat transfer coefficient of $17 \text{ W/m}^2\text{C}$ was used for h_o based on the recommendations of ASHRAE (1997) for typical building conditions.

Irradiance on the building shell was calculated by averaging the global radiation over the entire building surface. An exact solution to the sol-air temperature would require the calculation

of a separate value for each orientation of the building façade based on the beam and diffuse components of the incident radiation. However, the building model in this study does not distinguish wall orientations and considers the entire shell as a homogenous structure. Calculating the average irradiance on the shell is best understood if we view the structure as the hemisphere shown in figure 6.4.1.

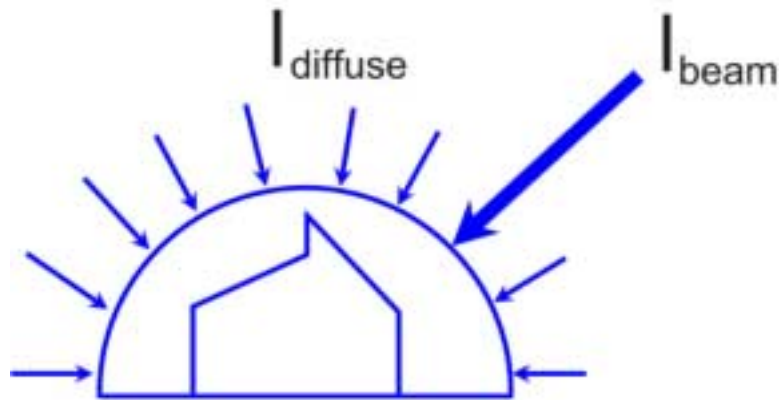


Figure 6.4.1 Representation of solar radiation components incident on building shell.

The average hemispherical radiation on the shell can be calculated by spreading the beam component evenly over the hemisphere and adding it to the diffuse component such that

$$I = I_{diffuse} + \frac{I_{beam}}{2\pi} \quad [6.4.4]$$

This homogenous irradiance I is substituted into equation 6.4.3 to yield the average sol-air temperature on the building shell. On a clear-sky day with an irradiance of $1,000 \text{ W/m}^2$ as measured normal to the beam component, the homogenous irradiance on the shell would be 160 W/m^2 yielding a sol-air temperature 8.4 C above the ambient. This sol-air temperature has the same effect as if the building balance temperature were lowered by 8.4 C , which in turn has a significant impact on the heating demands of the zone. Because the building foundation receives little to no solar irradiance, the sol-air temperature is considered equal to the local ambient temperature for the basement zone.

6.5 Auxiliary Furnace Capacity

To completely define the heat gains from the HVAC systems (Q_{HVAC}), the furnace capacity must be specified. Unlike the variable loads supplied by the solar system, the furnaces can be considered constant output devices that produce a specific heat output when they are on and no output when they are off. The flow rates through the furnaces were previously measured in section 3.4. The temperature rise across the furnace was used to calculate the full load heating capacity by

$$Q'_{furnace} = \dot{V}_{air} \rho_{air} C_{air} (T_{furnace,out} - T_{furnace,in}) \quad [6.5.1]$$

The temperature rise across the furnaces was measured after the furnace had been running for an entire 15 minute interval such that the air-air heat exchanger, ducts, and temperature sensors had achieved steady state. Approximately 50 separate intervals were measured over the course of the system calibration interval for both the office and basement systems to arrive at an average steady state temperature rise across the furnace. Values for the average furnace temperature rise, flow rate, and furnace capacity are listed in table 6.5.1. The temperature rise for the lecture hall furnace was not measured directly as there are no temperature sensors installed on the furnace inlet and outlet. However, the furnace used in the lecture hall system is identical to that used in the basement, and therefore was assumed to have the same capacity. The slight difference in the calculated temperature rise for the lecture hall furnace is due to the 4 percent increase in flow rate relative to the basement system.

Table 6.5.1 Furnace temperature rises and capacities.

	$\Delta T_{furnace} (^\circ C)$	$\dot{V}_{AHU} (CFM)$	$q_{furnace} (kJ/hr)$
Basement	31	2,093	130,548
Office	33	2,377	157,827
Lecture	30	2,173	130,548

6.6 Synopsis

All building zones were modeled with a 3-tier distributed capacitance that included the zone air mass, interior mass (i.e. partitions and furnishings), and the building shell. Passive solar gains through the windows in each zone were calculated within the simulation and included the shading effects of overhangs where they existed. Internal gains were calculated based on electric meter bills and the assumption that the total load was dissipated as sensible heat to the space after consumption from the air handler fans was subtracted out. To this equipment load was added an additional 90 W sensible output for the 30 building occupants to complete the internal gains.

The building shell was modeled as a lumped capacitance with the shell conductance calculated from the material properties and construction drawings. The effect of the soil on the basement foundation was treated by modeling it as a thermally massive structure with the conductance calculated following the methods of Latta and Boileau (1969). Effects of the sol-air temperature on the shell heat loss were evaluated by assuming a uniform irradiance on the entire shell together with a constant external heat transfer coefficient of $17 \text{ W/m}^2\text{-C}$ and a shell solar absorbance of 0.9.

Infiltration and ventilation were coupled directly to the zone air mass with an estimated forced ventilation rate of 10 percent of the air handler flows in the basement and office zones. Infiltration was based on an assumed exchange rate of 0.5 air changes per hour (ACH) for the office, and 0.1 ACH for the lecture hall and earth bermed basement. Furnace capacities for the HVAC systems were calculated based on measured air flows and temperature rises across the furnace during steady state operation. To avoid any confusion with regards to the parameters used for each zone model in the simulation, all the parameters are listed in table 6.6.1 exactly as they are found in the TRNSYS simulation code.

Table 6.6.1 Summary of building zone parameters used in simulation model.

	Wall Area (m ²)	Wall U-Value (W/m ² -C)	Wall Conductance (W/C)	Roof Area (m ²)	Roof U-Value (W/m ² -C)	Roof Conductance (W/C)
Basement	247	0.797 ¹	197	0	N/A	0
Office	178	0.363	64.6	469	0.216	101
Lecture	53	0.363	19.2	207	0.216	44.7
	Floor Area (m ²)	Floor U-Value (W/m ² -C)	Floor Conductance (W/C)	Window Area (m ²)	Window U-Value (W/m ² -C)	Window Conductance (W/C)
Basement	437	0.12	52.4	0	N/A	0
Office	437	N/A	0	39.4	2.51	98.9
Lecture	200	N/A	0	16.0	2.51	40.2
	Shell Conductance ² (W/C)	Shell Capacitance (kJ/C)	Interior Capacitance (kJ/C)	Infiltration (CFM)	Ventilation (CFM)	Internal Gains (kJ/day)
Basement	249.4	349,600	87,400	54	127	160,230
Office	264.5	43,700	65,550	327	208	80,160
Lecture	104.1	20,000	30,000	36	0	160,410

¹ Basement wall conductance is the weighted average for all foundation surfaces including the 4' of exposed foundation on the south side

² The building shell conductance is calculated from the sum of the walls, roof, floor, and windows.

7 TRNSYS Model Development

Up to this point in the study, all system components have been calibrated separately using numerical tools such as the Engineering Equation Solver (EES) developed at the Solar Energy Laboratory (Klein 2000). While simultaneous equation solvers like EES are powerful tools for parameter optimization under quasi-steady state operation, they are often not appropriate for dealing with the large data sets required by annual simulations and by the discrete changes in operating conditions caused by control logic. Large scale modular simulation tools such as TRNSYS (Solar Energy Laboratory 2000) provide a more robust environment for modeling systems level performance including a wealth of input and output data processing modules and better handling of discrete control logic. This section describes the framework of the TRNSYS model that will be used to assess building level performance at the McKay center. Implementation of the various simulation strategies, control logic, and the use of temperature interrupts will also be discussed

7.1 Simulation Framework & Component Layout

Each zone at the McKay center is modeled in separate TRNSYS simulation decks¹. These decks contain all the individual HVAC and zone components as well as data readers, output printers, and control logic. Within the simulation decks, components exist to model the current faults such as backflow and infiltration into the solar air handlers. These faults can be enabled or disabled within the simulation. The complexity and detail of the zone models results in large decks containing over 1500 lines of simulation code and approximately 55 units. Appendix C contains a schematic of the component layout, and a brief description of the model.

7.2 Simulation Control Logic

Operation and control of the HVAC systems can be modeled in three separate ways within the simulation. The first method of driving the simulation is to dictate operation of the modes exactly as they ran at the McKay center over the system calibration interval. This “forced” mode of operation is useful in the initial calibration of the simulation that will be discussed in section 8.

¹ Model simulation code is often referred to as a “deck” when dealing with TRNSYS. This terminology has roots back to the first sets of simulation code, which had to be fed into mainframe computers as decks of punchcards.

Two “free” modes of operation are modeled in the simulation. One reflects the actual control logic and the other an optimal storage logic discussed in section 7.2.3. These two “free” modes of operation allow for system performance to be assessed outside of the system test interval, where data on operating modes is not available.

7.2.1 Forced Mode Operation

Forcing the simulation to follow the actual operation of the McKay center over the duration of the system calibration interval cannot be done exactly. While the actual system can change operating modes at any instant in time, the simulation must remain in a single mode for an entire timestep. With the simulation timestep fixed at 15 minutes by the sampling interval of the temperature sensors, the actual mode dynamics had to be forced into 15 minute durations. The solution was to round the operating modes at each timestep to produce a binary output for whether or not the system was running in a particular mode during that timestep. As an example, if the system ran from 10:06 until 10:14 in mode 1, this would represent 8 minutes of operation during the 15 minute timestep spanning 10:00 to 10:15. The runtime fraction of 8/15 for this interval would be rounded up to a value of 1, instructing the simulation to run in mode 1 for the entire timestep. Alternately, if mode 1 had stopped running at 10:13 instead of 10:14, the runtime fraction of 7/15 would be rounded down to zero and the simulation would not enable mode 1 for the timestep.

A primary assumption for sorting operating modes by rounding the runtime fractions is that the fractions themselves are equally distributed from zero to unity. If some systematic characteristic resulted in a particular mode always running for less than 7 minutes (which would be rounded down), then that inherent bias would cause the rounding method to never enable the mode and therefore drastically under predict actual operation. Figure 7.2.1 is a histogram of the runtime fraction for all modes of the office system over the solar test interval. Only modes 1 and 4 show a bias with an under-representation for large runtime fractions. This is likely due to low heating requirements during mid-day conditions where mode 1 is enabled and by the high capacity of the furnace in mode 4, which can typically bring the zone through the heating deadband in less than half a timestep.

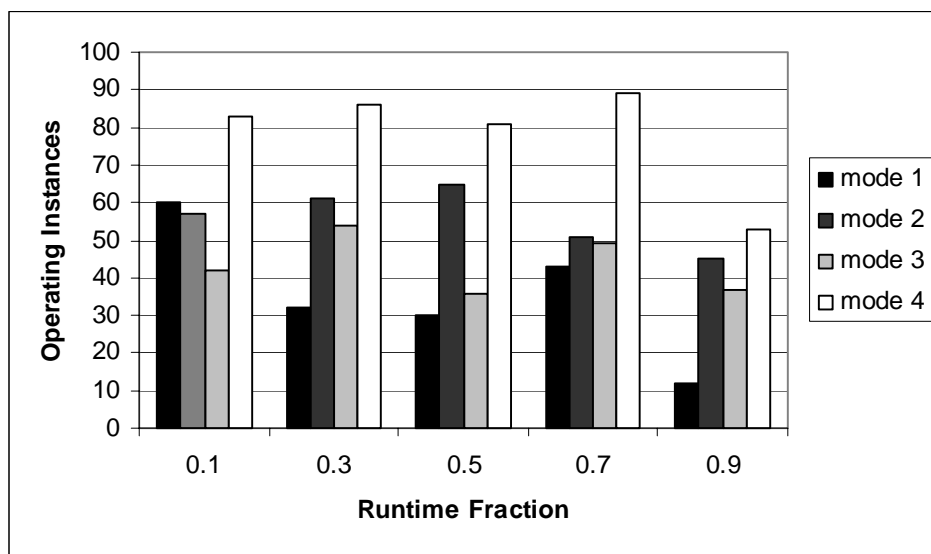


Figure 7.2.1 Operating mode histogram for office system over system calibration interval. Operating instances reflects the number of times the actual system operated at the specified runtime fraction (calculated for 15 minute timesteps).

Determining whether such a bias in runtime fractions results in a misrepresentation of mode operation can be performed by comparing the integrated run times for both the actual system and the simulation as calculated by rounding the fractions. Figure 7.2.2 depicts the integrated runtimes for each mode of operation in the office system over the system calibration interval. Only minor discrepancies occur with cumulative errors of less than 3 percent and daily errors no greater than 15 percent in modes 2 through 4. Higher daily errors of up to 51 percent were present in mode 1, but these errors were the result of small discrepancies in very short daily run times². Results were similar for the basement system with cumulative errors limited to 4 percent with daily variations of no more than 22 percent. Bias in the operation of the lecture hall auxiliary system could not be assessed due to limitations in the data recordings, which simply noted the furnace as being either “on” or “off” at the end of each 15 minute data recording interval. While some bias may be present in the lecture hall system, the energy supplied by this system is estimated to be only 15 percent of the building total, thereby limiting the effects of any inaccuracy with regards to total building performance.

² The maximum daily error of 51 percent in mode 1 was caused by a 5 minute difference between the measured and rounded runtimes for a total measured runtime of 10.2 minutes for the day. Because the minimum simulation runtime is 15 minutes, a large error results from operation over a single timestep.

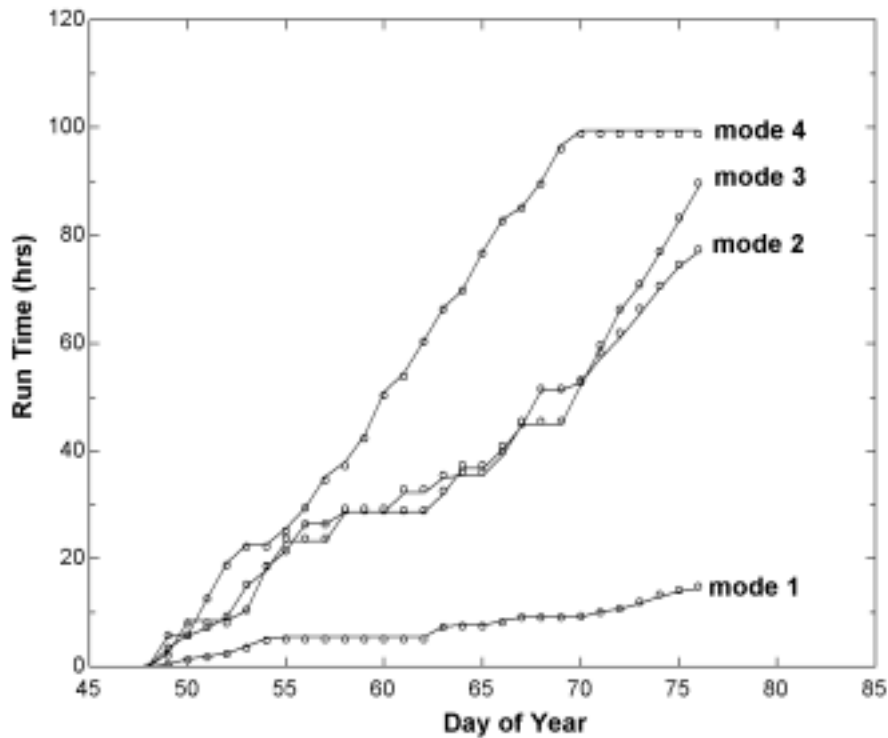


Figure 7.2.2 Integrated mode run times for exact measured (points) and rounded (solid lines) values for the office system over system calibration interval.

7.2.2 Existing Control Logic

The existing control scheme was written by engineers at the University of Wisconsin physical plant as part of the 1991 control system retrofit. Having no previous experience with active solar designs, the engineers attempted to replicate the behavior of the original Solaron controls as best they could. Temperature sensors located on the collector absorber plate (TS-6) and in the pebble bed retaining wall (TS-9) form the basis of the control strategy. Operation of the solar modes is dictated by differential controllers utilizing a combination of these two temperature sensors and several operator specified setpoints. Collection of solar energy by the array is controlled by the solar enable function, which is described by the logic diagram in figure 7.2.3. In addition to a temperature setpoint, the solar enable function is prevented from running during warm summer months by both ambient temperature and date lockouts. Actual mode operation is controlled by heating calls from the building, the state of the solar enable function, and differential controls on the pebble bed sensors as presented in figure 7.2.3. Setpoints and

comparators for the differential controllers are provided in table 7.2.1, which are identical between the simulation model and actual control system. The differential controllers are enabled when the “high” value exceeds the “low” value by the enable differential. Similarly, the controllers are disabled when the difference between the “high” and “low” values is less than the disable differential. The lack of any differentials for the solar enable and box discharge make these controllers simple setpoint comparators. Zone heat calls are driven by a differential (typically referred to as the dead-band) between the zone temperature and setpoint in order to avoid the control instabilities that would be caused by maintaining an exact setpoint. It is not known why a differential is included in the charge, but not the discharge controller of the pebble beds. Presumably, there may have been a control instability in the charging mode (mode 3) that caused the controls engineer to add these differentials.

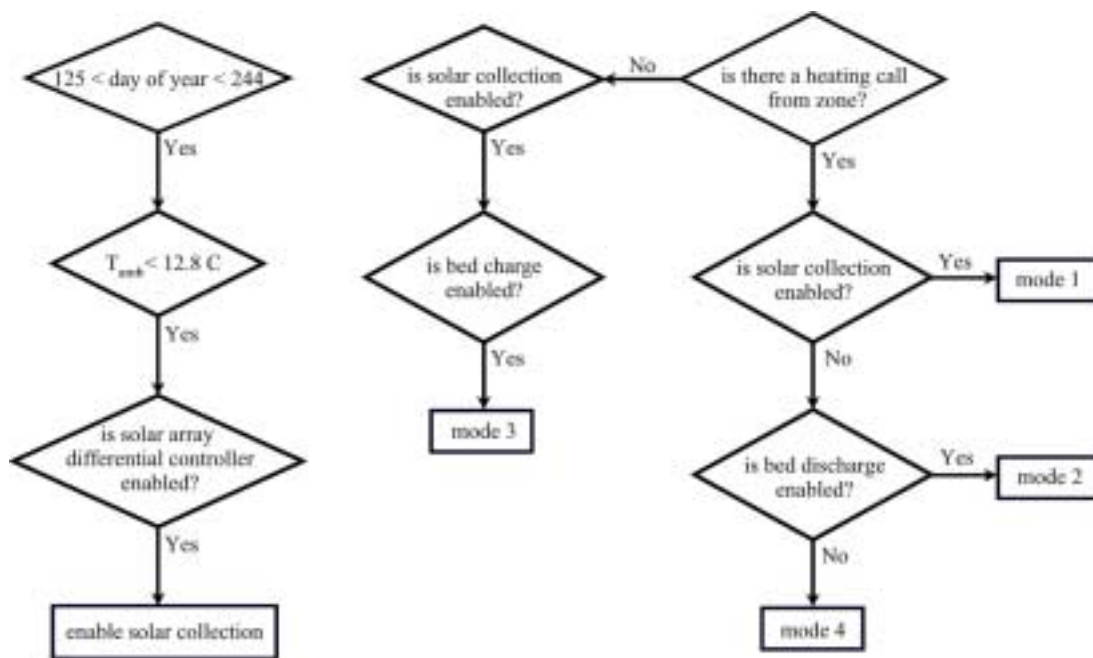


Figure 7.2.3 Control Logic diagrams for the enabling of the solar arrays (on left) and HVAC system operation (on right). Differential control logic setpoints are provided in table 7.2.1.

Table 7.2.1 Differential controller inputs and deadbands.

	High (C)	Low (C)	Enable Differential (C)	Disable Differential (C)
Solar Array	TS-6	40.0	0.0	0.0
Box Charge	TS-6	TS-9	5.6 - basement 16.6 - office	2.3 – basement 8.3 - office
Box Discharge	TS-9	32.2	0.0	0.0
Zone Heat Call	22.2	TS-2	0.0	1.7

7.2.3 Optimal Storage Control Logic

The improper location of the pebble bed sensors (TS-9) creates an inaccurate temperature reading for proper control of the pebble beds. The physical plant engineer has attempted to account for the sensor locations by assigning different differentials on the box charge controllers listed in table 7.2.1. Effects of thermal capacitance in the wall mass and changes in the convection coefficient within the pebble beds³ make the sensor reading at TS-9 an inferred temperature at best. To evaluate the effects of the sensor placement and controller setpoints, an optimal storage control strategy was developed, which can replace the existing pebble bed controllers in the simulation control strategy.

Optimal control of the beds was based on an effective COP of the solar air handler using the bed as a thermal reservoir such that

$$COP = \frac{q_{\text{stored-released}}}{q_{SAHU}} = \frac{\dot{m}_{\text{air}} C_{\text{air}} (TS7 - TS8)}{q_{SAHU}} \quad [7.2.1]$$

Where the thermal energy stored or released by the bed is defined by the mass flow rate \dot{m}_{air} , and the temperature difference between the supply and return ducts provided by TS-7 and TS-8. Fan power q_{SAHU} was previously measured in section 6.3. By specifying a COP at which to charge or discharge the beds, the simulation model calculates the temperature differentials at which the controllers are enabled.

³ Convective heat transfer on the inside wall surface is highly dependant on whether or not there is flow through the beds.

The choice of a proper COP can be based on either an emissions criteria (when running from storage produces less net emissions than auxiliary firing) or a cost based criteria (when running from storage costs less than auxiliary firing). These two criteria reflect the alternate goals of any solar installation, and the respective COP's will be based on the ratio of either specific cost or specific emissions of the respective energy sources as defined by

$$COP_{emissions-based} = \frac{E_{SAHU}}{E_{gas}}$$

where

[7.2.2]

E_{gas} = carbon emissions from combustion of natural gas per unit energy content

E_{SAHU} = carbon emissions from electricity generation used by SAHU fan

or

$$COP_{cost-based} = \frac{Cst_{SAHU}}{Cst_{gas}}$$

where

[7.2.3]

Cst_{gas} = cost of natural gas per unit energy content

Cst_{SAHU} = cost of electricity used by SAHU fan

Based on an emissions factor of 114 lb carbon per MBTU of electricity⁴ and a carbon content of 31.8 lb/MBTU for natural gas, the break even COP on an emissions basis is 3.6. On a residential cost basis of 0.07 \$/kWh electricity and 0.70 \$/therm gas, the cost based COP is 2.9. For the purpose of this analysis it was assumed that the system would be run on a cost basis with a COP of 3 used to enable discharging (mode 2) of the pebble beds for optimal operation. The COP for charging conditions must be doubled to a value of 6, because in the best case the fan power that is used to charge the bed will also be used to discharge it to recover the energy⁵. Performance of the system under these conditions will be explored in section 10.

⁴ This emissions factor is based on an average heat rate of 9,600 BTU/kWh for the Wisconsin coal plant fleet, which produces 75 percent of power production in the state (nuclear and hydro have no carbon emissions)

⁵ Flow non uniformities and bed losses will either increase the required fan energy or decrease the energy contained in the bed thus making the actual ideal charging COP slightly greater than twice the discharge value.

7.3 Temperature Interrupts

While the entire simulation model can be run using only solar irradiance and ambient temperature as inputs, the ability to feed the simulation with intermediate temperatures can be useful in calibration of the model. The thermal capacitance of several building components (principally the pebble beds, shell, and interior furnishings) builds a form of memory into the model where behavior at the current timestep is dependant on previous conditions. If the model is not properly calibrated then errors within any one component can propagate throughout the model causing the entire simulation to “drift” over time. Attempting to troubleshoot the offending component on a systems level can be extremely difficult with complex models such as those used to represent the McKay center⁶.

Temperature interrupts offer a way to “reset” the simulation at various points in the model and can thereby eliminate errors before they propagate to other components. Implementation of temperature interrupts is performed by replacing simulated values for specific duct temperatures with measured values recorded over the system calibration interval. Temperature interrupts were placed at locations in the model where transient behavior caused by changes in operating modes would not affect the measured values⁷. The locations least prone to error from intermittent mode changes were the zone return air (TS-3), collector outlet (TS-6), and bottom of the pebble bed (TS-8). Data from these three temperate sensors were used as possible temperature interrupts during the forced mode calibrations of the office and basement systems in section 8.

7.4 Ambient Conditions

Simulation forcing conditions of ambient temperature and solar irradiance can be selected from a combination of NOAA airport station data and ISIS irradiance measurements, or from TMY2 data for Madison compiled by the National Renewable Energy Laboratories (NREL). Sections 3.3 and 3.5 provide detailed descriptions of how these values are measured and the method in which radiation on the tilted array surface is calculated within the model.

⁶ Simulation models for a single zone approach 1500 lines of TRNSYS simulation code containing over 55 logical units, 1,500 component inputs, 90 equations, and 40 free variables.

⁷ This aspect of placing temperature interrupts is critical in situations where sensor temperatures are discretely sampled and not either measured continuously or at the time of a mode change. The problem often arises that the rounding of operating modes in “forced” mode control causes the simulation to run in a mode different from that at which the temperature measurement was made at a given sampling time. The simulation will then be fed a false value, which will introduce an error into the simulation.

7.5 Zone Simulation Outputs

Each zone model (i.e. basement, office, and lecture hall) creates several output files during the simulation runs. Modeled temperature values for all sensors indicated in figure 7.1.1 are provided alongside the actual recorded values (if they existed at the simulation timestep) to aid in system calibration. Figure 7.5.1 shows a screen-shot of the online temperature plot for the solar test interval illustrating how a comparison of modeled and measured values can be made. Energy quantities for each mode of operation for both the model and actual building are calculated at each timestep, and integrated values can be computed to provide daily, monthly, or annual cumulative readings. The simulation is also able to calculate the energy required to maintain the zone at setpoint and compare it to the energy supplied by the HVAC system. All of these outputs are used for systems level performance assessment and calibrations, which will be discussed in the following sections of this work.

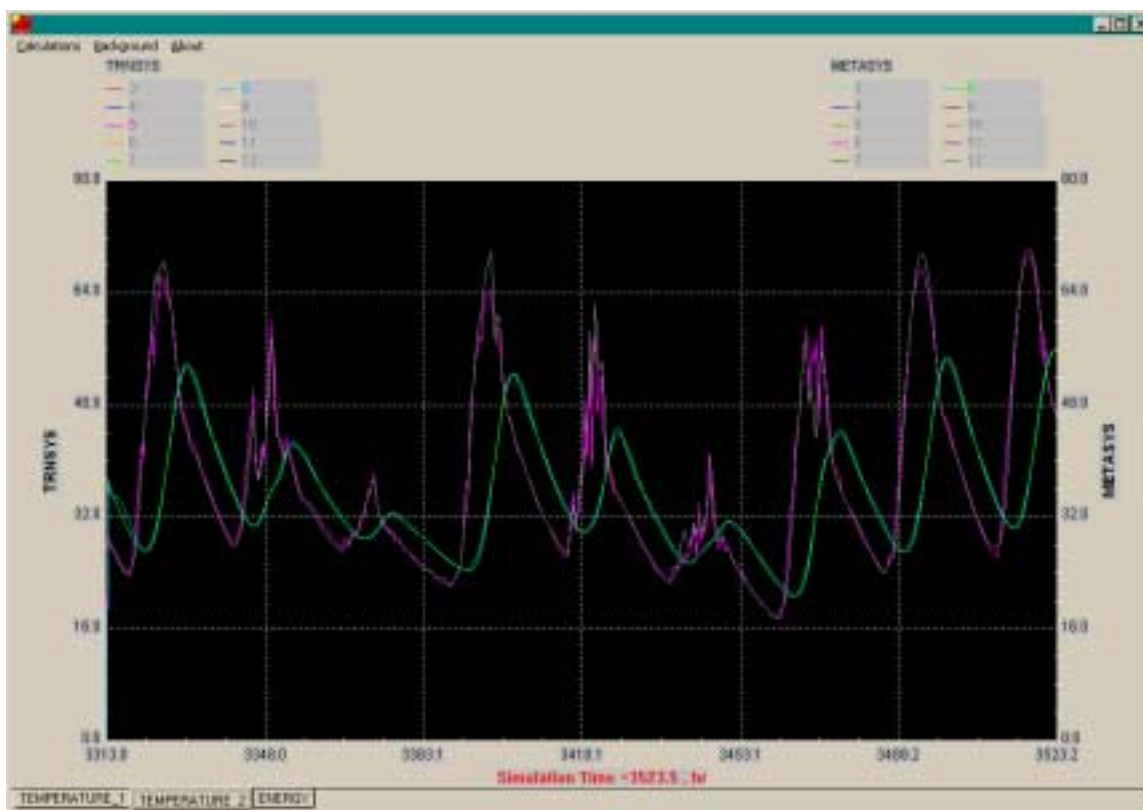


Figure 7.5.1 Screen-shot of online plotter showing collector and bed outlet temperatures for the basement over the solar calibration interval (temperature interrupts are enabled).

7.6 TRNSED Simulation Decks

With over 3,500 lines of TRNSYS simulation code containing over 120 individual components, managing the simulation decks became a problematic task. In the original formulation of the decks, changes were made by manually typing in new inputs, parameters, and equations directly into the input file. Problems quickly arose when a certain change, such as a temperature interrupt, was inserted into the code and forgotten. Several days later this same simulation deck would be used to calibrate another part of the system and would provide erroneous results because this calibration assumed that the simulation was using modeled and not measured data at the interrupt point. Over 100 hours of troubleshooting were performed on the simulation decks to track down minor manual changes that had been coded into the input file and forgotten.

The solution to spending countless hours screening the input file for hard-coded changes was to develop TRNSED⁸ decks that contained all the critical parameters (i.e. pebble bed flow distributions, collector SRCC parameters, zone loss coefficients, etc...) as well as check boxes and radio buttons that could both comment out and enable various parts of the simulation such as the controls strategy, weather data sets, and temperature interrupts. Although the TRNSED decks required a week to build, they have saved many times this effort in simplifying the simulation code to a simple windows screen containing all the pertinent data required for the entire range of simulation run options encountered in this study. Figure 7.6.1 is a screen-shot of the TRNSED interface and the TRNSYS simulation deck side by side. It is easy to see how the TRNSED interface provides a much clearer representation of the simulation than the hard-coded input file on which it is based. The TRNSED interface also makes the McKay center simulation code accessible and understandable to individuals not familiar with TRNSYS.

⁸ TRNSED is a special parsing language that can be read by the TRNSHELL program to create a dynamic on screen windows display from TRNSYS simulation decks.

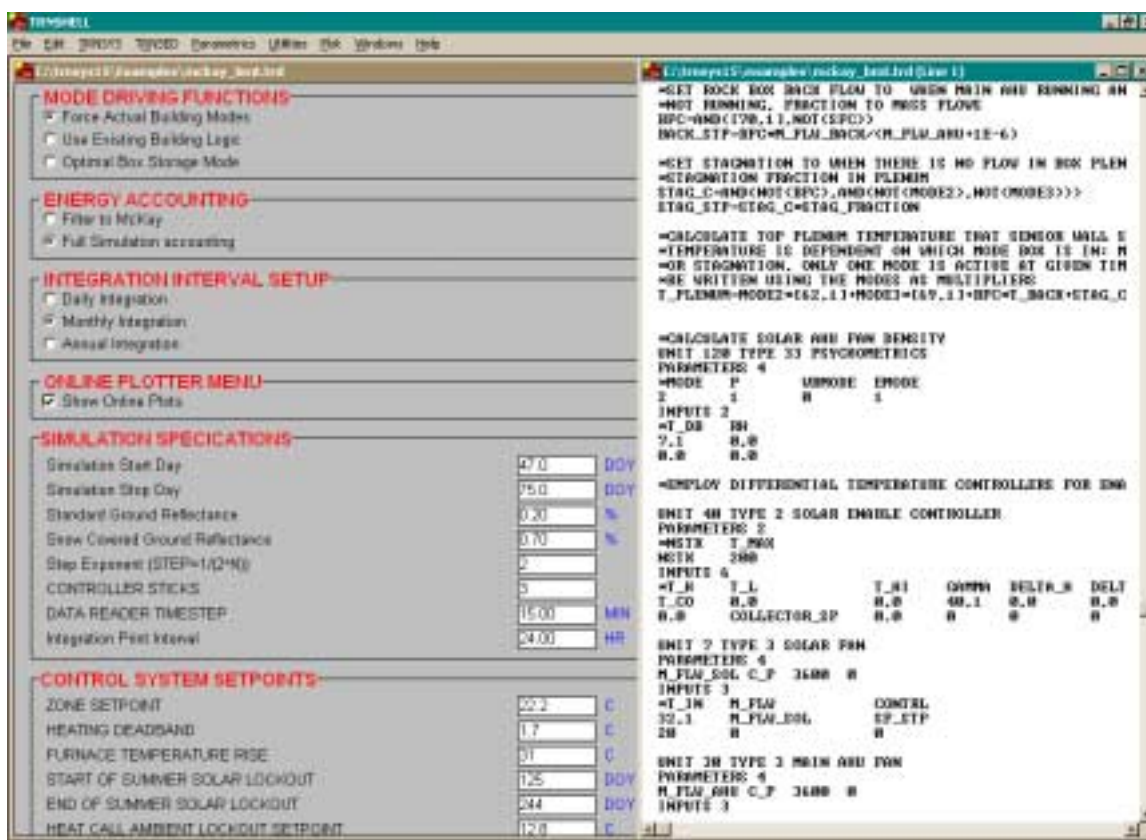


Figure 7.6.1 Screen-shot of TRNSYS interface (on left) and TRNSYS input file (on right) for the basement zone.

7.7 Simulation Summary Interface

Total building performance was calculated by adding together the energy outputs and demands from the three individual zone models. A separate TRNSYS deck was written to automatically read in the output files of each zone model and summarize the building simulation results. In addition to calculating the total solar and auxiliary contributions, the summary deck calculated the run times for each air handler, costs of electricity for running the air handlers, and natural gas consumption. Total carbon emissions resulting from the combustion of natural gas and consumption of electricity by air handler motors was also calculated. A sample of an online plot for the thermal performance of the McKay center is shown in figure 7.7.1. By combining the thermal performance, economic, and emissions indicators in one place, the summary deck provides the modeler with a clear overview of how the McKay center performs under any simulated condition.

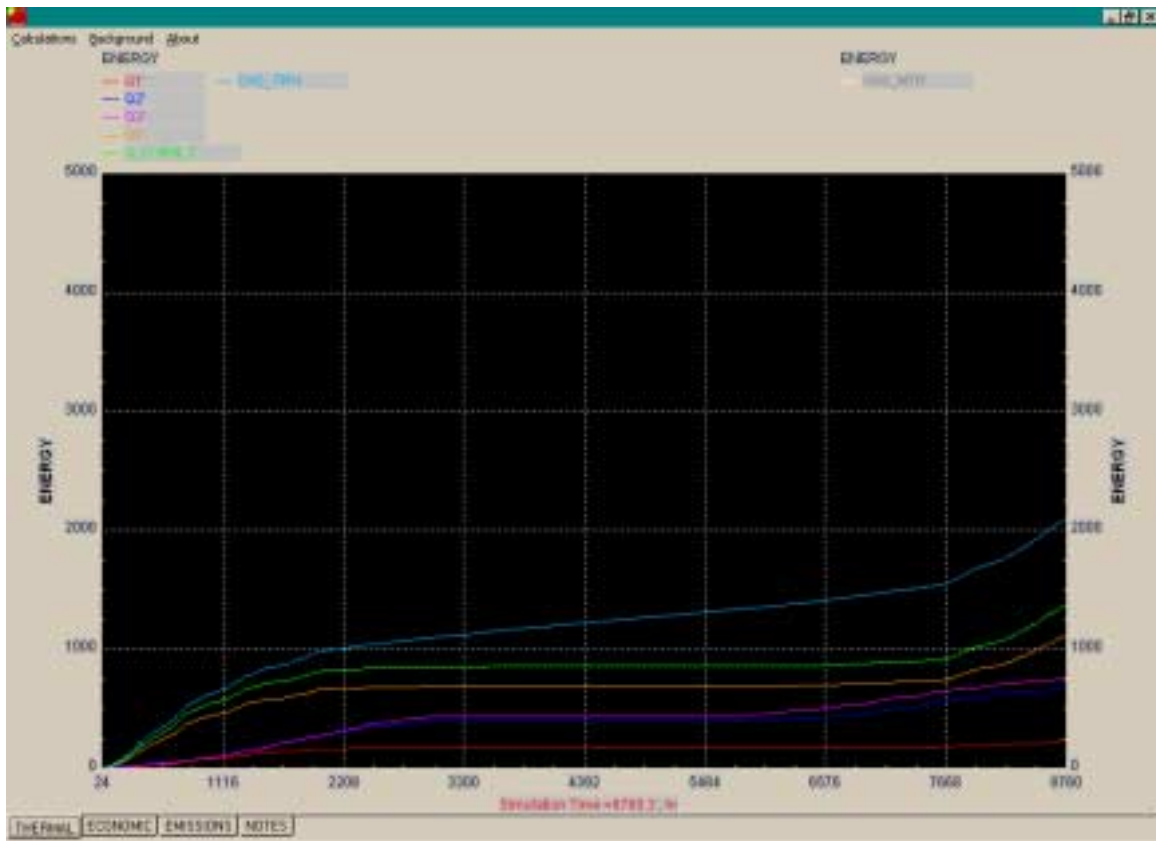


Figure 7.7.1 Sample screen-shot of annual integrated building energies including total predicted gas usage (including hot water loads and furnace efficiencies).

7.8 Synopsis

Complete building zone models (including the HVAC systems) were developed to run in the TRNSYS simulation environment. These models included the ability to insert temperature interrupts to facilitate systems level calibrations, and ambient conditions could be selected from 1999-2000 data measured from NOAA instrumentation or TMY2 data. To facilitate ease of use and reduce programming errors a TRNSED interface was built into the decks that provided a user friendly interface to key variables and forcing function. Descriptions of forced and free mode operation of the building controls was discussed and an optimal control strategy was presented for operation of the pebble beds using a cost based COP of 3. A final simulation deck was written to combine and summarize the results from the individual building zones providing the modeler with access to all the final results on a single screen.

8 Forced Mode Calibration

The first step in calibrating the entire building simulation entails forcing the model to run in the same modes of operation as the actual systems at the McKay center⁹. By running the simulation and physical system identically, the results of the model in terms of duct temperatures and mode energies can be directly compared with measured quantities. Thermal performance of the building zones can also be calibrated at this point by comparing the energy delivered to the zone by the simulation with the calculated amount required to maintain the zone at setpoint. Direct forcing of the modes allows these first steps of systems level calibration to be performed without the complications or confounding factors that might be introduced by inaccuracies in the simulated control strategy.

8.1 Comparison of Energies Within Each Mode of Operation

Mode energies correspond to the amount of energy stored or supplied by specific components in the HVAC system during operation of a particular mode. The energy produced in mode 1 is the useful solar gain of the array supplied directly to the zone, and is defined as

$$Q_{mode1} = \int \dot{m}_{air} C_{air} (TS5 - TS4) dt \quad [8.1.1]$$

Where \dot{m}_{air} represents the mass flow rate of the solar air handler, and the energy rate (i.e. the integrand) is evaluated over the time t for which the system operates in the specified mode. Due to the discrete data sampling of the duct temperatures and the simulation timestep, integrated mode energies were evaluated in 15 minute intervals. Similar integrated energies were defined for modes 2, 3, and 4 of operation by equations 8.1.2, 8.1.3, and 8.1.4 respectively. The mass flow rate for mode 4 corresponds to that of the main air handler that supplies the furnace unit.

$$Q_{mode2} = \int \dot{m}_{air} C_{air} (TS7 - TS8) dt \quad [8.1.2]$$

$$Q_{mode3} = \int \dot{m}_{air} C_{air} (TS7 - TS8) dt \quad [8.1.3]$$

⁹ A full description of forced mode control is provided in section 9.2.1

$$Q_{mode4} = \int \dot{m}_{air} C_{air} (TS11 - TS3) dt \quad [8.1.4]$$

Comparisons of integrated mode energies between the simulation and physical system rely on evaluating equations 8.1.1 through 8.1.4 using both simulated and measured duct temperatures. A complication that arises in the comparison of mode energies is that the measured energies can only be evaluated for instances where the temperatures have been accurately measured. This requires that the system was run in the desired mode at the time the temperature measurement was made. Additionally, it is necessary that the system ran in a given mode for several minutes prior to the temperature measurement so that the sensors were in thermal equilibrium with the duct air flow. These considerations limited the valid comparison durations to those where the system ran in the desired mode for the entire 15 minute timestep prior to the temperature measurement. The TRNSYS simulation model was able to account for the limited comparison range by parsing the mode energies to those where the McKay center ran in that mode for the entire timestep. For these timesteps, the model evaluated the energy based on both the modeled and measured duct temperatures¹⁰ and sent both energy quantities to an integrator. Figure 8.1.1 shows the integrated mode energies (parsed to full intervals) for the basement system over the system calibration interval with the temperature interrupts enabled in the model¹¹.

¹⁰ Measured duct air temperatures were read from an input file

¹¹ For a description of the temperature interrupts see section 9.3.

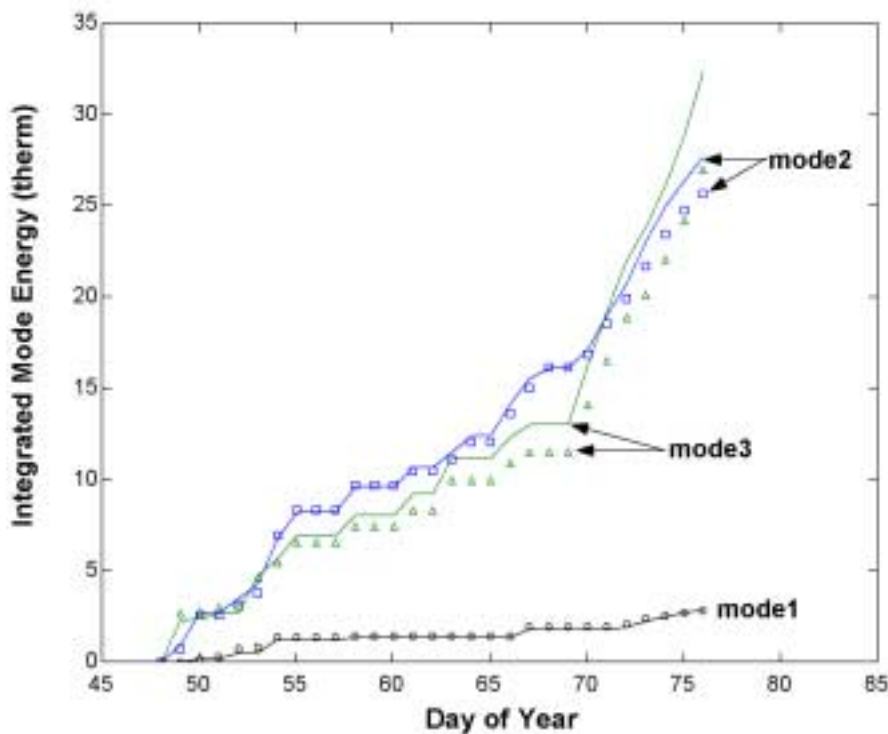


Figure 8.1.1 Measured (points) and simulated (solid lines) integrated mode energies for basement system with temperature interrupts. Energies have been parsed to account for full duration of operation at the McKay center.

Furnace energies (mode 4) were not included in the figure because they were defined identical for the simulation and physical system (i.e. they are a constant output device). Integrated operating mode energies for the office system appear quite similar as shown in figure 8.1.2. While the comparison between the measured and simulated energies was in good agreement for mode 1 in both systems, the results for modes 2 and 3 indicated that there were discrepancies that needed to be resolved

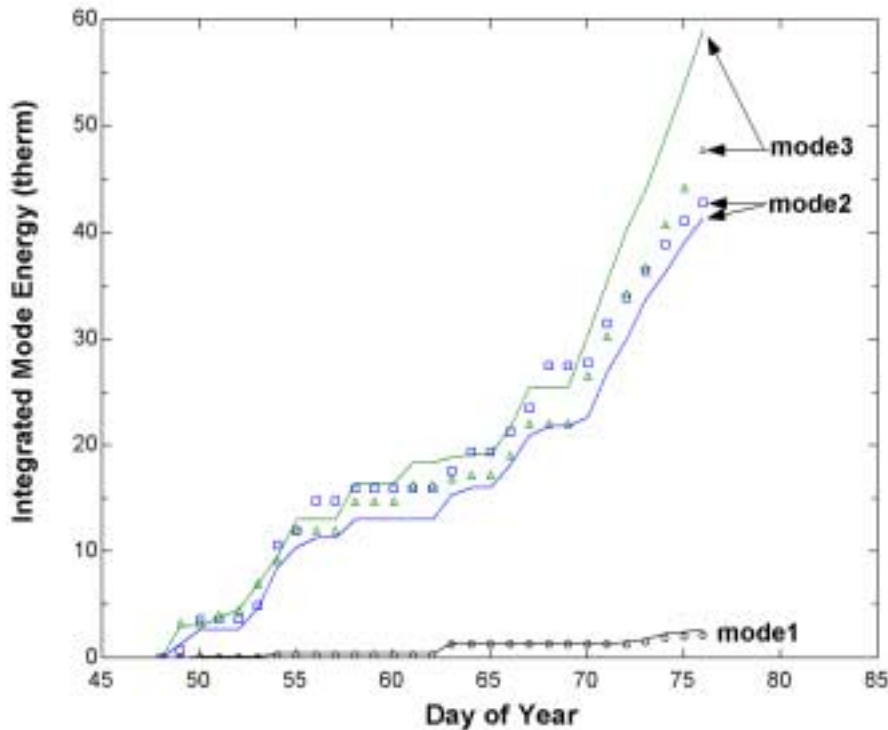


Figure 8.1.2 Measured (points) and simulated (solid lines) integrated mode energies for office system with temperature interrupts. Energies have been parsed to account for full duration of operation at the McKay center.

8.1.1 Malfunctioning Air Dampers

The first area to be investigated as a cause for the disagreement was a noticeable rise in the bottom plenum temperature of the pebble beds when the solar air handler was idle. Figures 8.1.3 and 8.1.4 are plots of the bottom plenum temperature (TS-8) for the measured, originally predicted, and final calibrated conditions of the basement and office systems over a portion of the system calibration interval. During times of near constant furnace firings, as indicated by the shaded bands, the measured plenum temperatures rose significantly above those predicted by the original model. Theoretically, the duct sensors should have remained near the zone setpoint (23 °C), which represents the stagnation temperature in these duct sections when the solar system was idle. It was hypothesized that the discrepancy between the predicted and measured values was caused by leakage in the damper (MD-1) that separates the solar subsystem from the main air handler. If MD-1 were not fully closed then a portion of the main air handler flow could have

been diverted back through the ductwork and into the pebble beds, effectively charging them at a low rate using the main air handler flow¹². The temperature of this backflow of air through the beds would be read by the temperature sensor (TS-8), thereby causing it to deviate from what would otherwise have been the stagnation temperature of the duct.

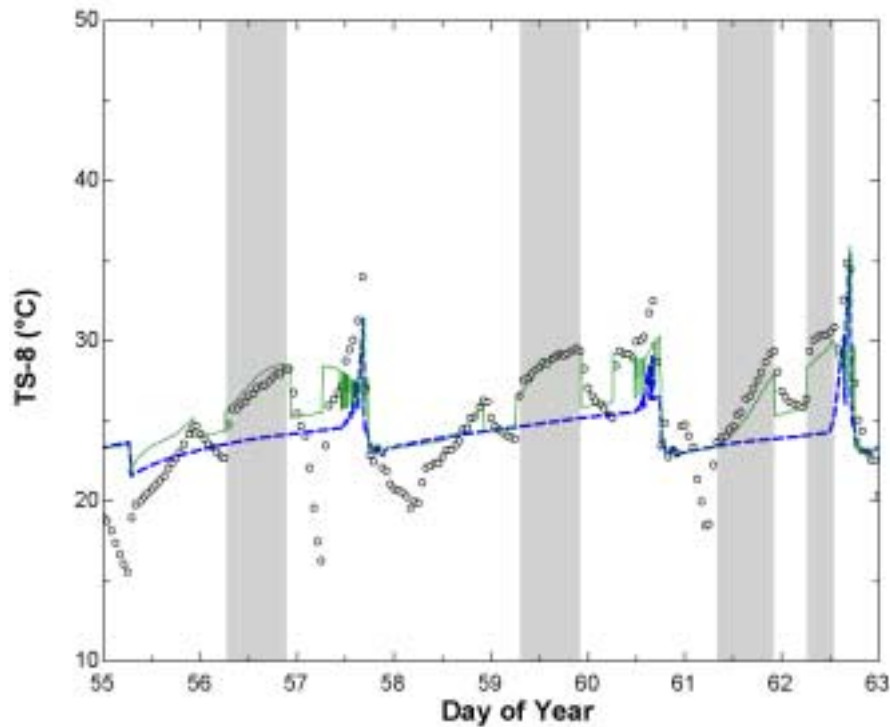


Figure 8.1.3 Measured (points), originally predicted (dashed line), and calibrated (solid line) bottom plenum temperatures for basement pebble bed. Shaded bands indicate times of near constant furnace firings (mode 4) when solar system was idle.

¹² This “backflow” from the main air handler may effectively charge or discharge the beds depending on whether or not the furnace is firing.

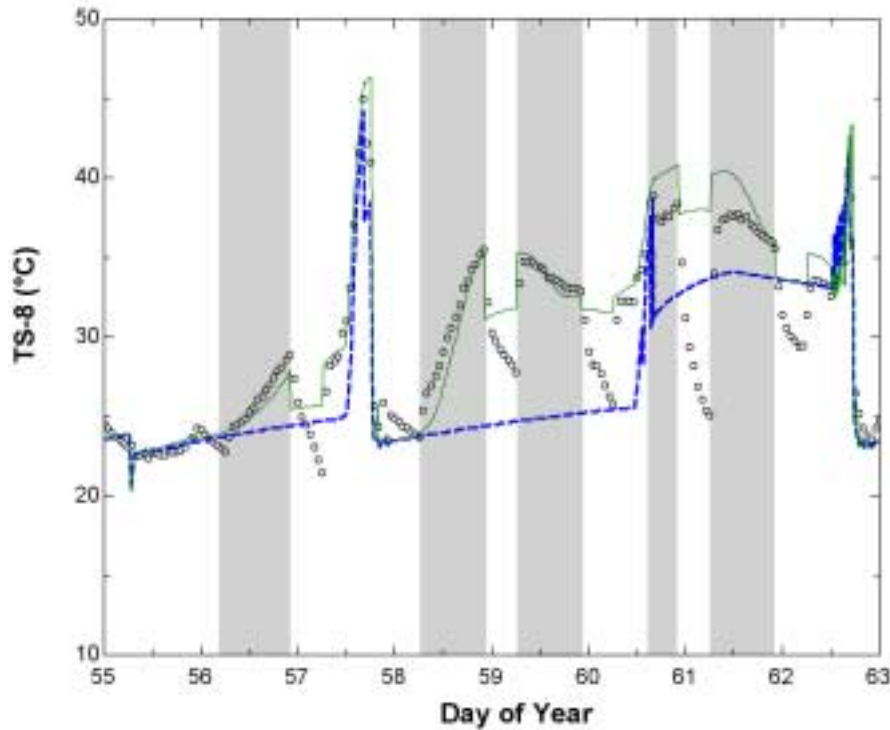


Figure 8.1.4 Measured (points), originally predicted (dashed line), and calibrated (solid line) bottom plenum temperatures for basement pebble bed. Shaded bands indicate times of near constant furnace firings (mode 4) when solar system was idle.

The hypothesis of backflow through MD-1 and into the pebble beds was tested by modeling the effect in the TRNSYS simulation model¹³. Various levels of backflow were tried with the best fits to the measured temperature at TS-8 produced with values of 125 CFM for the basement and 250 CFM for the office system. Visual inspections of the dampers were made to identify why such high leakage rates were present in the units. To the author's surprise, the dampers were not misadjusted but were fully open for times when the solar subsystem was idle. In a simple oversight, the controls engineer had forgotten to set an idle state for the system dampers. As a result MD-1 reverted to the un-energized state, which was fully open¹⁴. The high backflow rates of 150 and 250 CFM were simply driven by the pressure drops through the solar system relative to those in the HVAC supply air distribution ductwork.

¹³ For an explanation of how this is done see appendix C.

¹⁴ The controls have since been modified to close MD-1 when the system is idle.

8.1.2 Use of Temperature Interrupts

The utility of temperature interrupts in the fixed mode calibrations was questioned many times in this analysis. Because rounding of the modes may cause the simulation to use an incorrect duct temperature instead of the true output temperature of the desired component, it was debatable whether these false temperature readings introduced more error into the simulation than they were aimed at resolving. The final decision was to limit the temperature interrupts to the zone return air temperature measured by TS-3, which is located at the inlet to the main air handler. Since the main air handler runs continuously, TS-3 is an accurate measure on the airflow that supplies the collector array and pebble bed in modes 1 and 2 of operation.

Figures 8.1.5 and 8.1.6 show the integrated mode energies with temperature interrupts limited to TS-3 and levels of backflow set at 150 and 250 CFM for the basement and office systems. The remaining discrepancy in energies (particularly that of mode 2) were not consistent errors, but were instead caused by discrepancies on particular days.

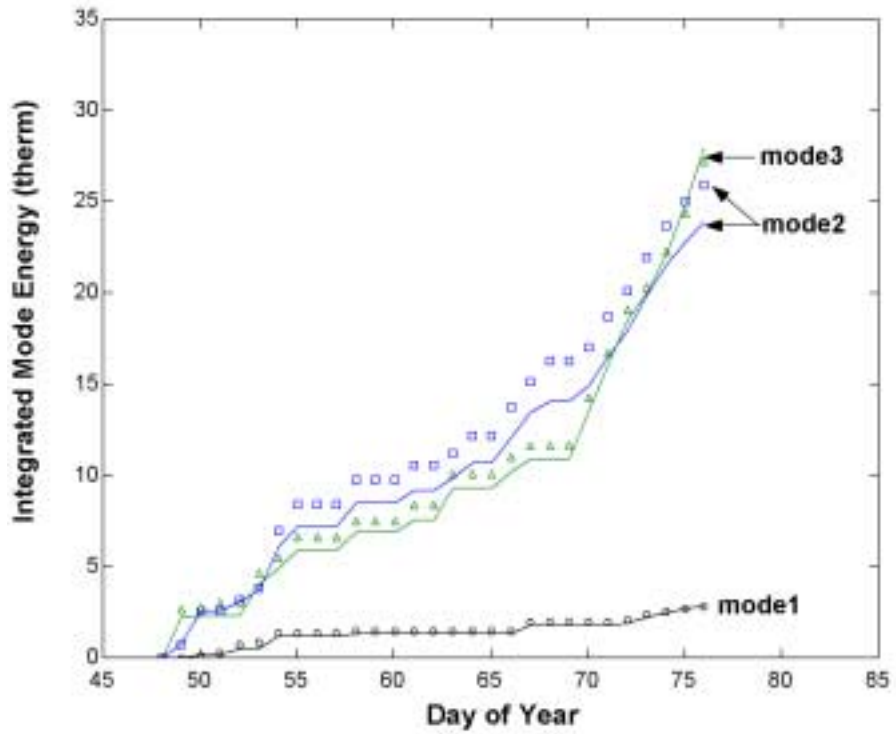


Figure 8.1.5 Measured (points) and simulated (solid lines) integrated mode energies for basement system with only TS-3 temperature interrupt enabled. Energies have been parsed to account for full duration of operation at the McKay center.

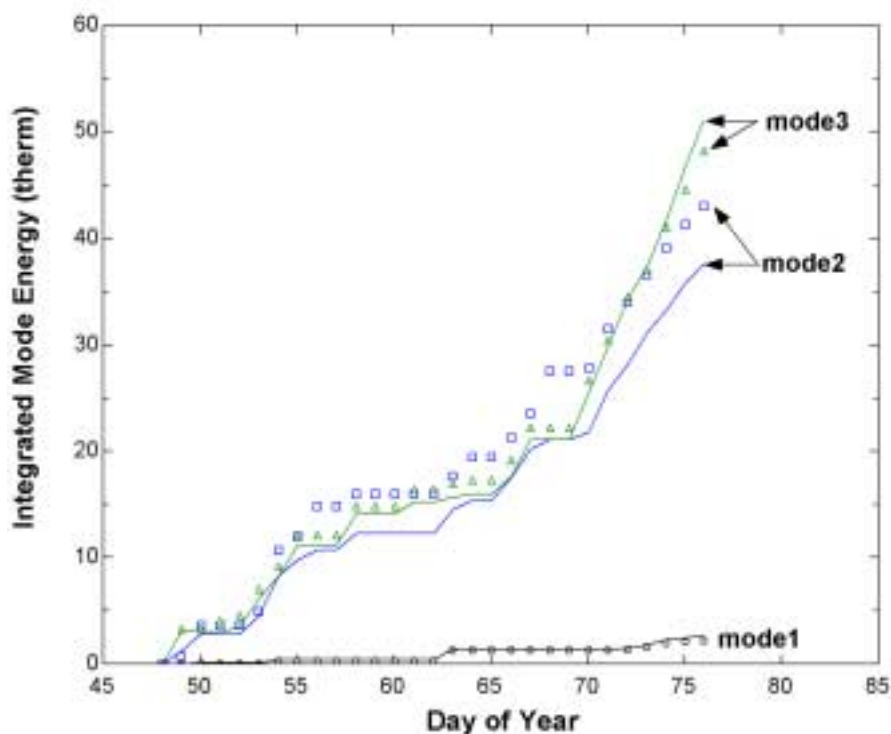


Figure 8.1.6 Measured (points) and simulated (solid lines) integrated mode energies for office system with only TS-3 temperature interrupt enabled. Energies have been parsed to account for full duration of operation at the McKay center.

8.1.3 Results of Mode Energy Comparisons

Figure 8.1.7 is a calibration plot comparing the measured and modeled mode energies integrated for each day of the system calibration interval. One of the most significant discrepancies can be seen in day 67 of the office system, which is highlighted in figure 8.1.7. On this day the simulation predicted that only 0.87 therms were discharged from the box in mode 2 of operation while the measured result was 3.95 therms. Figure 8.1.8 shows the measured and modeled values of the temperature sensor (TS-7) located in the upper duct to the office pebble bed for days 66 and 67. The shaded band to the left of figure 8.1.8 indicates a duration of several bed discharges (mode 2) during the night of day 66 while the band to the right was the constant discharge during the morning of day 67. The large difference between the measured and modeled temperatures on the morning of day 67 was responsible for the disagreement in energy quantities

for mode 2. The paramount question became one of discovering which value (measured or modeled) was correct.

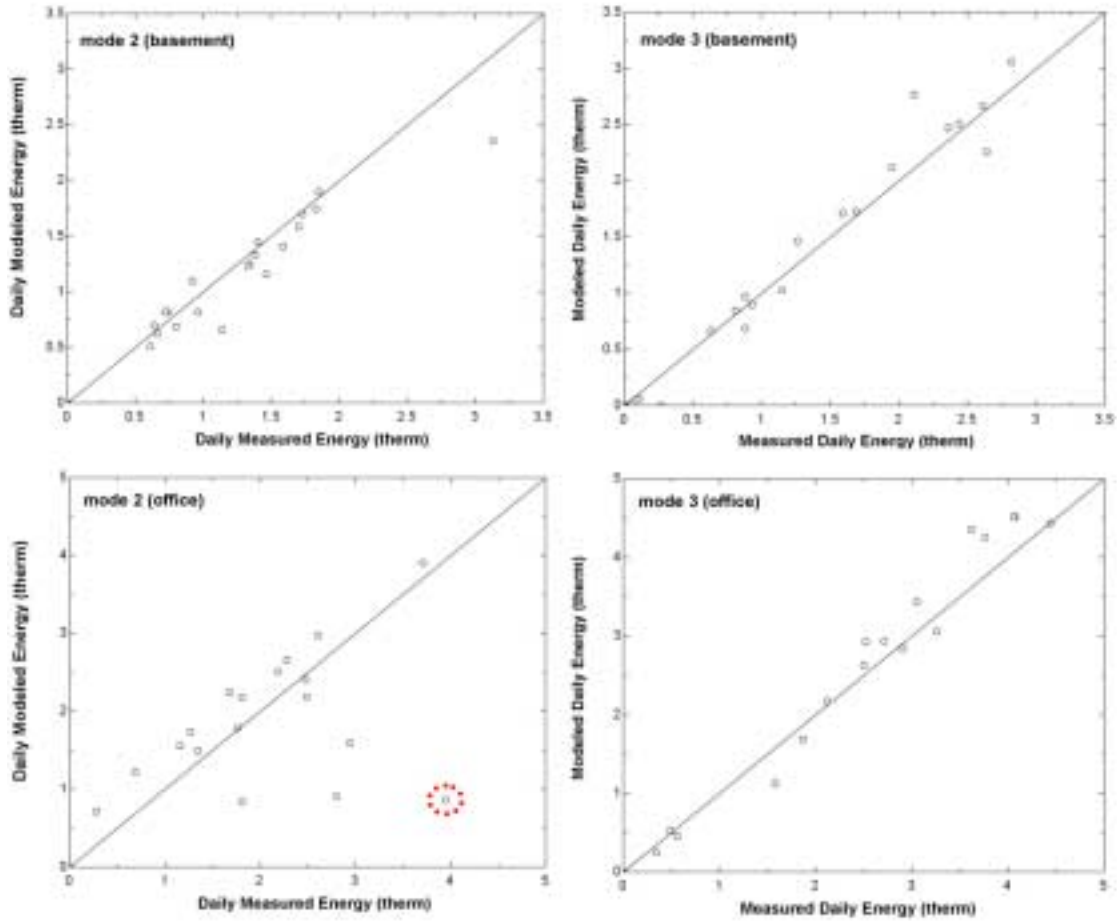


Figure 8.1.7 Calibration plots of daily integrated energies for office and basement systems. Temperature interrupts limited to TS-3.

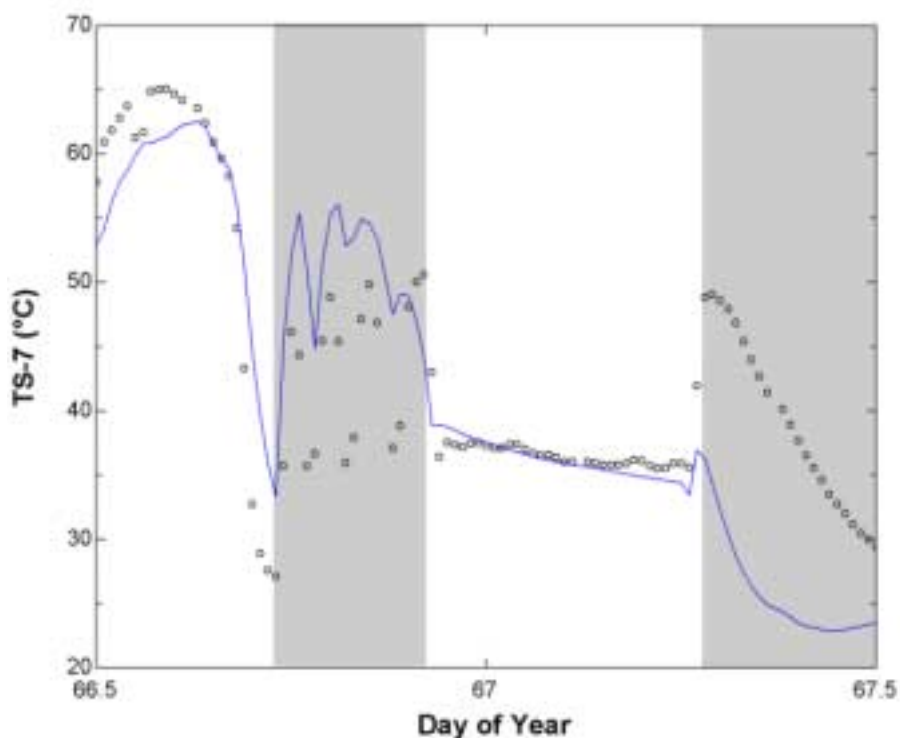


Figure 8.1.8 Measured (points) and predicted (solid line) pebble bed discharge temperature (TS-7) over portion of system calibration interval.

By plotting the integrated daily energy values vs. time, as shown in figure 8.1.9, it was possible to obtain a clear picture of how the system was operating leading up to day 67. Measured energies started out at zero on day 64 where neither mode 2 or 3 operated. The pebble bed then charged and discharged approximately 2 therms on day 65, and then charged 3 therms on day 66 while discharging just over 2 therms. The paradox of day 67 is how the bed could have discharged 4 therms when only a net charge of 1 therm should have been in the bed¹⁵.

The modeled output illustrates what would be expected on day 67 in that the bed discharges the net difference of what was not discharged on the previous day (i.e. day 66). While the mode energies of figure 8.1.8 have been parsed to full operating intervals only, they represent approximately 80 percent of the total energy quantities over the days shown and are characteristic

¹⁵ The net charge is the difference between the energy stored in the bed over the course of the day minus the amount discharged over the course of a day. The difference is the energy stored in the bed for the next day.

of the ratio of energy charged and discharged through the bed (i.e. integrating the full energy terms in the model would not turn up the missing energy).

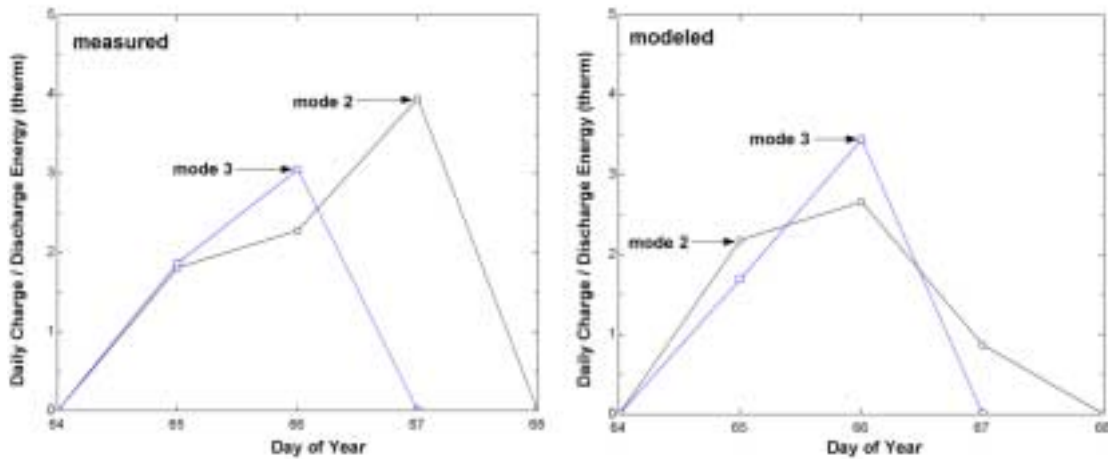


Figure 8.1.9 Daily integrated energies from modes 2 and 3 of operation for the office pebble bed.

Many attempts were made at forcing the simulation to produce the missing energy on day 67. The first effort was to reinstate all the temperature interrupts in case the simulation had drifted in terms of the thermal profile within the bed. Inserting the temperature interrupts, which tend to overstate the discharge energies due to the higher temperature stagnation readings, had almost no effect on the discharge energy of day 67 raising it from 0.87 to 0.89 therms, a change of little more than 2 percent. It was also thought that backflow from the furnace might have been able to charge the bed with the excess energy, but simulations with the backflow ranging from 250 up to 600 CFM were unable to raise the discharged energy above 1 therm for day 67. With many probable physical causes exhausted¹⁶, it was believed that the discrepancies in discharge energies in the calibration plots of figure 8.1.6 were the result of a small infiltration leak into the sensor channel of TS-7 during the negative duct pressures in mode 2 of operation. While calibration of this sensor during the summer of 1999 showed that the mastic seal was intact, the rubber gasket that seals the junction box to the duct is itself prone to leakage. The final conclusion of the fixed mode calibrations was to employ the single temperature interrupt of TS-3 together with calibrated backflows of 125 and 250 CFM for the basement and office respectively.

¹⁶ The possibility of the masonry walls of the pebble bed releasing energy back into the bed during discharge was also explored, but simulations run with this assumption provided poor agreement over the constant charging of the solar test interval indicating that the walls behave as near constant temperature sinks due to close thermal coupling with the building foundation and surrounding soil.

The resultant simulated energies for each mode of operation were then used to define the HVAC energy supply for zone energy calibrations.

8.2 Zone Energy Calibrations

With the energy supply from the HVAC system defined and calibrated, calibrations then focused on whether the energy delivered to the zone by the simulation matched the amount required to maintain the zone at the setpoint temperature. The total energy supplied to the zone is expressed as

$$q_{supply} = q_{gain,solar} + q_{gain,internal} + q_{HVAC} \quad [8.2.1]$$

Where $q_{gain,solar}$, $q_{gain,internal}$, and q_{HVAC} represent the energy supplied from passive solar gains, internal gains, and the HVAC system respectively¹⁷. The energy required to maintain the zone temperature is equal to the losses from the airmass.

$$q_{required} = q_{shell} + q_{infiltration} + q_{ventilation} \quad [8.2.2]$$

Where q_{shell} is the conduction through the building shell and $q_{infiltration}$ and $q_{ventilation}$ represent air exchanges with the ambient. Accuracy of the model was evaluated by comparing the daily integrated values of the supply and required energy as well as cumulative values integrated over the entire system calibration interval. Comparisons of the resultant zone temperatures to the setpoint also offered a qualitative assessment of simulation performance.

Figures 8.2.1 and 8.2.2 show comparisons of the cumulative and daily integrated supply and required energy values for the basement zone. On a cumulative basis, zone energy requirements were met to within 4 percent (162 therms were delivered vs. 169 therms required) over the course of the system calibration interval (figure 8.2.1). Daily requirements were satisfied to within 8 percent on average with a maximum daily variation of 20 percent (figure 8.2.2). The effects of these variations in supply (q_{supply}) and required ($q_{required}$) energies can be seen in figure 8.2.3 where the simulation produced a zone temperature very close to the measured

¹⁷ The HVAC system is defined by the energy outputs of both the solar system and auxiliary furnace.

setpoint. The undersupply of energy during the last 7 days of the solar test interval resulted in zone temperatures 1-2 °C below setpoint for days 69 through 75. The simulation model for the basement zone included the losses from the basement pebble bed and leaks from the solar air handler as internal gains into the interior capacitance (i.e. building partitions). These gains brought the basement zone performance to the current levels depicted in figures 8.2.1 through 8.2.3. Without these gains, the zone temperature during days 69 through 75 would have been 3-4 °C below setpoint.

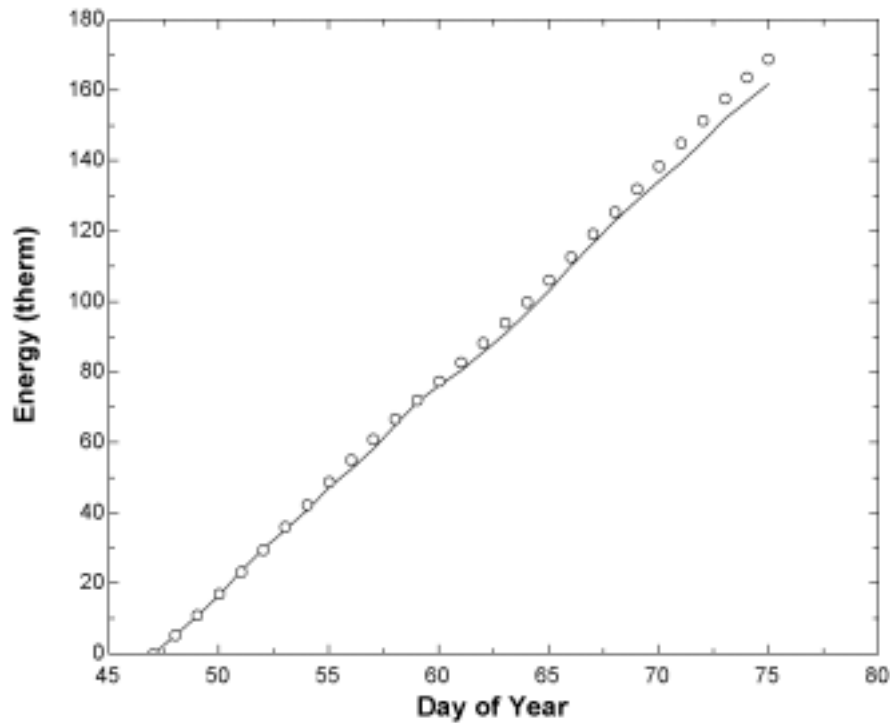


Figure 8.2.1 Comparison of cumulative integrated values of $q_{required}$ (points) and q_{supply} (solid line) for the basement zone.

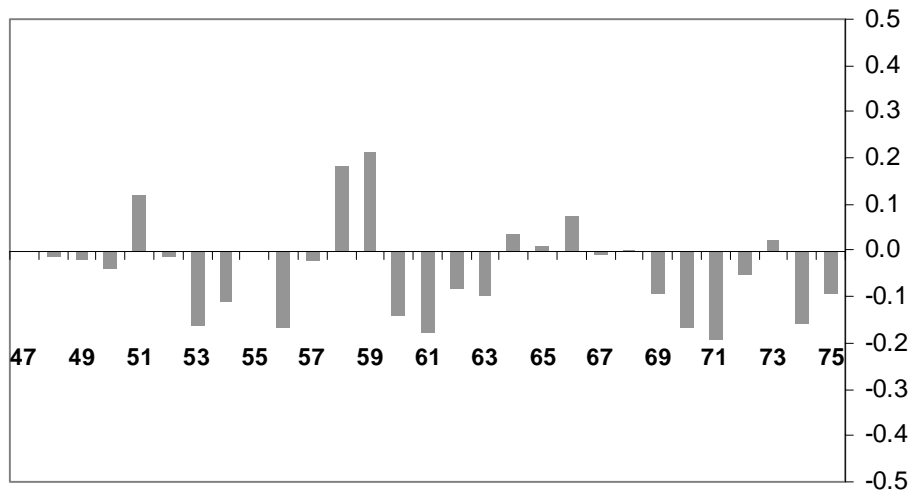


Figure 8.2.2 Percent deviations in q_{supply} from $q_{required}$ based on daily integrated values for the basement zone.

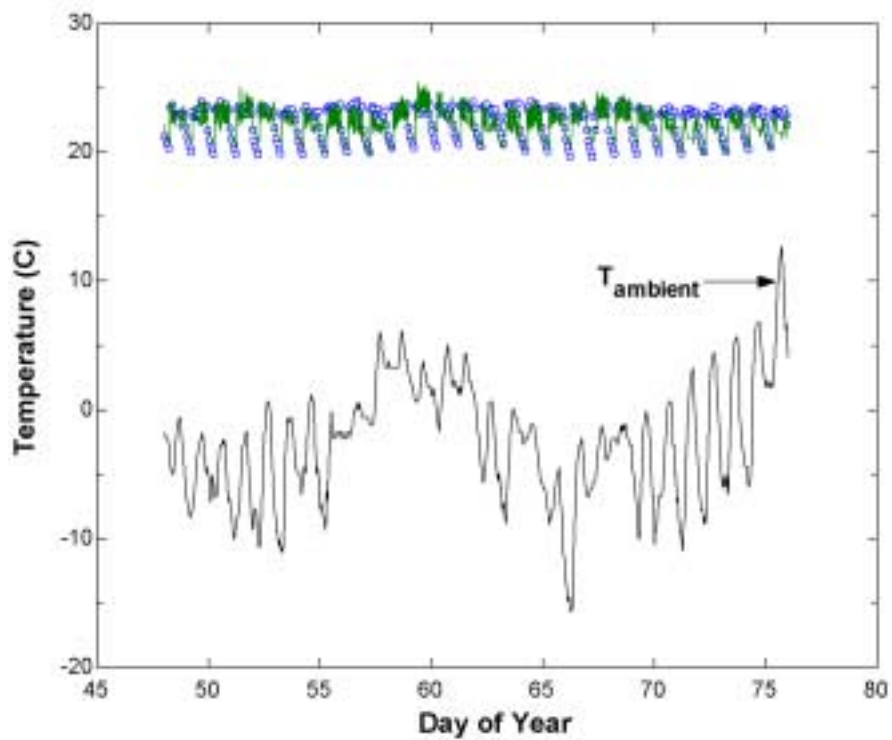


Figure 8.2.3 Zone temperatures in the basement zone resulting from energy supply and demand requirements specified in figure 8.2.1. Measured zone temperatures are indicated by points, and modeled temperature shown as solid line.

Comparisons of cumulative and daily energy terms for the office zone are shown in figures 8.2.4 and 8.2.5. Supply and demand energies matched well until day 59 when the system was supplied with nearly 100 percent excess energy, which drove the cumulative terms apart. Days 62 and 65 also supplied significant excess energy to the zone creating a net difference of 20 therms between the supply and required energies by the end of the system calibration interval.

Unlike the basement system, which has almost no operable openings, most of the windows in the office zone can be opened by the occupants. The combination of operable windows, and occupancy levels create a load dynamic within the office zone that is much more variable than what is found in the basement. The measured zone temperatures of figure 8.2.6 show that the zone temperatures during the night-time setback fell to extremely low levels for days 62 and 65 (the night-time temperatures are highlighted in figure 8.2.6). Moreover, the measured zone temperature took significantly longer to recover to setpoint after the HVAC system was enabled at 6:00 AM. The low night-time temperatures coupled with long recovery times are indicative of a window being left open overnight causing large infiltration losses in the zone.

Neither the low setback or the long recovery were apparent in day 59, which had the highest error, but these issues (low night temperatures and long recovery) only appear if the window is left open overnight. If the window was opened once the day started and closed before the occupants left then the infiltration would not likely affect the zone temperature (assuming the furnace capacity was sufficiently high), but would instead be reflected in increased heating requirements during the day. Since day 59 represented one of the first warm sunny days of spring, it is likely that the occupants would have opened some windows to cool off the building. This was confirmed in discussions with one of the building occupants who said that they typically opened the windows on warm days to “air out” the building.

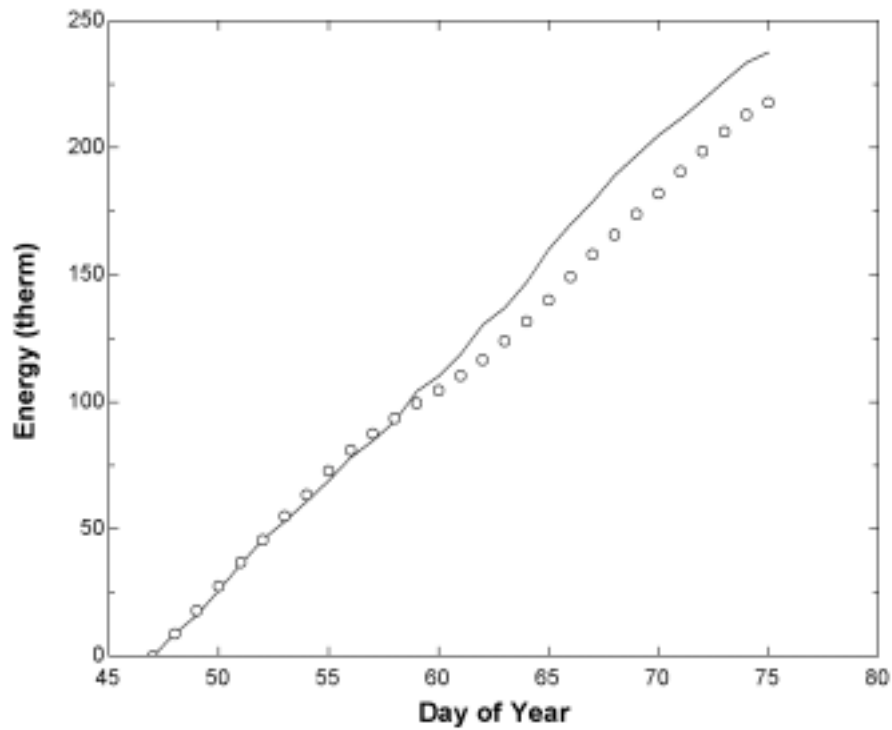


Figure 8.2.4 Comparison of cumulative integrated values of $q_{required}$ (points) and q_{supply} (solid line) for the office zone.

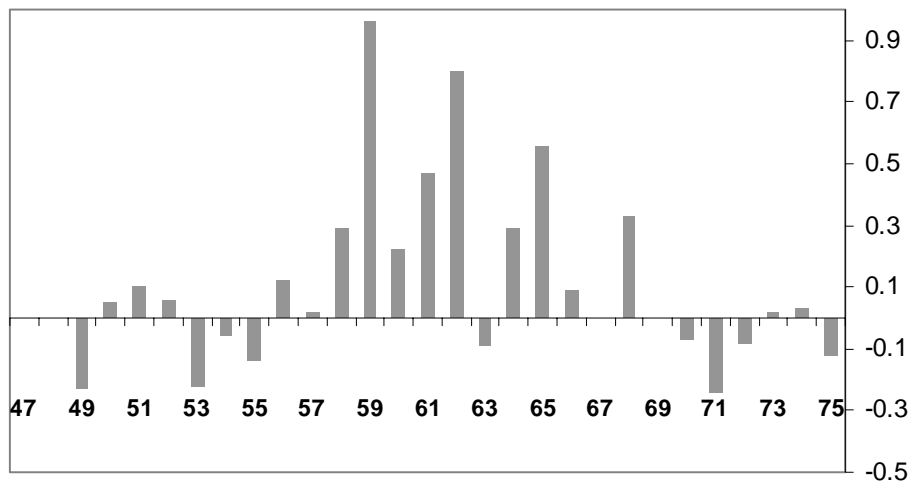


Figure 8.2.5 Percent deviations in q_{supply} from $q_{required}$ based on daily integrated values for the basement zone.

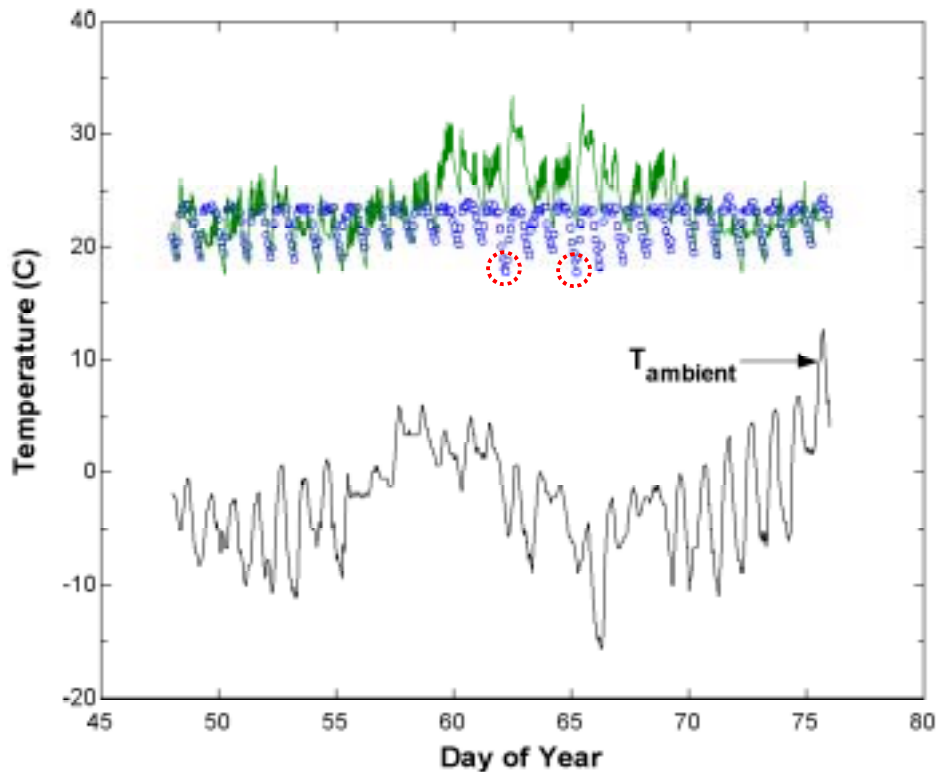


Figure 8.2.6 Zone temperatures in the basement zone resulting from energy supply and demand requirements specified in figure 8.2.1. Measured zone temperatures are indicated by points, and modeled temperature is shown as solid line.

While it would have been possible to increase the infiltration rate in the simulation to account for these variations, it was felt that the increase in infiltration on these days was not representative of true winter operation, and the days were removed from the calibration data set. Figure 8.2.7 shows the cumulative supply and required energies after days 59, 62, and 65 were removed from the data set. Agreement of the cumulative energies was 2.2 percent (202 therms delivered vs. 197 therms required). Daily energy values agreed within 15 percent on average with a maximum deviation of 47 percent (figure 8.2.5)¹⁸.

¹⁸ Again, days 59, 62, and 65 have been removed from the data set to obtain these values.

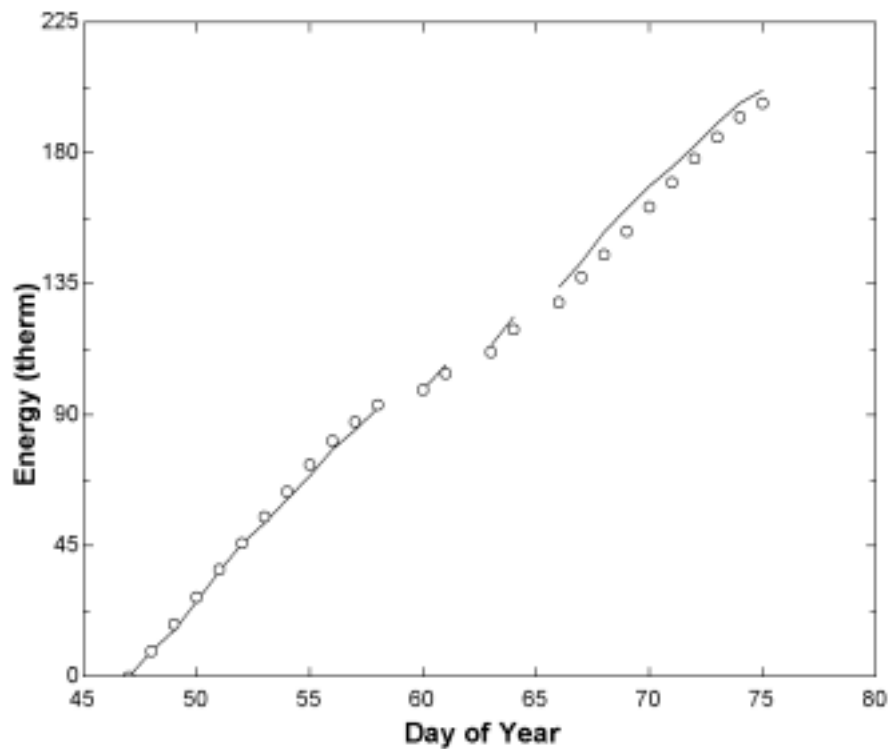


Figure 8.2.7 Comparison of cumulative integrated values of $q_{required}$ (points) and q_{supply} (solid line) for the office zone with days 59, 62, and 65 removed from the records.

Agreement within the lecture hall is shown in figure 8.2.8 with cumulative energies agreeing to within 7 percent (50.8 therms delivered vs. 54.4 therms required) and an average daily variation of 15 percent (figure 8.2.9). The larger uncertainty in the lecture hall zone was likely caused by the limited data set on the furnace firings described in section 7.2.1. It is also possible that there was some thermal communication between the office zone and lecture hall that moderated the energy requirements of the lecture hall through air exchanges.

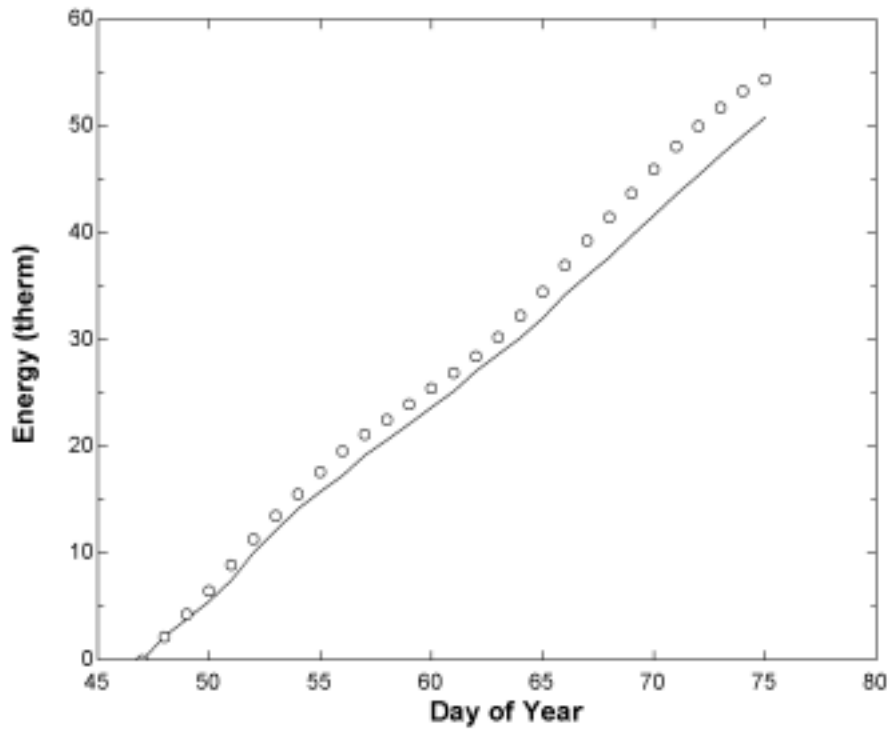


Figure 8.2.8 Comparison of cumulative integrated values of $q_{required}$ (points) and q_{supply} (solid line) for the lecture hall.

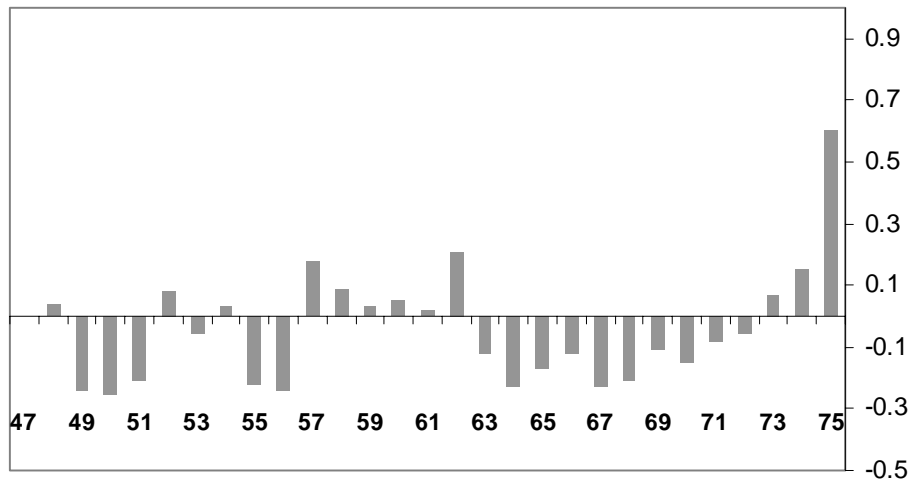


Figure 8.2.9 Percent deviations in q_{supply} from $q_{required}$ based on daily integrated values for the lecture hall.

8.3 Dynamic Mode Calibration of Pebble Bed Sensors

During the course of forced mode calibrations it was noticed that the pebble bed sensors (TS-9) failed to properly track the measured values. Although modeling of the sensors during the constant box charging of the solar test interval had shown good agreement¹⁹, dynamic charging and discharging cycles of the system calibration interval appeared to have introduced a phenomenon not accounted for in the simulation model. The shaded bands in figure 8.3.1 indicate the areas where the model deviated significantly from measured values. The durations within the shaded bands are those immediately following charging of the beds (mode 3) when the solar system was idle. While the model was constructed such that the sensor tracked the rock mass temperature in the uppermost node, the real sensor appeared to be coupled to a much lower reading during these periods.

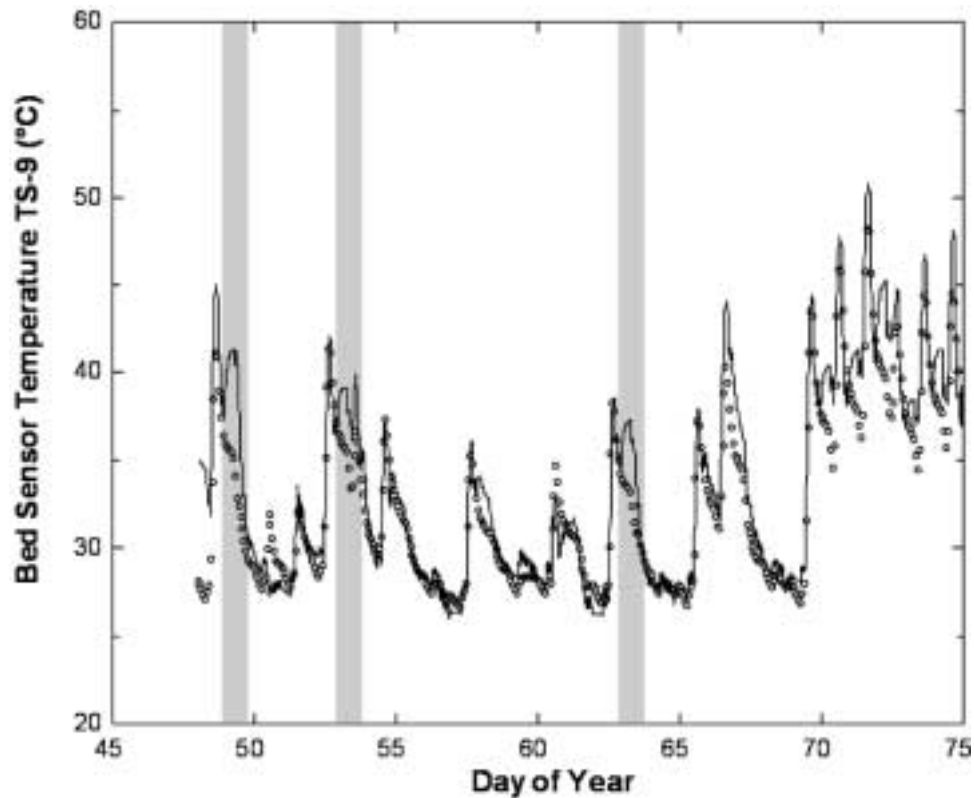


Figure 8.3.1 Measured (points) and modeled (solid line) temperatures for pebble bed sensor TS-9 in basement system. Shaded bands indicate durations where model departs from measured values.

¹⁹ See figures 7.12.3 and 7.12.4

When the solar system is idle, the air temperature in the upper plenum may not necessarily correspond to the temperature of the rock mass. This is especially true in the case of the current system where backflow from the main air handler passed through the beds. Because the sensor is located at the very top of the rock mass (see figure 5.12.2), it is possible that the sensor is more sensitive to the upper plenum temperature than the rock mass. By coupling the sensor to the plenum temperature, which rapidly decays when the bed is idle, it was possible to eliminate the anomalies indicated by the shaded bands in figure 8.3.1.

Although the plenum temperature is well defined when there is flow through the bed (it is simply the duct temperature TS-7), the temperature at which the plenum stagnates when the bed is idle is not known. The simulation model determined the temperature of the plenum during stagnation conditions based on a user specified fraction that defines where the temperature lies between the extremes of either the temperature of the rock mass or that of the solar equipment room. The plenum temperature that the sensor calculations were based on during no flow conditions was defined in terms of a “stagnation ratio” such that

$$T_{plenum, stagnation} = (1 - R_{stag})T_{rock} + (R_{stag})T_{solar, room} \quad [8.3.1]$$

Where R_{stag} represents the stagnation ratio, T_{rock} is the temperature of the uppermost node in the pebble bed, and $T_{solar-room}$ is the temperature of the room containing the solar equipment. The best fit for both the office and basement beds was for a stagnation ratio of 0.75 indicating that the plenum stagnated closer to the room temperature than that of the rock mass in both systems.

The good agreement produced during the constant charging of the solar test interval, which did not model the effects of stagnation, occurred because the entering air stream was always in thermal equilibrium with upper node temperature of the pebble bed. When the bed was idle, it was necessary to introduce the concept of a plenum stagnation temperature defined by equation 8.3.1 to achieve satisfactory results.

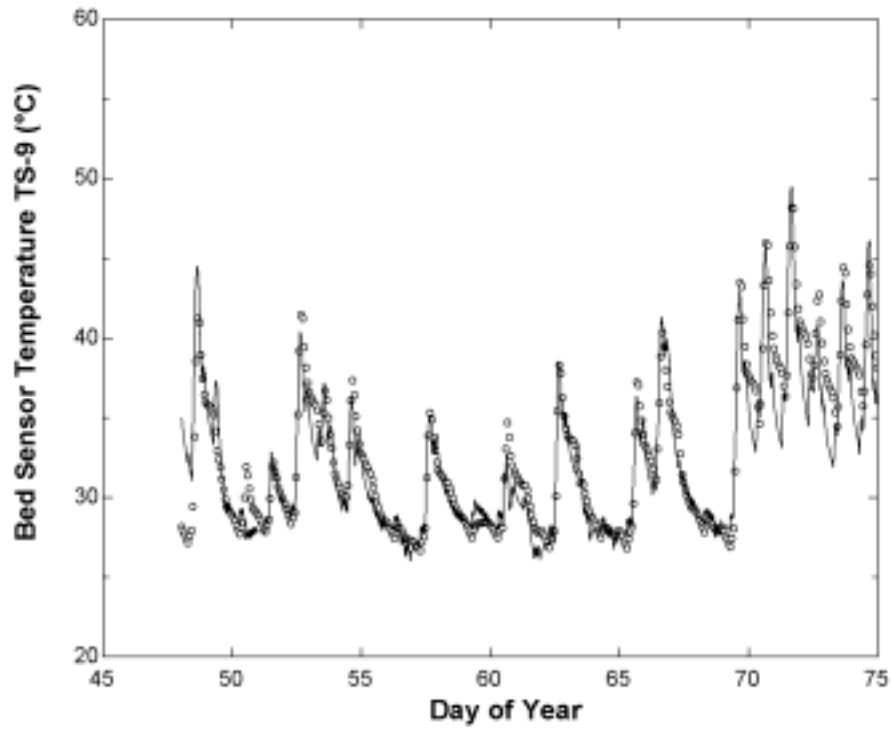


Figure 8.3.2 Measured (points) and modeled (solid line) temperatures for pebble bed sensor TS-9 in basement system. Stagnation fraction is 0.75.

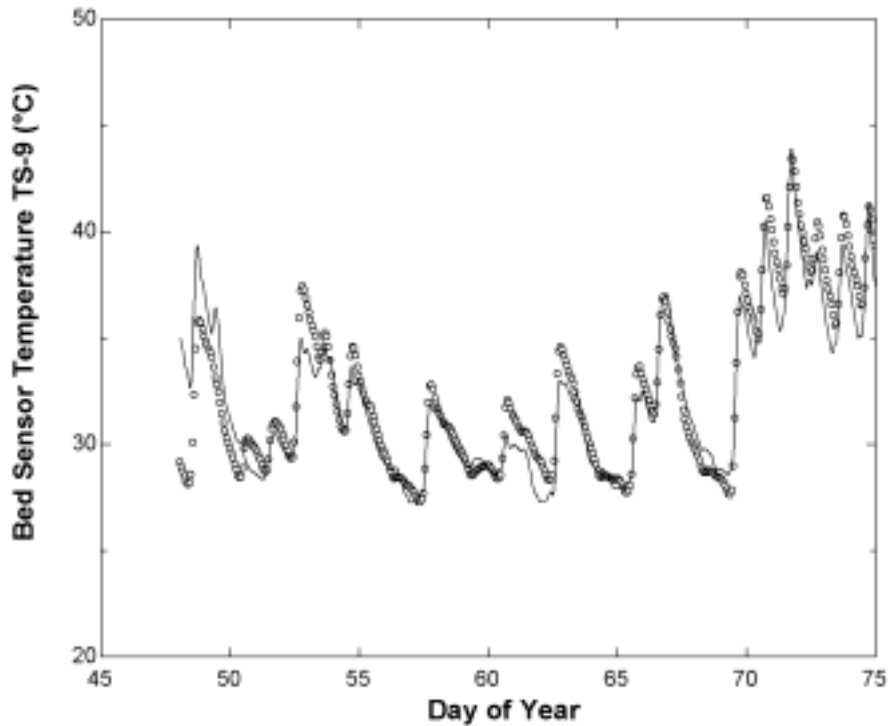


Figure 8.3.3 Measured (points) and modeled (solid line) temperatures for pebble bed sensor TS-9 in office system. Stagnation fraction is 0.75.

8.4 Synopsis

Energy quantities from each mode were calibrated by comparing the measured and modeled results during forced mode operation. Anomalies in the mode energies and the bottom plenums of the pebble beds showed that the motorized damper that separates the solar system from the main air handler was operating improperly. By failing to close during idle periods, this damper allowed airflows of 125 and 250 CFM (as determined through simulations) to flow back through the basement and office pebble beds.

The use of temperature interrupts was discarded from use in the systems calibration interval due to inherent inaccuracies that arose when the simulation used a stagnant duct temperature during forced mode operation. The temperature interrupt on the supply to the solar loop (TS-3) was kept because this measured temperature never stagnates due to the constant operation of the main air handlers. The temperature interrupts were very useful in early stages of model development where the simulation was validated against the solar test interval. During the

solar test interval a continuous mode of operation (mode 3) forced the system into quasi steady-state operation and therefore all the sensors could be trusted to be in equilibrium with the duct airflows. During dynamic mode operation, such as was present during the system calibration interval, the temperature interrupts could not be used.

Calibration of the zone thermal models was performed through a comparison of the energy delivered to the zone relative to that required to maintain the zones at the setpoint temperature. Cumulative energy requirements were satisfied to within 7 percent over the system calibration interval with average daily variations of less than 15 percent in all zones.

A final calibration of the pebble bed sensors required that a plenum stagnation temperature be used during times when the beds were idle with no flow. This stagnation temperature reflected the temperature of the plenum during no flow conditions as calculated by a fixed ratio of the rock mass temperature and that of the room containing the solar equipment. Coupling the sensor to this plenum stagnation temperature during no flow conditions provided a good fit to the measured sensor performance, which was critical in modeling the controls system behavior.

9 Free Mode Calibration

Free mode calibration is not truly a calibration at all (i.e. there are no free parameters left in the model), but instead reflects a final check on the simulated control logic. In prior calculations, the simulation had been forced to operate in the exact modes of the McKay center. If the simulation model is to be run outside the range of measured data however, then it must operate on internal control logic. In free mode calibration, the operation of the solar zones using simulated control logic (represented by the existing control logic discussed in section 7.2.2) was compared to the actual operation of the systems as measured at the McKay center.

During free mode operation, the simulation model was completely decoupled from measured building data and was driven solely by the inputs of ambient temperature and solar radiation. The accuracy of the simulation model and control logic was evaluated by comparing the operation under the forced and free modes of building control.

9.1 *Defining the Proper Operation of Building Modes*

Determining whether or not the simulated control logic is accurate requires that the final free mode simulation behave identically as the McKay center. While a comparison can be made using the run times for the various operating modes (i.e, did the simulation run in mode 1 for the same amount of time as the actual system), the actual energies produced and stored by each individual mode were used as the basis for comparison.

The energy quantities used as the basis of comparison were not parsed to full mode operation at the center, but were calculated for each timestep of the simulation and thus represent the simulated total energy quantities that were calibrated against measured values described in section 8.2. Figures 9.1.1 and 9.1.2 show the simulated total cumulative integrated energy quantities for each mode of operation in the basement and office zones. The goal of free mode calibrations was for the simulated control strategy to produce the same cumulative mode energies of figures 9.1.1 and 9.1.2.

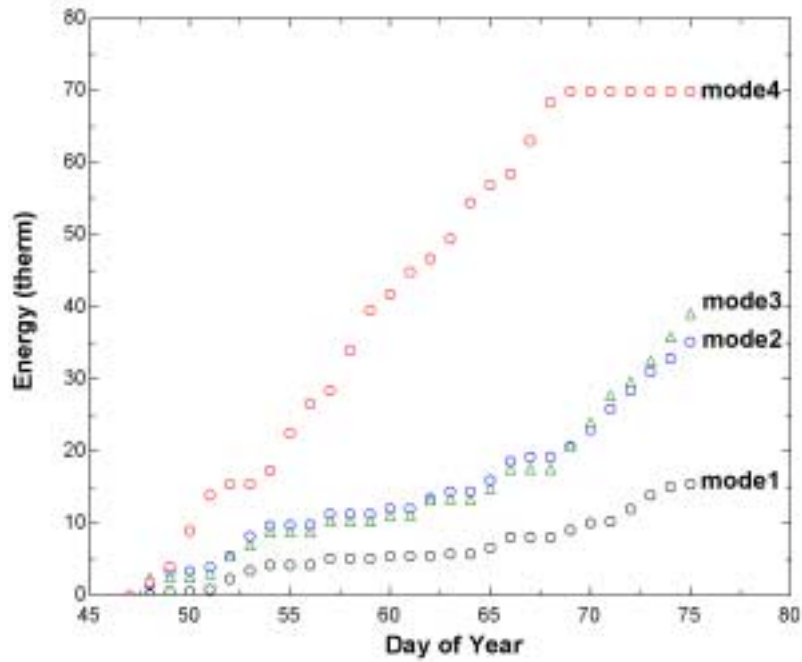


Figure 9.1.1 Cumulative mode energies for basement HVAC system over system calibration interval as calculated through forced mode calibrations.

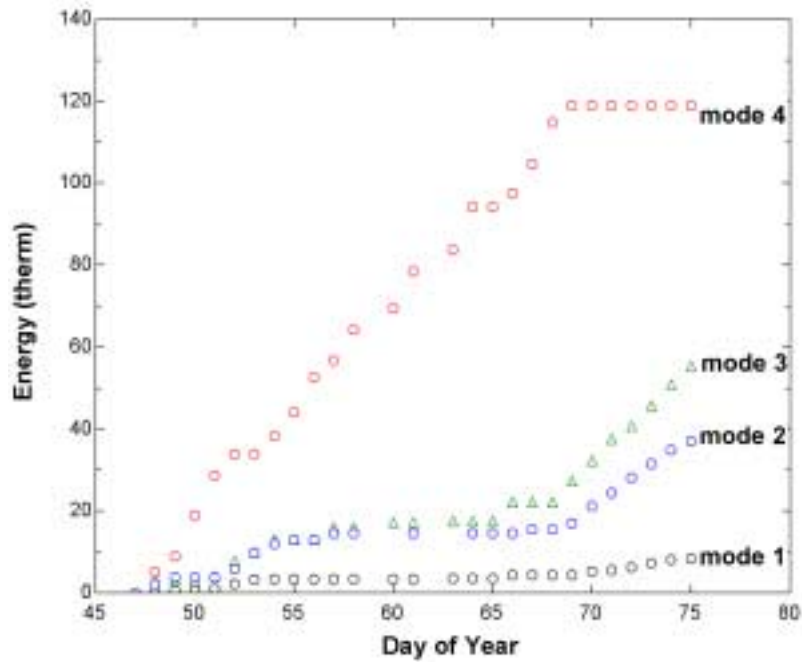


Figure 9.1.2 Cumulative mode energies for office HVAC system over system calibration interval as calculated through forced mode calibrations.

9.2 Performance of Simulated Control Logic

Figure 9.2.1 compares the energy quantities produced in the basement zone by the simulated control strategy to the fixed mode energies of figure 9.1.1. The only forced function in the simulated control logic was that the zone be maintained at setpoint. The simulated energy use closely tracked the measured energy, indicating that the simulated control strategy matched that of the actual building. From days 69 to 75, the simulated control strategy over-predicts the energy supplied by mode 4 of operation. This discrepancy was due to the fact that the energy supplied to the zone (equation 8.2.1) in fixed mode calibrations during this period was insufficient to maintain the setpoint temperature. To maintain the setpoint temperature, the simulated control strategy fired the furnace (mode 4) and thereby deviated from the actual operation.

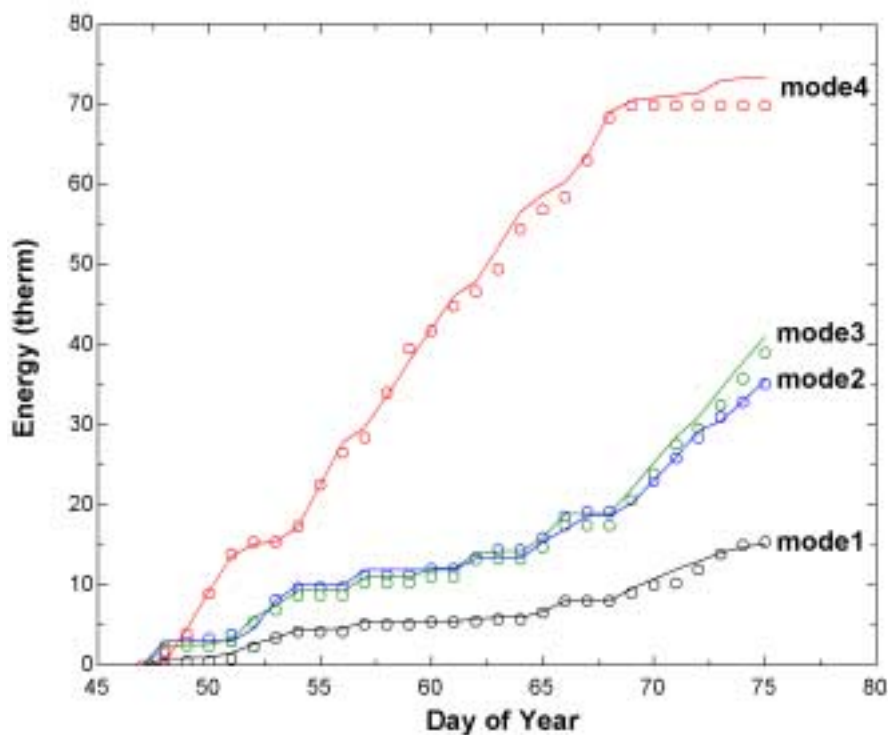


Figure 9.2.1 Comparison of cumulative mode energies for basement HVAC system over system calibration interval. Fixed mode quantities are indicated by points and free mode quantities are shown as solid lines.

The agreement for the office zone as shown in figure 9.2.2 was not as satisfactory as that of the basement. This was in large part due to the higher fluctuations in the building load and also the dynamic response of the pebble bed control sensor (TS-9). The sensor value for the office pebble bed was based on the plenum temperature of the basement bed²⁰. The basement plenum temperature was calculated by the basement model running in free mode and output to a text file. The office simulation then read in the plenum temperature to calculate the office sensor value for each timestep. The control of the pebble bed in the office system was therefore dependent on the control dynamic of the basement loop where any errors in the basement plenum temperature propagated through the office control system. The agreement in performance of the pebble beds as depicted by modes 2 and 3 of operation in figure 9.2.2 shows that the sensor value was properly modeled and the control system behaved appropriately.

²⁰ The office sensor is actually located in the wall of the basement bed as discussed in section 7.12.

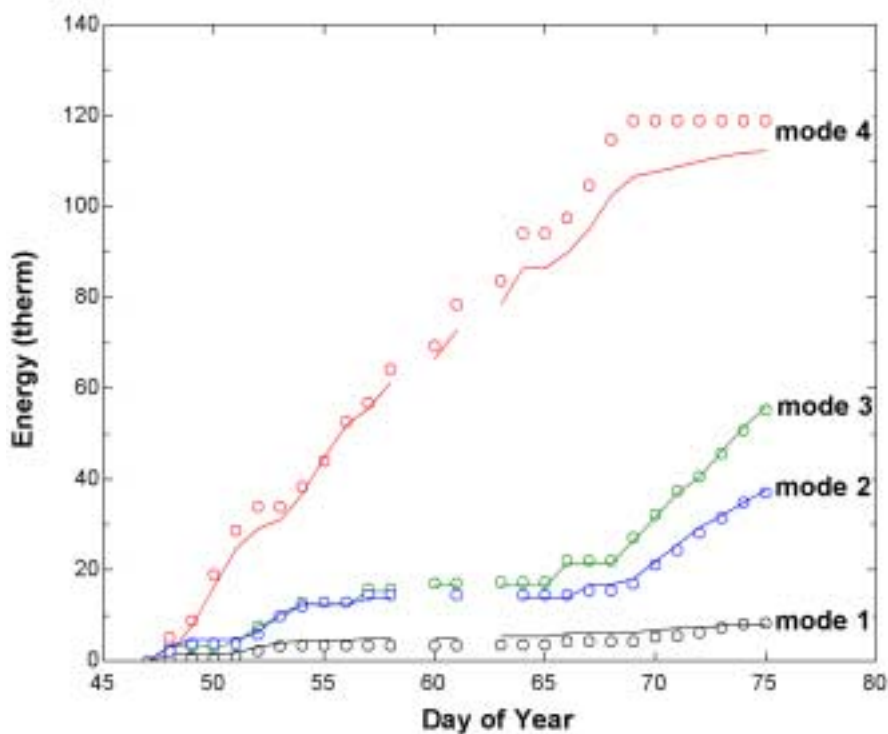


Figure 9.2.2 Comparison of cumulative mode energies for office HVAC system over system calibration interval. Fixed mode quantities are indicated by points and free mode quantities are shown as solid lines. Values from days 59, 62, and 65 have been removed from the data set²¹.

To provide the reader with a sense of how the zone thermal model (i.e. the load for the HVAC system) affects system performance, a simulation was run where the capacitance of the walls and interior were switched for the basement zone. Figure 9.2.3 shows a comparison of energies when the walls were specified as having the air mass capacitance and the air mass was given the massive thermal capacitance of the walls. By switching these capacitance values, the air mass had a much slower thermal response and zone behaved as though it were a lumped capacitance building.

The energy from the operating modes was quite different from the actual system when the load (i.e. the air mass) had a slower thermal response. The massive capacitance of the zone air allowed for much higher direct contributions from the solar array (mode 1) than were seen in

²¹ Because any uncertainty in the energy stored in the pebble beds on these days will be present in the energy discharged on the following day, energies from mode 2 of operation for days 60, 63, and 66 have also been removed from the record.

the actual system. Contributions from mode 1 in the actual system were limited by the low coincidence of heating calls and solar availability, which was primarily due to the structure of the internal gairns that we concentrated within the 9:00 to 5:00 workday. The large capacitance modeled in figure 9.2.3 also required large energy inputs to bring the thermal mass up to setpoint in the morning, which may explain the high auxiliary requirements if the pebble beds did not have sufficient energy.

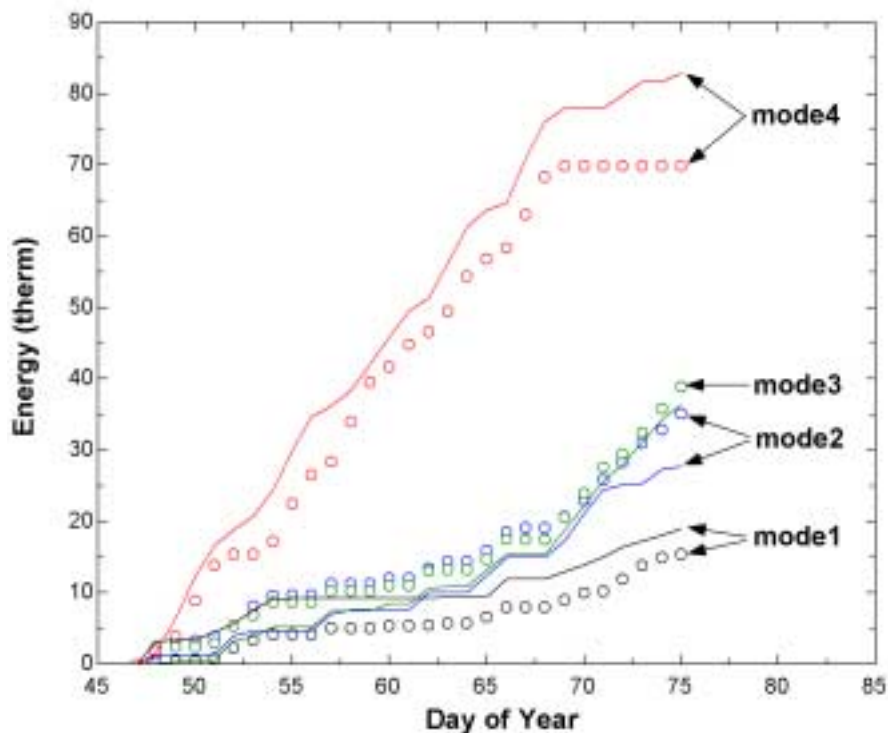


Figure 9.2.3 Comparison of cumulative mode energies for basement HVAC system over system calibration interval with the thermal capacitance of the wall and air mass switched. Fixed mode quantities are indicated by points and free mode quantities are shown as solid lines.

A minor adjustment was made to the office zone model to obtain the fit shown in figure 9.2.2. The ratio of surface area for the interior capacitance to that of the floor was increased from 4 to 8 to better match the operating mode performance. With the smaller surface ratio, the control system shifted the operating dynamic of the solar system such that mode 1 was over-predicted by 1.5 therms at the expense of similar reduction in mode 2 over the course of the system calibration interval. The higher area ratio used in the final simulations was justified by the large number of interior partitions that separate the individual offices in the office zone.

No results are provided for the lecture hall in this section as they would be identical to figure 8.2.8 of the forced mode calibrations. Because the lecture hall has a single heat source there was no complex control dynamic as in the basement and office systems, and the furnace energy (mode 4) for the lecture hall simply matches the required energy $Q_{required}$ in figure 8.2.8.

9.3 Synopsis

The results shown in figures 9.2.1 and 9.2.2 represent an optimization of over 40 parameters (describing individual system components) fit to 232 data points (the 29 integrated daily energies for each mode in each system). The argument is often made that any data set can be fit provided 40 free parameters are available. However, the simulation model used in this study was physically constrained and the 40 parameters were not completely free.

On the component level, model calibrations typically fit 2 and no more than 3 free parameters at any one time. In the case of the collectors, $F_r U_L$ was fit to night-time data independently of $F_r(\tau\alpha)$, which was fit to noon-time data. In a similar manner, the box loss coefficient was fit separately from the flow distributions, which were again 2 parameter optimizations. These component level calibrations formed the first rung in the series steps used to calibrate the simulation model as outlined in figure 9.3.1.

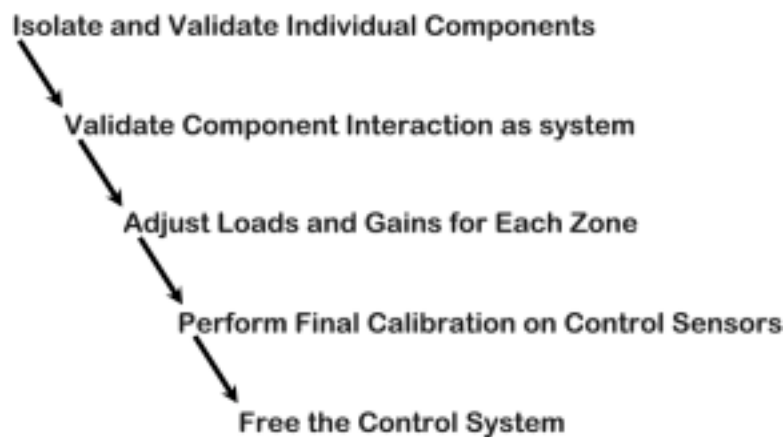


Figure 9.3.1 Flowchart of model calibration process.

After the individual components had been calibrated, they were incorporated into a system model, and calibrated again as a dynamic interconnected system during fixed mode calibrations. It was at this point that the malfunction in MD-1 was discovered and a “backflow” rate was

included in the model. After the behavior of the HVAC system was validated, the thermal response of the building zones was checked to ensure that the energy requirements were met. At this point the internal gains were assigned to each zone to best meet the energy demands. Infiltration rates as expressed in air changes per hour (ACH) were lowered from original estimates of 0.3 ACH for the basement and lecture hall to the currently used values of 0.1 ACH, representative of tighter construction. The zone models were calibrated using the two parameters of percentage of total internal gains assigned to each zone and the air changes, which were limited to values between 0.1 and 0.5 ACH. As a final step in the forced mode calibrations, the pebble bed sensors were modeled using a parameter that described the stagnation temperature of the upper plenum in the pebble beds. The final validation of the simulation was to drive the model using ambient temperature and solar radiation and evaluate how the simulated energy use compared to the actual energy use at the McKay Center.

A key aspect of calibrating the model in the manner described above is that parameters calibrated at any one level in figure 9.3.1 remained fixed and were never modified in subsequent levels of calibration. As an example, the box loss coefficient was fixed at the first level of calibration and was never used as a fitting parameter to yield better results during the forced mode calibrations. In this sense, calibration of the simulation model was not a 40 parameter optimization, but instead a series of several individual optimizations containing only 2 or 3 free parameters. By training the simulation at each level of the calibration process, and slowly releasing the free parameters, any inconsistencies in the model were isolated and accounted for.

10 Annual Simulation Results

With the model fully calibrated, actual weather data at the site was replaced with TMY2 data to simulate annual operating performance under typical meteorological conditions. Simulations for each building zone were run from January 1 to December 31 to calculate annual performance, and the results from each zone were accumulated by the simulation summary interface to provide final integrated energy quantities, costs, and CO₂ emissions. A range of simulations were performed to assess the impact of various factors such as, backflow, box losses, collector degradations, and bed flow profiles. By comparing the results of these various simulations, the effects of particular degradations on total system performance were quantified.

10.1 Definition of Key Performance Metrics

The performance of solar thermal systems is usually indicated by the solar fraction, which is simply the fraction of the load supplied by the solar component. However, the solar fraction only reveals a portion of the total performance because it is solely based on thermal energies and neglects any external inputs, such as the parasitic loads of the solar air handlers. Ultimately, there are two quantities of interest with regards to solar system performance. The first is the amount of money it saves, and the second is the amount of emissions (CO₂) it can prevent. By quantifying these terms, the overall performance of the solar installation can be reduced to a handful of key metrics.

10.1.1 Solar Fraction (SF)

The solar fraction is the best known indicator of system performance in the field. Throughout the literature, systems are rated by their solar fraction just as automobiles are rated by their gas mileage. By defining the fraction of the total load served by solar energy, the solar fraction provides a clear insight into the thermal performance of the system. For the purposes of this study the solar fraction was defined as

$$SF = 1 - \frac{Q_4}{Q_{HVAC}} \quad [10.1.1]$$

Where Q_4 and Q_{HVAC} represent the annual integrated energies produced by the furnace and supplied by the entire HVAC system. There is an important distinction in basing the solar fraction on the energy produced by the furnace and not the energy supplied by the furnace. If any losses are present in the system, such as the backflow leakage through MD-1 then the two quantities will differ and it is important to reflect the losses by basing the solar fraction on the thermal energy that is consumed and thereby produced by the furnace. In the existing system where backflow is present, it is possible to have a negative solar fraction on cloudy days when there is no solar contribution to the load²². Q_{HVAC} also includes the effects of losses characterized by the infiltration leak in the solar air handler and is based not on the energy produced from the collector array or pebble bed, but only on the fraction of the energy that makes it to the zone.

10.1.2 Cost Reduction Factor (CRF)

In solar systems that rely on external inputs, such as the electricity requirements of the fans in the solar air handlers, the solar fraction alone is unable to fully quantify performance. This occurs because optimal performance under the criteria of the solar fraction would require running the solar air handler any time there is thermal energy available. Although this may be the most efficient mode of operation from the viewpoint of energy content, it is often not the most economical or thermally efficient. At some level it is simply not worth extracting the available energy. Behavior of the system in economic terms can be quantified through the cost reduction factor (CRF), which calculates the fraction of total heating costs saved by the solar system.

$$CRF = 1 - \frac{Cst_{solar}}{Cst_{conventional}} \quad [10.1.2]$$

Where Cst_{solar} is the annual cost of running the solar air handler and furnace, and includes the electricity cost of the solar fans and the natural gas consumption of the furnaces. $Cst_{conventional}$ represents the annual cost of natural gas to service an identical load with the same furnaces, but

²² On these days a fraction of the energy produced by the furnace is lost to the solar system, and the furnace must therefore produce more energy than what is supplied to the load, thereby yielding a negative solar fraction.

no solar equipment²³. The cost of electricity and natural gas were assumed to be local residential rates of \$0.07 per kWh and \$0.70 per therm. To estimate gas consumption, furnace efficiencies were estimated at 0.85 for the office furnace, which is a newer condensing unit and 0.70 for the basement and lecture hall furnaces, which are the original non-condensing units installed with the building in 1976. Assessment of $Cst_{conventional}$ was made by disabling operation of the solar system in the simulation deck and running annual simulations for all zones. The total cost of running a conventional system at the McKay center was \$1,861 and therefore each 1 percent increase in the CRF represents an annual savings of \$18.61.

10.1.3 Emissions Reduction Factor (ERF)

Aside from the annual operating costs savings expressed through the CRF, users of solar systems are also typically concerned about the emissions that that are prevented by operation of the system. The principal motivation for many installations is environmental and not purely economic. As such, it is of interest to derive a metric that describes the relative emissions reduction provided by the solar installation over one of conventional design. This metric will be referred to as the emissions reduction factor (ERF) for CO₂ and is expressed as

$$ERF = 1 - \frac{E_{solar}}{E_{conventional}} \quad [10.1.3]$$

Where E_{solar} represents the CO₂ emissions produced by running the solar and furnace systems, and includes the emissions due to both electricity generation and combustion of natural gas in the furnaces. $E_{conventional}$ represents the natural gas emissions to service an identical load with the same furnaces, but no solar equipment²⁴. The emissions from natural gas are 5.3 kg CO₂ per therm, and emissions from electricity consumption are 0.65 kg CO₂ per kWh²⁵. Assessment

²³ The cost of running the main air handlers has been left out of both cost evaluations because operation of the main air handlers is driven by circulation air requirements, which would exist even in the absence of heating demands.

²⁴ The emissions produced by running the main air handlers has been excluded because operation of the main air handlers is driven by circulation air requirements, which would exist even in the absence of heating demands.

²⁵ This emissions factor is based on an average heat rate of 9,600 BTU/kWh for the Wisconsin coal plant fleet, which produces 75 percent of power production in the state (nuclear and hydro have no carbon emissions)

of $C_{conventional}$ was made by disabling operation of the solar system in the simulation deck and running annual simulations for all zones. The total emissions produced from running a conventional system at the McKay center was 14,061 kg CO₂, and therefore each 1 percent increase in the ERF represents an annual emissions reduction of 140.6 kg CO₂.

10.1.4 Coefficient of Performance (COP)

If the solar system is viewed as a heat pump then the annual average COP can be defined by

$$COP = \frac{\hat{Q}_1 + \hat{Q}_2}{Q_{SAHU}} \quad [10.1.4]$$

Where \hat{Q}_1 and \hat{Q}_2 represent the annual energies supplied to the zone from modes 1 and 2 of operation. Again, these energy terms (\hat{Q}_1 and \hat{Q}_2) reflect any losses in the system and may therefore be lower than the actual energy produced from the collector array (Q_1) or pebble bed (Q_2). Q_{SAHU} is the total electric energy consumption of the solar air handling units in all modes of operation (including mode 3). The COP provides an indication of the average thermal performance in terms of the tradeoff between electric inputs and thermal output. The COP can also be useful in comparing thermal performance of the solar array to other energy sources, such as geothermal heat pumps.

10.2 Description of Simulated Configurations

Eight different configurations of the solar system at the McKay center were simulated to assess annual performance under TMY2 conditions. These configurations span the spectrum from the system as it was found at the outset of this study to how it would have performed with optimal controls and the original component performance parameters. Each case represents a marginal improvement over the previous one, and therefore the effect of the improvement can be assessed through a comparison of the performance metrics between the two cases.

Case 1: existing control

Case 1 represents how the system operated when this study was first initiated. It is characterized by the existing control logic, current component parameters, backflow of main air handler flow through MD-1, and infiltration leaks into the solar air handlers.

Case 2: existing control, no backflow

Case 2 is identical to case 1 except that operation of MD-1 has been corrected such that there is no backflow through the pebble beds. This case represents how the system currently performs as of May 2000.

Case 3: existing control, no backflow, no SAHU leaks

Case 3 is a further improvement of case 2 in that the leaks in the solar air handling units (SAHU's) have also been eliminated in addition to the backflow.

Case 4: optimal control, no leaks

Case 4 is physically identical to case 3 where no leaks from either MD-1 or infiltration into the solar air handlers are present. However, the existing control strategy has been replaced with optimal storage control (see section 7.2.3).

Case 5: optimal control, no leaks, uniform flow

Case 5 tests the effects of non-uniform flow through the pebble beds by modeling their performance with uniform flow. The results from this case can then be compared with those of case 4 to estimate the marginal benefit of uniform flow

Case 6: optimal control, no leaks, uniform flow, original box insulation

Case 6 represents the beginning of large physical changes to the system aimed at bringing it back to the original performance characteristics. This case represents an improvement over case 5 in that the level of insulation within the pebble beds has been brought back to the design specifications of $1.54 \text{ m}^2\text{-C/W}$ for the 2" of polystyrene on the box interior specified by the original construction drawings.

Case 7: optimal control, no leaks, uniform flow, original box insulation, original collectors

Case 7 is the final improvement required to bring the system back to the original as installed condition. For this case, the collector performance parameters have been reset to their original values summarized in table 4.6.3.

Case 8: optimal control, no leaks, uniform flow, original box insulation, original collectors, doubled bed length

Case 8 models the original components with pebble beds having twice the depth of the existing systems. Because the thermal waves were seen to break through the beds on most days of charging (as indicated by measured data), this case assesses the impact of providing more thermal storage in order to lower the collector supply temperature during mode 3 of operation.

10.3 Results of Annual Simulations

Figures 10.3.1, 10.3.2, and 10.3.3 show the running sums of thermal energy quantities, costs, and emissions from the various components for case 2, which represents the current state of the system. Although these figures show only a single case, the distribution of emissions and costs are fairly representative of most cases and show the influence of the main air handlers²⁶. Annual integrated energy quantities and performance metrics for each case simulated under TMY conditions are presented in table 10.3.1.

²⁶ Although the effects of the main air handlers in terms of cost and emissions are not reflected in any performance metric, it is helpful to understand the scale in which they contribute.

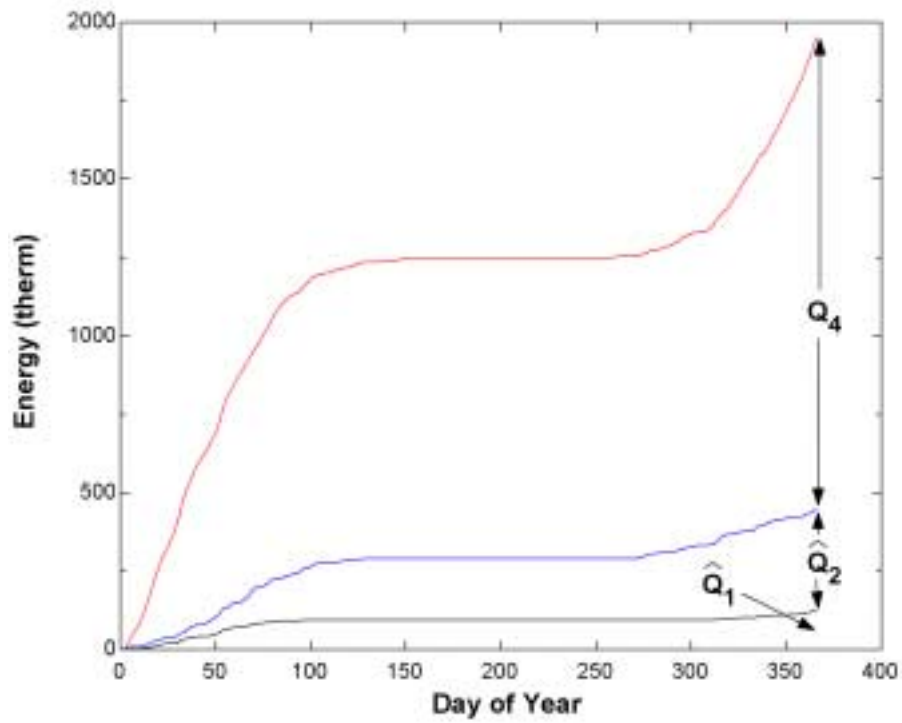


Figure 10.3.1 Integrated energy quantities supplied to load for case 2.

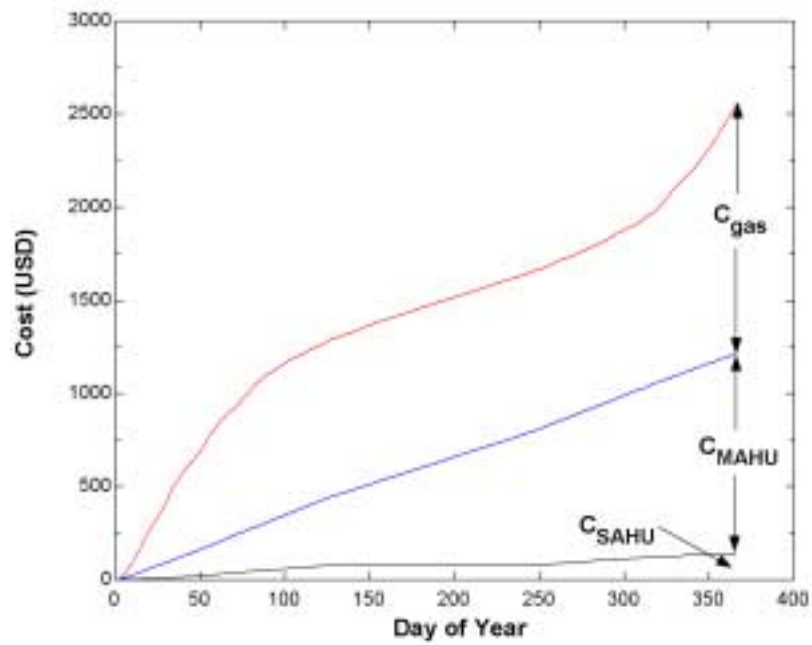


Figure 10.3.2 Integrated operating costs for case 2.

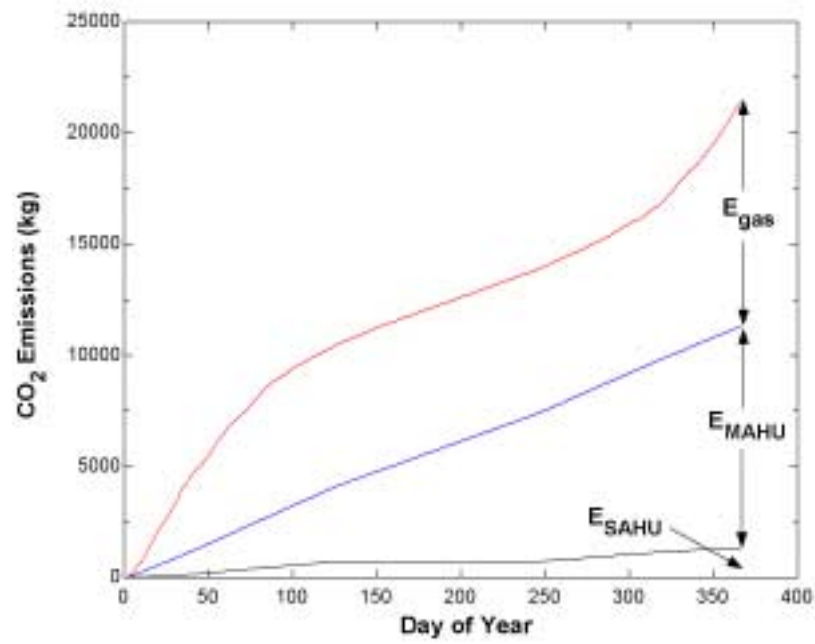


Figure 10.3.3 Integrated CO₂ emissions for case 2.

Table 10.3.1 Annual simulation results for cases under study.

Configuration	\hat{Q}_1	\hat{Q}_2	Q_3	Q_4	SF	COP	ERF	CRF
Case 1: existing control	135	289	620	1686	0.15	6.0	0.10	0.12
Case 2: existing control, no backflow	128	319	567	1507	0.23	6.4	0.18	0.20
Case 3: existing control, no backflow, no SAHU leaks	136	347	599	1509	0.24	6.9	0.18	0.20
Case 4: optimal control, no leaks	178	469	617	1374	0.32	8.7	0.24	0.26
Case 5: optimal control, no leaks, uniform flow	179	466	627	1370	0.32	8.7	0.24	0.26
Case 6: optimal control, no leaks, uniform flow, original bed insulation	162	520	576	1366	0.33	10.0	0.25	0.27
Case 7: optimal control, no leaks, uniform flow, original bed insulation, original collectors	227	684	800	1118	0.45	11.7	0.36	0.38
Case 8: optimal control, no leaks, uniform flow, original bed insulation, original collectors, doubled bed length	233	689	876	1073	0.46	10.8	0.37	0.39

The performance of the solar system for case 1 was extremely poor with a solar fraction of 15 percent and correspondingly low values for the CRF and ERF. Correcting damper operation to eliminate the backflow in case 2 had a dramatic effect on performance as it both lowered the furnace requirements (less furnace energy is lost to the solar system) and raised energy recovery from the pebble beds (the beds are not discharged by the backflow). When the infiltration leaks in the solar air handlers were eliminated in case 3, the energy that was contained in the exhaust stream appeared in the solar energy operating modes and was thereby included in the solar fraction, raising it to 24 percent. Both the ERF and CRF remained identical between cases 2 and 3 because on a systems level it made no difference whether the energy entered the zone through an exhaust stream or the supply duct¹.

Replacing the existing control logic with optimal bed control, as was done for case 4, raised the solar fraction by 8 percentage points and increased both the ERF and CRF by 6 percentage points. These gains were not attributable to any physical change in the system, but were due entirely to how it was operated. Figure 10.3.4 represents a operating histogram of the collector array for both cases and provides the key insight into how these gains were achieved. The bins (x axis) into which collector operating hours are sorted represent the operating points that can be found on the x axis of standard SRCC plots (see figure 4.3.3). Based on the measured array parameters of table 4.4.1, operating points beyond values of $0.12 \text{ m}^2\text{-C/W}$ will result in negative collector efficiencies for both the basement and office arrays. It is surprising then that the existing control logic of case 3 operated the collectors at negative efficiency for 98 hours annually for the office array and 161 hours for the basement array. Together, these durations at negative efficiency represented 15 percent of the total operating time for the collector arrays. This erroneous control behavior results from failing to monitor the collector inlet temperature TS-4, and basing the differential controller on the bed sensor instead, which itself provided an erroneous temperature. The result of such poor control layout was to have the collector operated in the manner presented in figure 10.3.4, and to loose several percentage points on the system performance characteristics. By contrast, the optimal control logic never operated below the zero efficiency point because it was based on a COP that would not enable the array if the thermal payback was negative.

¹ In reality the exhaust stream may effect system performance in that the uncontrolled release of energy may overheat the zone in early spring and late fall. The infiltration-exhaust leak in the basement solar air handler is relatively small at 100 CFM however, and it is likely that the effect if any is minimal.

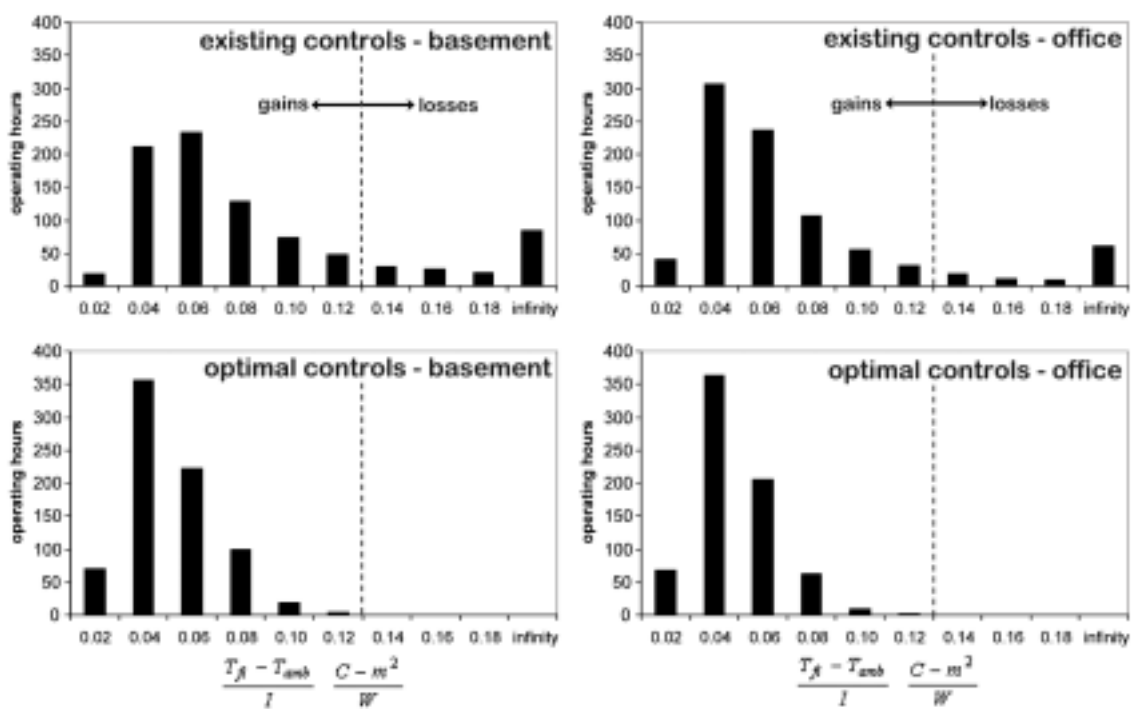


Figure 10.3.4 Annual operating histograms for collector arrays under existing controls (case 3) and optimal controls (case 4). The bins on the x-axis define the collector operating point, and the dashed line indicates the operating point for zero collector efficiency.

Case 5 is interesting in that it shows no benefit in restoring the beds to uniform flow when the system was driven by optimal control. Evidently the effect of early breakthrough of the thermal wave was moderated by lower afternoon temperatures (due to the mixing of the various thermal waves), which fed the collector array with a lower inlet temperature thereby operating it at higher efficiency. Not only were the thermal energies nearly identical between the uniform and non-uniform flow cases, but the COP, CRF, and ERF all indicate that no additional fan power was required to either store or recover energy from the bed under conditions of non-uniform flow. These results are quite surprising as one might imagine that the uneven charge and discharge flow ratios (see table 5.14.1) would cause some loss in availability of the stored energy. If there was any such loss, the effects were limited to less than 1 percent with regards to systems level performance metrics. Moreover, establishing uniform flow requires creating a pressure drop through the bed that is sufficiently higher than that encountered in the plenums (Hollands 1984). This pressure drop will increase the parasitic power consumption of the solar air handler and may result in a decrease in the cost and emissions performance of the system.

Restoring the level of insulation within the bed, as was done in case 6, resulted in a marginal improvement of one percentage point in system performance metrics. Part of the reason for such a modest improvement was because the losses from the basement pebble bed were assumed to be coupled directly into the basement zone within the simulation. However, losses from the office pebble bed, which were true losses to the environment should have been significant in case 5 given the large conductance of $7.5 \text{ W/m}^2\text{-C}$. Lowering this conductance eleven fold to $0.65 \text{ W/m}^2\text{-C}$ for case 6 resulted in only modest performance gains. The small performance gains for increased bed insulation can be explained by a corresponding decrease in the performance of the collector array. By increasing the bed insulation, the average collector inlet temperature (i.e. the box outlet temperature) was increased thereby moving the collector operating point to a lower efficiency. This effect can be seen by comparing the energy stored within the box (Q_3) for cases 5 and 6, which shows a decrease in the stored energy of 51 therms when the original insulation levels are reinstated. This decrease in Q_3 is exactly equal to the decreased output of the collector array caused by operating it at higher inlet temperatures. It is this decrease in collector output that moderates what we would think should be a greater benefit of insulating the pebble beds.

The final restoration of the system for bringing it back to the as installed condition was performed in case 7 where the collector have the original performance parameters. Restoring the arrays yielded significant benefits by raising the solar fraction by 12 percentage points and correspondingly increasing both the ERF and CRF by 11 percentage points. These benefits were due to the increased output of the collector array that directly serviced the load (\hat{Q}_1) and was stored in the pebble beds (Q_3).

The final case examined in this study was to determine if the pebble beds were properly sized. Doubling the bed depths for case 8 yielded only single percentage point increases in the performance metrics, thus indicating that the increased cost and space requirements of doubling the bed volumes was not economical. This was at first a surprising result because actual measurements from the system consistently showed that the thermal wave broke though the bed before noon resulting in elevated collector inlet temperatures. It was believed that increasing the bed depth would alleviate this issue and increase the collector output. The simulation results reveal that this was not the case when the system was run with optimal controls. A comparison of the bed charge and discharge energies (Q_3 and \hat{Q}_2) between cases 3 and 4 explain the unexpected result. Although these two cases are physically identical, and charge the beds with roughly

equivalent energy (599 vs. 617 therms), the energy discharged under optimal control is 35 percent higher than with the existing control logic. Due to the poor sensor location in the existing control loop, 122 therms were left in the bed that could have been economically extracted. A negative consequence of leaving remnant energy in the bed is that consequent charging of the bed on the following day will result in a premature breakthrough of the thermal wave (the bed was already partially charged). By fully discharging the bed to satisfy the night-time and early morning heating calls, the optimal control strategy was able to leave the bed with a minimal charge and thereby provided the maximum possible capacity for charging during the following day. Case 8 illustrates that the beds need be no larger than they currently are, they simply must be operated with an optimal control strategy.

10.4 Synopsis

Annual simulations of calibrated systems models showed that the existing system, as it was found when this study initiated, had very poor operating characteristics with a solar fraction of 15 percent. Correcting the operation of the dampers and eliminating leaks in the solar handlers raised the solar fraction to 24 percent. Optimal control of the existing system could further raise the solar contribution to 32 percent, which surpasses the original design specifications of 30 percent targeted by the systems designers in 1977.

Degradations of the collector arrays translated into large systems losses resulting in a drop of 12 percentage points in the solar fraction.

The non-uniform flow through the bed had no measurable effect on system performance when compared to uniform flow conditions. Moreover, reinstating the original bed insulation, which has a thermal resistance 11 times the current measured value, showed only a 1 percent performance gain. Doubling the bed depth also yielded only marginal improvements of 1 percentage point indicating that the beds are properly sized for the system when used in conjunction with optimal controls.

In summary, the two largest factors that have effected system performance at the McKay center over the 20 years since the system was installed have been the controls strategy at a 16 percent drop in the solar fraction², and the collector arrays causing an additional 12 percent drop

² The effects of backflow have been included in this estimate as they truly represented an error in the existing control scheme.

in the solar fraction. In contrast, the effects of non uniform flow and decreased insulation levels within the pebble beds decreased the solar fraction by only 1 percentage point.

11 Sensitivity of the Simulation to Load Dynamics

When the TRNSYS simulation model was first developed for the McKay center it did not include the effects of the sol-air temperature or the scheduling of internal gains. These refinements were later added to resolve disparities between the simulation and physical system during the forced and free mode calibrations. In many instances model developers do not have measured data to calibrate simulations against, and refinements that have been included in the final model of the McKay center are often omitted. This section assesses the impact on annual system performance caused by omitting these refinements. The effect of the simulation timestep on the solution is also explored.

11.1 Scheduling of Internal Gains

The original simulation model assumed that the internal gains within each zone were spread uniformly over the entire day. While the assumption of uniform gains did not affect the daily energy requirements during forced mode calibrations, it did affect the times at which energy was required.

When internal gains were concentrated within the 9:00 to 5:00 occupancy hours of the building, energy demands from the HVAC system during this period were reduced and shifted to the early morning and night when the internal gains returned to lower levels³. This effect can be seen in figure 11.1.1 and table 11.1.1 where the calibrated model (described by case 7) controlled the HVAC system quite differently than a model that assumed uniform gains. Although both systems delivered nearly the same solar contribution (the sum of modes 1 and 2), the concentrated internal gains of the calibrated model lowered the coincidence of solar availability and heating calls, and the controller responded by storing the available solar energy in the pebble beds so that it could be delivered later through mode 2 of operation. Although the behavior of operating modes changed with the structure of the internal gains, table 11.1.1 shows that the performance metrics remained the same to within 1 percent.

³ Internal gains at the McKay center were structured such that 80 percent of the daily gains occurred during the 9:00 to 5:00 occupancy of the building. The remaining 20 percent were spread over the remaining hours of the day.

Table 11.1.1 Comparison of performance metrics for case 7, and case 7 with uniform gains. All energies are in therms,

Configuration	\hat{Q}_1	\hat{Q}_2	Q_3	Q_4	SF	COP	ERF	CRF
Case 7	227	684	800	1118	0.45	11.7	0.36	0.38
Case 7, uniform gains	272	629	750	1117	0.45	11.9	0.36	0.38

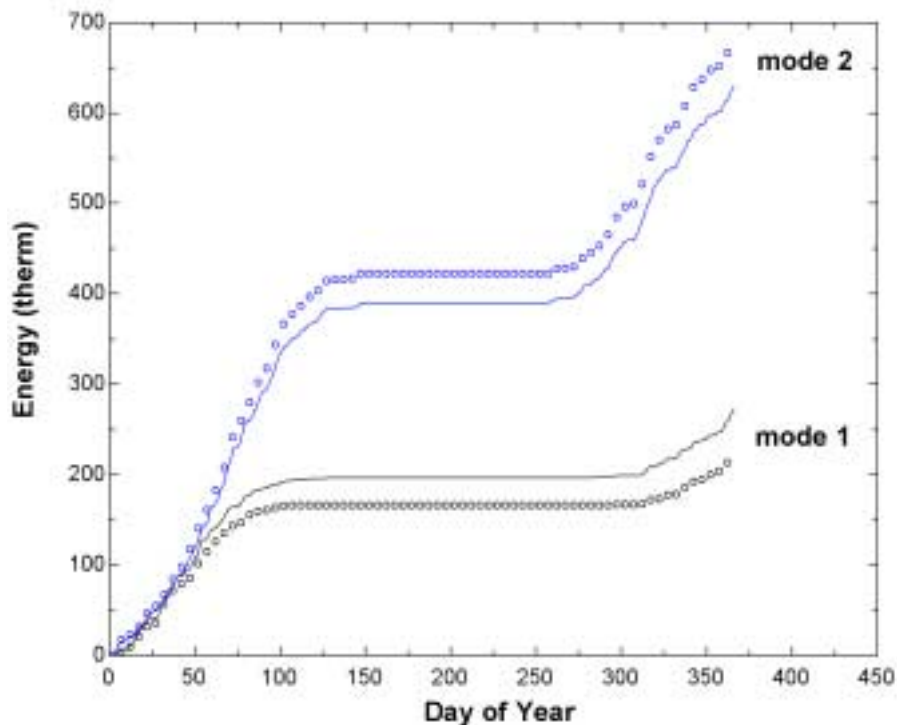


Figure 11.1.1 Comparison of annual solar operating energies for case 7 of calibrated model (points) and identical system with uniform internal gains.

11.2 Effects of the Sol-Air Temperature

The sol-air temperature has an effect similar to that of scheduling the internal gains. By lowering the loss of the building shell on sunny days, the sol-air temperature reduces the coincidence of solar availability and heating calls. Figure 11.2.1 illustrates the further shift in mode operation when the sol-air temperature is omitted along with the assumption of uniform internal gains. In addition to shifting operating mode energies, omission of the sol-air temperature also results in an over-prediction of losses from the building shell. The additional

losses result in increased auxiliary demands indicated in table 11.2.1. The increased losses also increase the COP of the solar system by utilizing a larger fraction of the energy stored in the pebble beds, which raises the contribution of mode 2. This increase in energy from mode 2 helps to offset the increased auxiliary energy, thereby keeping the solar fraction close to that of the calibrated model in case 7. The ERF and CRF are both highly affected by the increased load caused by omission of the sol-air temperature and drop 10 percentage points each. Because they are based solely on the amount of energy purchased relative to the calibrated base case (see section 10.1), the ERF and CRF are more accurate reflections of the performance loss caused by omitting the sol-air temperature.

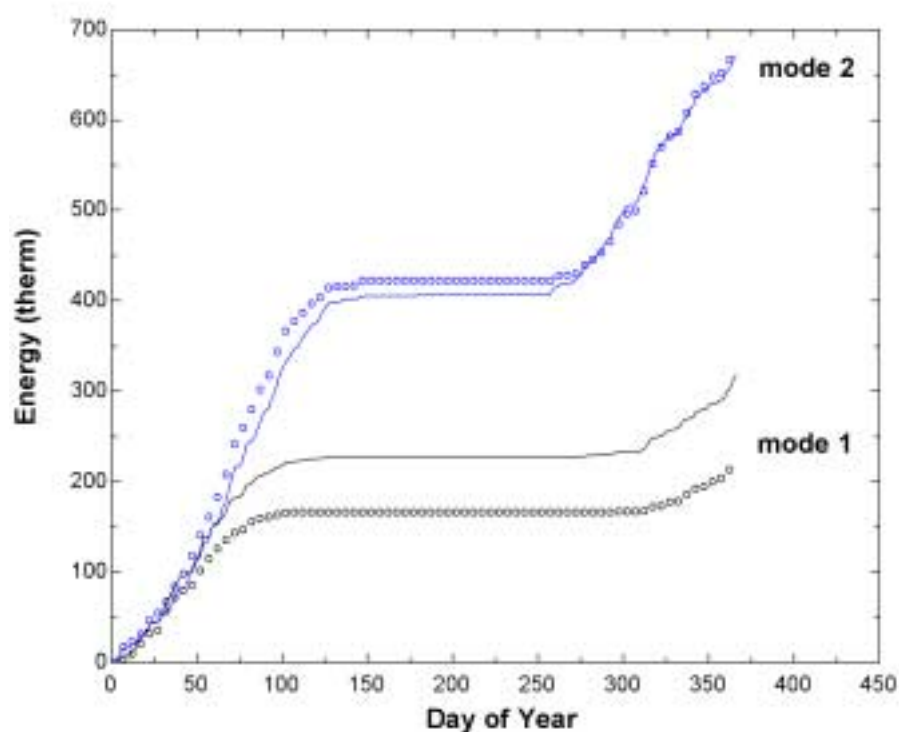


Figure 11.2.1 Comparison of annual solar operating energies for case 7 of calibrated model (points) and identical system with uniform internal gains and omission of the sol-air temperature.

Table 11.2.1 Comparison of performance metrics for case 7, and case 7 with uniform gains and omission of the sol-air temperature. All energies are in therms.

Configuration	\hat{Q}_1	\hat{Q}_2	Q_3	Q_4	SF	COP	ERF	CRF
Case 7	227	684	800	1118	0.45	11.7	0.36	0.38
Case 7, uniform gains, no sol-air temperature	318	670	767	1325	0.43	12.4	0.26	0.28

11.3 Effects of the Simulation Timestep

All TRNSYS simulations performed in this study utilized a 15 minute timestep. This timestep was selected because it matched the data recording interval at the McKay center, and because it was thought to be sufficiently short to capture the dynamic behavior of the zone and control loops at the McKay center (which it did as illustrated by the free mode calibration of section 9). The choice of an appropriate simulation timestep often differs among the modeling community. Many simulations performed at the Solar Energy Laboratory employ 1 hour timesteps for annual simulations. By contrast, a recent discussion with a European modeler revealed that they typically use 90 second timesteps in modeling solar combi-systems (Menzi 2000).

For any given system and set of forcing conditions (i.e. loads, controllers, and weather) there exists a particular timestep past which the simulation is unable to properly model the dynamic behavior of the system. This critical timestep can be determined by making successive simulations and increasing the timestep on each run. The timestep before which the simulation results begin to depart represents the critical timestep, and all simulations should be modeled using timesteps equal to or less than this critical value.

The simulation model described by case 7 was run at timesteps of one-half hour and one hour to determine the effects of using increased timesteps, and to determine if the critical timestep occurred within this range. Figure 11.3.1 and table 11.3.1 show the results of case 7 run at 15, 30, and 60 minute timesteps. The simulation behaved similarly under all values of the timestep, but small departures were evident in the individual mode energies. Auxiliary energy requirements increased approximately 1 percent for each successive doubling of the timestep. This increase in the auxiliary requirements resulted in corresponding decreases in key performance metrics (table 11.2.1).

The increase in auxiliary requirements with larger timesteps is thought to be due to the increase in capacitance of the zone air mass dictated by equation 6.1.1. This equation adjusts the capacitance of the zone air mass such that the temperature rise in the zone will not exceed 2 dead-band temperature differences in a single timestep when the furnace is in operation. This adjustable capacitance was required for numerical stability within the model, and results in a larger zone air mass capacitance for larger timesteps. This increase in capacitance changes the load response and may require more auxiliary energy to bring the zone through the controller deadband if the solar contribution is insufficient⁴.

Table 11.3.1 Comparison of performance metrics for case 7, and case 7 with uniform gains and no sol-air temperature. All energies are in therms.

Configuration	\hat{Q}_1	\hat{Q}_2	Q_3	Q_4	SF	COP	ERF	CRF
Case 7, 15 minute	227	684	800	1118	0.45	11.7	0.36	0.38
Case 7, 30 minute	215	690	806	1130	0.44	11.4	0.35	0.37
Case 7, 60 minute	238	678	788	1146	0.44	11.1	0.34	0.36

⁴ To understand the effect of capacitance and simulation timestep on control behavior, imagine an instance where the solar system has just enough energy to bring the zone air mass through the heating deadband for a single 15 minute interval. If the simulation timestep is set at 15 minutes, the controller will enable operation of the appropriate solar mode to satisfy the temperature setpoint of the zone. Now imagine an identical instance, but with a simulation timestep of 60 minutes. The controller may still decide to enable the solar modes, but the energy within the solar system will be insufficient to meet the setpoint criteria over the 60 minute duration, and the controller will be forced to fire the furnace during this timestep instead. Longer timesteps may therefore cause a loss in solar availability because the output of the solar system may not be able to meet the larger energy demands created by longer timesteps.

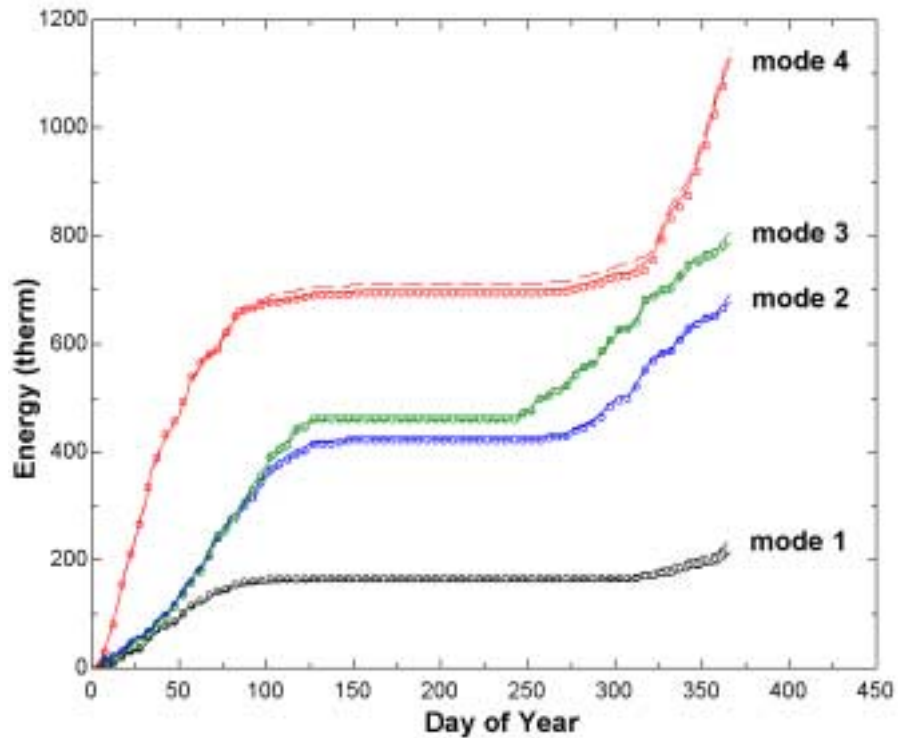


Figure 11.3.1 Operating energies for case 7 run with 15 minute (points), 30 minute (solid line), and 60 minute (dashed line) timesteps.

11.4 Synopsis

The structure of internal gains has no noticeable effect on annual performance parameters, but the way in which the gains are structured can strongly influence how energy is stored and utilized within the solar system (figure 11.1.1). If uniform gains are assumed, the simulation will predict a lower utilization of the storage within the system. This may lead designers to believe they can reduce storage capacity and still achieve optimal performance, while in reality the additional storage is required for optimal performance.

The effects of sol-air temperature are significant and should always be included in any simulation. Like the structure of internal gains, the sol-air temperature lowers heating demands during mid-day (on sunny days) and forces the solar system to utilize storage to a higher degree. The sol-air temperature also reduces losses from the building shell, thereby lowering total energy demands from 2,313 therms when the sol-air temperature is neglected to 2,029 therms when it is

included in simulations of the McKay center. The increase of 14 percent in total energy demands lowers key performance parameters (the ERF and CRF) by 10 percentage points indicating that the sol-air temperature has a strong influence on total system performance. If the designer were to neglect the effects of the sol-air temperature then the array would likely be oversized with inadequate storage.

The choice of simulation timestep has a moderate effect on simulation performance. Increasing the timestep from 15 to 60 minutes increases the auxiliary requirements by 2 percent causing a decrease of 2 percentage points in key performance metrics (the ERF and CRF). The daily response of the system was similar across all timescales however (figure 11.3.1), indicating that it may be possible to use larger timesteps to assess behavior under a wide range of conditions, and to then reduce the timescale to produce final simulation results. With current simulation times of approximately 3 hours on a Pentium II 450 MHz machine for a 15 minute timestep, the 4X reduction that could be achieved with a 60 minute timestep would allow many more variations in the system design to be explored. Ultimately, the effects of the simulation timestep must be evaluated for each design and control strategy.

12 Discussion and Recommendations

The conclusions of this study fall into several categories ranging from the effects of component degradation on system performance to the accuracy and application of calibration techniques. Many of the conclusions and findings of this study have been non-intuitive, and in some cases outright counter-intuitive in that the model yielded results that were at first not believed, but were later verified through physical inspections. By handling the complex interaction of components at the McKay center, the simulation models reduced the system to a handful of user adjustable parameters and key performance metrics that could be easily understood and interpreted.

12.1 Component Degradation and System Performance

Life cycle degradations in the pebble beds, which were characterized by large flow non-uniformities and high box loss coefficients, had almost no noticeable effect on overall system performance. While prior recommendations specified high pressure drops for uniform flow in pebble beds (Close 1965, Duffie and Beckman 1992), the behavior of the actual non-uniform beds at the McKay center under simulations employing optimal control showed no measurable deterioration in performance. This lack of systems level performance degradation is in agreement with the findings of Hollands (1984), who reported overall performance losses of less than 2 percent in non-uniform beds through simulation. Effects of insulation within the bed were evaluated for bed loss coefficients of 0.65 and 7.5 W/m²-C, which are representative of the current box with no insulation and one insulated with 2" of polystyrene. The use of polystyrene within the box increased system performance by only 1 percentage point. This small improvement is caused by a counteracting response in the collector array, which operates at a lower efficiency due to the higher bed outlet temperatures of the insulated box.

Deterioration in performance of the collector arrays due to the possible effects of deposits and condensation within the cover system and air infiltration was characterized by a decrease in $F_r(\tau\alpha)$ from 0.57 to 0.48 in the basement array and from 0.58 to 0.49 in the office array. The loss coefficient of the arrays, as defined by $F_r U_L$, also degraded from 3.21 to 4.01 W/m²-C for the basement array, and from 3.24 to 3.91 W/m²-C for the office array. These degradations in collector performance translated more directly into system level performance, lowering the solar fraction by 12 percentage points.

The largest factor affecting system performance at the McKay center was not attributable to any physical component, but was due entirely to the control logic that operated the components. The combination of poor sensor placement and failure to close MD-1 during idle periods resulted in a 16 percentage point degradation in the solar fraction. This result stresses the need to properly install and validate operation of system controls.

12.2 Recommendations and Future Work

Recommendations for the McKay center are focused on repairing those items that have contributed most to the loss of system performance. The malfunction in damper operation has already been repaired by a patch in the control logic. Implementation of an optimal control scheme is also being worked on, and will likely be based on duct sensors TS-7 and TS-8. Only an outline of this scheme can be referred to here as it is still in development, but in simple terms the micro-controller in the system will calculate the energy stored in the bed by directly calculating equation 8.1.3 using temperature sensors TS-7 and TS-8. Once the stored energy surpasses a certain threshold, a binary flag will be set to one in the logic to acknowledge that there is energy in the bed and that mode 2 can be enabled if a heating call is made. The binary flag will be reset to zero when the duct sensors TS-7 and TS-8 indicate that operation of the bed in mode 2 results in a COP (equation 10.1.4) of less than 3. Future modeling efforts will focus on determining the proper charging threshold that closest approximates optimal control of the system⁵. The results of this technique will be interesting in that it will use inferred measurements of bed energy instead of actual sensor values.

Restoration work on the collector array has already begun in the planning phase with a small grant of \$2,500 secured for reworking the existing cover systems. Restoration entails removing all cover systems, separating the glazings from the aluminum spacers, and re-attaching a single glazing to newly brazed aluminum spacers and installing them back into the array. Although the new single glazed covers will result in performance below that of the of the original collectors, they will avoid the pitfall of pressure variations between the covers that compromised the original design. Apparently, Solaron discovered this pitfall (pressure variations in double covers) the year after the series 2000 collectors were purchased for the McKay center. The Solaron 3000 series collectors, which were introduced in 1978 employed a selective absorber

⁵ This modeling work will be performed by the author in conjunction with the controls engineer at the physical plant

with a single glazing. The rest of the solar industry appears to have learned the same lesson and nearly all collectors on the market today employ single glazed selective absorbers.

Of all the components at the McKay center, the pebble beds have weathered time the best. It's rather hard to break a pile of rocks, and the sheer simplicity of the pebble beds makes them the most elegant form of thermal storage your author could imagine. Even with the high flow non-uniformities and low insulating qualities, the beds showed less than a 1 percent degradation on system performance relative to the original design conditions. Additionally, the fear of possible mold growth in the beds has proved unfounded at the McKay center, and spore counts in the air leaving the bed are at $1/10^{\text{th}}$ the level of the outside air. The only deterioration of concern within the beds is the delamination of the plywood cover. Although the flow non-uniformities caused by the delamination are not currently causing any significant degradation, if the edge that is supported by the center divide should fall the entire bed surface would be covered. If this were to happen, the airflow through the beds would be blocked to such a degree that the static pressure drop across the bed might burn out the motor in the solar air handler. For this reason, it is suggested that blocks be removed from the retaining wall in the upper plenum and the delaminated cover be torn apart⁶ and removed from the plenum.

Plywood covers should never be used in pebble beds without a separation layer of sheet metal or other appropriate material. The extremes of temperature and humidity experienced by the bed covers in the McKay center have caused successive contraction and expansion leading to delamination. A sheet metal or other skin placed on the underside of the plywood would have prevented the delamination from falling into the plenum and should be incorporated into future bed designs.

The largest obstacle to maintaining the long-term performance of solar thermal systems is not the components themselves, but the manner in which they are controlled. The components may be the most efficient available, but if they are not controlled optimally, the efficiency of the system will not reflect that of the components. A good illustration of this follows from a story told by Greg Armstrong, director of the McKay Center and UW Arboretum. Greg recalled that some years back people working in the basement complained of a whine that had been coming from the solar equipment room for some months. When personnel from the physical plant finally inspected the equipment they discovered that the fan belts were entirely shredded and the fan motor was spinning freely. For months the system controller had been blindly running the system

⁶ The delamination appears to consist of only one paper thin section that can easily be torn and removed piecewise.

as though nothing were wrong. More recently, the physical plant staff serviced the air handlers this past winter and discovered that the fan bushings were worn away. Again, the system had been running at decreased capacity due to friction on the fan shaft. As a final example, Dan Dudley discovered during his 1987 investigation that the solar system had made no contribution to the load for the past 4 years! At fault were burned out motors located in the air handler cabinets and faulty damper operation.

Bill Beckman once joked that people often assessed whether solar systems were operating by running outside to see if the sun was shining and then quickly running back inside and grabbing the collector return pipe. If the pipe was hot the system worked, and if it was cold it was broken. Laugh as we may, this simple method of troubleshooting would be an improvement over nothing at all, which often represents the diagnostic capabilities on many systems. The single largest benefit that could be added to most systems would be a set of diagnostics built into the controller that could detect common faults in the system and alert the user in a manner similar to fault indicators on the dashboard of modern automobiles. The question is how to construct such diagnostic tools at a reasonable cost.

Although the data set used for modeling the McKay center consisted of 12 temperature sensors in each zone HVAC system, the entire solar system could be modeled using just 3 sensors located as indicated in figure 12.3.1. The two sensors in the solar loop can be used to calibrate both the array and the pebble beds. Moreover, if airflows within the solar loop are initially measured, the box parameters can be calibrated to measure the flow as described in section 5.1.1. Any decrease in flow rates caused by slipping of fan belts or worn bushings can then be discovered by the speed of the thermal waves passing through the bed. Additionally, any infiltration into the solar loop can be measured by these sensors and would appear as sudden increases in the loss coefficient of the collector array or pebble beds. Since it is unlikely that the insulating properties of either component would significantly change, the loss can likely be attributed to infiltration. The location of infiltration can be further isolated to the array or pebble bed side of the solar loop depending on which loss coefficient increases (i.e. the loss of the bed or $F_r U_L$ of the array). This method of fault detection requires that the original system performance be initially evaluated to provide “baseline” parameters that define proper performance.

It is recommended that such a baseline be established in all large systems as part of the acceptance criteria of the construction contract. If the system cannot meet design criteria at installation, then it was not properly installed and adjustments must be made before the contract is

released. The performance of the system during the acceptance run can then be used as the baseline in future fault detection. Your author regrets not having more time to explore the ability of a two sensor model to predict system faults, but strongly feels that it will be successful, and hopes it will be pursued.

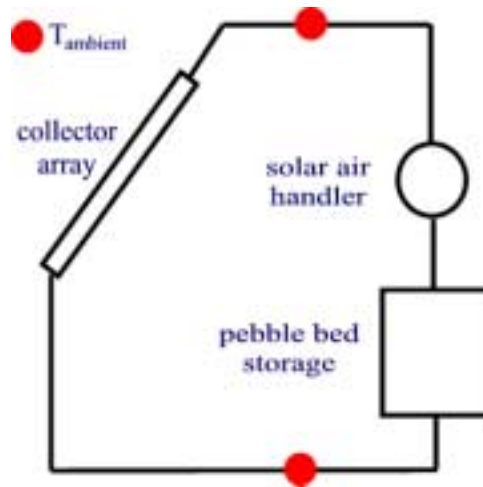


Figure 12.2.1 Schematic of ideal diagnostic sensor locations for air based systems.

12.3 A Narrative on Component and System Calibrations

In writing many sections of this thesis, the objective prose demanded by technical writing stripped the pure facts from 2 years of work and arranged them in a logical progression. The real story of the McKay center actually followed a series of paths, but only the most direct path was discussed in the main text of this study. What follows is a narrative of how these paths were found (at times by literally being stumbled upon) and provides an explanation how many things described in the previous pages came to be.

I remember sitting across a table from Bill Beckman in the Solar Lab over a year ago describing how I was proposing to calibrate the pebble beds, and I can recall his response: “there’s no way that will work.”

Sometimes breakthroughs are the result of attempting the impossible simply because you didn’t know any better. Never having had any previous experience with pebble beds, I’d attempted to calibrate them based on two temperature sensors. The process of calibrating pebble beds using two sensors relied on the sheer power of today’s current numerical engines. The numerical code was provided the objective of matching the measured bed outlet temperature

using two parameters that described the flow distribution (equation 5.2.2). The key aspect of such an approach is that we needn't know anything about how the flow passes through the bed so long as it obeys the laws of thermodynamics and heat transfer. The agreement provided by such an optimization was beyond expectations, but the resulting flow distributions and bed losses appeared unreasonable given the physical construction of the box. The optimized model predicted a 3:1 flow non-uniformity and a bed loss coefficient 11 times the expected value. One of the small triumphs of this study is that the model predictions were validated by visual inspections of the bed plenums, and the corroboration of the loss coefficient through independent measurements made by the bed sensor (TS-9).

The bed calibrations represent a clear example of the insights that can be achieved through a combination of proper thermodynamic models and numerical tools. With a model using only the temperature of the air entering and exiting the bed, it was possible to predict what was occurring within the bed, and to calibrate the bed parameters appropriately. In past experiments by Persons (1978) and Hollands (1984), arrays of several dozen thermocouples were staggered through the bed to provide the same insights. I'd imagined that such instrumentation might be required at the McKay center, but in my naïveté had attempted to calibrate the beds regardless. The result of that effort was a discovery that the beds loss and flow distributions can be calibrated using only two temperature sensors provided numerical optimization tools are available.

I should also confess at this point that the 2-point collector calibration method was stumbled upon by chance. In working with the 5,000,000 point data set from the system calibration interval, the treatment of daylight savings time created timing discrepancies between the temperature data recorded at the center and the radiation data recorded by NOAA. Variations in timing as small as 10 minutes could skew the operating points on the SRCC charts making it impossible to perform regression analysis for the collector parameters.

Timing discrepancies were resolved by using the measured temperatures at the center to back out the incident radiation with the Hottel-Whillier collector model⁷. This radiation value, which was entirely based on the data from the McKay center was then compared to the radiation recorded by the NOAA data logger. The comparison showed that after daylight savings time the radiation predicted by the McKay was perfectly shifted and peaked one hour after solar noon. This was caused by the Windows operating system on the data recorder at the McKay center

⁷ Approximate values of $F_r(\tau\alpha)$ and $F_r U_L$ must be supplied in order to calculate the radiation

resetting the clock. A comparison of the two predicted radiation values also showed that the temperature based radiation value always settled above zero during the night on one array and just below zero at night on the other array. Theoretically, both collectors should have predicted an irradiance of zero if the value of $F_r U_L$ was correct. It was at this point that the accuracy of the assumed incidence angle modifiers was questioned and found to be at fault, and calibrations of the collectors parameter $F_r U_L$ were based on night-time data.

The use of night-time operation to calibrate collector parameters is not obvious when current methods focus exclusively on noon-time testing. Night-time testing has several benefits however in that $F_r U_L$ can be calculated without any knowledge of solar radiation or effects of incidence angles. Austin Whillier supposedly performed this type of calibration during his research at MIT⁸ during the 50's. The fact that such a useful method has disappeared in the interim still confounds me, and it's ironic that it took a timing error in the data sets to stumble across the usefulness on night-time data.

Of all the lessons learned in this study, both by accident and purposeful, the most important was the value and insight that could be provided by proper modeling of the systems. All of the faults discovered in this study were initially found by modeling techniques, where the model would produce a solution that differed from the measured data. Sitting behind a desk on the 13th floor of the engineering research building late at night, ideas of what could have physically caused the discrepancy were coded into the model. Only after simulations predicted that the change coded into the model resolved the discrepancy were visual inspections made to validate that such a physical change actually existed in the system.

Visual inspections were not arbitrarily made in the bed plenums or for the operation of the motorized damper MD-1. Instead, the simulation predicted that there had to be faults at these locations, which led to visual inspections that identified the cause in every case. As a prime example, the simulation predicted that the temperature profile of the bed under discharge conditions could not physically follow the measured value described in section 5.10. Within an hour of this discovery I walked into the McKay center, through the basement, and directly to the electrical junction box labeled TS-7. Two screws were removed and the fault that had been predicted an hour before was lying on the cover (see figure 5.10.2). The mastic putty that sealed

⁸ I have yet to obtain an actual copy of Austin Whillier's dissertation to confirm whether he performed night-time testing, but personal correspondences with those active in the solar thermal field indicate that he did test using a similar method.

the access hole to the temperature sensor had melted away leaving the sensor exposed to infiltration of air through the access hole. It is hard to imagine that such a subtle fault could be predicted from a dataset of duct temperatures, but this is where the power of numerical models becomes evident.

Models that have been properly calibrated to the data set will be able to detect any number of faults within the data, and if the model is a physical one (as opposed to neural networks) then it can pinpoint the cause of the fault and predict the performance of the system after the fault has been corrected. It is this power of numerical simulations that was exploited in this study to calibrate the systems at the McKay center, locate the existing faults, and to predict the original performance by correcting the parameters that described the faults.

Bibliography

Adebisi, G.A., and D.J. Chenevert, "An Appraisal of One-Dimensional Analytical Models for the Packed Bed Thermal Storage Systems Utilizing Sensible Heat Storage Materials", *Trans. ASME J. Energy Resources Technology*, Vol. 118, 1996.

ASHRAE (American Society of Heating, Refrigeration, and Air-Conditioning Engineers Inc.) "ASHRAE Fundamentals Handbook", ASHRAE, 1997

Borrenson, B.A., "Thermal Room Models for Controls Analysis" *ASHRAE Transactions*, Vol. 87, Part 2, 1981

Close, D.J., "Rock Pile Storage for Comfort Air Conditioning" *Mech. And Chem. Engr. Trans. Of the Inst. of Enginers*, 1965

Cole-Appel, B.E., G.O.G. Löf, L.E. Shaw, and B.B. Fischer, "The Improvement of Solar Air Collectors – Study and Experimental Research Project" *DOE Contract Report EY-76-C-04-3713*, Solaron Corp., 1978

Daly, H.E., and K.N. Townsend "Valuing the Earth: Economics, Ecology, Ethics", MIT Press, 1996

Duffie, J.A., and W.A. Beckman, "Solar Engineering of Thermal Processes", 2nd Edition, John Wiley & Sons, 1991

Hill, J.E., and E.R. Streed, "Method of Testing for Rating Solar Collectors Based on Thermal Performance" *Solar Energy*, Vol. 18, 1976

Hottel, H.C., and A. Whillier, "Evaluation of Flat Plate Collector Performance" *Trans. Of the Conference on the Use of Solar Energy*, Vol. 2, Part 1, Univ. of Arizona Press, 1958

Hollands, K.G.T., T.E. Unny, G.D. Raithby, and L. Konicek, "Free Convection Heat Transfer Across Inclined Air Layers" *ASME J. of Heat Transfer*, Vol. 98, 1976

Hollands, K.G.T., and E.C. Shewen "Optimization of Flow Passage Geometry for Air-Heating, Plate-Type Solar Collectors" *ASME J. Solar Energy Engineering*, Vol. 103, 1981

Hollands, K.G.T., H.F. Sullivan, and E.C. Shewen "Flow Uniformity in Rock Beds" *ASME J. Solar Energy Engineering*, Vol. 32, No. 3, 1984

- Hughes, P.J., "The Design and Predicted Performance of Arlington House" *Masters Thesis*, U. of Wisconsin Madison, 1975
- Hughes, P.J., S.A. Klien, and D.J. Close, "Packed Bed Thermal Storage Models for Solar Air Heating and Cooling Systems" *Trans. ASME J. Heat Transfer*, Vol 98, 1976
- JAMA (Journal of the American Medical Association), Highlights from the ALA/ATS meeting 1997, available online www.ama-assn.org (1997).
- JAMA (Journal of the American Medical Association), Asthma Information Center, available online www.ama-assn.org (2000).
- Jeffreson, C.P., "Prediction of Breakthrough Curves in Packed Beds" *AIChE Journal*, Vol. 18, No. 2, 1972
- Klein, S.A., "EES – Engineering Equation Solver" *User Manual*, 2000
- Krarti, M., "Time Varying Heat Transfer From Partially Insulated Basements" *Int. J. Heat Mass Transfer*, Vol 37, No. 11, 1994
- Latta, J.K., and G.G. Boileau, "Heat Losses From House Basements" *Canadian Building*, Vol. 19, No. 10, 1969
- Levy, J., J.D. Spengler, D. Hlinka, and D. Sullivan "Estimated Public Health Impacts of Criteria Pollutant Air Emissions from the Salem Harbor and Brayton Point Power Plants" A report by the Harvard School of Public Health, May (2000).
- Lof, G.O.G., and R.W. Hawley, "Unsteady State Heat Transfer Between Air and Loose Solids" *Ind. and Engr. Chemistry*, Vol. 40, 1948
- Menzi, B. Personal Communication, 2000
- NREL (National Renewable Energy Laboratory) www.nrel.gov (2000)
- Oonk, R.L., G.O.G. Lof, L.E. Shaw, and B.E. Cole-Appel, "A Method of Comparing Flat-Plate Air and Liquid Solar Collectors for Use in Space Heating Applications" *Joint Conference Proceedings of ASES, ISES, and the Solar Energy Society of Canada*, 1976
- Perez, R., R. Seals, R. Ineichen, R. Stewart, and D. Menicucci, "A New Simplified Version of the Perez Diffuse Irradiance Model for Tilted Surfaces" *Solar Energy*, Vol. 39, 1987

- Persons, R.W., "Rock Bed Storage Performance – Arlington Solar House" *Masters Thesis*, U. of Wisconsin Madison, 1978
- Riaz, M., "Analytical Solutions for Single and Two-Phase Models of Packed-Bed Thermal Storage Systems" *ASME J. of Heat Transfer*, Vol. 99, 1977
- Sadler, G.W., and E.Y. Leung, "A Summary of Operation Results for the Air Solar Heating System for Module 6 of the Alberta Home Heating Research Facility" *Solar Energy*, Vol 40, No. 2, 1988
- Schumann, T.E.W., "Heat Transfer: A Liquid Flowing Through a Porous Prism" *J. Franklin Inst.*, Vol. 405, 1929
- Solar Energy Laboratory, "TRNSYS – A Transient System Simulation Program" *User Manual*, 2000.
- Solaron Corp. Installation Manual for Series 2000 Collectors, (1977).
- Souka, A.F., and H.H. Safwat, "Optimum Orientations for the Double Exposure Flat-Plate Collector and Its Reflectors" *Solar Energy*, Vol. 10, 1966
- Sparrow, E.M., J.W. Ramsey, and E.A. Mass, "Effect of Finite Width on Heat Transfer and Fluid Flow About an Inclined Rectangular Plate", *ASME J. of Heat Transfer*, Vol. 101, 1979
- Wallace, L.S., "Descriptions, Problems. And Performance Data of the Arlington Solar House" *Masters Thesis*, U. of Wisconsin Madison, 1978
- Whillier, A. "Solar Energy Collection and Its Utilization for House Heating" *Doctoral Dissertation*, Massachusetts Institute of Technology, 1953
- Wyle Laboratories "Indoor Test for Thermal Performance Evaluation of Solaron (Air) Solar Collector" *DOE/NASA Contractor Report CR-150572*, 1978.

Appendix A History of Dairy Forage and Vet-Med Center

The solar installations at the Dairy Forage and Veterinary Medicine (Vet-Med) centers are inherently different from the McKay center. These systems have no storage component, and the collector arrays form the structural roof. Whereas the system at the McKay center is still functional, the collector array at the Dairy Forage center was removed in 1995, and the array at the Vet-Med center may suffer a similar fate. The collector arrays in both system have not held up structurally, and the subsequent water damage caused to the buildings has resulted in calls for their removal. Although neither of these systems was studied in detail, a short oral history on each is provided here for reference.

Vet-Med Center

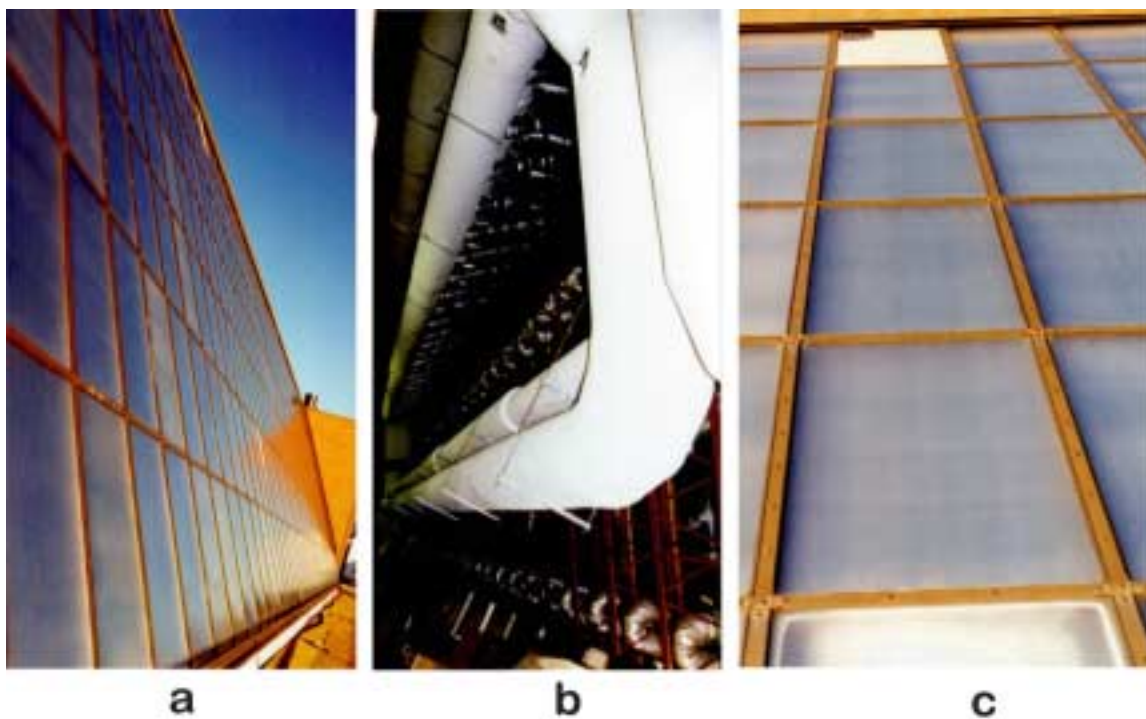


Figure A1 Collector array at Vet-Med center (a). Insulated supply and return ductwork (b). Shattered cover system (c).

The installation at the Vet-Med center is comprised of 360 Suncell collectors manufactured by Research Products of Madison Wisconsin, which were installed in 1982 for a cost of

approximately \$110,000. The collectors are used to preheat the ventilation air for two air handling units servicing the bovine area located on the bottom floor of the building¹. The collectors are connected in a series arrangement of two, and each side of the array (East and West) is ducted to a separate air handling unit. Figure A1b shows that each collector requires a separate connection (shown by the short u-bends of foil faced ducts), which is significantly more complicated than the internal manifolds of the Solaron products.

The Suncell collectors employ double glazing covers made from patterned low iron glass that does not appear to have flamed edges and is likely not tempered². In discussions with the site supervisor, several dozen panels were replaced at great expense during the early 1990's due to moisture penetration inside the covers³. Nearly all the panels in the array have moisture and deposits inside the covers, including those that were replaced. Figure A1c shows an extreme example of collector degradation where both glazings in a collector on the top row have shattered. This shattered collector along with leaks in the weather-stripping and flashing are currently causing water damage to documents stored below the array.

The control system operating the array also failed, and has since been replaced with a small photosensor installed by the physical plant. Although the system is functional (i.e. it is still physically able to preheat the ventilation air), it was not functioning during the author's last visit to the site in the spring of 1999⁴. Also, bushings in the solar booster fans⁵ were worn to a degree that made the fans unusable, but they have since been replaced by the physical plant.

It is an interesting note to mention that the solar system was installed at the expense of a small food court that would have been built for the students⁶. The poor reliability of the array, and issues of water damage have not left a good impression of solar at this site, especially since they are now left with a leaking \$110,000 solar array instead of a place to eat.

Dairy Forage Center

The exact construction of the system at the dairy forage center is not known because it was removed in 1995 due to leaks that were causing excessive water damage to the building. Discussions with building maintenance personnel indicated that the system had not been operated

¹ Animal stock pens like the bovine area are required to have a 100 percent ventilation rate.

² The cover system appears to be made out of glass used in interior fluorescent lighting fixtures.

³ Replacement of the covers requires a large hydraulic lift to access the panels.

⁴ This is likely due to an error in the controls, and when first inspected during March of 1999 the photosensor was found fully taped over, presumably in an effort to disable the system.

⁵ Booster fans are located on the outlet of the collector array before they feed into the main air handler.

⁶ Because of budget constraints, the food court was eliminated and the solar array installed instead

since 1985. The solar system was constructed at the same time as the original building in 1978, and is believed to have used the same Suncell collectors as the Vet-Med center, but this cannot be verified. From inspections of the remaining ductwork, the system appears to have been a direct preheater for the main air handlers operating from the zone return air. An air-water heat exchanger was installed in the ductwork to provide hot water for the building.

The double glazed covers on the collectors experienced the same problems as those at the Vet-Med and McKay centers where seals were broken and moisture and deposits accumulated between the covers. During the early years of operation (1978-1985), any covers with moisture penetration were replaced. The average replacement rate was 6 covers per year at an installed cost of \$1,000 per cover. At this rate, it is almost certain that the annual maintenance costs exceeded any possible fuel savings from the system.

Design “Accidents”

Apart from obvious design and construction mistakes in the collector covers and weather-stripping, several errors were made in the physical layout of both systems indicating the inexperience of the designers. A good example is the hot water heat exchanger installed at the dairy forage center. This heat exchanger never contributed to the hot water load in the building because the total load could be supplied by steam traps in the heating system. Steam supplied by the district heating system on campus must continually run through the circuits so that it does not condense. Although the flow rate is greatly reduced when there are no heating demands, the energy contained in the idle flow rate was sufficient to preheat the full hot water load through the steam traps located in the water heater. The installation of the heat exchanger in the solar system was therefore superfluous and unnecessary.

At the Vet-Med center a mode of operation appears to be possible where the collector loop is isolated from the air handler when solar energy is available, but there are no heating demands. During these periods the air is re-circulated in the solar loop by the booster fan until a heating call is made. At this time the collector loop is again opened to the main air handler and ventilation intake to supply preheated air.

It is not known why the designer did not let the collectors stagnate during these idle periods. If the array had simply been left to stagnate, then the thermal capacitance of the stagnated absorber plate would supply more energy to the load than if the air had been re-circulated. Also, the parasitic load consumed by the booster fan could be eliminated.

Another issue at Vet-Med center concerns the exhaust from the solar array during the summer. During the summer, the solar booster fan is run and a damper diverts the exhaust from the solar array to an outside air vent. This was apparently done to avoid the high stagnation temperatures that the designer must have thought would damage the array. Not only are the parasitic loads from the booster fan significant during this period (the booster fan uses a several horse-power motor), but the choice of location for the exhaust of the solar array could not have been worse. By locating the solar exhaust duct within ten feet of the air intake for the main air handler, the designer imposed a significant cooling load on the system. Discussions with personnel from the physical plant, and initial measurements made on the system for this study indicated that a portion of the solar exhaust was picked up by the main air handler raising the intake air several degrees above the ambient, and therefore added a sensible load to the cooling coils. The collector array should have been designed to stagnate during the summer to avoid the complications caused by venting the system during the summer.

Appendix B Air Handler Flow Rates

The tables below list the air velocity measurements used to calculate air handler flow rates. These velocities have been corrected to account for the offset in the Solmat hot wire anemometer and thus represent calibrated values. All air velocities represent 90 second averages expressed in units of feet per minute.

Single measurements were made for the main air handlers on the negative pressure side of the fans. Air flow rates for the solar air handlers are the average of two readings taken from the negative pressure side of the fan just before the solar air handler and another on the positive pressure side after the pebble beds near the location of TS-4.

Table B1 Velocity distribution on negative pressure side of office solar air handler. Duct size is 3 square feet yielding a volumetric flow rate of 1,998 CFM.

Distance (in)	7.5	23	38	53.5	68.5	84
4	584	481	716	742	564	272
11.5	629	625	720	786	612	618
19	679	713	791	828	742	602
26.5	656	743	692	779	813	598

Table B2 Velocity distribution on positive pressure side of office solar air handler. Duct size is 3.47 square feet yielding a volumetric flow rate of 2,156 CFM.

Distance (cm)	10	30	50	70	90
4	996	911	470	192	279
12	1078	1008	567	158	249
20	1122	1015	692	179	185
28	1049	1070	764	252	189

Table B3 Velocity distribution on negative pressure side of basement solar air handler. Duct size is 1.77 square feet yielding a volumetric flow rate of 1,247 CFM.

Distance (cm)	4.5	13.5	22.5	31.5	40.5
4.5	463	433	433	454	591
13.5	656	715	709	713	817
22.5	663	736	762	813	941

31.5	594	683	733	786	1023
40.5	596	680	722	838	1062

Table B4 Velocity distribution on positive pressure side of basement solar air handler. Duct size is 2.11 square feet yielding a volumetric flow rate of 1,273 CFM.

Distance (cm)	10	30	50	70	90
2.5	463	433	433	454	591
7.5	656	715	709	713	817
12.5	663	736	762	813	941
17.5	594	683	733	786	1023

Table B5 Velocity distribution on negative pressure side of office main air handler. Duct size is 4.84 square feet yielding a volumetric flow rate of 2,377 CFM.

Distance (cm)	10	30	50	70	90
9	145	131	94	121	123
18	500	645	584	559	572
27	551	542	636	571	575
36	678	616	764	715	693

Table B6 Velocity distribution on negative pressure side of basement main air handler. Duct size is 1.87 square feet yielding a volumetric flow rate of 2,093 CFM.

Distance (cm)	6	18	30	42	54
6	710	1039	754	870	874
12	1228	1201	920	1043	1214
18	1256	1307	1075	1179	1419
24	1105	1381	1221	1277	1281

Table B7 Velocity distribution on negative pressure side of lecture hall main air handler. Duct size is 1.87 square feet yielding a volumetric flow rate of 2,174 CFM.

Distance (cm)	6	18	30	42	54
6	780	947	1147	567	851
12	853	1197	1312	1281	1314
18	904	1308	1419	1399	1386
24	895	1304	1451	1439	1455

Appendix C TRNSYS Simulation Framework

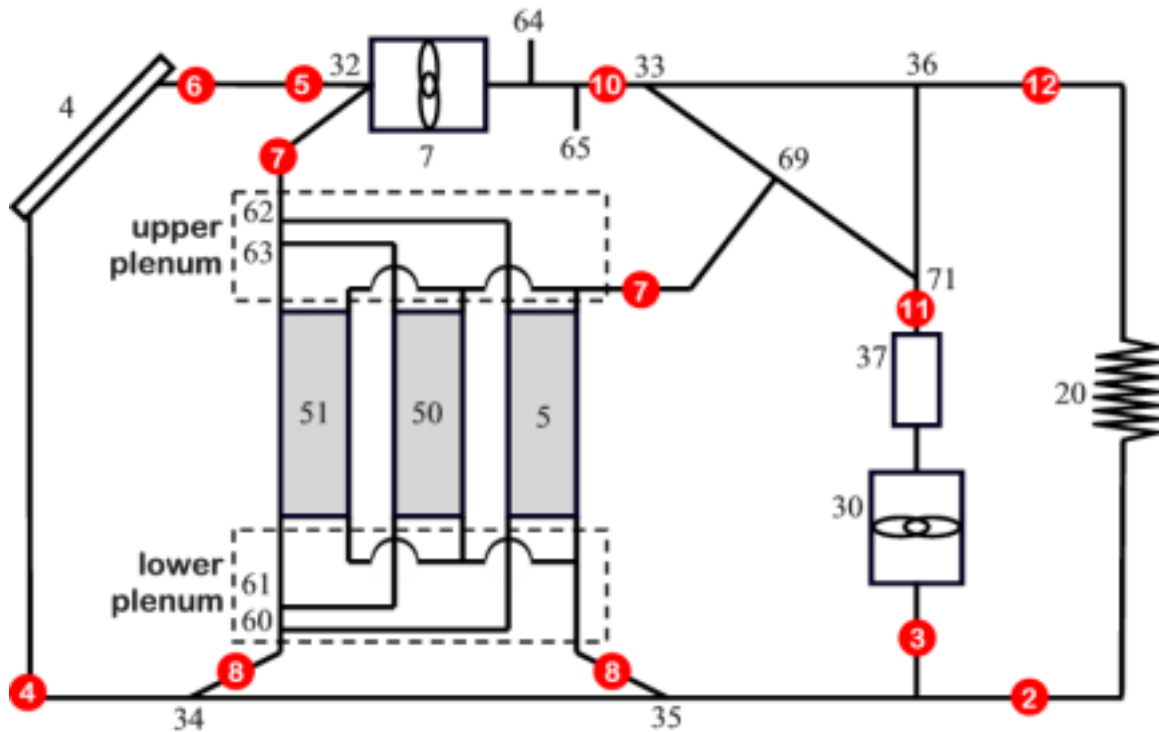


Figure C1 Schematic of TRNSYS simulation model for HVAC systems in basement and office zones. Simulation components are labeled with the logical unit numbers of the TRNSYS simulation code. Modeled locations of installed temperature sensors (TS-2 through 12) are shown in circles.

Figure 1 shows the component layout used to model the solar and auxiliary HVAC systems within TRNSYS. Table C1 provides a listing of each component, the TRNSYS type describing it, and a short description. The HVAC system model is directly coupled to the building model in the simulation code by viewing the zone air mass (unit 20 of figure C1) as a heat exchanger with an effectiveness of unity. Thermal energy delivered by the HVAC system is calculated from the mass flow rate through the duct, and the supply and return temperatures assuming that the zone air mass has a homogenous temperature such that

$$q_{HVAC} = \dot{m}_{HVAC} C_{air} (TS_{12} - TS_2) \quad [1]$$

Both the supply temperature (TS-12) and flow rate are determined by the flows of the solar air handler (unit 7) and auxiliary furnace (unit 37), which are combined at a mixing tee (unit

36) before being supplied to the zone. The return air temperature (TS-2) is that of the zone air mass, which is solved implicitly at each timestep.

Table C1 Listing of logical unit numbers, TRNSYS types, and descriptions for components shown in figure 1.

Unit #	Type	Description
4	1	Solar collector array
5	10	Pebble bed (segment 1)
7	3	Solar air handler
20	12	Zone air mass
30	3	Main air handler
32	11	Controlled flow mixer representing motorized damper
33	11	Controlled flow diverter representing motorized damper
34	11	Controlled flow mixer representing motorized damper
35	11	Controlled flow diverter representing motorized damper
36	11	Mixing Tee for solar and main air handlers
37	6	Auxiliary furnace
50	10	Pebble bed (segment 2)
51	10	Pebble bed (segment 3)
60	11	Final mixing tee representing lower plenum of pebble bed
61	11	Initial mixing tee representing lower plenum of pebble bed
62	11	Final mixing tee representing upper plenum of pebble bed
63	11	Initial mixing tee representing upper plenum of pebble bed
64	11	Mixing tee representing infiltration leak into solar air handler
65	11	Controlled flow diverter representing exhaust of infiltration leak
69	11	Mixing tee representing combination of solar and main air handler flows into upper bed plenum
71	11	Controlled flow diverter representing backflow of main air handler through MD-1 and into pebble beds

Control and direction of airflow within the solar system is governed by the motorized dampers, which are modeled by units 32, 33, 34, and 35. Although only one supply and return

duct service the pebble beds in the physical system, two must be used in the simulation model as there is no simple way of including bi-directional duct flow within TRNSYS. In either charging (mode 3) or discharging (mode 2), the flows into the three bed segments (units 5, 50, and 51) are forced by a common supply temperature and the calibrated flow percentages from table 7.14.1. Resulting bed exit temperatures are computed from the exhaust of the mixing tees on each bed segment by units 60 and 61, which represent the lower bed plenum, and units 62 and 63, which represent the upper bed plenum. The two locations of the pebble bed duct sensors (TS-7, TS-8) are required to reflect the proper temperature depending on the mode of operation for the beds.

Three units exist in the simulation model to reflect faults in the physical system. The flow inlet (unit 64) and exhaust (unit 65) ports after the solar air handler represent the infiltration leak through the drive belt slot in the solar air handler. The mixing tee at the supply to the upper bed plenum (unit 69) reflects the possibility of leakage in the motorized damper (MD-1) that separates the solar from the main air handler. Unit 69 allows a portion of the main air handler to flow back through the damper and enter the pebble beds, effectively discharging them.

Appendix D CD-ROM Files

All the simulation code, output files, and electronic copies of this thesis are included on the accompanying CD-ROM. The reader is free to use these materials so long as the original source is cited. The TRNSYS simulation code and TRNSED files can be used to study scenarios that have not been included in this study. Copies of the simulation cases described in section 10 are included and can form the basis of further study. The original data sets recorded from the McKay center are also included.

TRNSYS Program Files

A fully functional and compiled version of TRNSYS 15 is included in the directory //TRNSYS15/. This directory must be copied directly to the root directory of the C: drive on any machine that will be used to run simulations included on the CD-ROM. Other versions of TRNSYS are not compatible with the simulation decks as the simulations contain some proprietary unit types that are not defined in standard versions of TRNSYS.

Weather & Recorded Data Files

Weather and data files common to all simulation runs are contained in //TRNSYS15/Weather/ on the CD-ROM. The following is a list of the applicable files in this directory:

- airport_daily.txt: 1999 daily snow cover, wind speed, and wind direction recorded by NOAA at Madison airport.
- basement.txt: 1999 temperature and mode data recorded for basement zone at McKay center in 15 minute intervals.
- isis.dat: 1999 irradiance data from NOAA instrumentation cluster located on the roof of the Solar Energy Laboratory.
- lecture.txt: 1999 temperature and mode data recorded for lecture zone at McKay center in 15 minute intervals.
- madison.tm2: TMY2 weather data for Madison, WI.
- office.txt: 1999 temperature and mode data recorded for office zone at McKay center in 15 minute intervals.

- t_airport.dat: 1999 hourly temperature data recorded by NOAA at Madison airport.

The structure of these datasets can be interpreted by viewing the data-readers in the TRNSED files.

Processed Simulation Runs

Cases 1 through 8, as described in section 10 of this study, have been included on the CD-ROM in the directory //simulation runs/[case #]. All of the files contained in each case directory reflect the outputs of that run, and the parameters specified in the TRNSED deck reflect the exact conditions under which the run was made.

To re-run a simulation or to view the outputs from the summary interface (section 7.7), the contents from the appropriate case directory (//simulation runs/[case #]) must first be copied into the directory //TRNSYS15/examples/ on the C: drive of the host computer. From the examples directory, the user can then open the appropriate TRNSED deck to adjust the parameters and re-run the zone model. To view the results of the summary interface, open and run the deck titled "mckay_sum.trd". The on screen plot will then display the integrated thermal energies, costs, and emissions for that case. The text file labeled "mk_summary.out" will contain the integrated values of the online plot printed in 24 hour intervals.

Electronic Documents

Electronic copies of this thesis are included in the directory //documents/. The files thesis_press.pdf and thesis_port.pdf are press quality and compressed portable versions of the entire thesis respectively. The portable format is suitable for internet distribution while the press quality copy contains the original resolution of all charts and photographs suitable for printing as a high quality document. Depending on the copy of the CD-ROM, there may be a file titled thesis.doc, which is an editable version of this work in Word 2000 from which tables and figures may be copied and pasted into other documents.